

FACT (Version 2.0) - Subsurface Flow and Contaminant Transport Documentation and User's Guide

RECORDS ADMINISTRATION



R0186875

by

S. E. Aleman

Westinghouse Savannah River Company

Savannah River Site

Aiken, South Carolina 29808

L. L. Hamm

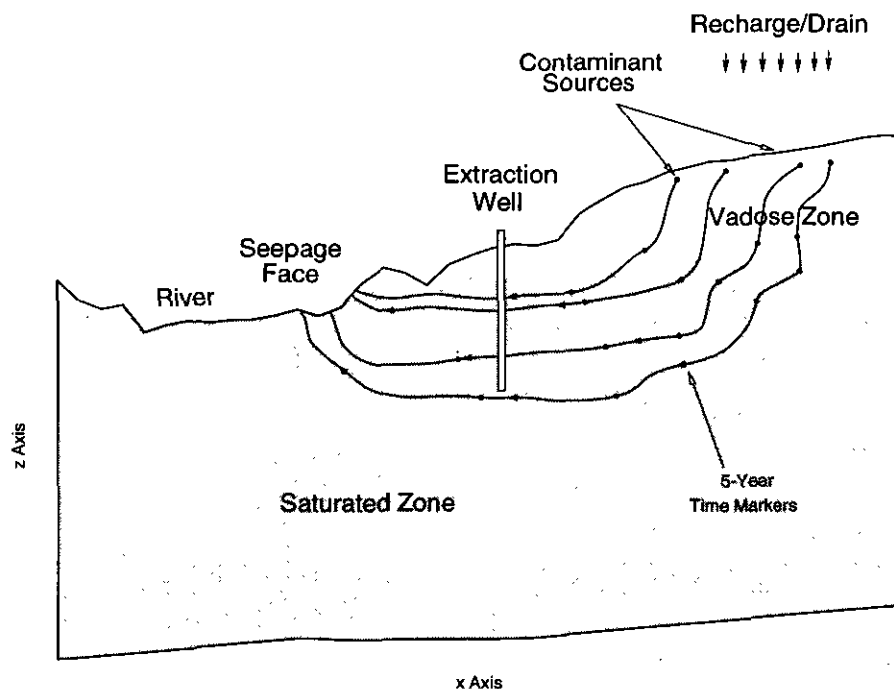
DOE Contract No. **DE-AC09-96SR18500**

This paper was prepared in connection with work done under the above contract number with the U. S. Department of Energy. By acceptance of this paper, the publisher and/or recipient acknowledges the U. S. Government's right to retain a nonexclusive, royalty-free license in and to any copyright covering this paper, along with the right to reproduce and to authorize others to reproduce all or part of the copyrighted paper.

FACT

(Version 2.0)

Subsurface Flow and Contaminant Transport Documentation and User's Guide (U)



Westinghouse Savannah River Company
Savannah River Site
Aiken, SC 29808

Prepared for the U.S. Department of Energy under Contract No. DE-AC09-96SR18500

DISCLAIMER

This report was prepared as an account of work sponsored by an agency of the United States Government. Neither the United States Government nor any agency thereof, nor any of their employees, makes any warranty, express or implied, or assumes any legal liability or responsibility for the accuracy, completeness, or usefulness of any information, apparatus, product or process disclosed, or represents that its use would not infringe privately owned rights. Reference herein to any specific commercial product, process or service by trade name, trademark, manufacturer, or otherwise does not necessarily constitute or imply its endorsement, recommendation, or favoring by the United States Government or any agency thereof. The views and opinions of authors expressed herein do not necessarily state or reflect those of the United States Government or any agency thereof.

This report has been reproduced directly from the best available copy.

Available for sale to the public, in paper, from: U.S. Department of Commerce, National Technical Information Service, 5285 Port Royal Road, Springfield, VA 22161, phone: (800) 553-6847

fax: (703) 605-6900

email: orders@ntis.fedworld.gov

online ordering: <http://www.ntis.gov/ordering.htm>

Available electronically at <http://www.doe.gov/bridge>

Available for a processing fee to U.S. Department of Energy and its contractors, in paper, from: U.S. Department of Energy, Office of Scientific and Technical Information, P.O. Box 62, Oak Ridge, TN 37831-0062, phone: (865) 576-8401

fax: (865) 576-5728

email: reports@adonis.osti.gov

WSRC-TR-99-00282

Keywords: Environmental
Hydrogeology
Groundwater

Retention: Permanent

FACT

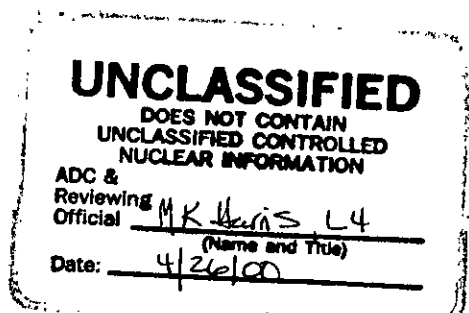
(Version 2.0)

Subsurface Flow and Contaminant Transport Documentation and User's Guide

(U)

by

**L. Larry Hamm
Sebastian E. Aleman**



A Software Product of



Savannah River Technology Center

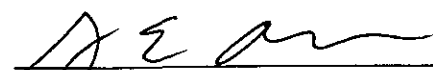
Publication Date: March 2000

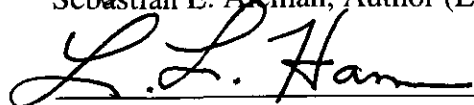
**Westinghouse Savannah River Company
Savannah River Technology Center
Aiken, South Carolina 29808**

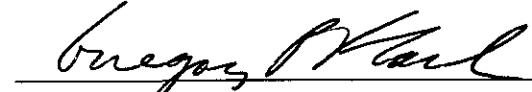
FACT CODE MANUAL

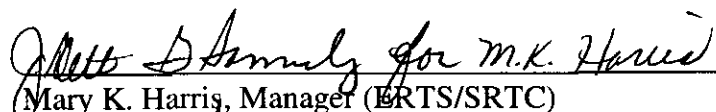
DOCUMENT: WSRC-TR-99-00282
TITLE: FACT (Version 2.0) Subsurface Flow and Contaminant
Transport Documentation and User's Guide (U)

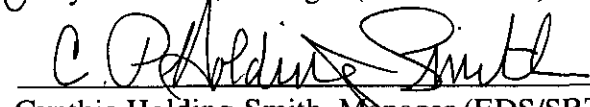
APPROVALS


Sebastian E. Aleman, Author (ERTS/SRTC) Date: 4/24/00

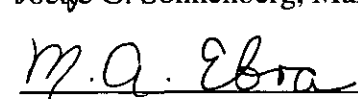

L. Larry Hamm, Author (EDS/SRTC) Date: 4/24/00


Gregory P. Flach, Technical Reviewer (ERTS/SRTC) Date: 4/24/00


Mary K. Harris, Manager (ERTS/SRTC) Date: 4-24-00


Cynthia Holding-Smith, Manager (EDS/SRTC) Date: 4/24/00


Joette G. Sonnenberg, Manager (ERTS/SRTC) Date: 4-24-00


Martha A. Ebra, Manager (EDS/SRTC) Date: 4/24/00

UNCLASSIFIED
DATE 10/20/00 BY 2000
ALL INFORMATION CONTAINED
HEREIN IS UNCLASSIFIED
EXCEPT WHERE SHOWN
OTHERWISE

Changes: v1.1 to v2.0

The following changes to FACT v1.1 have been incorporated in FACT v2.0

1. Two-point Gauss Legendre quadrature option for the flow and transport equations. This option is highly recommended for meshes with vertical distortion. The influence matrix formulation is still available.
2. A Dual-Domain mass transfer model (mobile-immobile water phase solute transport model) option for the transport equation with linear adsorption and first-order irreversible reactions. The previous mobile-immobile boundary condition option has been removed.
3. Streamline-Upwind Petrov-Galerkin (SUPG) weighting for the advection terms in the transport equation.
4. Vertical recirculation well boundary condition option. The recirculation well is modeled as a single pass extraction well with an extraction and injection screen. The extracted solute is assumed to be well mixed, air-stripped (single pass extraction efficiency factor), and injected back to the aquifer.
5. The vertical pumping/injection well boundary condition has been modified to work for solute injection.

WESTINGHOUSE SAVANNAH RIVER COMPANY

Manual: WSRC-TR-99-00282

Section: Contents, Rev. 0

Date: 3/2000

FACT CODE MANUAL

Page: iv of xxiv

(This Page Intentionally Left Blank)

Table of Contents

1	Introduction	1-1
1.1	Overview of Code Capabilities and Salient Features	1-2
1.2	Applicability of the Code	1-4
1.3	Code User Requirements	1-4
1.4	Computer Equipment Requirements	1-4
2	Governing Mathematical Models	2-1
2.1	Governing and Auxiliary Equations for Variably Saturated Groundwater Flow	2-1
2.2	Governing and Auxiliary Equations for Variably Saturated Solute Transport	2-5
2.3	Governing Equations for Variably Saturated Mobile/ Immobile Solute Transport	2-13
2.3.1	Background	2-13
2.3.2	Parameter Definitions	2-14
2.3.3	Mobile-Solid Governing Equation for Transport	2-17
2.3.4	Immobile-Solid Governing Equation for Transport	2-18
2.4	Assumptions of Flow and Transport Models	2-20
2.5	Limitations	2-20
2.6	Input Data	2-21
2.6.1	Input Data for Flow Problems	2-21
2.6.2	Input Data for Solute Transport Problems	2-22
3	Numerical Solution Techniques	3-1
3.1	Numerical Techniques for Variably Saturated Flow	3-1
3.1.1	Galerkin Formulation	3-2
3.1.2	Eight-noded Constrained Trilinear Hexahedron Element	3-4
3.1.3	Numerical Integration	3-5
3.1.4	Transformations for First Order Terms	3-7
3.1.5	Flow Equation Element Matrix Computation	3-9
3.1.5.1	Element Seepage (Conductance) Matrix	3-9
	Influence Coefficient Matrices	3-12
	Two-point Gauss-Legendre Quadrature	3-14
3.1.5.2	Element Storage (Capacitance) Matrix	3-14
	Influence Coefficient Matrix	3-15
	Two-point Gauss-Legendre Quadrature	3-16
3.1.5.3	RHS Forcing Function Vector	3-16
3.1.6	Line Source/Sink within 3D Element	3-19
3.1.6.1	Flux Specified Line Source within 3D Element	3-19

FACT CODE MANUAL

3.1.6.2	Head-Dependent Line Sink within 3D Element.....	3-27
3.1.6.3	Uniform Flux Specified Vertical Well Option.....	3-32
3.1.6.4	Uniform Flux Specified Vertical Recirculation Well Option	3-35
3.1.7	Head-Dependent Flux Boundary Conditions.....	3-37
3.1.7.1	Head-Dependent Recharge & Drain Boundary Conditions.....	3-39
3.1.8	Numerical Solution of Flow Equation.....	3-43
3.1.9	Darcy and Phasic Velocity Computation.....	3-49
3.1.10	Vertical Observation Well Option	3-54
3.2	Numerical Techniques for Variably Saturated Solute Transport	3-57
3.2.1	Upstream-Weighted Residual Formulation	3-58
3.2.2	Eight-noded Constrained Hexahedron Element.....	3-62
3.2.3	1-D Asymmetric Weighting Functions	3-63
3.2.4	3-D Asymmetric Weighting Functions	3-69
3.2.5	Transport Equation Elemental Matrix Computation	3-71
3.2.5.1	The Elemental Storage (Capacitance) Matrix	3-71
3.2.5.2	The Elemental Advection-Dispersion Matrix	3-72
	Influence Coefficient Matrices	3-73
	Two-point Gauss-Legendre Quadrature	3-75
3.2.5.3	The Elemental Radioactive and First-Order Decay Matrix	3-76
3.2.5.4	The Elemental and Global Source/Sink Matrix	3-77
3.2.5.5	The Elemental and Global RHS Forcing Function Vector.....	3-78
3.2.6	Numerical Solution of Transport Equation.....	3-79
3.2.7	Treatment of Transport Boundary Conditions	3-81
3.3	Numerical Techniques for Variably Saturated Mobile/Immobile Solute Transport	3-85
3.3.1	Upstream-Weighted Residual Formulation of the Mobile-Phase Transport Equation	3-85
3.3.2	Bubnov-Galerkin Weighted Residual Formulation of the Immobile- Phase Transport Equation	3-87
3.3.3	Mobile-Phase Transport Equation Elemental Matrix Computation	3-88
3.3.3.1	The Mobile-Phase Elemental Storage (Capacitance) Matrix	3-88
3.3.3.2	The Elemental Advection-Dispersion Matrix	3-88
3.3.3.3	The Mobile-Phase Elemental Radioactive and First-Order Decay Matrix	3-89
3.3.3.4	The Mobile-Phase Elemental and Global Source/Sink Matrix	3-89
3.3.3.5	The Mobile-Phase Elemental and Global RHS Forcing Function Vector	3-89
3.3.3.6	The Elemental Interfacial Mass Transfer Matrix	3-89
3.3.4	Immobile-Phase Transport Equation Elemental Matrix Computation	3-90
3.3.4.1	The Immobile-Phase Elemental Storage (Capacitance) Matrix	3-90
3.3.4.2	The Immobile-Phase Elemental Radioactive and First-Order Decay Matrix	3-90
3.3.5	Numerical Solution of the Mobile/Immobile Transport Equations	3-91

FACT CODE MANUAL

3.3.6	Treatment of Mobile/Immobile Transport Boundary Conditions	3-93
3.4	Matrix Solution Techniques	3-93
3.4.1	Symmetric PCG Solver	3-94
3.4.2	Asymmetric PCG Solver	3-97
3.5	Spatial and Temporal Discretizations	3-100
3.6	Material Mass Balance Options	3-102
3.6.1	Flow Equation Mass Balance	3-103
3.6.2	Transport Equation Mass Balance	3-108

4 Verification Tests and Results 4-1

4.1	Groundwater Flow Problems	4-3
4.1.1	Steady-state, One-Dimensional Flow in a Confined Aquifer	4-3
4.1.2	Steady-State, One-Dimensional Flow in an Unconfined Aquifer	4-7
4.1.3	Steady-State, Two-Dimensional Flow Through a Heterogeneous Aquifer System	4-13
4.1.4	Unconfined Aquifer Subject to a Combined Recharge/Drain BC	4-18
4.1.5	Transient, One-Dimensional Flow to a Well in a Confined Aquifer (Theis, 1935)	4-21
4.1.6	Transient, One-Dimensional Flow to a Well in an Anisotropic Confined Aquifer (Hantush and Thomas, 1966)	4-27
4.1.7	Transient, One-Dimensional Flow to a Well in a Leaky Confined Aquifer (Hantush and Jacob, 1955)	4-34
4.1.8	Transient, Two-Dimensional Flow to a Well in an Unconfined Aquifer (Neuman, 1975)	4-38
4.1.9	Transient, Two-Dimensional Flow in an Unconfined Aquifer	4-44
4.1.10	Unsaturated Vertical Soil Column	4-48
4.2	Solute Transport Problems	4-51
4.2.1	One-Dimensional Saturated Solute Transport in a Uniform Flow Field	4-51
4.2.2	Two-Dimensional Saturated Solute Transport in a Uniform Flow Field	4-77
4.2.3	Three-Dimensional Saturated Solute Transport in a Uniform Flow Field	4-96
4.3	Dual-Domain (Mobile/Immobile) Transport Problems	4-105
4.3.1	One-Dimensional Saturated Solute Transport in a Uniform Flow Field with First-Order Mobile/Immobile Mass Transfer (van Genuchten and Wierenga analytical cases)	4-105
4.3.2	One-Dimensional Saturated Solute Transport in a Uniform Flow Field with First-Order Mobile/Immobile Mass Transfer (VERSE-LC Comparison)	4-123

5 Problem Definition and Simulation Procedure 5-1

5.1	Conceptual Model	5-1
5.2	Model Grid	5-1
5.3	Material Properties and Boundary Conditions	5-4
5.4	FACT Input Files	5-5
5.5	FACT Execution	5-5

FACT CODE MANUAL

6	Code Structure	6-1
6.1	Code Organization and Program Unit Description	6-1
6.2	Program Unit Descriptions	6-1
6.3	Internal Data Structure	6-7
6.3.1	Memory Allocation	6-9
6.4	FACT Subprogram Call Tree	6-15
7	Input and Output	7-1
7.1	Super File	7-1
7.2	Input and Output Files	7-1
7.3	File Content and Organization	7-2
7.3.1	Main input file	7-4
7.3.2	Printed output file	7-31
7.3.3	Initial condition head file	7-32
7.3.4	Initial condition concentration file	7-32
7.3.5	Initial condition immobile concentration file	7-32
7.3.6	Flow solution elemental (Darcy) velocity file	7-33
7.3.7	Flow solution water saturation file	7-33
7.3.8	Flow solution nodal (phasic) velocity file	7-33
7.3.9	Flow solution mass balance flow file (NOT USED)	7-34
7.3.10	Flow solution recharge/drain flow file	7-34
7.3.11	Flow solution water table file	7-34
7.3.12	Head solution file	7-35
7.3.13	Concentration solution file	7-35
7.3.14	Immobile concentration solution file	7-35
7.3.15	Elemental (Darcy) velocity solution file	7-35
7.3.16	Water saturation solution file	7-36
7.3.17	Nodal velocity solution file	7-36
7.3.18	Mass balance nodal flows file	7-36
7.3.19	Recharge/drain flows file	7-37
7.3.20	Water table elevations file	7-37
7.3.21	Steady-state observation well statistics file	7-37
7.4	Tecplot™ post-processing files	7-38
7.4.1	Nodal Results (nplto = 0, 1, 2, 6, or 9)	7-38
7.4.2	Elemental Results (flow simulation, nplto = 3 or 4)	7-39
7.4.3	Water Table Elevations (variably saturated flow simulation, nplto = 5)	7-39
7.4.4	Surface Fluxes (flow simulation, mass balance, nplto = 7)	7-39
7.4.5	Observation Well Group Heads (flow simulation, iobswg = 1)	7-39
7.4.6	Observation Well Group Concentrations (transport simulation, iobswg = 1)	7-40
7.4.7	Peclet and Courant Numbers (transport simulation)	7-40
7.4.8	Solute Mass Removed by Recharge/Drain (transport simulation, nrch = -1)	7-40
7.4.9	Maximum Concentration (transport simulation)	7-41

7.4.10	Areal Solute Mass Per Unit Area (transport simulation, nplto = 8)	7-41
7.4.11	Total Solute Mass (transport simulation, nplto = 8)	7-41
7.4.12	Nodal Surface Mass Fluxes Due to Recharge/Drain (transport simulation, nrch = -1, nplto = 8)	7-41
7.4.13	Vertically-averaged Aquifer Concentrations (transport simulation, nplto = 8)	7-42
8	References	8-1
	Appendix A - Test Problem Listing	A-1
	Appendix B - Flow Test Problem Input Files	B-1
B.1	Steady-State, One-Dimensional Flow in a Confined Aquifer	B-1
B.2	Steady-State, One-Dimensional Flow in an Unconfined Aquifer	B-4
B.3	Steady-State, Two-Dimensional Flow through a Heterogeneous Aquifer System	B-8
B.4	Unconfined Aquifer Subject to a Combined Recharge/Drain Boundary Condition	B-11
B.5	Transient, One-Dimensional Flow to a Well in an Isotropic Confined Aquifer (Theis, 1935)	B-17
B.6	Transient, Two-Dimensional Flow to a Well in an Anisotropic Confined Aquifer (Hantush and Thomas, 1966)	B-27
B.7	Transient, One-Dimensional Flow to a Well in a Leaky Confined Aquifer (Hantush and Jacob, 1955)	B-37
B.8	Transient, Two-Dimensional Flow to a Well in an Unconfined Aquifer (Neuman, 1975)	B-45
B.9	Transient, Two-Dimensional Flow in an Unconfined Aquifer	B-67
B.10	Unsaturated Vertical Soil Column	B-70
	Appendix C - Flow Test Problem Output Sample	C-1
C.1	Main Output File	C-1
	Appendix D - Transport Test Problem Input Files	D-1
D.1	One-Dimensional Saturated Solute Transport in a Uniform Flow Field	D-1
D.2	Two-Dimensional Saturated Solute Transport in a Uniform Flow Field	D-8
D.3	Three-Dimensional Saturated Solute Transport in a Uniform Flow Field	D-12
D.4	One-Dimensional Saturated Solute Transport in a Uniform Flow Field with First-Order Mobile/Immobile Mass Transfer: VanGenuchten and Wierenga Test Suite.	D-14
D.4.1	Calculated Effluent Curves for a Sorbing Medium as Influenced by the Fraction of Mobile Water, ϕ	D-14
D.4.2	Calculated Effluent Curves for a Sorbing Medium as Influenced by the Fraction of the Adsorption Sites in the Dynamic Region, f	D-16

FACT CODE MANUAL

D.4.3	Calculated Effluent Curves for a Sorbing Medium as Influenced by the Mass Transfer Coefficient, α	D-18
D.4.4	Calculated Effluent Curves for a Sorbing Medium as Influenced by the Dispersion Coefficient, D	D-20
D.4.5	Calculated Effluent Curves for a Sorbing Medium as Influenced by the Distribution Coefficient, K	D-22
D.5	One-Dimensional Saturated Solute Transport in a Uniform Flow Field with First-Order Mobile/Immobile Mass Transfer: VERSE-LC Comparison	D-25
D.5.1	Calculated Effluent Curves and Column Profiles as Influenced by the Surface Mass Transfer Coefficient, $k_f(\alpha)$	D-25

Appendix E - Transport Test Problem Output Sample	E-1
--	------------

E.1	Main Output File	E-1
-----	------------------------	-----

List of Figures

2	Governing Mathematical Models	2-1
Figure 2.3.1	Schematic Illustrating the Various Processes Addressed in the Variably Saturated Mobile/Immobile Transport Model at the Element Level.....	2-14
3	Numerical Solution Techniques	3-1
Figure 3.1.1	Eight-noded constrained trilinear hexahedron element showing node numbering and local and global coordinate systems.	3-4
Figure 3.1.2	3-D Rectangular Prism Element with Vertical Line Source Along its Line Segment between Nodes 1 and 5.....	3-20
Figure 3.1.3	Example of Vertical Line Source (specified strength) Extending over Two Elements.....	3-22
Figure 3.1.4	3-D Rectangular Prism Element with Vertical Line Source along a Portion of its Line Segment between Nodes 1 and 5.....	3-23
Figure 3.1.5	Example of Vertical Line Source (specified strength) extending into Three Rectangular Prism Elements.....	3-24
Figure 3.1.6	3-D Rectangular Prism Element with Vertical Line Source along a Portion of its Line Segment between Nodes 1 and 5.....	3-26
Figure 3.1.7	Extraction Well Contained within an Unconfined Aquifer Unit.....	3-29
Figure 3.1.8	Notation Used for Head-dependent Line Sink Model.....	3-29
Figure 3.1.9	A Vertical Well whose Screen Extends across Several Aquifer Units.	3-34
Figure 3.1.10	Schematic of Basic Flow Pattern Under Vertical Recirculation Well Operation.....	3-36
Figure 3.1.11	Typical Head-Dependent Flux Boundary Condition (River or Stream).	3-37
Figure 3.1.12.	Source Bed Boundary Condition for Simultaneous Treatment of Surface Recharge and Drainage.	3-41
Figure 3.2.1	Eight-noded Trilinear Hexahedron Element Showing Node Numbering in Local and Global Coordinate Systems.	3-63
Figure 3.2.2	Linear Line Element Showing Node Numbering in Local and Global Coordinate Systems.	3-63
Figure 3.2.3	Optimal Weighting Factor for the One-Dimensional Unsteady Convection-Diffusion Equation using Petrov-Galerkin Weighting Functions.	3-69
Figure 3.2.4	An example for illustrating the treatment of transport boundary conditions and source terms.	3-84
Figure 3.5.1	Areal Slice through Example Mesh Illustrating Nodal and Elemental Numbering Conventions.	3-101
Figure 3.5.2	Vertical Slice through Example Mesh Illustrating Nodal and Elemental Numbering Conventions.	3-102

4 Verification Tests and Results**4-1**

Figure 4.1.1.1	Schematic diagram of a confined aquifer with a constant head boundary condition at $x = 0$ and either a general head (Problem 1) or river (Problem 2) boundary condition at $x = L$.	4-3
Figure 4.1.1.2	FACT grid.	4-5
Figure 4.1.1.3.	Comparison of analytic solution to FACT numerical results for Problem 1.	4-5
Figure 4.1.1.4	FACT Darcy velocity for Problem 2.	4-6
Figure 4.1.2.1.	Schematic diagram of an unconfined aquifer with no recharge and constant head boundary conditions (Problem 1).	4-8
Figure 4.1.2.2.	Schematic diagram of an unconfined aquifer with recharge and mixed boundary conditions (Problem 2).	4-8
Figure 4.1.2.3	FACT grid for Problem 1 shown in Figure 4.1.2.1.	4-9
Figure 4.1.2.4	FACT grid for Problem 2 shown in Figure 4.1.2.2.	4-10
Figure 4.1.2.5	Comparison of analytic solution and FACT results for Problem 1 shown in Figure 4.1.2.1 with $\text{rampw} = 1.0$, $\text{upstr} = 1.0$ and $S_{wr} = 0.05$.	4-10
Figure 4.1.2.6	Comparison of analytic solution and FACT results for Problem 2 shown in Figure 4.1.2.2 with $\text{rampw} = 1.0$, $\text{upstr} = 1.0$ and $S_{wr} = 0.005$.	4-11
Figure 4.1.2.7	Pseudo-soil property parameter study for Problem 1 shown in Figure 4.1.2.1.	4-11
Figure 4.1.2.8a	Pseudo-soil property parameter study for Problem 2 shown in Figure 4.1.2.2.	4-12
Figure 4.1.2.8b	Pseudo-soil property parameter study for Problem 2 shown in Figure 4.1.2.2.	4-12
Figure 4.1.3.1	A heterogeneous subsurface system consisting of an unconfined aquifer, confining unit and confined aquifer.	4-14
Figure 4.1.3.2	Finite element mesh from x-z view ($20 \times 1 \times 20$ elements).	4-16
Figure 4.1.3.3	Approximate analytical and FACT hydraulic head profiles for the unconfined and confined aquifer portions of the heterogeneous subsurface system shown in Figure 4.1.3.1.	4-18
Figure 4.1.4.1	Schematic illustration of an unconfined aquifer experiencing both recharge and drainage at the ground surface; seepage line unknown a priori.	4-19
Figure 4.1.4.2	FACT finite element mesh with FACT and analytical water table overlain.	4-20
Figure 4.1.5.1	Radial flow to a pumping well in a confined aquifer.	4-22
Figure 4.1.5.2	FACT coarse full grid.	4-24
Figure 4.1.5.3	Theis solution and FACT coarse full grid transient results at $r = 55$ meters.	4-24
Figure 4.1.5.4	FACT drawdown at 1 day for coarse full grid.	4-25
Figure 4.1.5.5	FACT coarse quadrant grid.	4-25

FACT CODE MANUAL

Figure 4.1.5.6	Theis solution and FACT quadrant grid transient results at $r = 55$ meters.	4-26
Figure 4.1.5.7	FACT fine quadrant grid.	4-26
Figure 4.1.6.1	Anisotropic confined aquifer with $K_x/K_y = 10$	4-28
Figure 4.1.6.2	FACT drawdown at 1 day for full grid.	4-29
Figure 4.1.6.3	Analytic solution and FACT full grid results at $x = 55$ m.	4-29
Figure 4.1.6.4	Analytic solution and FACT full grid results at $y = 55$ m.	4-30
Figure 4.1.6.5	Analytic solution and FACT full grid results at $x = 55$ m, $y = 55$ m.	4-30
Figure 4.1.6.6	Analytic solution and FACT quadrant grid results at $x = 55$ m.	4-31
Figure 4.1.6.7	Analytic solution and FACT quadrant grid results at $y = 55$ m.	4-31
Figure 4.1.6.8	Analytic solution and FACT quadrant grid results at $x = 55$ m, $y = 55$ m.	4-32
Figure 4.1.7.1	Schematic diagram of a leaky confined aquifer with constant discharge from a single, fully-penetrating well.	4-35
Figure 4.1.7.2	Comparison of Hantush and Jacob (1955) analytic drawdown solution and FACT numerical results for two grids.	4-36
Figure 4.1.7.3	FACT coarse grid.	4-37
Figure 4.1.7.4	FACT fine grid.	4-37
Figure 4.1.8.1	Radial flow to a pumping well in an unconfined aquifer.	4-39
Figure 4.1.8.2	FACT grid.	4-41
Figure 4.1.8.3	Neuman solution, pump test data and FACT results at $r = 31$ ft, $z = 23$ ft.	4-41
Figure 4.1.8.4	Neuman solution and FACT results at $z = 23$ ft, $t = 6.94$ days.	4-42
Figure 4.1.9.1	Schematic diagram of an unconfined aquifer with a transient prescribed head boundary condition at $x = 0$ and a combination of drain and no flow boundary conditions at $x = 20$	4-44
Figure 4.1.9.2	FACT grid.	4-45
Figure 4.1.9.3	FACT water table height.	4-46
Figure 4.1.9.4	FACT Darcy velocity at $x = 20'$, $z = 30'$	4-46
Figure 4.1.10.1	Schematic illustration of FACT mesh and unsaturated test cases.	4-49
Figure 4.1.10.2	Soil characteristic curves for Silt Loam G.E. 3 (van Genuchten, 1980) with FACT code results overlain.	4-49
Figure 4.2.1.1	Schematic diagram for 1D solute transport in a confined aquifer.	4-52
Figure 4.2.1.2	FACT mesh and boundary conditions for 1D transport.	4-55
Figure 4.2.1.3	Concentration profiles for 1D transport of the base case.	4-59
Figure 4.2.1.4	Concentration profiles for 1D transport showing effect of retardation.	4-59
Figure 4.2.1.5	Concentration profiles for 1D transport showing effect of radioactive decay.	4-60
Figure 4.2.1.6	Concentration profiles for 1D transport showing combined effect of retardation and radioactive decay.	4-60
Figure 4.2.1.7	Concentration profiles for 1D transport showing effect of grid size.	4-61

Figure 4.2.1.8	Concentration profiles for 1D transport showing effect of time-step size.	4-61
Figure 4.2.1.9	Concentration profiles for 1D transport showing effect of spatial differencing.	4-62
Figure 4.2.1.10	Concentration profiles for 1D transport showing effect of temporal differencing.	4-62
Figure 4.2.1.11	Concentration profiles for 1D transport showing combined effect of temporal and spatial differencing.	4-63
Figure 4.2.1.12	Concentration profiles for 1D transport at high Peclet number showing effect of dispersion.	4-63
Figure 4.2.1.13	Concentration profiles for 1D transport at high Peclet number showing effect of complete upstream spatial differencing.	4-64
Figure 4.2.1.14	Concentration profiles for 1D transport at high Peclet number showing effect of optimal upstream spatial differencing.	4-64
Figure 4.2.2.1	Schematic diagram for 2D areal solute transport in a confined aquifer.	4-77
Figure 4.2.2.2	FACT parallel mesh and boundary conditions for 2D transport.	4-83
Figure 4.2.2.3	FACT diagonal mesh and boundary conditions for 2D transport.	4-84
Figure 4.2.2.4	FACT concentration profile for 2D transport of the base case on the parallel grid.	4-87
Figure 4.2.2.5	FACT concentration profile for 2D transport of the base case on the diagonal grid.	4-87
Figure 4.2.2.6	Concentration profiles for 2D transport of the base case along plume centerline.	4-88
Figure 4.2.2.7	Concentration profiles for 2D transport of the base case transverse to plume centerline located 420 m downstream of the source.	4-88
Figure 4.2.2.8	Concentration profiles for 2D transport of the base case transverse to plume centerline located 0 m downstream of the source.	4-89
Figure 4.2.2.9	Effect of complete upstream spatial differencing on concentration profiles for 2D transport transverse to plume centerline located 0 m downstream of the source.	4-89
Figure 4.2.2.10	FACT concentration profile (carpet plot) for 2D transport of the base case showing the effect of centered spatial differencing.	4-90
Figure 4.2.2.11	FACT concentration profile (carpet plot) for 2D transport of the base case showing the effect of complete upstream spatial differencing.	4-90
Figure 4.2.2.12	Concentration profiles for 2D transport showing effect of retardation.	4-91
Figure 4.2.2.13	Concentration profiles for 2D transport showing effect of radioactive decay.	4-91

Figure 4.2.3.1	FACT parallel mesh and boundary conditions for 3D transport. A 3D perspective was chosen where a section of the domain has been cut out to highlight the plume centerline.	4-101
Figure 4.2.3.2	FACT concentration profile for 3D transport of the base case on a parallel grid where a section of the domain has been cut out to highlight the plume centerline and its axisymmetric behavior.....	4-102
Figure 4.2.3.3	Concentration profile for 3D transport of the base case along plume centerline.	4-103
Figure 4.2.3.4	Concentration profiles for 3D transport of the base case transverse to plume centerline (in both y and z directions) located 210 m downstream of the source.....	4-103
Figure 4.3.1.1	Calculated breakthrough curves for a sorbing medium as influenced by the fraction of mobile liquid, ϕ	4-121
Figure 4.3.1.2	Calculated breakthrough curves for a sorbing medium as influenced by the fraction of adsorption sites in the dynamic region, f	4-121
Figure 4.3.1.3	Calculated breakthrough curves for a sorbing medium as influenced by the mass transfer coefficient, α	4-122
Figure 4.3.1.4	Calculated breakthrough curves for a sorbing medium as influenced by the dispersion coefficient, D	4-122
Figure 4.3.1.5	Calculated breakthrough curves for a sorbing medium as influenced by the adsorption coefficient, K	4-123
Figure 4.3.2.1	Relative solute concentration profile comparison for VERSE-LC at 50 minutes	4-130
Figure 4.3.2.2	Break-through curve comparison for VERSE-LC at 500 cm.....	4-130

5 Problem Definition and Simulation Procedure **5-1**

Figure 5.1	Schematic drawing of an example groundwater flow and solute transport problem.	5-5
Figure 5.2	An example FACT mesh with boundary conditions overlain on Fig. 5.1 schematic.....	5-6
Figure 5.3	FACT node and element numbers for mesh shown in Fig. 5.2.....	5-7
Figure 5.4	Deformed eight-noded hexahedron element.	5-8

WESTINGHOUSE SAVANNAH RIVER COMPANY

Manual: WSRC-TR-99-00282

Section: Contents, Rev. 0

Date: 3/2000

FACT CODE MANUAL

Page: xvi of xxiv

(This Page Intentionally Left Blank)

List of Tables

3	Numerical Solution Techniques	3-1
Table 3.1.1	Gauss-Legendre Abscissas and Weights.	3-7
Table 3.2	Input and key computed parameters for GPT3 simulation.....	3-67
Table 3.3	Optimal upwind parameters as a function of Peclet number.....	3-68
4	Verification Tests and Results	4-1
Table 4.1.1.1	Comparison of analytic solution and FACT numerical results for Problem 1.	4-7
Table 4.1.1.2	FACT Darcy velocity at node 11 for Problem 2.....	4-7
Table 4.1.2.1	Comparison of analytic solution and FACT numerical results.	4-13
Table 4.1.3.1	Approximate analytical and FACT hydraulic head values for the unconfined and confined aquifer portions of the heterogeneous subsurface system shown in Fig. 4.1.1.	4-17
Table 4.1.4.1	FACT and analytical water table comparison.	4-21
Table 4.1.5.1	Comparison of Theis solution and FACT numerical results.	4-27
Table 4.1.6.1	Comparison of analytic solution and FACT numerical results at $x = 55$ m.....	4-33
Table 4.1.6.2	Comparison of analytic solution and FACT numerical results at $y = 55$ m.....	4-33
Table 4.1.6.3	Comparison of analytic solution and FACT numerical results at $x=y = 55$ m.	4-34
Table 4.1.7.1	Comparison of analytic solution and FACT numerical results at $r = 60$ ft.	4-38
Table 4.1.8.1	Neuman solution at $r = 31$ ft, at $r = 31$ ft, $z = 23$ ft.	4-43
Table 4.1.8.2	Pump test data.	4-43
Table 4.1.8.3	FACT numerical results.	4-43
Table 4.1.8.4	Neuman solution at $z = 23$ ft, $t = 6.94$ days.....	4-43
Table 4.1.8.5	FACT numerical results.	4-44
Table 4.1.9.1	FACT Darcy velocity at $x = 20'$, $z = 30'$	4-47
Table 4.1.10.1	Water retention curve and FACT comparison of saturation.	4-50
Table 4.2.1.1	Values of the physical parameters, the finite element grid, time-step data, and some key parameters used in the one-dimensional transport problem (base case and its variations).....	4-54
Table 4.2.1.2	Summary of simulations performed (base case and its variations) on the one-dimensional transport problem	4-56
Table 4.2.1.3	Comparison of analytical and numerical concentration (kg/m ³) results for the transient 1D transport problem (base case).	4-65
Table 4.2.1.4	Comparison of analytical and numerical concentration (kg/m ³) results for the transient 1D transport problem (retardation $R=2.0$).	4-66

FACT CODE MANUAL

Table 4.2.1.5	Comparison of analytical and numerical concentration (kg/m ³) results for the transient 1D transport problem (radioactive decay $\lambda_r = 0.01$)	4-67
Table 4.2.1.6	Comparison of analytical and numerical concentration (kg/m ³) results for the transient 1D transport problem (retardation $R=2.0$, radioactive decay $\lambda_r = 0.01$)	4-68
Table 4.2.1.7	Effect grid size (Δx) has on the numerical concentration (kg/m ³) results for the transient 1D transport problem (time $t=50$ days)	4-69
Table 4.2.1.8	Effect time-step size (Δt) has on the numerical concentration (kg/m ³) results for the transient 1D transport problem (time $t=50$ days)	4-70
Table 4.2.1.9	Effect upwind differencing has on the numerical concentration (kg/m ³) results for the transient 1D transport problem (spatial differencing $\alpha = 1.0$)	4-71
Table 4.2.1.10	Effect backward Euler has on the numerical concentration (kg/m ³) results for the transient 1D transport problem (temporal differencing $\omega = 1.0$)	4-72
Table 4.2.1.11	Effect backward Euler plus upwind differencing has on the numerical concentration (kg/m ³) results for the transient 1D transport problem (temporal differencing $\omega = 1.0$, spatial differencing $\alpha = 1.0$)	4-73
Table 4.2.1.12	Effect low longitudinal dispersivity has on the numerical concentration (kg/m ³) results for the transient 1D transport problem (longitudinal horizontal dispersivity $\alpha_{LH} = 0.01$)	4-74
Table 4.2.1.13	Effect low longitudinal dispersivity plus upwind differencing has on the numerical concentration (kg/m ³) results for the transient 1D transport problem (longitudinal horizontal dispersivity $\alpha_{LH} = 0.01$, spatial differencing $\alpha = 1.0$)	4-75
Table 4.2.1.14	Effect low longitudinal dispersivity plus partial (optimal) upwind differencing has on the numerical concentration (kg/m ³) results for the transient 1D transport problem (longitudinal horizontal dispersivity $\alpha_{LH} = 0.01$, spatial differencing $\alpha = 0.27$)	4-76
Table 4.2.2.1	Values of the physical parameters, the finite element grid, time-step data, and some key parameters used in the two-dimensional transport problem (base case and its variations)	4-81
Table 4.2.2.2	Summary of simulations performed (base cases and their variations) on the two-dimensional transport problem	4-85
Table 4.2.2.3	Effect grid orientation has on the numerical concentration (kg/m ³) results along the plume centerline for the transient 2D transport problem (base case, $t=1400$ days)	4-92
Table 4.2.2.4	Effect grid orientation has on the numerical concentration (kg/m ³) results transverse to the plume centerline (located 420 m	

FACT CODE MANUAL

	downstream of the source) for the transient 2D transport problem (base case, t=1400 days).....	4-93
Table 4.2.2.5	Effect grid orientation has on the numerical concentration (kg/m ³) results transverse to the plume centerline (located 0 m downstream of the source) for the transient 2D transport problem (base case, t=1400 days).....	4-93
Table 4.2.2.6	Effect grid orientation and complete upstream spatial differencing has on the numerical concentration (kg/m ³) results transverse to the plume centerline (located 0 m downstream of the source) for the transient 2D transport problem (spatial differencing $\alpha = 1.0$, t=1400 days).....	4-94
Table 4.2.2.7	Effect retardation or radioactive decay has on the numerical concentration (kg/m ³) results along the plume centerline for the transient 2D transport problem (retardation R=2.0 or radioactive decay $\lambda_r = 0.005$, t=1400 days)	4-95
Table 4.2.3.1	Values of the physical parameters, the finite element grid, time- step data, and some key parameters used in the three-dimensional transport problem (base case).....	4-100
Table 4.2.3.2	Comparison of analytical and numerical concentration (kg/m ³) results for the transient 3D transport problem (base case, t=1400 days).	4-104
Table 4.3.1.1	Parameters for van Genuchten ϕ Analytical Case	4-108
Table 4.3.1.2	Parameters for van Genuchten f Analytical Case	4-109
Table 4.3.1.3	Parameters for van Genuchten α Analytical Case	4-110
Table 4.3.1.4	Parameters for van Genuchten D Analytical Case	4-111
Table 4.3.1.5	Parameters for van Genuchten K Analytical Case	4-112
Table 4.3.1.6	Base Parameters in FACT simulation of van Genuchten Analytical Cases	4-115
Table 4.3.1.7	Parameter Settings in FACT simulation of van Genuchten ϕ Analytical Case.....	4-116
Table 4.3.1.8	Parameter Settings in FACT simulation of van Genuchten f Analytical Case.....	4-117
Table 4.3.1.9	Parameter Settings in FACT simulation of van Genuchten α Analytical Case.....	4-118
Table 4.3.1.10	Parameter Settings in FACT simulation of van Genuchten D Analytical Case.....	4-119
Table 4.3.1.11	Parameter Settings in FACT simulation of van Genuchten K Analytical Case.....	4-120
Table 4.3.2.1	Parameter Settings for the VERSE-LC Simulations	4-126
Table 4.3.2.2	Parameter Settings in FACT simulation of VERSE-LC Test Case...	4-128
6	Code Structure	6-1
Table 6.1	Brief Description of Each Program Unit in FACT v2.0.....	6-1

FACT CODE MANUAL

Table 6.2	Brief Description of Each Module File in FACT v2.0.....	6-8
Table 6.3	FACT Array Memory Allocation	6-9

7 Input and Output 7-1

Table 7.1	Super File Format	7-1
Table 7.2	Summary of FACT Input and Output Files	7-3
Table 7.3	FACT directory path for Tecplot files	7-4
Table 7.4	Summary of Tecplot™ binary and ASCII files	7-38

Appendix A - Test Problem Listing A-1

Table A1	Summary of Verification Simulations Performed on the FACT Code	A-1
----------	---	-----

Table of Notation

A	Flow area, L^2 .
A	Seepage (conductance) matrix.
b	Aquifer thickness, L .
B	Hantush's leakage factor, $\sqrt{Te'/K'}$, L .
B	Storage (capacitance or mass) matrix.
Bi	Immobile-phase transport storage matrix.
c	Solute concentration, M/L^3 .
c	Mobile-phase nodal solute concentration vector, M/L^3 .
ci	Immobile-phase nodal solute concentration vector, M/L^3 .
c_{im}	Immobile-phase solute concentration, M/L^3 .
c_m	Mobile-phase solute concentration, M/L^3 .
\bar{c}	Mass of solute sorbed per dry unit weight of solid, M/M .
c*	Incoming contaminant concentration at mass point source/sink, M/L^3 .
C	Specific moisture capacity, L^{-1} .
D	Apparent hydrodynamic dispersion tensor, $\theta_m \mathbf{D}_m$, L^2/T .
D_{ka}	Hydrodynamic dispersion tensor with respect to phase k , L^2/T .
D_{wa}	Hydrodynamic dispersion tensor with respect to water phase, L^2/T .
D_m	Mobile-phase hydrodynamic dispersion tensor, L^2/T .
D°	Apparent molecular diffusion coefficient for an unsaturated media, L^2/T .
D*	Bulk molecular diffusion coefficient, L^2/T .
e	Thickness of an aquifer, measured in a direction orthogonal to its confining beds, L .
E	Advection-dispersion matrix.
f	Fraction of adsorption sites that are in contact with the mobile water phase.
F	RHS forcing function vector, L/T .
F_f	Boundary integral term of the RHS forcing function vector, L/T .
F_s	Volume integral term of the RHS forcing function vector, L/T .
g	Acceleration due to gravity, L/T^2 .
G	Residual vector of flow equation or mobile-phase radioactive decay and first-order reaction rate matrix.
Gi	Immobile-phase radioactive decay and first-order reaction rate matrix.
h	Hydraulic head, L .
h₀	Prescribed hydraulic head, L .
h_i	Nodal hydraulic head, L .
H	Height of rectangular prism element, L .
I	Interfacial mass transfer matrix.
j_a	Dispersive flux of species "a", $ML^{-3}T^{-1}$.
J_n	Bessel function of the first kind of order n .
J	Jacobian coordinate transformation matrix.

FACT CODE MANUAL

k	Intrinsic permeability tensor.
k_d	Distribution coefficient (slope of the linear sorption isotherm), L/M.
k_{rw}	Relative permeability with respect to the water phase.
K	Saturated hydraulic conductivity tensor, L/T.
ℓ	Length of rectangular prism element, L.
m	Width of rectangular prism element, L, or Picard/Newton iteration number.
M	Consistent mass matrix.
ML	Lumped mass matrix.
n	Vector normal to a surface, oriented outward.
n	Time step number.
n_{ka}	Total flux of species "a" within phase k, $ML^{-3}T^{-1}$
ne	Number of elements in finite element mesh.
np	Number of nodes in finite element mesh.
p_a	Air pressure, $ML^{-1}T^{-2}$.
p_w	Water pressure, $ML^{-1}T^{-2}$.
P_c	Capillary suction head, L.
P	Source/sink term matrix.
Pe	Peclet number.
q	Volumetric flow rate per unit volume of porous medium, T^{-1} .
q_β	Volumetric flow rate per unit length of line source/sink located at (x_β, y_β) .
Q	Volumetric flow rate per unit surface area withdrawn from the aquifer, L/T or the constant flow rate of a well, L^3/T .
$Q_{\beta i}$	Volumetric flow rate contribution at node I from point sink/source located at x_β .
r	Distance to the origin in polar coordinates, L.
r_{ka}	Production of species "a" by homogeneous reactions within phase k, $ML^{-3}T^{-1}$
r_{sa}	Production of species "a" by homogeneous reactions within solid phase, $ML^{-3}T^{-1}$
r_{wa}	Production of species "a" by homogeneous reactions within water phase, $ML^{-3}T^{-1}$
R	Retardation coefficient in transport equation.
R_m	Mobile-phase retardation coefficient.
R_{im}	Immobile-phase retardation coefficient.
s	Drawdown in an aquifer, L.
S	Storage coefficient of a confined aquifer.
S_e	Effective water saturation
S_s	Specific storage coefficient of a confined aquifer, L^{-1} .
S_w	Water saturation.
S_{wr}	Residual (irreducible) water saturation.

FACT CODE MANUAL

t	Time, T.
T	Transmissivity of an aquifer, L^2/T .
\mathbf{T}	Transmissivity tensor of an aquifer, L^2/T .
u	Theis' dimensionless time, $4Tt/r^2S$.
\mathbf{u}	Phasic velocity vector of a fluid, L/T .
\mathbf{u}_k	Phasic velocity of phase k, L/T .
u'	Hantush and Thomas dimensionless time, $4T_x T_y t / (x^2 T_y + y^2 T_x) S$.
\mathbf{U}	Darcy's velocity vector in a porous medium (or filtration velocity vector), L/T .
U_n	Normal component of Darcy velocity vector, L/T .
w_k	Weight of the kth Gauss point.
$W(u)$	Theis' well function.
$W'(u, r/B)$	Hantush's well function.
\mathbf{x}	Position vector in 1, 2 or 3 dimensions, L.
x_a	Mass fraction of species a.
y_a	Solute "a" concentration in solid phase, M/L^3 .
y_m	Solute solid-phase mass fraction on surface in contact with the mobile water phase, MM^{-1} .
y_{im}	Solute solid-phase mass fraction on surface in contact with the immobile water phase, MM^{-1} .
z	Elevation above a reference datum, L.

GREEK

α	van Genuchten empirical constant, compressibility of the porous media (L^{-1}), mass transfer coefficient (T^{-1}), or upstream weighting factor.
α_k	Volume fraction of phase k.
α_s	Volume fraction of solid phase.
α_w	Volume fraction of water phase.
α_{LH}	Longitudinal horizontal dispersivity of a porous medium, L.
α_{LV}	Longitudinal vertical dispersivity of a porous medium, L.
α_{TH}	Transverse horizontal dispersivity of a porous medium, L.
α_{TV}	Transverse vertical dispersivity of a porous medium, L.
β	Compressibility of the fluid, L^{-1} .
Γ_k	Input of species "a" into phase k at interface by mass transfer and heterogeneous reactions, $ML^{-3}T^{-1}$.
Γ_s	Input of species "a" into solid phase at interface by mass transfer and heterogeneous reactions, $ML^{-3}T^{-1}$.
Γ_{sm}	Mass transfer rate from solid surface to mobile water phase, $ML^{-3}T^{-1}$.

FACT CODE MANUAL

Γ_{si}	Mass transfer rate from solid surface to immobile water phase, $ML^{-3}T^{-1}$
$\delta(x)$	Dirac delta function.
δ	Kronecker delta.
ζ	Mapping of z global coordinate into local coordinate system, $-1 \leq \zeta \leq 1$.
η	Mapping of y global coordinate into local coordinate system, $-1 \leq \eta \leq 1$.
θ	Water content
θ_m	Mobile water content
θ_{im}	Immobile water content
λ_m	First-order reaction rate for the mobile phase, T^{-1} .
λ_{im}	First-order reaction rate for the immobile phase, T^{-1} .
λ_r	Solute radioactive decay constant, T^{-1} .
μ_w	Dynamic viscosity of water, $ML^{-1}T^{-1}$.
ξ	Mapping of x global coordinate into local coordinate system, $-1 \leq \xi \leq 1$.
ρ_b	Bulk density of the solid, ML^{-3} .
ρ_s	Particle density of the solid, ML^{-3} .
ρ_k	Density of phase k, ML^{-3} .
ρ_w	Density of water, ML^{-3} .
σ	Elevation of the aquifer base, L, or solution boundary.
τ	Tortuosity of the porous medium.
ϕ	Porosity of the porous medium.
ϕ_e	Effective or drainage porosity of the porous medium.
Φ	Fraction of water residing within the mobile phase.
Φ_{min}	Minimum fraction of water residing within the mobile phase.
Φ_{sat}	Fraction of water residing within the mobile phase at saturation.
ϕ_i	Basis function for the trilinear isoparametric element.
ψ	Pressure head, L.
ψ_a	Air entry pressure head, L.
ψ_i	Asymmetric weighting functions for advection term in transport equation.
ω	Time differencing parameter for transport equation, $0 \leq \omega \leq 1$.
ω_d	Specific yield or drainage porosity.
Ω	Solution domain.
∇_x	Gradient operator in global coordinate system, L^{-1}
∇_ξ	Gradient operator in local coordinate system, L^{-1}

1 Introduction

This report documents a finite element code designed to model subsurface flow and contaminant transport, named FACT. FACT is a transient three-dimensional, finite element code designed to simulate isothermal groundwater flow, moisture movement, and solute transport in variably saturated and fully saturated subsurface porous media. The code is designed specifically to handle complex multi-layer and/or heterogeneous aquifer systems in an efficient manner and accommodates a wide range of boundary conditions. Additionally, 1-D and 2-D (in Cartesian coordinates) problems are handled in FACT by simply limiting the number of elements in a particular direction(s) to one. The governing equations in FACT are formulated only in Cartesian coordinates.

Certain problems can, due to the physics, be reduced dimensionally by expressing them in a different coordinate system (e.g., cylindrical coordinates). One such example would be the 1-D axisymmetric flow to a single extraction well in a confined homogeneous aquifer. In FACT this problem must be handled in Cartesian coordinates where the mesh chosen would be one element long in the vertical z-direction and multiple elements in both directions areally. Even though the FACT model for this basically 1-D problem will contain a far larger number of unknowns than necessary for a given accuracy level, FACT still remains somewhat competitive computationally due to its efficiency.

Groundwater flow and solute transport simulations can be performed in one computer run concurrently or in two sequential computer runs, whichever is more appropriate for the particular problem being considered. A wide range of aquifer conditions (e.g., confined, unconfined or partially confined with storage conversion) commonly encountered in the field can be handled. Material heterogeneity and anisotropy are handled by taking advantage of the finite element discretization approach. Spatial discretization is either performed automatically within FACT or read in through input. The code uses simple rectangular (plane or brick) elements and also offers great flexibility in creating grids for complex flow domains.

FACT handles groundwater flow and solute transport in an unconfined aquifer system whose soil moisture retention functions and relative permeability relationships do not exhibit hysteresis. Spatial and temporal variations of water table elevations (due to mounding, de-watering and pumping effects) are taken into account using a variably saturated modeling approach with user supplied soil-water retention curves. After a converged numerical solution to the nonlinear flow problem is obtained, the position of the water table can also be located by the code.

The groundwater flow equation is approximated using the Bubnov-Galerkin finite element method in conjunction with an efficient symmetric PCG (Preconditioned Conjugate Gradient, ICCG) matrix solver. The solute transport equation is approximated using an upstream-weighted residual finite element method designed to overcome (or alleviate) numerical oscillations. Transport mechanisms considered include: advection, hydrodynamic dispersion, linear equilibrium adsorption, mobile/immobile first-order mass transfer, first-order degradation and radioactive decay effects. An efficient

FACT CODE MANUAL

asymmetric PCG (ORTHOMIN) matrix solver is employed. For both the flow and transport equations, an efficient element matrix generation scheme (analytical) is utilized based on the choice of simple rectangular prism elements (where vertical distortion of each element is allowed) where element matrices are computed from influence coefficient formulas or computed using two-point Gauss-Legendre quadrature. For solving non-linear flow problems Newton-Raphson linearization and Picard iteration options are available along with under-relaxation formulas to further enhance convergence properties.

Many types of boundary conditions can be treated conveniently. For flow simulations, the boundary conditions permitted include steady-state and/or transient prescribed values of hydraulic head, fluid flux, pumping/injection wells, recirculation wells, head-dependent source beds, vertical head-dependent line sources, recharge/drain combination and groundwater recharge. For transport simulations, the boundary conditions permitted include prescribed concentration, prescribed solute mass fluxes, pumping/injection wells, recirculation wells, recharge/drain combination and groundwater recharge.

Many of the modules in FACT are modified versions taken from the HydroGeoLogic, Inc. codes:

- Saturated code named SAFT3D, Version 1.3, developed by Huyakorn, et. al. (1991)
- Variably saturated code named VAM3DCG, Version 2.4, developed by Huyakorn, et. al. (1992)

The original FACT was a reduced version of SAFT3D that handles only three-dimensional flow geometries. This original FACT also had numerous improvements made in its input/output structure, as well as, internal documentation within the source listing. The current version of FACT has incorporated a variety of improvements (e.g., new boundary condition options, improved numerics, dynamic memory allocation, binary Tecplot™ files, and a physically based variably saturated model from VAM3DCG).

Comprehensive sets of verification test examples are presented to check various formulations, aspects, and numerical schemes used in the code. The given examples range from simple one-dimensional to complex three-dimensional and multi-layer flow and transport problems. This document is intended for use as a theory manual, a user's manual, and contains detailed information on the model performance and design specifications, the structuring of the code, input/output organizations, input preparation guides, as well as sample input and output files for the selected test problems. Also included are specific instructions for problem definition, job setup, and restart procedures.

1.1 Overview of Code Capabilities and Salient Features

Multi-dimensional modeling of water flow and waste migration in variably saturated and/or fully saturated subsurface systems can be a formidable task unless one is equipped with the proper code that accommodates various field conditions and does so in an efficient manner. Recognizing this point, FACT was developed to have not only the essential modeling capabilities, but also some salient features that help facilitate its practical use. An overview of these aspects of FACT are:

FACT CODE MANUAL

- FACT utilizes dynamic memory allocation features of Fortran 90 (allocate and deallocate).
- FACT can perform transient analyses or single step steady-state analyses of both variably saturated isothermal groundwater flow and isothermal solute transport problems. If the flow and transport problems are associated, a dual simulation can be made by solving the problems concurrently or sequentially in a single computer run.
- Many of the finite element formulations and nonlinear solution procedures in FACT are based on state-of-the-art technology designed to accommodate a wide range of field conditions including highly nonlinear moisture characteristics, material heterogeneity and anisotropy, and rapidly fluctuating transient boundary conditions.
- FACT uses highly efficient matrix generation and matrix solution techniques. Elemental matrix generation is performed using analytical "influence matrix coefficients" or computed using two-point Gauss-Legendre quadrature. Global matrix solution is obtained with Pre-conditioned Conjugate Gradient-like (PCG) solvers (i.e., ICCG(0) for symmetric matrices and ORTHOMIN for asymmetric matrices). These PCG solvers are designed to efficiently handle problems with a large number of nodal unknowns (on the order of several thousand or more).
- Several iteration strategies are available for solving the nonlinear flow equations. These equations can be solved by Picard iteration, full Newton-Raphson iteration, or modified Newton-Raphson iteration. Under-relaxation of the solution at each iteration is also performed to enhance convergence.
- For highly heterogeneous aquifers an option to incorporate some degree of upstream weighting of the relative permeabilities is available.
- The flow simulator of FACT can handle various boundary conditions (type 1, type 2, and type 3) and physical processes including infiltration, well pumping, seepage faces, and varying water table conditions. Temporal variations in head, mixture flow, and recharge flux boundary conditions can be handled conveniently using either Heaviside, linear or cubic spline representation of input data.
- FACT handles variably saturated conditions by use of user specified soil-water retention curves. The user supplies in tabular form for each soil: (1) water saturation as a function of pressure head, and (2) relative permeability as a function of water saturation.
- The transport simulator of FACT is designed to handle both conservative and non-conservative solutes. Its formulation is designed to have an upstream weighting capability as an option to help circumvent numerical oscillations typically observed at high cell Peclet numbers for centered differencing (recommended).
- FACT handles linear homogeneous and heterogeneous solute reaction rates, such as radioactive decay and linear sorption isotherms, respectively.
- The transport simulator of FACT is designed to handle the isothermal transport of a single solute through a variably saturated porous media using a single or dual domain (porosity) formulation with mobile/immobile first-order mass transfer. Its current

formulation does not account for potential interactions between multiple solutes (e.g., the impacts associated with mother-daughter radioactive chains).

1.2 Applicability of the Code

The FACT code has many practical applications. Typical examples include the following:

- Ground-water resource evaluation - used to predict the response of a ground-water basin to different schemes of well pumping and recharge operations. The program computes spatial and temporal variations of piezometric head, groundwater flow velocities, and flow rates.
- Assessment of well performance and pumping test analysis - used to analyze flow in the vicinity of pumped wells, to predict well performance, and to prepare type curves for evaluation of pumping test data.
- Ground-water contamination investigations - used to predict extent of contaminant plumes and the rate of plume migration, to aid in the design of ground-water quality monitoring programs, and to design and assess the effectiveness of remedial schemes for ground-water contamination.
- Hazardous waste subsurface disposal - used to perform a risk analysis by assessing ground-water flow and potential migration from a waste site, and used to evaluate tracer test data.
- Regional aquifer studies - because of the special design feature of the FACT code, it is ideally suited for use in studying large regional multi-aquifer systems.

1.3 Code User Requirements

In order to apply the FACT code effectively, the user will need:

- a thorough understanding of hydrogeological principles
- a basic understanding of finite element techniques
- an awareness of the code's capabilities and limitations
- familiarity with the editor, operating system, and file handling concepts of the computer system used.

It is also recommended that the user run some of the test problems provided to gain confidence and understanding in using the code.

1.4 Computer Equipment Requirements

FACT is mostly written in ANSI Standard Fortran 77 with Fortran 90 features. The Fortran 90 features include the use of modules, procedures and dynamic memory allocation (allocate and deallocate). The binary Tecplot[™] functions require a C compiler.

The source code was developed and tested on a Silicon Graphics Indigo2 workstation and an IBM PC. FACT was compiled on the SGI workstation using f90 and cc under IRIX 6.5. FACT was ported without source changes to the IBM PC using Microsoft[®] Visual

FACT CODE MANUAL

Studio™ 97 as the development environment under Windows 95. The Fortran compiler is Digital™ Visual Fortran 5.0 and the C compiler is Microsoft® Visual C++ 5.0.

All memory allocation is dynamic in FACT. There are fixed array sizes, such as the 8x8 elemental matrices, which do not depend on the size of the problem. Therefore memory requirements depend mainly on whether the chosen problem and solution technique (Picard versus Newton) yield a symmetric or non-symmetric matrix, the number of nodes/elements, boundary conditions and number of observation nodes and/or well groups.

(This Page Intentionally Left Blank)

2 Governing Mathematical Models

The FACT code can perform three-dimensional finite element simulations of water flow and solute (contaminant) transport in variably saturated and fully saturated porous media. The code employs state-of-the-art numerical technology to provide efficient steady-state and transient solutions of practical problems encountered in the assessment, mitigation, and remediation of soil and groundwater contamination due to the disposal or accidental releases of chemicals and/or nuclear wastes. Due to the level of implicitness employed in solving these equations, steady-state analyses can be performed by disregarding all storage terms of the governing equations, thus avoiding the necessity of time marching. Transient analyses are performed by time marching until the prescribed number of time steps is reached. For water flow simulations, FACT can handle a variety of boundary conditions including well pumping or injection, groundwater recharge, leakage from seepage faces, homogeneous/heterogeneous aquifer and aquitard units, and a variety of source bed types. For solute transport simulations, FACT accounts for advection, hydrodynamic dispersion, equilibrium linear adsorption, mobile/immobile first-order mass transfer, first-order reaction rates and radioactive decay. Single component transport of conservative and non-conservative solutes can be treated.

FACT employs a right-handed Cartesian coordinate system (x,y,z) to generate a three-dimensional rectangular grid for finite element analysis. The grid is oriented such that the z-axis points in the vertical upward direction. In the areal extent the grid is confined to be comprised of rectangular elements, while in the vertical direction distorted elements are handled. Based upon the formulation chosen and accuracy considerations, the level of vertical elemental distortion from a rectangular shape should be kept to a minimum. As a general rule of thumb, the majority of elements within the domain should maintain their vertical angles within the range $90^\circ \pm 10^\circ$. In the majority of practical situations, this limitation on mesh distortion will not be reached.

2.1 Governing and Auxiliary Equations for Variably Saturated Groundwater Flow

The governing equation for water flow in variably saturated soils (containing water and air) can be obtained by combining a special form of Darcy's law (derived from the water phasic momentum balance) and the continuity equation written for the water phase. Darcy's law takes the form

$$\mathbf{U} = -\frac{\mathbf{k}k_{rw}}{\mu_w}(\nabla p_w + \rho_w g \nabla z) \quad (2.1.1)$$

where \mathbf{k} are components of the intrinsic permeability tensor, k_{rw} is relative permeability with respect to the water phase, ρ_w and μ_w are density and dynamic viscosity of water, p_w is the water pressure, g is the gravitational acceleration and z is the elevation above a reference datum.

FACT CODE MANUAL

The continuity equation for the mobile water phase is presented in the form

$$\frac{\partial}{\partial t}(\rho_w \theta_m) + \nabla \cdot (\rho_w \mathbf{U}) = \rho_w q \quad (2.1.2)$$

where $\theta_m = \phi_e S_w$ is the mobile water content, ϕ_e is the effective or kinematic porosity of the soil medium, S_w is the water saturation and q is the volumetric flow rate via sources (or sinks) per unit volume of the porous medium.

Substituting Eq. (2.1.2) into (2.1.1), we obtain

$$\nabla \cdot \left[\frac{\rho_w \mathbf{k} k_{rw}}{\mu_w} (\nabla p_w + \rho_w g \nabla z) \right] = \frac{\partial}{\partial t}(\rho_w \theta_m) - \rho_w q \quad (2.1.3)$$

Equation (2.1.3) can be written in terms of a pressure head ψ , defined as

$$\psi = (p_w - p_a) / \rho_w g \quad (2.1.4)$$

where p_a is pressure in the air phase, assumed to be constant and equal to the atmospheric pressure. Instead, to eliminate the spatial derivative of the elevation in Eq. (2.1.3), we choose to define Eq. (2.1.3) in terms of piezometric or hydraulic head defined as

$$h = \psi + z \quad (2.1.5)$$

Substitution of Eqs. (2.1.4) and (2.1.5) into (2.1.3) results in

$$\nabla \cdot [\mathbf{K} k_{rw} \rho_w \nabla h] = \frac{\partial}{\partial t}(\rho_w \theta_m) - \rho_w q \quad (2.1.6)$$

where \mathbf{K} is the saturated hydraulic conductivity tensor, defined as

$$\mathbf{K} = \rho_w g \mathbf{k} / \mu_w \quad (2.1.7)$$

The first term of the right-hand side of Eq. (2.1.6) can be restated in terms of hydraulic head through the use of additional constitutive assumptions. Expansion of the time derivative in Eq. (2.1.6) yields

$$\frac{\partial}{\partial t}(\rho_w \theta_m) = \rho_w \phi_e \frac{\partial S_w}{\partial t} + \rho_w S_w \frac{\partial \phi_e}{\partial t} + \phi_e S_w \frac{\partial \rho_w}{\partial t} \quad (2.1.8)$$

The compressibility of the porous media is defined as

$$\alpha \equiv \frac{\partial \phi_e}{\partial p_w} = \frac{\partial h}{\partial p_w} \frac{\partial \phi_e}{\partial h} = \frac{1}{\rho_w g} \frac{\partial \phi_e}{\partial h} \quad (2.1.9)$$

where the second term in Eq. (2.1.8) becomes

$$\rho_w S_w \frac{\partial \phi_e}{\partial t} = \rho_w S_w \frac{\partial \phi_e}{\partial h} \frac{\partial h}{\partial t} = \rho_w S_w \alpha \rho_w g \frac{\partial h}{\partial t} \quad (2.1.10)$$

FACT CODE MANUAL

To evaluate the temporal change in fluid density the compressibility of the fluid defined as

$$\beta \equiv \frac{1}{\rho_w} \frac{\partial \rho_w}{\partial p_w} = \frac{1}{\rho_w} \frac{\partial h}{\partial p_w} \frac{\partial \rho_w}{\partial h} = \frac{1}{\rho_w^2 g} \frac{\partial \rho_w}{\partial h} \quad (2.1.11)$$

is invoked to give

$$\frac{\partial \rho_w}{\partial t} = \frac{\partial \rho_w}{\partial h} \frac{\partial h}{\partial t} = \beta \rho_w^2 g \frac{\partial h}{\partial t} \quad (2.1.12)$$

Substitution of Eq. (2.1.10) and (2.1.12) into (2.1.8) yields

$$\frac{\partial}{\partial t} (\rho_w \theta_m) = \rho_w \phi_e \frac{\partial S_w}{\partial t} + \rho_w S_w \rho_w g (\alpha + \phi_e \beta) \frac{\partial h}{\partial t} \quad (2.1.13)$$

Combination of Eq. (2.1.6) and (2.1.13) and assuming that the gradient of the fluid density is negligible, reduces the flow equation to

$$\nabla \cdot [\mathbf{K} \mathbf{k}_{rw} \nabla h] = \phi_e \frac{\partial S_w}{\partial t} + S_w S_s \frac{\partial h}{\partial t} - q \quad (2.1.14)$$

where $S_s = \rho_w g (\alpha + \phi_e \beta)$ is the coefficient of specific storage. Equation (2.1.14) contains three unknowns: h , S_w , and k_{rw} . Thus to solve it, we require two auxiliary equations. These equations depend on the soil properties and may be written in functional form as follows:

$$S_w = S_w(\psi) \quad (2.1.15a)$$

$$k_{rw} = k_{rw}(S_w) \quad (2.1.15b)$$

By neglecting hysteresis effects in the wetting and drying of soils, S_w , and k_{rw} may be considered as single-valued functions. Differentiation of Eq. (2.1.15a) with respect to time gives

$$\frac{\partial S_w}{\partial t} = \frac{dS_w}{d\psi} \frac{\partial \psi}{\partial h} \frac{\partial h}{\partial t} = \frac{C}{\phi_e} \frac{\partial h}{\partial t} \quad (2.1.16a)$$

where C is called the specific moisture capacity, defined as

$$C = \phi_e (dS_w / d\psi) \quad (2.1.16b)$$

Substitution of Eq. (2.1.16a) into (2.1.14) yields

$$\nabla \cdot [\mathbf{K} \mathbf{k}_{rw} \nabla h] = (C + S_w S_s) \frac{\partial h}{\partial t} - q \quad (2.1.17)$$

Equations (2.1.17), (2.1.15a), and (2.1.15b) form the required governing equation and auxiliary equations for variably saturated flow problems. Because of the highly nonlinear nature of the relations between relative permeability, water saturation, and pressure head, the governing equation is highly nonlinear in the unsaturated zone.

FACT CODE MANUAL

For a complete description of a particular flow situation, Eq. (2.1.17) must be supplemented by the appropriate initial and boundary conditions. The initial conditions are simply

$$h(x,0) = h_0(x) \quad (2.1.18a)$$

where h_0 is a prescribed function of x .

The boundary conditions take the form of either prescribed head or prescribed normal flux, and these are given by

$$h(x,t) = \bar{h} \quad \text{on } B_1 \quad (2.1.18b)$$

$$-k_{rw} \mathbf{K} \nabla h \cdot \mathbf{n} = q \quad \text{on } B_2 \quad (2.1.18c)$$

where \bar{h} and q are prescribed functions of x and t , and \mathbf{n} is the unit outward normal vector on B_2 .

In order to solve the variably saturated flow problem, it is also necessary to specify the relationships of relative permeability versus water saturation, and water saturation versus pressure head. Two alternative functional expressions are widely used to describe the relationship of relative permeability versus water saturation. These functions are given by (Brooks and Corey, 1966):

$$k_{rw} = S_e^n \quad (2.1.19a)$$

and van Genuchten (1980):

$$k_{rw} = \sqrt{S_e} \left[1 - \left(1 - S_e^{1/\gamma} \right)^\gamma \right]^2 \quad (2.1.19b)$$

where n and γ are empirical parameters and S_e is the effective water saturation defined as

$$S_e = \frac{S_w - S_{wr}}{1 - S_{wr}} \quad (2.1.19c)$$

with S_{wr} being referred to as the residual water saturation.

The relationship of pressure head versus water saturation is described by the following function:

$$\frac{S_w - S_{wr}}{1 - S_{wr}} = \begin{cases} \frac{1}{\left[1 + \left(\alpha |\psi - \psi_a| \right)^\beta \right]^\gamma} & \text{for } \psi < \psi_a \\ 1 & \text{for } \psi \geq \psi_a \end{cases} \quad (2.1.19d)$$

FACT CODE MANUAL

where α and β are empirical parameters, ψ_a is the air entry pressure head. The parameters β and γ are usually related by $\gamma = 1 - 1/\beta$. The van Genuchten functions for the relative permeability and moisture retention characteristics can be measured in the laboratory for a given soil. The second functional expressions are called pseudo soil functions. The pseudo soil functions are used when the relative permeability and moisture retention functions of a soil are unknown. The pseudo soil functions given below are also used when the water table levels are desired but the moisture behavior in the unsaturated zone is unimportant.

$$k_{rw} = S_w \quad (2.1.20a)$$

$$S_w(\psi) = \begin{cases} \max \left\{ 1 + \frac{\psi}{r_w}, S_{wr} \right\} & \text{for } \psi < 0 \\ 1 & \text{for } \psi \geq 0 \end{cases} \quad (2.1.20b)$$

where r_w is the approximate ramp width. The actual ramp width is $r_w(1 - S_{wr})$.

2.2 Governing and Auxiliary Equations for Variably Saturated Solute Transport

The governing equation describing the transport of a particular species through a variably saturated porous media is obtained by the formal integration (i.e., space and time averaging over a small representative volume of the porous media) of that solute's local and instantaneous phasic transport equation for each phase, k , contained within the porous medium. Typically, this transport equation is referred to as the scalar advection-dispersion transport equation. In this context each immiscible fluid represents a phase and the solid is considered a separate phase. Typically, we are concerned with at most three phases, which we shall denote as liquid (w), gas (g), and solid (s). For species "a" in phase k we can write the (after space/time averaging) transport equation as

$$\frac{\partial}{\partial t}(\alpha_k \rho_k x_a) + \nabla \cdot (\alpha_k \mathbf{n}_{ka}) = \alpha_k r_{ka} + \Gamma_k + q(\rho_k x_a)^* \quad (2.2.1)$$

where

$$\mathbf{n}_{ka} = \rho_k x_a \mathbf{u}_k + \mathbf{j}_a \quad (2.2.2)$$

$$\mathbf{j}_a = -\rho_k \mathbf{D}_{ka} \nabla x_a \quad (2.2.3)$$

and the terms of Eq. (2.2.1) are defined as

$\frac{\partial}{\partial t}(\alpha_k \rho_k x_a)$ accumulation term,

$\nabla \cdot (\alpha_k \mathbf{n}_{ka})$ total flux of species "a" within phase k with respect to a fixed coordinate system,

$\alpha_k r_{ka}$ creation of species "a" by homogeneous reactions within phase k ,

FACT CODE MANUAL

Γ_k input of species "a" into phase k at interface by mass transfer and heterogeneous reactions,

$q(\rho_k x_a)^*$ source of species "a" by injection or withdrawal.

In Eq. (2.2.1), α_k is the volume fraction of phase k, ρ_k the phase density, x_a the mass fraction of species "a". In Eq. (2.2.2), u_k is the phasic velocity. In Eq. (2.2.3), D_{ka} is the hydrodynamic dispersion tensor with respect to phase k.

Equation (2.2.1) describes the transport of species "a" through a porous media under very general conditions. In FACT, we shall consider the transport of species "a" limited to the following assumptions:

- We shall restrict ourselves to situations where the concentration level of species "a" is sufficiently small (typically referred to then as a solute) to have negligible effect on the liquid's (typically referred to then as the solvent) mixture density.
- We limit ourselves to only binary dispersion. Only diffusive and dispersive effects associated with a binary system have been considered. The molecular diffusion coefficient requested as input represents the system's binary mass diffusion coefficient.
- In FACT, there are only three phases present: a gas phase (typically atmospheric air in the subsurface), a liquid phase (typically groundwater), and a solid phase (typically the soil).
- We shall restrict ourselves to the transport of a single solute that is dissolved in the liquid phase. Therefore, potential interactions that might occur between multiple transported solutes is not addressed.
- We shall assume that the solute does not exist in the gas phase and that the solute has infinite diffusive capability within the solid phase (i.e., no concentration gradients of species "a" within the solid phase).
- We will assume that the solid phase is stationary ($v_s = 0$) and that the liquid phase compressibility to be negligible.
- No energy balance calculations are performed within FACT; therefore, the transport of solute "a" is restricted to isothermal (or nearly isothermal) conditions.

Using the general balance given by Eq. (2.2.1), and employing the listed assumptions, we can write out for each phase its species "a" continuity (mass) balance:

f-fluid balance (we shall use the symbol w)

$$\frac{\partial}{\partial t}(\alpha_w \rho_w x_a) + \nabla \cdot (\rho_w x_a \alpha_w \mathbf{u}_w) = \nabla \cdot (\alpha_w \mathbf{D}_{wa} \rho_w \nabla x_a) + \alpha_w r_{wa} + \Gamma_w + q(\rho_w x_a)^* \quad (2.2.4)$$

s-solid balance (we shall use y_a for solute "a" concentration in solid)

$$\frac{\partial}{\partial t}(\alpha_s \rho_s y_a) = \alpha_s r_{sa} + \Gamma_s \quad (2.2.5)$$

g-gas balance

$$0 = 0 \quad (2.2.6)$$

A mass balance for solute "a" at the interface between the liquid and solid phases becomes (where it is assumed that no heterogeneous reactions are occurring):

$$\Gamma_w + \Gamma_s = R_{\text{Hetero}} = 0 \quad (2.2.7)$$

An overall mass balance for solute "a" is obtained by summing up Eqs. (2.2.4), (2.2.5), and applying the constraint in Eq. (2.2.7) to give

$$\begin{aligned} \frac{\partial}{\partial t}(\alpha_w \rho_w x_a + \alpha_s \rho_s y_a) + \nabla \cdot (\rho_w x_a \alpha_w \mathbf{u}_w) = \nabla \cdot (\alpha_w \mathbf{D}_{wa} \rho_w \nabla x_a) + \alpha_w r_{wa} \\ + \alpha_s r_{sa} + q(\rho_w x_a)^* \end{aligned} \quad (2.2.8)$$

Redefining some terms as

$$\alpha_w = \theta_m \quad (2.2.9a)$$

$$\alpha_s = 1 - \phi \quad (2.2.9b)$$

$$\mathbf{U} = \alpha_w \mathbf{u}_w \quad (2.2.9c)$$

$$\mathbf{D}_m = \mathbf{D}_{wa} \quad (2.2.9d)$$

where \mathbf{U} is the Darcy velocity for phase w and assuming that the only homogeneous reaction taking place within each phase is the radioactive decay of solute "a" (i.e., first order reaction rates)

$$r_{wa} = -(\lambda_m + \lambda_r) \rho_w x_a \quad (2.2.10a)$$

$$r_{sa} = -\lambda_r \rho_s y_a \quad (2.2.10b)$$

where λ_m first-order reaction rate for the mobile phase and λ_r is the decay constant and is defined in terms of the half-life $t_{1/2}$ as

$$\lambda_r = (\ln 2)/t_{1/2} \quad (2.2.10c)$$

we substitute Eqs. (2.2.9)-(2.2.10) into Eq. (2.2.8) to obtain

$$\begin{aligned} \frac{\partial}{\partial t} [\theta_m c + (1 - \phi) \rho_s \bar{c}] + \nabla \cdot (c \mathbf{U}) = \nabla \cdot (\theta_m \mathbf{D}_m \nabla c) - \theta_m \lambda_m c \\ - \lambda_r [\theta_m c + (1 - \phi) \rho_s \bar{c}] + q c^* \end{aligned} \quad (2.2.11)$$

where

q volumetric flow source per unit volume of porous medium,

FACT CODE MANUAL

$c = \rho_w x_a$ solute "a" conc. in w-phase, mass of "a" per unit volume of w-phase,

$\bar{c} = y_a$ solute "a" concentration in s-phase, mass of "a" per unit mass of s-phase,

* evaluated within source/sink flow term.

Equation (2.2.11) contains the two unknown concentrations, c and \bar{c} . Therefore, some auxiliary equations are required to relate these two variables. We shall constrain these concentrations through a commonly used empirical relationship for the absorption of solute "a", the Freundlich equilibrium (sorption) isotherm

$$y_a = \beta(x_a)^{1/m} \quad \text{or} \quad \bar{c} = \rho_w k_d (x_a)^{1/m} \quad (2.2.12a)$$

If $m = 1$ then the expression becomes the linear equilibrium sorption isotherm used by FACT

$$\bar{c} = k_d c \quad (2.2.12b)$$

where k_d is the distribution coefficient.

For the following derivations we shall assume that Eq. (2.2.12b) applies. Substituting Eq. (2.2.12b) into Eq. (2.2.11) yields

$$\frac{\partial}{\partial t}(\theta_m R c) + \nabla \cdot (c \mathbf{U}) = \nabla \cdot (\mathbf{D} \nabla c) - \theta_m R \lambda_r c - \theta_m \lambda_m c + q c^* \quad (2.2.13)$$

where $R = 1 + (1 - \phi) \rho_s k_d / \theta_m$ is the retardation coefficient and $\mathbf{D} = \theta_m \mathbf{D}_m$ is the apparent hydrodynamic dispersion tensor. In an open laminar flow field the spreading of a solute from the path determined by advection (e.g., along its streamline) is the result of molecular diffusion. In a porous media an additional process referred to as mechanical dispersion (or hydraulic dispersion) occurs and may become dominant. The sum of the two processes, molecular diffusion and mechanical dispersion, is called hydrodynamic dispersion.

Molecular diffusion is caused by the thermal-kinetic energy (i.e., Brownian motion of particles) of the solute molecules within the flowing solvent mixture and is dependent on local solute concentration gradients. This diffusion process is independent of fluid velocity and is important only in areas of low fluid (phasic) velocity. For a binary mixture the microscopic process of molecular diffusion results in the molecular diffusion flux

$$\mathbf{j}_a^* = -\mathbf{D}_{wa} \nabla c \quad (2.2.14a)$$

known as Fick's first law of diffusion (Bird, et. al. (1960)). The molecular diffusion coefficient is a scalar that is a function of local fluid properties.

In a porous media as the interstitial velocity (also referred to as phasic, average pore, average linear, or seepage velocity) increases mechanical dispersion becomes dominant. At the macroscopic level, mechanical dispersion is caused entirely by the motion of the

FACT CODE MANUAL

fluid about the solid substrate. Dispersion is a process whereby mixing occurs due to differing interstitial velocities at the pore level:

- Velocity profiles within pore channels exist across adjacent solid particles.
- Neighboring pore channel bulk velocities differ due to pore sizes.
- Complex pathways due to tortuosity, branching, and inter-fingering of pore channels.

The spreading of a solute in the direction of bulk flow is known as longitudinal dispersion; while, spreading in directions perpendicular to the bulk flow is called transverse dispersion. Typically, longitudinal dispersion is much stronger than transverse dispersion. At the aquifer level, further dispersive effects can occur due to aquifer heterogeneity. Overall, mechanical dispersion is dependent on interstitial velocity and in general is a tensor quantity for an aquifer unit. Bear (1972) and Freeze and Cherry (1979) provide additional descriptions of hydrodynamic dispersion.

The functional form for the overall dispersion tensor that is in general use is that for an isotropic porous media that is also isotropic with respect to dispersivity. For a binary mixture the overall process of mechanical dispersion plus molecular diffusion results in the dispersive flux

$$\mathbf{j}_a = -D\nabla c \quad (2.2.14b)$$

where the functional form for the overall dispersion tensor becomes velocity dependent.

The following is a simple derivation (see Scheidegger, 1961) for the mechanical dispersion tensor in two dimensions that can be extended to the general three dimensional case. For the case of a three dimensional isotropic medium, the mechanical dispersion tensor takes the following form when orientated along the principle axes of dispersion:

$$\mathbf{D}_P^M = \left\{ \begin{array}{l} \begin{bmatrix} \alpha_L|U| & 0 & 0 \\ 0 & \alpha_T|U| & 0 \\ 0 & 0 & \alpha_T|U| \end{bmatrix} \quad \text{for 3D} \\ \begin{bmatrix} \alpha_L|U| & 0 \\ 0 & \alpha_T|U| \end{bmatrix} \quad \text{for 2D} \end{array} \right\} \quad (2.2.15)$$

If one assumes that the principle axes of dispersion coincide locally with the velocity field, then in 2D the coordinate transformation becomes the rotation operator

$$\mathbf{R} = \begin{bmatrix} \cos \theta & \sin \theta \\ -\sin \theta & \cos \theta \end{bmatrix} \quad (2.2.16a)$$

where

$$\cos \theta = \frac{U_x}{|U|} \quad \text{and} \quad \sin \theta = \frac{U_y}{|U|} \quad (2.2.16b)$$

FACT CODE MANUAL

and the above refer to Darcy velocity components.

We can obtain the local mechanical dispersion tensor from the principle axes tensor, Eq. (2.2.15), by the coordinate tensor transformation

$$\mathbf{D}^M = \mathbf{R}^T \mathbf{D}_p^M \mathbf{R} \quad (2.2.17)$$

Substituting in the rotation operator and its direction cosine definition, results in

$$\mathbf{D}^M = |\mathbf{U}| \begin{bmatrix} \alpha_T & 0 \\ 0 & \alpha_L \end{bmatrix} + \frac{(\alpha_L - \alpha_T)}{|\mathbf{U}|} \begin{bmatrix} U_x^2 & U_x U_y \\ U_x U_y & U_y^2 \end{bmatrix} \quad (2.2.18)$$

The extension to 3D is straight forward given the 3D rotation operator. Note that the 3D rotation operator can be generated by three sequential 2D orthogonal operations

$$\mathbf{R}_{3D} = \mathbf{R}_\theta \mathbf{R}_\phi \mathbf{R}_\alpha \quad (2.2.19)$$

and when applied to Eq. (2.2.17) results in the general expression

$$\mathbf{D}^M \rightarrow D_{ij}^M = \alpha_T |\mathbf{U}| \delta_{ij} + (\alpha_L - \alpha_T) \frac{U_i U_j}{|\mathbf{U}|} \quad (2.2.20)$$

where α_L and α_T are longitudinal and transverse dispersivities, respectively, and δ_{ij} is the Kronecker delta.

The apparent molecular diffusion coefficient for an unsaturated media takes the form

$$D^o = (\theta_m \tau) D^* \quad (2.2.21)$$

where D^* is the bulk molecular diffusion coefficient and τ is the tortuosity through the unsaturated porous media. Millington and Quirk (1961) provide an expression for evaluating τ given by

$$(S_w \phi \tau) = (S_w)^{\frac{10}{3}} \phi^{\frac{4}{3}} \Rightarrow \tau = (S_w)^{\frac{7}{3}} \phi^{\frac{1}{3}} \quad (2.2.22)$$

Collecting terms, the overall ("hydrodynamic") dispersion tensor for an isotropic porous media that is also isotropic with respect to dispersivity becomes (i.e., the sum of the mechanical and molecular contributions)

$$\mathbf{D} \rightarrow D_{ij} \equiv D^o + D_{ij}^M = (\alpha_T |\mathbf{U}| + \theta_m \tau D^*) \delta_{ij} + (\alpha_L - \alpha_T) \frac{U_i U_j}{|\mathbf{U}|} \quad (2.2.23)$$

In deriving Eq. (2.2.23) the porous media was assumed to be isotropic (in addition to the assumption of isotropic dispersion). The correct form for anisotropic systems (see Bear and Bachmat, 1986) unfortunately requires five independent dispersivities, which may be difficult to obtain in most field situations. In many situations the model domain will consist of many aquifer units layered one on top of the other. To account for this limited type of anisotropic porous media (e.g., vertically stratified porous media), and in the

FACT CODE MANUAL

absence of any clear alternatives, Burnett and Frind (1987) suggest a slightly modified form of the conventional dispersion tensor that at least allows the use of two transverse dispersivities, a transverse horizontal dispersivity α_{TH} and a transverse vertical dispersivity α_{TV} . We further modify this dispersion tensor by defining two longitudinal dispersivities, a longitudinal horizontal dispersivity α_{LH} and a longitudinal vertical dispersivity α_{LV} . The above approximations for the hydrodynamic dispersion tensor components become:

$$D_{xx} = \theta_m \tau D^* + \alpha_{LH} \frac{U_x^2}{|U|} + \alpha_{TH} \frac{U_y^2}{|U|} + \alpha_{TV} \frac{U_z^2}{|U|} \quad (2.2.24a)$$

$$D_{yy} = \theta_m \tau D^* + \alpha_{TH} \frac{U_x^2}{|U|} + \alpha_{LH} \frac{U_y^2}{|U|} + \alpha_{TV} \frac{U_z^2}{|U|} \quad (2.2.24b)$$

$$D_{zz} = \theta_m \tau D^* + \alpha_{TV} \frac{U_x^2}{|U|} + \alpha_{TV} \frac{U_y^2}{|U|} + \alpha_{LV} \frac{U_z^2}{|U|} \quad (2.2.24c)$$

$$D_{xy} = D_{yx} = (\alpha_{LH} - \alpha_{TH}) \frac{U_x U_y}{|U|} \quad (2.2.24d)$$

$$D_{xz} = D_{zx} = (\hat{\alpha}_L - \alpha_{TV}) \frac{U_x U_z}{|U|} \quad (2.2.24e)$$

$$D_{yz} = D_{zy} = (\hat{\alpha}_L - \alpha_{TV}) \frac{U_y U_z}{|U|} \quad (2.2.24f)$$

where
$$\hat{\alpha}_L \equiv \frac{\alpha_{LH} + \alpha_{LV}}{2} \quad (2.2.24g)$$

and z is the index for the vertical direction. Note that Eqs. (2.2.24a) to (2.2.24f) collapse back to Eq. (2.2.23) when

$$\alpha_{LH} = \alpha_{LV} = \alpha_L \quad \text{and} \quad \alpha_{TH} = \alpha_{TV} = \alpha_T \quad (2.2.24h)$$

Also note that Eqs. (2.2.24a) to (2.2.24f) assume isotropic dispersion. The current version of FACT does not account for anisotropic dispersion. Anisotropic dispersion would result in dispersivities that were dependent upon the angle between the velocity vector and the principle axes of the anisotropic media.

For the linear isotherm approximation ($m=1$), Eq. (2.2.12b), the "effective" retardation coefficient is defined as

$$R = 1 + \frac{(1-\phi)\rho_s k_d}{\theta_m} = 1 + \frac{\rho_b k_d}{\theta_m} \quad (2.2.25)$$

FACT CODE MANUAL

where the bulk density of the solid, ρ_b , is defined as $(1-\phi)\rho_s$. When solving retardation problems, care should be taken in applying appropriate (consistent) concentration and adsorption units.

Equation (2.2.13) is in conservative form and the non-conservative form is considered to be more convenient for finite element discretization. To accomplish the transformation, use is made of the flow (mixture mass balance) equation, Eq. (2.1.2) in its incompressible form:

$$\frac{\partial \theta_m}{\partial t} = -\nabla \cdot \mathbf{U} + q \quad (2.2.26)$$

Substituting Eq. (2.2.26) into (2.2.13), with expanded advective and mass accumulation terms, yields

$$\begin{aligned} \theta_m R \frac{\partial c}{\partial t} + c \frac{\partial \theta_m}{\partial t} + c \frac{\partial}{\partial t} (\rho_b k_d) + \mathbf{U} \cdot \nabla c - c \frac{\partial \theta_m}{\partial t} + qc = \\ \nabla \cdot (\mathbf{D} \nabla c) - \theta_m R \lambda_r c - \theta_m \lambda_m c + qc^* \end{aligned} \quad (2.2.27)$$

Assuming that the time derivative of $\rho_b k_d$ is negligible, Eq. (2.2.27) reduces to

$$\theta_m R \left(\frac{\partial c}{\partial t} + \lambda_r c \right) + \mathbf{U} \cdot \nabla c = \nabla \cdot (\mathbf{D} \nabla c) - \theta_m \lambda_m c - q(c - c^*) \quad (2.2.28)$$

which is the equation used in FACT.

In obtaining the solution of the solute transport equation, one must specify as an initial condition the concentration distribution at some initial time, say $t = 0$, at all points in the flow domain. In addition, boundary conditions must also be specified at all times. The types of boundary conditions of practical interest include the conditions of prescribed concentration and prescribed material flux. The initial and boundary conditions associated with Eq. (2.2.28) are as follows:

$$\text{Initial condition} \quad c(\mathbf{x}, 0) = c_0(\mathbf{x}) \quad (2.2.29a)$$

$$\text{Dirichlet} \quad c(\mathbf{x}, t) = \tilde{c} \text{ on boundary portion } B'_1 \quad (2.2.29b)$$

$$\text{Neumann} \quad \mathbf{n} \cdot \mathbf{D} \nabla c = \mathbf{j}_n \text{ on boundary portion } B'_2 \quad (2.2.29c)$$

$$\text{Cauchy} \quad \mathbf{n} \cdot (\mathbf{D} \nabla c - c\mathbf{U}) = N_n \text{ on boundary portion } B'_3 \quad (2.2.29d)$$

where B'_1 is the portion of the boundary where concentration is prescribed as \tilde{c} , and B'_2 and B'_3 are portions of the boundary where the dispersive and the total solute mass fluxes are prescribed as \mathbf{j}_n and N_n , respectively. Note that incoming is positive by convention.

2.3 Governing Equations for Variably Saturated Mobile/Immobile Solute Transport

Accurately simulating macrodispersion in field-scale solute transport applications is a challenge. Explicitly modeling the smaller scale heterogeneities that cause macrodispersion is often not practical due to computer and/or data limitations. A common alternative is to employ a second-order (Fickian) dispersion term in the solute transport formulation to deal with heterogeneity at a sub-grid level, as shown in the previous section (e.g. Eq. (2.2.28)). With the proper selection of dispersivities, bulk aspects of plume behavior can often be adequately simulated. However, this conventional advection-dispersion formulation exhibits well-known deficiencies such as excessive upstream dispersion and the absence of heavy-tailing in simulated plumes. These deficiencies become more pronounced with increasing natural heterogeneity.

Recent studies suggest that the mobile-immobile concept of solute transport is a more effective alternative for dealing with heterogeneity at the sub-grid level, especially for highly heterogeneous applications (Harvey and Gorelick, 2000; see also Nkedi-Kizza et al., 1983 and Van Genuchten, 1976). The mobile-immobile formulation, also referred to as a 'dual-domain' or 'dual-porosity', is particularly effective at describing the extensive tailing typically observed in the field and laboratory column experiments. With this approach, the subsurface is divided into 'mobile' and 'immobile' regions corresponding to relatively high (e.g. sand) and low (e.g. clay, silt) conductivity regions, respectively. Only mobile groundwater advects across computational cells, while intra-cell solute mass transfer occurs between the mobile and immobile regions.

In this section we present the mobile-immobile water phase model and derive our specific implementation of this model for incorporating it into the FACT code.

2.3.1 Background

The following is a derivation of the implementation within FACT of the mobile-immobile water-phase solute transport model. A listing of the assumptions comprising this conceptual model is provided in Bear and Bachmat (1991). Our conceptual model is shown in Fig. 2.3.1. We consider the general case of a mobile and immobile water phase system within an unsaturated zone in the soil. We model the spatial transport of a dilute contaminant (solute species) in the mobile water phase by advection, dispersion, and diffusion. The immobile water phase does not transport solute spatially; instead, the immobile phase acts as a storage tank either supplying or receiving solute (i.e., source/sink) to or from the neighboring mobile water phase. Solid surface adsorption based on a linear adsorption isotherm model is used to account for water-solid reactions. Also, distributed first-order decay reactions can occur in both the mobile and immobile water phases.

Interfacial mass transfer of solute between the mobile and immobile water phases is handled through a linear film model where the mass transfer rate is proportional to the

FACT CODE MANUAL

solute concentration difference between the two water phases. The fluid mixture density is assumed to be constant, while the solid matrix is assumed to be rigid and stationary.

In Fig. 2.3.1, the mobile water phase is considered to be a continuous phase, while the immobile water phase is modeled as a discrete phase. Consider for purposes of the derivations to follow that the domain shown in Fig. 2.3.1 represents one finite element within the elemental mesh where immobile water exists. Figure 2.3.1 represents a plan view of this particular element (e).

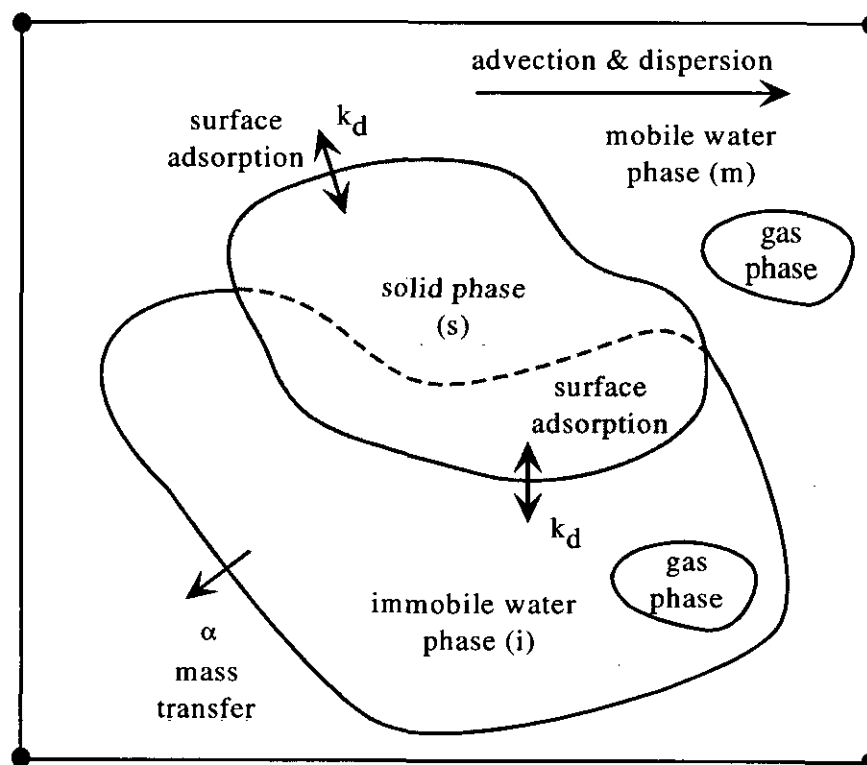


Fig. 2.3.1. Schematic Illustrating the Various Processes Addressed in the Variably Saturated Mobile/Immobile Transport Model at the Element Level

Algorithmically, the existence of the immobile water phase is established on an elemental basis. Through input the user specifies which of the finite elements are to have an immobile water phase in addition to the mobile phase. The properties associated with the immobile water phase are considered to be constant within the domain of a finite element. Since spatial transport of the solute through the immobile phase is prohibited, then the specified elements having immobile water can be placed at any location within the finite element mesh (i.e., no spatial continuity requirements are placed on their locations).

2.3.2 Parameter Definitions

The variably saturated mobile-immobile water phase transport model increases the number of modeling input parameters. Below a definition of these additional parameters is provided.

FACT CODE MANUAL

The mobile-immobile transport model also conforms to and encompasses what is typically called a dual porosity domain model in the MT3DMS transport code (see Zheng, C., and P. P. Wang, 1998). Some of the key processes being modeled are shown in the schematic provided in Figure 2.3.1. Material properties are defined on an elemental basis and generally these properties are specified as elemental (centroidal) averaged values.

As shown in Figure 2.3.1, a specified fraction of the solid phase surface, f , is in direct contact with the mobile water phase. The remaining surface area is in direct contact with the immobile water phase. Adsorption is assumed to take place on the entire surface of the solid material, since this surface is assumed to be in contact with water everywhere. The parameters f and $(1-f)$ define the fractional amount of available adsorption sites that are in contact with the mobile and immobile water phases, respectively. To limit the number of input parameters necessary, we shall assume that the same fractions represent the corresponding fractions of the solid mass that interacts with the two apparent water phases. This last assumption may under certain conditions be a limiting choice and the user should be aware of such limitations. This parameter is defined as:

$$f \equiv \frac{V_{sm}}{V_s} = \frac{A_{sm}}{A_s} = \frac{A_s - A_{sim}}{A_s} \quad (2.3.1)$$

where

V_{sm} volume of solid phase that is associated with mobile water phase.

V_s volume of solid phase.

A_{sm} interfacial surface area between solid phase and mobile phase.

A_{sim} interfacial surface area between solid phase and immobile phase.

A_s surface area of solid phase.

In the mobile-immobile conceptual model several fluid phases exist. Specifically, there exists a mobile water phase, an immobile water phase, and a gas phase (predominantly containing air), which occupy, together, the entire void space. To describe the size (i.e., volumetric magnitude) of these fluid phases in unsaturated media the following two definitions are employed:

$$\theta_\alpha \equiv \frac{V_\alpha}{V_e}, \quad 0 \leq \theta_\alpha \leq \phi, \quad \sum_\alpha \theta_\alpha = \phi \quad (2.3.2)$$

which is called the fluid content (and moisture content for the particular case of water), and

$$S_\alpha \equiv \frac{V_\alpha}{V_v}, \quad 0 \leq S_\alpha \leq 1, \quad \sum_\alpha S_\alpha = 1 \quad (2.3.3)$$

which is called the fluid saturation (or volumetric saturation). The above two definitions are related to each other by

$$\theta_\alpha = \phi S_\alpha \quad (2.3.4)$$

FACT CODE MANUAL

and ϕ is the total porosity within the element defined as

$$\phi \equiv \frac{V_v}{V_e} = \frac{V_e - V_s}{V_e}, \quad 0 \leq \phi \leq 1 \quad (2.3.5)$$

where

V_α volume of α -fluid in element.

V_v volume of voids in element.

V_e volume of element.

V_s volume of solid phase contained within element.

In both definitions, the sum is over all the fluid phases present in the void space. Typically, an interfacial area (i.e., surface) is formed where one fluid phase is in contact with another phase (e.g., a liquid immiscible with the first, a gas, or a solid). Here, we also define an interface between the mobile and immobile water phases; even though, these two water phases are traditionally miscible. From a mass transfer perspective these two water domains behave differently.

The above definitions can also be applied to the total water present (i.e., both mobile and immobile water) as:

$$\theta \equiv \theta_m + \theta_{im} = \frac{V_m + V_{im}}{V_e} \quad \text{and} \quad S_w \equiv S_m + S_{im} = \frac{V_m + V_{im}}{V_v} \quad (2.3.6)$$

where

V_m volume of mobile water phase contained within element.

V_{im} volume of immobile water phase contained within element.

The fraction of water residing within the mobile phase is defined as:

$$\Phi \equiv \frac{\theta_m}{\theta} = \frac{S_m}{S_w} = \frac{V_m}{V_w} = \frac{V_m}{V_m + V_{im}} \quad (2.3.7)$$

What is typically referred to as an "effective" (or kinematic) porosity is equivalent to a mobile-phase porosity when under saturated conditions:

$$\phi_m = \phi \Phi_{sat} \quad (2.3.8)$$

The above definition of a mobile-phase porosity is also used under variably saturated conditions where now this porosity becomes a function of local water saturation.

In terms of the above definitions the mobile and immobile water phase moisture contents become, respectively:

$$\theta_m = \Phi \phi S_w \quad \text{and} \quad \theta_{im} = (1 - \Phi) \phi S_w \quad (2.3.9)$$

In general, the fraction of water contained within the mobile water phase will vary (e.g., proportionally more of the water resides within the immobile water phase as the residual

FACT CODE MANUAL

water saturation is approached). To provide the user flexibility, the following linear functional form for the mobile water fraction is required as input:

$$\Phi = \begin{cases} \Phi_{\min} & \text{for } 0 \leq S_w \leq S_{wr} \\ \left(\frac{S_w - S_{wr}}{1 - S_{wr}} \right) (\Phi_{\text{sat}} - \Phi_{\min}) + \Phi_{\min} & \text{for } S_{wr} < S_w \leq 1 \end{cases} \quad (2.3.10)$$

where a constant mobile water fraction is obtained by setting the minimum and saturated values equal.

These porosities, moisture contents, and water saturations represent elemental averages.

2.3.3 Mobile-Solid Governing Equation for Transport

The conservative form of the solute mass balance for the mobile water-phase is

$$\frac{\partial}{\partial t} (\theta_m c_m) + \theta_m (\lambda_r + \lambda_m) c_m + \nabla \cdot (U c_m) = \nabla \cdot (D \nabla c_m) + \Gamma_{sm} - \alpha (c_m - c_{im}) + q c^* \quad (2.3.10)$$

where

c_m solute concentration in the mobile phase, ML^{-3}

c_{im} solute concentration in the immobile phase, ML^{-3}

c^* solute concentration entering the domain through sources or leaving the domain through sinks, ML^{-3}

$D = \theta_m D_m$ apparent dispersion tensor for mobile phase, $L^2 T^{-1}$

q volumetric flowrate per unit volume of aquifer representing fluid sources (positive) and sinks (negative) in the mobile phase, T^{-1}

U soil moisture flux in the mobile phase, LT^{-1}

α mass transfer coefficient, T^{-1}

Γ_{sm} mass transfer rate from solid surface to mobile water phase, $ML^{-3} T^{-1}$

λ_m first-order reaction rate for the mobile phase, T^{-1}

λ_r solute radioactive decay constant, T^{-1}

θ_m mobile water content, $L^3 L^{-3}$

The conservative form of the solute mass balance for the solid surface that is in direct contact with the mobile water-phase is expressed as

$$\frac{\partial}{\partial t} \{ f(1-\phi) \rho_s y_m \} + f(1-\phi) \lambda_r \rho_s y_m = -\Gamma_{sm} \quad (2.3.11)$$

where

- f fraction of the solid surfaces in contact with the mobile phase,
 L^2L^{-2}
- y_m solute solid-phase mass fraction on surface in contact with the
 mobile water-phase, MM^{-1}
- ϕ total porosity, L^3L^{-3}
- ρ_s solid phase density, ML^{-3}

By adding Eqs. (2.3.10) and (2.3.11) together we obtain the conservative form of the "composite" solute mass balance for the mobile water-phase plus solid phase as

$$\frac{\partial}{\partial t} [\theta_m c_m + f(1-\phi)\rho_s y_m] + \lambda_r [\theta_m c_m + f(1-\phi)\rho_s y_m] + \nabla \cdot (U c_m) = \quad (2.3.12)$$

$$+ \nabla \cdot (D \nabla c_m) - \theta_m \lambda_m c_m - \alpha(c_m - c_{im}) + qc^*$$

The mobile-phase linear equilibrium sorption isotherm and retardation coefficient are, respectively

$$y_m = k_d c_m \quad \text{and} \quad R_m = 1 + \frac{f(1-\phi)\rho_s k_d}{\theta_m} = 1 + \frac{f\rho_b k_d}{\theta_m} \quad (2.3.13)$$

Substituting Eqs. (2.2.26) and (2.3.13) into (2.3.12), with expanded advective and mass accumulation terms, yields

$$\theta_m R_m \frac{\partial c_m}{\partial t} + c_m \frac{\partial \theta_m}{\partial t} + c_m \frac{\partial}{\partial t} (f\rho_b k_d) + U \cdot \nabla c_m - c_m \frac{\partial \theta_m}{\partial t} + qc_m = \quad (2.3.14)$$

$$\nabla \cdot (D \nabla c_m) - \theta_m R_m \lambda_r c_m - \theta_m \lambda_m c_m - \alpha(c_m - c_{im}) + qc^*$$

Assuming that the time derivative of $f\rho_b k_d$ is negligible, Eq. (2.3.14) reduces to

$$\theta_m R_m \left(\frac{\partial c_m}{\partial t} + \lambda_r c_m \right) + U \cdot \nabla c_m = \nabla \cdot (D \nabla c_m) - \theta_m \lambda_m c_m \quad (2.3.15)$$

$$- \alpha(c_m - c_{im}) - q(c_m - c^*)$$

which is the mobile-solid governing equation for transport in FACT.

In obtaining the solution of the mobile-phase solute transport equation, one must specify initial mobile-phase concentrations at all nodes in the flow domain. In addition, boundary conditions must also be specified at all times. The initial and boundary conditions associated with Eq. (2.3.15) are given in Eqs. (2.2.29a) to (2.2.29d).

2.3.4 Immobile-Solid Governing Equation for Transport

The conservative form of the solute mass balance for the immobile water-phase is

$$\frac{\partial}{\partial t} (\theta_{im} c_{im}) + \theta_{im} (\lambda_r + \lambda_{im}) c_{im} = \Gamma_{si} - \alpha(c_m - c_{im}) \quad (2.3.16)$$

FACT CODE MANUAL

where

Γ_{si} mass transfer rate from solid surface to immobile water phase,

$$ML^{-3}T^{-1}$$

λ_{im} first-order reaction rate for the immobile phase, T^{-1}

θ_{im} immobile water content, L^3L^{-3}

The conservative form of the solute mass balance for the solid surface that is in direct contact with the immobile water-phase is expressed as

$$\frac{\partial}{\partial t} \{ (1-f)(1-\phi)\rho_s y_{im} \} + (1-f)(1-\phi)\lambda_r \rho_s y_{im} = -\Gamma_{si} \quad (2.3.17)$$

where

y_{im} solute solid-phase mass fraction on surface in contact with the immobile water-phase, MM^{-1}

By adding Eqs. (2.3.16) and (2.3.17) together we obtain the conservative form of the "composite" solute mass balance for the immobile water-phase plus solid phase as

$$\frac{\partial}{\partial t} [\theta_{im} c_{im} + (1-f)(1-\phi)\rho_s y_{im}] + \lambda_r [\theta_{im} c_{im} + (1-f)(1-\phi)\rho_s y_{im}] = \alpha(c_m - c_{im}) - \theta_{im} \lambda_{im} c_{im} \quad (2.3.18)$$

The immobile-phase linear equilibrium sorption isotherm and retardation coefficient are, respectively

$$y_{im} = k_d c_{im} \quad \text{and} \quad R_{im} = 1 + \frac{(1-f)(1-\phi)\rho_s k_d}{\theta_{im}} = 1 + \frac{(1-f)\rho_b k_d}{\theta_{im}} \quad (2.3.19)$$

Substituting Eqs. (2.3.19) into (2.3.18), with expanded mass accumulation term, yields

$$\theta_{im} R_{im} \frac{\partial c_{im}}{\partial t} + c_{im} \frac{\partial \theta_{im}}{\partial t} + c_{im} \frac{\partial}{\partial t} [(1-f)\rho_b k_d] = \alpha(c_m - c_{im}) - \theta_{im} R_{im} \lambda_r c_{im} - \theta_{im} \lambda_{im} c_{im} \quad (2.3.20)$$

Assuming that the time derivative of $(1-f)\rho_b k_d$ is negligible and steady-state immobile flow $\partial \theta_{im} / \partial t = 0$, Eq. (2.3.20) reduces to

$$\theta_{im} R_{im} \left(\frac{\partial c_{im}}{\partial t} + \lambda_r c_{im} \right) = \alpha(c_m - c_{im}) - \theta_{im} \lambda_{im} c_{im} \quad (2.3.21)$$

which is the immobile-solid governing equation for transport in FACT.

In obtaining the solution of the immobile-phase solute transport equation, one must specify initial immobile-phase concentrations at all nodes in the flow domain.

2.4 Assumptions of Flow and Transport Models

FACT contains both groundwater flow and single-species solute transport models.

Major assumptions of the flow model are as follows:

- Darcy's law is valid and hydraulic head gradients are the only significant driving force for fluid motion.
- Water is the only flowing fluid phase (i.e., the air phase is assumed to be inactive).
- The fluid is considered to be slightly compressible and homogeneous.
- The soil or rock medium may be represented by a single continuum porous medium of spatially invariant properties.
- The porosity and saturated hydraulic conductivity are constant with time.
- Gradients of fluid density, viscosity, and temperature do not affect the velocity distribution.

Major assumptions of the solute transport model are as follows:

- Fluid properties are independent of concentrations of contaminants.
- Injected solutes (contaminants) are miscible with flowing fluid.
- Interactions between solutes are negligible.
- Variations in fluid properties are negligible over expected temperature range.
- Diffusive/dispersive transport in the porous medium system is governed by Fick's law. The hydrodynamic dispersion coefficient is defined as the sum of the coefficients of mechanical dispersion and molecular diffusion. The medium dispersivity is assumed to correspond to that of an isotropic medium, where α_L and α_T are the longitudinal and transverse dispersivities, respectively.
- Adsorption and decay of the solute may be described by a linear equilibrium isotherm and a first-order decay constant, respectively.

2.5 Limitations

The major limitations of FACT include:

- The code is tailored to isothermal unsaturated and fully saturated porous medium systems (solves the Richard's equation). Flow and transport in fractured systems are not taken into account.
- In performing a variably saturated flow analysis, the code handles only single-phase flow of the liquid (i.e., water) and ignores the flow effects from other potential phases (i.e., air or other non-aqueous phases) which, in some instances, can be significant.
- Non-Darcy flow that may occur near pumping wells is neglected.
- The code simulates single-component transport only, and does not take into account decay chain reactions.

FACT CODE MANUAL

- In performing a solute transport analysis, the code does not take into account variations in mixture fluid density associated with changes in solute concentration.
- The code does not take into account non-linear adsorption, non-linear biodegradation, or kinetic sorption effects which, in some instances, may be important.

2.6 Input Data

Data required for the groundwater flow simulation include values of the saturated hydraulic conductivity and specific storage of each aquifer and aquitard material, the geometry and configuration of the flow region, as well as, initial and boundary conditions associated with the flow equation. For unconfined aquifers, it is also necessary to know specific yield and aquifer base elevation.

Data required for the simulation of solute transport include values of (longitudinal-horizontal, longitudinal-vertical, transverse-horizontal, and transverse-vertical) dispersivities, molecular diffusion, total porosity, retardation and decay constants, values of Darcy velocity components, as well as, initial and boundary conditions associated with the transport equation.

2.6.1 Input Data for Flow Problems

Input data of the flow model include the following:

(1) System Geometry

- Horizontal and vertical dimensions including hydrostratigraphic layering (L)

(2) Porous Medium Properties (Hydraulic properties of soil)

- Saturated hydraulic conductivity component, K_{xx} (L/T)
- Saturated hydraulic conductivity component, K_{yy} (L/T)
- Saturated hydraulic conductivity component, K_{zz} (L/T)
- Saturated hydraulic conductivity component, K_{xy} (L/T)
- Saturated hydraulic conductivity component, K_{xz} (L/T)
- Saturated hydraulic conductivity component, K_{yz} (L/T)
- Specific storage, S_s (L^{-1})
- Effective or kinematic porosity, ϕ_e

(3) Constitutive Relationships for Variably Saturated Flow

- Spline multiplier of water saturation versus pressure head
- Spline index of water saturation versus pressure head
- Spline multiplier of relative permeability versus water saturation
- Spline index of relative permeability versus water saturation

(4) Initial Conditions

- Initial values of hydraulic head

(5) Boundary Conditions

- Specified head nodes
- Specified mixture flow nodes
- Recirculation wells
- Pumping/injection wells
- Head-dependent source beds
- Vertical head-dependent line sources
- Recharge/drain combination
- Groundwater recharge

2.6.2 Input Data for Solute Transport Problems

Input data of the solute transport model include the following:

(1) System Geometry

- Horizontal and vertical dimensions including hydrostratigraphic layering (L)

(2) Soil-solute Transport Properties

- Distribution coefficient for linear adsorption, k_d , (L^3M)
- Particle mass density, ρ_s , (L^3M^{-1})
- Total porosity, ϕ
- Longitudinal horizontal dispersivity, α_{LH} , (L)
- Longitudinal vertical dispersivity, α_{LV} , (L)
- Transverse horizontal dispersivity, α_{TH} , (L)
- Transverse vertical dispersivity, α_{TV} , (L)
- Apparent molecular diffusion coefficient, D_0 , (L^2T^{-1})
- Solute decay coefficient, λ_r , (T^{-1})
- First-order reaction rate for the mobile phase, λ_m , (T^{-1})
- Minimum fraction of mobile water, Φ_{min}
- Maximum (saturated) fraction of mobile water, Φ_{sat}
- Fraction of adsorption sites in contact with mobile phase, f
- First-order reaction rate for the immobile phase, λ_{im} , (T^{-1})
- Spline multiplier of mass transfer coefficient between mobile and immobile water, α , (T^{-1})
- Spline index of mass transfer coefficient between mobile and immobile water

(3) Water saturation and Darcy velocity components

- S_w, U_x, U_y and U_z (LT^{-1})

(4) Initial Conditions

- Initial values of mobile and/or immobile concentrations, $c_m(x,0), c_{im}(x,0)$

FACT CODE MANUAL

(5) Boundary Conditions

- Specified concentration nodes
- Specified mass flow nodes
- Recirculation wells
- Pumping/injection wells
- Recharge/drain combination
- Groundwater recharge

(This Page Intentionally Left Blank)

3 Numerical Solution Techniques

In this chapter, numerical techniques for approximating the variably saturated flow equation and the non-conservative solute transport equation are described. The flow equation is treated using the traditional Bubnov-Galerkin finite element method resulting in a set of ordinary differential equations (ODEs). This set of ODEs is finite differenced in time generating a set of algebraic equations (AEs). In general the resulting set of AEs are non-linear and this non-linearity is treated using either the Picard method or Newton-Raphson iterative technique. At each iteration a set of AEs are solved (i.e., the Picard scheme produces a symmetrical set of AEs while the Newton-Raphson technique produces an asymmetrical set of AEs).

The solute (contaminant) transport equation (sometimes referred to as the advection-dispersion transport equation) is treated using a modified Petrov-Galerkin finite element method. This modified Petrov-Galerkin approach is based on an upstream-weighting of the total flux (i.e., dispersive and advective fluxes) designed to circumvent numerical oscillations characteristic at high cell Peclet numbers when the traditional Bubnov-Galerkin finite element method is employed (Huyakorn et al., 1977, 1979). Our current transport model is limited to first order homogeneous (e.g., radioactive decay) and heterogeneous (e.g., a linear sorption isotherm) reaction rates resulting in a set of linear ODEs. This set of ODEs is finite differenced in time generating a set of linear AEs that are asymmetric due to the advection terms.

For both flow and transport problems, spatial discretization is performed using rectangular or distorted brick elements. Element matrices are computed using highly efficient influence coefficient matrix formulas (Huyakorn et al., 1986, 1987) or two-point Gauss-Legendre quadrature. For the fully three-dimensional analysis, the resulting matrix equations are solved efficiently using Preconditioned Conjugate Gradient (PCG) algorithms designed to accommodate a large number of nodal unknowns.

3.1 Numerical Techniques for Variably Saturated Flow

Numerical approximations of the groundwater flow equations describing fully 3-D problems are obtained using the Galerkin finite element technique. In the Galerkin finite element approximation procedure, the flow region is first discretized into a network of finite elements, and an interpolating trial function is used to represent the unknown dependent variable (hydraulic head) over the discretized region. An integral approximation of the flow equation is then obtained using the Galerkin weighted residual criterion. Spatial integration is performed piecewise over each element. Upon assemblage of the elements and incorporation of boundary conditions, a system of nodal equations is obtained. For a steady-state simulation, these nodal equations are algebraic equations. For a transient simulation, the nodal equations are first-order in time ordinary differential equations (and possibly nonlinear) that are integrated using a finite difference approximation. For each time step, this gives rise to a system of algebraic nodal equations that are solved using an iterative matrix solution procedure.

FACT CODE MANUAL

3.1.1 Galerkin Formulation

Equation (2.1.17) is solved employing the Galerkin finite element method. In the Galerkin procedure, the hydraulic head function is approximated as a finite linear combination of trial (basis) functions of the form

$$h(\mathbf{x}, t) = \sum_{J=1}^{np} \phi_J(\mathbf{x}) h_J(t) \quad (3.1.1.1)$$

where $\phi_J(\mathbf{x})$ are basis functions, $h_J(t)$ are nodal values of hydraulic head at time t , respectively, and np is the number of nodes in the finite element network. Applying the Galerkin criterion to (2.1.17) yields

$$\int_{\Omega} \phi_I \nabla \cdot (\mathbf{K} \mathbf{k}_{rw} \nabla h) d\Omega = \int_{\Omega} \phi_I \left\{ (C + S_w S_s) \frac{\partial h}{\partial t} - q \right\} d\Omega, \quad \text{for } I = 1, 2, \dots, np \quad (3.1.1.2)$$

Since we shall choose C_0 continuous basis functions, ϕ_I , the integral on the LHS is evaluated by applying the divergence theorem (actually, Green's first identity, the multidimensional equivalent of integration by parts) to obtain

$$\begin{aligned} \int_{\Omega} \phi_I \nabla \cdot (\mathbf{K} \mathbf{k}_{rw} \nabla h) d\Omega &= \int_{\Omega} \nabla \cdot (\phi_I \mathbf{K} \mathbf{k}_{rw} \nabla h) d\Omega - \int_{\Omega} \nabla \phi_I \cdot (\mathbf{K} \mathbf{k}_{rw} \nabla h) d\Omega \\ &= \int_{\sigma} \phi_I \mathbf{k}_{rw} \mathbf{n} \cdot (\mathbf{K} \nabla h) d\sigma - \int_{\Omega} \nabla \phi_I \cdot (\mathbf{K} \mathbf{k}_{rw} \nabla h) d\Omega \quad (3.1.1.3) \\ &= - \int_{\sigma} \phi_I (\mathbf{n} \cdot \mathbf{U}) d\sigma - \int_{\Omega} \nabla \phi_I \cdot (\mathbf{K} \mathbf{k}_{rw} \nabla h) d\Omega \end{aligned}$$

where Ω is the solution domain with boundary σ , and the Darcy velocity vector is expressed as $\mathbf{U} = -\mathbf{K} \mathbf{k}_{rw} \nabla h$.

Substituting Eqs. (3.1.1.1) and (3.1.1.3) into (3.1.1.2) gives the expression

$$\begin{aligned} \sum_{J=1}^{np} \left\{ \int_{\Omega} (C + S_w S_s) \phi_I \phi_J d\Omega \right\} \frac{dh_J}{dt} + \sum_{J=1}^{np} \left\{ \int_{\Omega} \nabla \phi_I \cdot \mathbf{K} \mathbf{k}_{rw} \nabla \phi_J d\Omega \right\} h_J \\ - \int_{\Omega} \phi_I q d\Omega - \int_{\sigma} \phi_I U_n d\sigma = 0 \end{aligned} \quad (3.1.1.4)$$

where the outward normal component of the Darcy velocity vector is $U_n = -\mathbf{n} \cdot \mathbf{U}$.

Equation (3.1.1.4) can be written more concisely as

$$B_{IJ} \frac{dh_J}{dt} + A_{IJ} h_J - F_I = 0, \quad I = 1, 2, \dots, np \quad (3.1.1.5)$$

FACT CODE MANUAL

where

$$A_{IJ} = \int_{\Omega} \nabla \phi_I \cdot k_{rw} \mathbf{K} \nabla \phi_J d\Omega \quad (3.1.1.6a)$$

$$B_{IJ} = \int_{\Omega} (C + S_w S_s) \phi_I \phi_J d\Omega \quad (3.1.1.6b)$$

$$F_I = \int_{\Omega} \phi_I q d\Omega + \int_{\sigma} \phi_I U_n d\sigma \quad (3.1.1.6c)$$

The set of time-dependent non-linear ordinary differential equations defined by Eq (3.1.1.5) can also be presented in its equivalent vector form as

$$\mathbf{B} \frac{d\mathbf{h}}{dt} + \mathbf{A}\mathbf{h} - \mathbf{F} = 0 \quad (3.1.1.7)$$

where

- B** Storage (capacitance) matrix
- A** Seepage (conductance) matrix
- F** RHS forcing function vector
- h** Total "hydraulic" head vector
- t** Time

Equation (3.1.1.7) represents the standard Galerkin approximation to Eq. (2.1.17) and sometimes is referred to as the Galerkin Weak Statement to Eq. (2.1.17). Note that the RHS forcing function contains both a volume integral, as well as a surface integral. Upon assemblage of the elemental contributions to establish the global equation set, surface integral contributions for internal surfaces of elements cancel out. What remains of these surface integrals corresponds to those elemental surfaces residing on the exterior surface of the model domain. Also note that once the contributions from the volume and surface integrals have been allocated out to their appropriate nodes, their original source (either volume or surface) is indistinguishable when viewed from the nodal level. How we handle the forcing function volume and surfaces integrals may appear very similar in the sections to follow; however, the reader should keep the subtle differences in mind.

The sign convention for U_n is the same as for q . That is, U_n is positive for inward flow and negative for outward flow. F_i represents all sources, sinks and other boundary conditions. The global coefficient matrices A_{ij} , B_{ij} , and F_i are assembled as a sum of the element matrices for a general 8 noded orthogonal curvilinear element. Influence coefficient techniques presented by Huyakorn et al. (1984) and Huyakorn et al. (1986) for linear basis functions along the coordinate axis, can be effectively used for assembling slightly distorted 8 noded prism elements. Since FACT allows for element distortion in the z -direction, the 2-point Gauss-Legendre quadrature option is recommended for integration of the elemental matrices. The seepage (conductance) coefficients provide the appropriate connectivity for flow between nodes of the element. The finite element structure of 27-points has a full nearest-neighbor connectivity. The influence coefficients

FACT CODE MANUAL

for the 27-point lattice connectivity are provided by Huyakorn et al. (1986, 1987). A fully lumped mass matrix is used for the 27-point lattice connectivity.

3.1.2 Eight-noded Constrained Trilinear Hexahedron Element

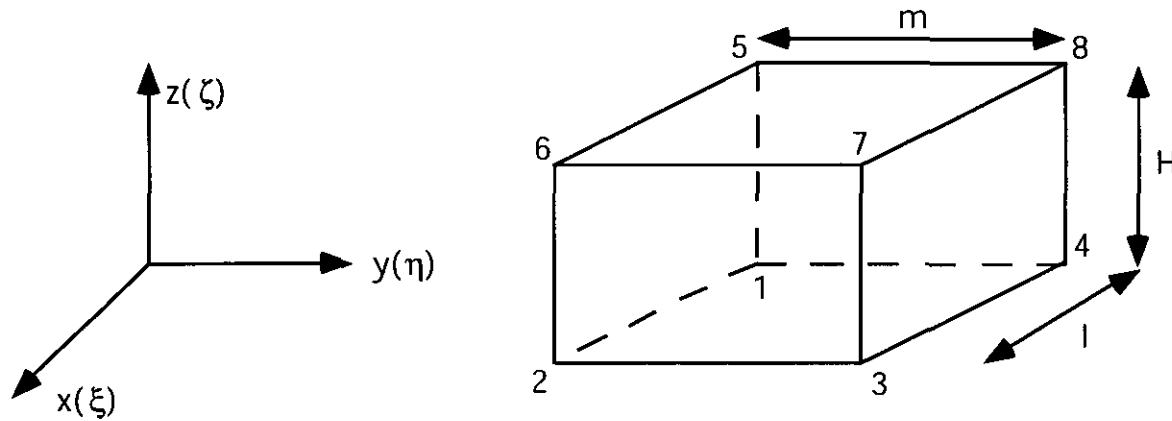


Fig. 3.1.1. Eight-noded constrained trilinear hexahedron element showing node numbering and local and global coordinate systems.

Consider two coordinate systems, a local (ξ, η, ζ) system and a global Cartesian system (x, y, z) that are colinear. Three-dimensional rectangular prism or constrained hexahedron elements in (x, y, z) are mapped into cubes in local coordinates. The x - y coordinates are assumed to be orthogonal while distortion of the brick element is allowed in the z -direction. Furthermore, let the cube in (ξ, η, ζ) be such that its corners are located at $\xi = \pm 1$, $\eta = \pm 1$, and $\zeta = \pm 1$. The relationship between global and local coordinates can be established by introducing a general expression of the form

$$x = \sum_{i=1}^8 \varphi_i x_i, \quad y = \sum_{i=1}^8 \varphi_i y_i, \quad \text{and} \quad z = \sum_{i=1}^8 \varphi_i z_i \quad (3.1.2.1)$$

where φ_i are the basis functions for this trilinear isoparametric element, given in a local coordinate system, as

$$\varphi_i = \frac{1}{8} (1 + \xi \xi_i) (1 + \eta \eta_i) (1 + \zeta \zeta_i) \quad (3.1.2.2)$$

and x_i , y_i , and z_i are global coordinates in x , y , and z .

The gradient of the basis (shape) function is

$$\nabla_{\xi} \varphi_i = \begin{bmatrix} \frac{\xi_i}{8} (1 + \eta \eta_i) (1 + \zeta \zeta_i) \\ \frac{\eta_i}{8} (1 + \xi \xi_i) (1 + \zeta \zeta_i) \\ \frac{\zeta_i}{8} (1 + \xi \xi_i) (1 + \eta \eta_i) \end{bmatrix} \quad (3.1.2.3)$$

FACT CODE MANUAL

with nodal parameters

i	ξ_i	η_i	ζ_i
1	-1	-1	-1
2	1	-1	-1
3	1	1	-1
4	-1	1	-1
5	-1	-1	1
6	1	-1	1
7	1	1	1
8	-1	1	1

(3.1.2.4)

The gradient of the basis function evaluated at the element centroid is

$$\nabla_{\xi} \phi_i(0) = \begin{bmatrix} \frac{\xi_i}{8} \\ \frac{\eta_i}{8} \\ \frac{\zeta_i}{8} \end{bmatrix} \quad (3.1.2.5)$$

3.1.3 Numerical Integration

Before interpreting the first order differential terms in Eq. (3.1.1.6a) the procedures used for integration will be outlined.

Consider a general form of Eq. (3.1.1.3) in terms of global coordinates,

$$\iiint_{\Omega} G(x, y, z) dx dy dz \quad (3.1.3.1)$$

For an element this can be written, in terms of normalized curvilinear (local) coordinates,

$$\int_{-1}^{+1} \int_{-1}^{+1} \int_{-1}^{+1} G(\xi, \eta, \zeta) |J| d\xi d\eta d\zeta \quad (3.1.3.2)$$

where $|J|$ is the determinant of the Jacobian coordinate transformation matrix. Eq. (3.1.3.2) can be integrated using two different integration techniques in FACT.

The first integration scheme is the method of "influence coefficient matrices" developed by Huyakorn et al. (1986) to avoid costly numerical integration. In this technique the constrained hexahedron element is transformed to a rectangular prism element by arithmetically averaging the z coordinates for the top and bottom face of the constrained hexahedron element. For a rectangular prism element and constant material properties within an element, the integrand in Eq. (3.1.3.2) for the element seepage and storage

FACT CODE MANUAL

matrix can be integrated analytically. For example, the integrand G for the element seepage matrix is

$$G = G_{ij} = \nabla \phi_i \mathbf{K} \nabla \phi_j \quad (3.1.3.3)$$

where

\mathbf{K}' permeability tensor

i, j local node numbers, $1 \leq (i, j) \leq 8$

For illustration, let us assume that the permeability tensor is diagonal. Equation (3.1.3.3) becomes

$$G_{ij} = \begin{bmatrix} \frac{\partial \phi_i}{\partial \xi} & \frac{\partial \phi_i}{\partial \eta} & \frac{\partial \phi_i}{\partial \zeta} \end{bmatrix} \begin{bmatrix} K'_{11} & 0 & 0 \\ 0 & K'_{22} & 0 \\ 0 & 0 & K'_{33} \end{bmatrix} \begin{bmatrix} \frac{\partial \phi_j}{\partial \xi} \\ \frac{\partial \phi_j}{\partial \eta} \\ \frac{\partial \phi_j}{\partial \zeta} \end{bmatrix} \quad (3.1.3.4)$$

$$= K'_{11} \frac{\partial \phi_i}{\partial \xi} \frac{\partial \phi_j}{\partial \xi} + K'_{22} \frac{\partial \phi_i}{\partial \eta} \frac{\partial \phi_j}{\partial \eta} + K'_{33} \frac{\partial \phi_i}{\partial \zeta} \frac{\partial \phi_j}{\partial \zeta}$$

Substituting Eq. (3.1.3.4) into (3.1.3.2) yields

$$\begin{aligned} & \langle K'_{11} \rangle |J| \int_{-1}^{+1} \int_{-1}^{+1} \int_{-1}^{+1} \frac{\partial \phi_i}{\partial \xi} \frac{\partial \phi_j}{\partial \xi} d\xi d\eta d\zeta + \langle K'_{22} \rangle |J| \int_{-1}^{+1} \int_{-1}^{+1} \int_{-1}^{+1} \frac{\partial \phi_i}{\partial \eta} \frac{\partial \phi_j}{\partial \eta} d\xi d\eta d\zeta \\ & + \langle K'_{33} \rangle |J| \int_{-1}^{+1} \int_{-1}^{+1} \int_{-1}^{+1} \frac{\partial \phi_i}{\partial \zeta} \frac{\partial \phi_j}{\partial \zeta} d\xi d\eta d\zeta \end{aligned} \quad (3.1.3.5)$$

where $\langle \rangle$ implies the property is constant within the element. For a rectangular prism element the determinant of the Jacobian is a constant, simply the volume ratio of the element and the computational cube.

Each triple integral in Eq. (3.1.3.5) represents an 8 x 8 "influence coefficient matrix" which can be integrated analytically. In FACT, the "influence coefficient matrices" are stored in static 8 x 8 arrays requiring only the material properties and determinant of the Jacobian to be computed for each element to complete element integrals.

The second numerical integration procedure available in FACT is where the sampling points are the Gauss points. In particular the two-point Gauss-Legendre quadrature in each dimension is used leading to a high accuracy. The Gauss-Legendre quadrature rule leads to an equation of the form

$$\int_{-1}^{+1} \int_{-1}^{+1} \int_{-1}^{+1} G(\xi, \eta, \zeta) |J| d\xi d\eta d\zeta = \sum_{k=1}^8 G(\xi_k, \eta_k, \zeta_k) w_k |J(\xi_k, \eta_k, \zeta_k)| \quad (3.1.3.6)$$

where

FACT CODE MANUAL

k number of the Gauss point

ξ_k, η_k, ζ_k abscissa of the k^{th} Gauss point

w_k weight of the k^{th} Gauss point

With two sampling points a polynomial of degree three could be evaluated exactly. In practice, the integrand of the element seepage matrix is a polynomial of degree greater than three, thereby, requiring more than two gauss points in each direction. For practical purposes, two Gauss points was deemed adequate. The values of Gauss-Legendre abscissas and weights is tabulated in Table 3.1.1.

Table 3.1.1 Gauss-Legendre Abscissas and Weights

k	ξ_k	η_k	ζ_k	w_k
1	$-1/\sqrt{3}$	$-1/\sqrt{3}$	$-1/\sqrt{3}$	1.0
2	$+1/\sqrt{3}$	$-1/\sqrt{3}$	$-1/\sqrt{3}$	1.0
3	$+1/\sqrt{3}$	$+1/\sqrt{3}$	$-1/\sqrt{3}$	1.0
4	$-1/\sqrt{3}$	$+1/\sqrt{3}$	$-1/\sqrt{3}$	1.0
5	$-1/\sqrt{3}$	$-1/\sqrt{3}$	$+1/\sqrt{3}$	1.0
6	$+1/\sqrt{3}$	$-1/\sqrt{3}$	$+1/\sqrt{3}$	1.0
7	$+1/\sqrt{3}$	$+1/\sqrt{3}$	$+1/\sqrt{3}$	1.0
8	$-1/\sqrt{3}$	$+1/\sqrt{3}$	$+1/\sqrt{3}$	1.0

3.1.4 Transformations for First Order Terms

If a local coordinate system is to be used then it is necessary to transform derivatives in global coordinates to local coordinates. This is achieved through the use of the chain rule of partial differentiation which leads to

$$\frac{\partial \phi_i}{\partial \xi} = \frac{\partial \phi_i}{\partial x} \frac{\partial x}{\partial \xi} + \frac{\partial \phi_i}{\partial y} \frac{\partial y}{\partial \xi} + \frac{\partial \phi_i}{\partial z} \frac{\partial z}{\partial \xi} \quad (3.1.4.1a)$$

$$\frac{\partial \phi_i}{\partial \eta} = \frac{\partial \phi_i}{\partial x} \frac{\partial x}{\partial \eta} + \frac{\partial \phi_i}{\partial y} \frac{\partial y}{\partial \eta} + \frac{\partial \phi_i}{\partial z} \frac{\partial z}{\partial \eta} \quad (3.1.4.1b)$$

$$\frac{\partial \phi_i}{\partial \zeta} = \frac{\partial \phi_i}{\partial x} \frac{\partial x}{\partial \zeta} + \frac{\partial \phi_i}{\partial y} \frac{\partial y}{\partial \zeta} + \frac{\partial \phi_i}{\partial z} \frac{\partial z}{\partial \zeta} \quad (3.1.4.1c)$$

which maybe be re-written in matrix form as

$$\begin{Bmatrix} \frac{\partial \phi_i}{\partial \xi} \\ \frac{\partial \phi_i}{\partial \eta} \\ \frac{\partial \phi_i}{\partial \zeta} \end{Bmatrix} = \begin{bmatrix} \frac{\partial x}{\partial \xi} & \frac{\partial y}{\partial \xi} & \frac{\partial z}{\partial \xi} \\ \frac{\partial x}{\partial \eta} & \frac{\partial y}{\partial \eta} & \frac{\partial z}{\partial \eta} \\ \frac{\partial x}{\partial \zeta} & \frac{\partial y}{\partial \zeta} & \frac{\partial z}{\partial \zeta} \end{bmatrix} \begin{Bmatrix} \frac{\partial \phi_i}{\partial x} \\ \frac{\partial \phi_i}{\partial y} \\ \frac{\partial \phi_i}{\partial z} \end{Bmatrix} = \mathbf{J} \begin{Bmatrix} \frac{\partial \phi_i}{\partial x} \\ \frac{\partial \phi_i}{\partial y} \\ \frac{\partial \phi_i}{\partial z} \end{Bmatrix} \quad (3.1.4.2)$$

Multiplying both sides of Eq. (3.1.4.2) by the inverse of \mathbf{J} , we get the global variation in the basis functions as

$$\nabla_x \phi_i = \mathbf{J}^{-1} \nabla_\xi \phi_i \quad (3.1.4.3)$$

where \mathbf{J} is the Jacobian matrix. Differentiation of Eqs. (3.1.2.1) with respect to the local coordinates reveals that \mathbf{J} can be easily evaluated numerically from the relationship

$$\mathbf{J} = \begin{bmatrix} \sum_{i=1}^8 \frac{\partial \phi_i}{\partial \xi} x_i & \sum_{i=1}^8 \frac{\partial \phi_i}{\partial \xi} y_i & \sum_{i=1}^8 \frac{\partial \phi_i}{\partial \xi} z_i \\ \sum_{i=1}^8 \frac{\partial \phi_i}{\partial \eta} x_i & \sum_{i=1}^8 \frac{\partial \phi_i}{\partial \eta} y_i & \sum_{i=1}^8 \frac{\partial \phi_i}{\partial \eta} z_i \\ \sum_{i=1}^8 \frac{\partial \phi_i}{\partial \zeta} x_i & \sum_{i=1}^8 \frac{\partial \phi_i}{\partial \zeta} y_i & \sum_{i=1}^8 \frac{\partial \phi_i}{\partial \zeta} z_i \end{bmatrix} = \begin{bmatrix} x_\xi & y_\xi & z_\xi \\ x_\eta & y_\eta & z_\eta \\ x_\zeta & y_\zeta & z_\zeta \end{bmatrix} \quad (3.1.4.4)$$

For the special case (used by FACT) of the trilinear isoparametric element distorted only in the z-direction we have

$$x_1 = x_4 = x_5 = x_8 \quad (3.1.4.5a)$$

$$x_2 = x_3 = x_6 = x_7 \quad (3.1.4.5b)$$

$$y_1 = y_2 = y_5 = y_6 \quad (3.1.4.5c)$$

$$y_3 = y_4 = y_7 = y_8 \quad (3.1.4.5d)$$

$$z_b = \frac{1}{4} \sum_{i=1}^4 z_i \quad \text{and} \quad z_t = \frac{1}{4} \sum_{i=5}^8 z_i \quad (\mathbf{IM}) \quad (3.1.4.5e)$$

where (\mathbf{IM}) and (\mathbf{GL}) refer to "influence matrix" and Gauss-Legendre numerical quadrature, respectively. The Jacobian after substitution of Eqs. (3.1.2.3) and (3.1.4.5) into (3.1.4.4) becomes

$$\mathbf{J} = \begin{bmatrix} x_\xi & 0 & z_\xi \\ 0 & y_\eta & z_\eta \\ 0 & 0 & z_\zeta \end{bmatrix} \quad (3.1.4.6)$$

where

FACT CODE MANUAL

$$x_{\xi} = (x_2 - x_1)/2 = \ell/2 \quad (3.1.4.7a)$$

$$y_{\eta} = (y_3 - y_1)/2 = m/2 \quad (3.1.4.7b)$$

$$z_{\xi} = 0, \quad z_{\eta} = 0, \quad z_{\zeta} = (z_t - z_b)/2 = H/2 \quad (\text{IM}) \quad (3.1.4.7c)$$

$$z_{\xi} = \sum_{i=1}^8 \frac{\partial \phi_i}{\partial \xi} z_i, \quad z_{\eta} = \sum_{i=1}^8 \frac{\partial \phi_i}{\partial \eta} z_i, \quad z_{\zeta} = \sum_{i=1}^8 \frac{\partial \phi_i}{\partial \zeta} z_i \quad (\text{GL}) \quad (3.1.4.7d)$$

The local derivatives of z in Eq. (3.1.4.7d) are evaluated at the Gauss points.

The determinant of the Jacobian matrix is

$$|J| = x_{\xi} y_{\eta} z_{\zeta} \quad (3.1.4.8)$$

The inverse of the Jacobian can be found by using standard matrix inversion techniques as

$$J^{-1} = \frac{1}{|J|} \begin{bmatrix} y_{\eta} z_{\zeta} & 0 & -y_{\eta} z_{\xi} \\ 0 & x_{\xi} z_{\zeta} & -x_{\xi} z_{\eta} \\ 0 & 0 & x_{\xi} y_{\eta} \end{bmatrix} \quad (3.1.4.9)$$

The transpose of the inverse of the Jacobian is

$$(J^{-1})^T = \frac{1}{|J|} \begin{bmatrix} y_{\eta} z_{\zeta} & 0 & 0 \\ 0 & x_{\xi} z_{\zeta} & 0 \\ -y_{\eta} z_{\xi} & -x_{\xi} z_{\eta} & x_{\xi} y_{\eta} \end{bmatrix} \quad (3.1.4.10)$$

In addition to transforming the derivative from (x,y,z) to (ξ,η,ζ) , the differential volume must be changed using the relation

$$d\Omega = dx dy dz = |J| d\xi d\eta d\zeta \quad (3.1.4.11)$$

3.1.5 Flow Equation Element Matrix Computation

The element matrices A_{ij} , B_{ij} , and RHS vector F_i resulting from the Galerkin approximation to the variably saturated flow equation are computed using influence matrices or Gauss-Legendre quadrature.

3.1.5.1 Element Seepage (Conductance) Matrix

From Eq. (3.1.1.6a) the expression for the element seepage coefficient matrix is obtained as

$$A_{ij} = \int_{\Omega_x} \nabla_x \phi_i \cdot k_{rw} \mathbf{K} \nabla_x \phi_j d\Omega_x \quad (3.1.5.1)$$

FACT CODE MANUAL

where the components of the saturated hydraulic conductivity tensor \mathbf{K} are specified with respect to the global coordinate system. Transforming the seepage matrix, A_{ij} , from a global to local coordinate system, yields

$$\begin{aligned} A_{ij} &= \int_{\Omega_x} \nabla_x \phi_i \cdot k_{rw} \mathbf{K} \nabla_x \phi_j d\Omega_x \\ &= \int_{\Omega_\xi} (\mathbf{J}^{-1} \nabla_\xi \phi_i)^T \cdot k_{rw} \mathbf{J}^T \mathbf{K}_\xi \mathbf{J} (\mathbf{J}^{-1} \nabla_\xi \phi_j) \mathbf{J} d\Omega_\xi \\ &= \int_{\Omega_\xi} (\nabla_\xi \phi_i)^T \cdot k_{rw} \mathbf{K}_\xi \nabla_\xi \phi_j \mathbf{J} d\Omega_\xi \end{aligned} \quad (3.1.5.2)$$

which implies that A_{ij} is invariant with respect to coordinate transformation. \mathbf{K}_ξ is the saturated conductivity tensor in the local coordinate system.

In the general case the principal axes of a material (i.e., subsurface porous media) will vary with location

$$\mathbf{K}^m = \begin{bmatrix} K_{xx}^m & 0 & 0 \\ 0 & K_{yy}^m & 0 \\ 0 & 0 & K_{zz}^m \end{bmatrix} \quad (3.1.5.3)$$

where the subscript m implies a material and its principal axes directions. To estimate local saturated conductivity tensor values for a given material based on the material's principal coordinate axes (i.e., x_m , y_m , z_m), a coordinate transformation rule for a second rank cartesian tensor must be applied. Converting a given material saturated conductivity tensor into a tensor based on the local coordinate system becomes:

$$\mathbf{K} = (\mathbf{J}^m)^T \mathbf{K}^m \mathbf{J}^m \quad (3.1.5.4)$$

where \mathbf{J}^m represents the Jacobian between the material's principal axes and the global coordinate system.

To illustrate how Eq. (3.1.5.4) might be used, we shall limit ourselves to where only a transformation of rotations within the areal plane (i.e., rotation about the z axis) is allowed. Thus, our vertical components z and z_m are assume to be parallel and stationary. Basically we obtain the tensors

$$\begin{bmatrix} K_{xx}^m & 0 & 0 \\ 0 & K_{yy}^m & 0 \\ 0 & 0 & K_{zz}^m \end{bmatrix} \Rightarrow \begin{bmatrix} K_{xx} & K_{xy} & 0 \\ K_{xy} & K_{yy} & 0 \\ 0 & 0 & K_{zz} \end{bmatrix} \quad (3.1.5.5)$$

FACT CODE MANUAL

where the symmetric property of the saturated conductivity tensor has been incorporated. We obtain the above result by a rotation about the z axis from our material-to-model coordinate system transformation given the expression

$$\mathbf{K} = \mathbf{R}(\theta)^T \mathbf{K}^m \mathbf{R}(\theta) \quad (3.1.5.6a)$$

where

$$\mathbf{R}(\theta) = \begin{bmatrix} \cos \theta & \sin \theta & 0 \\ -\sin \theta & \cos \theta & 0 \\ 0 & 0 & 1 \end{bmatrix} \quad (3.1.5.6b)$$

and θ represents a counter-clockwise rotation from the material-to-model coordinate system.

In many situations a good approximation can be made where it is assumed that a material's principal axes are invariant. Under such conditions it is possible to align the global coordinate system parallel to the material's principal axes resulting in the off-diagonal components of the saturated conductivity tensor becoming zero

$$\mathbf{K} = \begin{bmatrix} K_{xx} & 0 & 0 \\ 0 & K_{yy} & 0 \\ 0 & 0 & K_{zz} \end{bmatrix} \quad (3.1.5.7)$$

(e.g., the typical case where the x and y directions are parallel to the plane of stratification while the z direction is normal to this stratification plane).

\mathbf{K}_ξ can now be determined from \mathbf{K} using the coordinate transformation rule for a second rank Cartesian tensor based on the elemental Jacobian matrix by

$$\mathbf{K} = \mathbf{J}^T \mathbf{K}_\xi \mathbf{J} \Rightarrow \mathbf{K}_\xi = (\mathbf{J}^T)^{-1} \mathbf{K} \mathbf{J}^{-1} = (\mathbf{J}^{-1})^T \mathbf{K} \mathbf{J}^{-1} \quad (3.1.5.8)$$

In general, the saturated hydraulic conductivity tensor, \mathbf{K}_ξ , in the local coordinate is not known. To evaluate the element seepage matrix, we express the global gradients of the shape functions in the local coordinate system and leave the saturated hydraulic tensor in the global coordinate system. The resulting integral for the element seepage matrix becomes

$$\begin{aligned} A_{ij} &= \int_{\Omega_\xi} \left(\mathbf{J}^{-1} \nabla_\xi \phi_i \right)^T \cdot k_{rw} \mathbf{K} \left(\mathbf{J}^{-1} \nabla_\xi \phi_j \right) \mathbf{J} d\Omega_\xi \\ &= \int_{-1}^{+1} \int_{-1}^{+1} \int_{-1}^{+1} \left(\mathbf{J}^{-1} \nabla_\xi \phi_i \right)^T \cdot k_{rw} \mathbf{K} \left(\mathbf{J}^{-1} \nabla_\xi \phi_j \right) \mathbf{J} d\xi d\eta d\zeta \end{aligned} \quad (3.1.5.9)$$

To alleviate numerical difficulties which manifest themselves as oscillations in the vicinity of sharp fronts (for example, the water table), "upstream weighting" of the relative permeability is available as an option in FACT. The product $k_{rw} \mathbf{K}$ in Eq. (3.1.5.9) with no upstream weighting of the relative permeability is evaluated as

$$k_{rw} \mathbf{K} = \langle k_{rw} \rangle \begin{bmatrix} K_{xx} & K_{xy} & K_{xz} \\ K_{xy} & K_{yy} & K_{yz} \\ K_{xz} & K_{yz} & K_{zz} \end{bmatrix} \quad (3.1.5.10)$$

and with upstream weighting of the relative permeability as

$$k_{rw} \mathbf{K} = \begin{bmatrix} \langle k_{rw}^x \rangle K_{xx} & \langle k_{rw} \rangle K_{xy} & \langle k_{rw} \rangle K_{xz} \\ \langle k_{rw} \rangle K_{xy} & \langle k_{rw}^y \rangle K_{yy} & \langle k_{rw} \rangle K_{yz} \\ \langle k_{rw} \rangle K_{xz} & \langle k_{rw} \rangle K_{yz} & \langle k_{rw}^z \rangle K_{zz} \end{bmatrix} \quad (3.1.5.11)$$

where

$$\langle k_{rw} \rangle = \sum_{i=1}^8 \phi_i(0) k_{rw}(S_w(\psi_i)) = \frac{1}{8} \sum_{i=1}^8 k_{rw}(S_w(\psi_i)) \quad (3.1.5.12a)$$

$$\langle k_{rw}^d \rangle = \sum_{i=1}^8 w_i^d k_{rw}(S_w(\psi_i)) \quad d = x, y, z \quad (3.1.5.12b)$$

Influence Coefficient Matrices

The gradient of the shape function in global coordinates and the determinant of the Jacobian in Eq. (3.1.5.9) for the rectangular prism element are, respectively

$$\mathbf{J}^{-1} \nabla_{\xi} \phi_i = \begin{bmatrix} 2/\ell & 0 & 0 \\ 0 & 2/m & 0 \\ 0 & 0 & 2/H \end{bmatrix} \begin{bmatrix} \partial \phi_i / \partial \xi \\ \partial \phi_i / \partial \eta \\ \partial \phi_i / \partial \zeta \end{bmatrix} = \begin{bmatrix} \frac{2}{\ell} \frac{\partial \phi_i}{\partial \xi} & \frac{2}{m} \frac{\partial \phi_i}{\partial \eta} & \frac{2}{H} \frac{\partial \phi_i}{\partial \zeta} \end{bmatrix} \quad (3.1.5.13)$$

$$|\mathbf{J}| = \frac{\ell m H}{8} \quad (3.1.5.14)$$

Substituting Eqs. (3.1.5.13) and (3.1.5.14) into Eq. (3.1.5.9) and expanding yields the expression for the element seepage coefficient matrix as

$$A_{ij} = \frac{mH}{2\ell} \langle k_{rw} K_{xx} \rangle A_{ij}^{xx} + \frac{\ell H}{2m} \langle k_{rw} K_{yy} \rangle A_{ij}^{yy} + \frac{\ell m}{2H} \langle k_{rw} K_{zz} \rangle A_{ij}^{zz} \\ + \frac{H}{2} \langle k_{rw} K_{xy} \rangle A_{ij}^{xy} + \frac{m}{2} \langle k_{rw} K_{xz} \rangle A_{ij}^{xz} + \frac{\ell}{2} \langle k_{rw} K_{yz} \rangle A_{ij}^{yz} \quad (3.1.5.15)$$

where the quantities in angle brackets correspond to values of the hydraulic properties of the elements in Eqs. (3.1.5.11) or (3.1.5.12); A_{ij}^{xx} , A_{ij}^{yy} , A_{ij}^{zz} , A_{ij}^{xy} , A_{ij}^{xz} , and A_{ij}^{yz} are influence coefficient matrices with matrix elements computed as

$$A_{ij}^{xx} = \int_{-1}^{+1} \int_{-1}^{+1} \int_{-1}^{+1} \varphi_{i,\xi} \varphi_{j,\xi} d\xi d\eta d\zeta \quad (3.1.5.16a)$$

$$A_{ij}^{yy} = \int_{-1}^{+1} \int_{-1}^{+1} \int_{-1}^{+1} \varphi_{i,\eta} \varphi_{j,\eta} d\xi d\eta d\zeta \quad (3.1.5.16b)$$

$$A_{ij}^{zz} = \int_{-1}^{+1} \int_{-1}^{+1} \int_{-1}^{+1} \varphi_{i,\zeta} \varphi_{j,\zeta} d\xi d\eta d\zeta \quad (3.1.5.16c)$$

$$A_{ij}^{xy} = \int_{-1}^{+1} \int_{-1}^{+1} \int_{-1}^{+1} \{ \varphi_{i,\xi} \varphi_{j,\eta} + \varphi_{i,\eta} \varphi_{j,\xi} \} d\xi d\eta d\zeta \quad (3.1.5.16d)$$

$$A_{ij}^{xz} = \int_{-1}^{+1} \int_{-1}^{+1} \int_{-1}^{+1} \{ \varphi_{i,\xi} \varphi_{j,\zeta} + \varphi_{i,\zeta} \varphi_{j,\xi} \} d\xi d\eta d\zeta \quad (3.1.5.16e)$$

$$A_{ij}^{yz} = \int_{-1}^{+1} \int_{-1}^{+1} \int_{-1}^{+1} \{ \varphi_{i,\eta} \varphi_{j,\zeta} + \varphi_{i,\zeta} \varphi_{j,\eta} \} d\xi d\eta d\zeta \quad (3.1.5.16f)$$

where

$$\varphi_{i,\xi} = \partial \varphi_i / \partial \xi, \quad \varphi_{i,\eta} = \partial \varphi_i / \partial \eta, \quad \varphi_{i,\zeta} = \partial \varphi_i / \partial \zeta \quad (3.1.5.16g)$$

Substituting the expressions for the derivatives of the basis functions from Eqs. (3.1.2.3) into Eqs. (3.1.5.16) and performing the triple integration for each matrix element yields:

$$A^{xx} = \frac{1}{18} \left[\begin{array}{c|c} 2a^{xx} & a^{xx} \\ \hline a^{xx} & 2a^{xx} \end{array} \right] \quad \text{and} \quad A^{yy} = \frac{1}{18} \left[\begin{array}{c|c} 2a^{yy} & a^{yy} \\ \hline a^{yy} & 2a^{yy} \end{array} \right] \quad (3.1.5.17a,b)$$

$$A^{zz} = \frac{1}{18} \left[\begin{array}{c|c} a^{zz} & -a^{zz} \\ \hline -a^{zz} & a^{zz} \end{array} \right] \quad \text{and} \quad A^{xy} = \frac{1}{6} \left[\begin{array}{c|c} 2a^{xy} & a^{xy} \\ \hline a^{xy} & 2a^{xy} \end{array} \right] \quad (3.1.5.17c,d)$$

$$A^{xz} = \frac{1}{6} \left[\begin{array}{c|c} a^{xz} & \hat{a}^{xz} \\ \hline -\hat{a}^{xz} & -a^{xz} \end{array} \right] \quad \text{and} \quad A^{yz} = \frac{1}{6} \left[\begin{array}{c|c} a^{yz} & \hat{a}^{yz} \\ \hline -\hat{a}^{yz} & -a^{yz} \end{array} \right] \quad (3.1.5.17e,f)$$

where

$$a^{xx} = \begin{bmatrix} 2 & -2 & -1 & 1 \\ -2 & 2 & 1 & -1 \\ -1 & 1 & 2 & -2 \\ 1 & -1 & -2 & 2 \end{bmatrix} \quad a^{yy} = \begin{bmatrix} 2 & 1 & -1 & -2 \\ 1 & 2 & -2 & -1 \\ -1 & -2 & 2 & 1 \\ -2 & -1 & 1 & 2 \end{bmatrix} \quad (3.1.5.18a,b)$$

$$a^{zz} = \begin{bmatrix} 4 & 2 & 1 & 2 \\ 2 & 4 & 2 & 1 \\ 1 & 2 & 4 & 2 \\ 2 & 1 & 2 & 4 \end{bmatrix} \quad a^{xy} = \begin{bmatrix} 1 & 0 & -1 & 0 \\ 0 & -1 & 0 & 1 \\ -1 & 0 & 1 & 0 \\ 0 & 1 & 0 & -1 \end{bmatrix} \quad (3.1.5.18c,d)$$

FACT CODE MANUAL

$$\mathbf{a}^{xz} = \begin{bmatrix} 2 & 0 & 0 & 1 \\ 0 & -2 & -1 & 0 \\ 0 & -1 & -2 & 0 \\ 1 & 0 & 0 & 2 \end{bmatrix} \quad \hat{\mathbf{a}}^{xz} = \begin{bmatrix} 0 & -2 & -1 & 0 \\ 2 & 0 & 0 & 1 \\ 1 & 0 & 0 & 2 \\ 0 & -1 & -2 & 0 \end{bmatrix} \quad (3.1.5.18e,f)$$

$$\mathbf{a}^{yz} = \begin{bmatrix} 2 & 1 & 0 & 0 \\ 1 & 2 & 0 & 0 \\ 0 & 0 & -2 & -1 \\ 0 & 0 & -1 & -2 \end{bmatrix} \quad \hat{\mathbf{a}}^{yz} = \begin{bmatrix} 0 & 0 & -1 & -2 \\ 0 & 0 & -2 & -1 \\ 1 & 2 & 0 & 0 \\ 2 & 1 & 0 & 0 \end{bmatrix} \quad (3.1.5.18g,h)$$

Note that each influence coefficient matrix is an 8 x 8 matrix partitioned into four (4 x 4) submatrices and that these integrals have been verified by evaluation of each using Mathematica™. As can be seen submatrices of any individual influence matrix differ from one another by a constant multiple. Furthermore, the submatrices are easy to evaluate and require virtually no computational effort.

Two-point Gauss-Legendre Quadrature

For the constrained (z distorted) hexahedron element, the element seepage integral cannot be solved analytically since the Jacobian is spatially varying. Since the integrand varies from -1 to +1 in each direction we can employ a two-point Gauss-Legendre integration. The element seepage matrix is computed as

$$\begin{aligned} A_{ij} &= \int_{-1}^{+1} \int_{-1}^{+1} \int_{-1}^{+1} \left(\mathbf{J}^{-1} \nabla_{\xi} \phi_i \right)^T \cdot k_{rw} \mathbf{K} \left(\mathbf{J}^{-1} \nabla_{\xi} \phi_j \right) \mathbf{J} d\xi d\eta d\zeta \\ &= \sum_{g=1}^8 \left(\mathbf{J}_g^{-1} \nabla_{\xi}^g \phi_i \right)^T k_{rw} \mathbf{K} \left(\mathbf{J}_g^{-1} \nabla_{\xi}^g \phi_j \right) w_g |\mathbf{J}_g| \end{aligned} \quad (3.1.5.19)$$

where

g number of the Gauss point

∇_{ξ}^g local gradient operator evaluated at the g^{th} Gauss point

\mathbf{J}_g^{-1} inverse Jacobian matrix evaluated at the g^{th} Gauss point

w_g weight of the g^{th} Gauss point

3.1.5.2 Element Storage (Capacitance) Matrix

From Eq. (3.1.1.6b) the expression for the element storage coefficient matrix is obtained as

$$B_{ij} = \int_{\Omega_e} (C + S_w S_s) \phi_i \phi_j d\Omega_e \quad (3.1.5.20)$$

FACT CODE MANUAL

where C is the specific moisture capacity, S_w is the water saturation and S_s is the specific storage. Transforming the storage matrix, B_{ij} , from global to local coordinate system and substituting the following equations

$$C = \left\langle \phi_e \frac{dS_w}{d\psi} \right\rangle = \phi_e \sum_{i=1}^8 \varphi_i(0) \left(\frac{dS_w}{d\psi} \right)_i = \frac{\phi_e}{8} \sum_{i=1}^8 \left(\frac{dS_w}{d\psi} \right)_i \quad (3.1.5.21a)$$

$$S_w S_s = \langle S_w S_s \rangle = S_s \sum_{i=1}^8 \varphi_i(0) S_w(\psi_i) = \frac{S_s}{8} \sum_{i=1}^8 S_w(\psi_i) \quad (3.1.5.21b)$$

yields

$$B_{ij} = \left\langle \phi_e \frac{dS_w}{d\psi} + S_w S_s \right\rangle M_{ij} \quad (3.1.5.22)$$

where

$$M_{ij} = \int_{-1}^{+1} \int_{-1}^{+1} \int_{-1}^{+1} \varphi_i \varphi_j |J| d\xi d\eta d\zeta \quad (3.1.5.23)$$

is the mass matrix. In the FACT code, for numerical considerations the mass matrix \mathbf{M} is lumped by adding all elements in each row of \mathbf{M} and putting the sum on the diagonal. The mass matrix \mathbf{M} is then replaced by the lumped influence matrix defined by

$$M_{ij}^L = \begin{cases} \sum_{j=1}^8 M_{ij} & i = j \\ 0 & i \neq j \end{cases} \quad (3.1.5.24)$$

where

$$\sum_{j=1}^8 M_{ij} = \int_{-1}^{+1} \int_{-1}^{+1} \int_{-1}^{+1} \varphi_i |J| d\xi d\eta d\zeta \quad (3.1.5.25)$$

The lumped storage matrix, \mathbf{B} , used by FACT can now be written as

$$B_{ij} = \left\langle \phi_e \frac{dS_w}{d\psi} + S_w S_s \right\rangle M_{ij}^L \quad (3.1.5.26)$$

The diagonal nature of the lumped storage matrix resembles the stencils employed by finite difference and finite volume techniques for their temporal terms.

Influence Coefficient Matrix

Substituting the expression for the basis function from Eq. (3.1.2.2) into (3.1.5.25) and performing the triple integration for each influence matrix element yields

$$M_{ij}^L = \frac{\ell m H}{8} \delta_{ij} \quad (3.1.5.27)$$

where δ_{ij} is the kronecker delta function.

Two-point Gauss-Legendre Quadrature

For the constrained (z distorted) hexahedron element, the lumped element storage integral can be solved analytically since the integrand is a polynomial. Since the integrand varies from -1 to +1 in each direction we can employ a two-point Gauss-Legendre integration. The element mass matrix is computed as

$$M_{ij}^L = \sum_{k=1}^8 \phi_i^k \delta_{ij} w_k |J_k| \quad (3.1.5.28)$$

where

ϕ_i^k shape function evaluated at the k^{th} Gauss point

3.1.5.3 RHS Forcing Function Vector

Next, we deal with the boundary integral term of the right-hand side vector in Eq. (3.1.1.6c). For the case in which a certain boundary portion (say, the bottom rectangular face 1-2-3-4) corresponds to the flux boundary, the boundary flux term exists, and the last term in Eq. (3.1.1.6c) can be written as

$$F_{fi} = \int_{\sigma} \phi_i U_n d\sigma = |J| \int_{-1}^{+1} \int_{-1}^{+1} \phi_i U_n d\xi d\eta \quad (3.1.5.29)$$

Assume that U_n varies linearly over the face:

$$F_{fi} = \frac{\ell m}{4} \sum_{j=1}^4 \left\{ \int_{-1}^{+1} \int_{-1}^{+1} \phi_i \phi_j d\xi d\eta \right\} U_{nj} \quad (3.1.5.30)$$

where U_{n1} , U_{n2} , U_{n3} , and U_{n4} are the values of U_n at nodes 1, 2, 3 and 4, respectively. As before, it can be shown that the integral above becomes the influence matrix \mathbf{M} . Thus,

$$\mathbf{F}_f = \left(\frac{\ell m}{4} \right) \frac{1}{9} \begin{bmatrix} 4 & 2 & 1 & 2 \\ 2 & 4 & 2 & 1 \\ 1 & 2 & 4 & 2 \\ 2 & 1 & 2 & 4 \end{bmatrix} \begin{bmatrix} U_{n1} \\ U_{n2} \\ U_{n3} \\ U_{n4} \end{bmatrix} \quad (3.1.5.31)$$

If the normal component of the Darcy velocity is assumed to be constant over the face of the element, then lumping of the influence matrix in Eq. (3.1.5.31) occurs to give the form of the flux boundary vector as

$$\mathbf{F}_f = \left(\frac{\ell m}{4} \right) \begin{bmatrix} 1 & 0 & 0 & 0 \\ 0 & 1 & 0 & 0 \\ 0 & 0 & 1 & 0 \\ 0 & 0 & 0 & 1 \end{bmatrix} \begin{bmatrix} U_{n1} \\ U_{n2} \\ U_{n3} \\ U_{n4} \end{bmatrix} \quad (3.1.5.32)$$

$$= \left(\frac{\ell m}{4} \right) [U_{n1} \quad U_{n2} \quad U_{n3} \quad U_{n4}]^T$$

In a traditional finite element formulation, the user would specify the normal components of the Darcy velocity along some boundary of the solution domain and then assemble the global RHS vector \mathbf{F} as

$$F_i = \sum_{ef} \sum_{j=1}^4 M_{ij}^{ef} U_{nj} \quad (3.1.5.33)$$

where M_{ij}^{ef} and $|J_{ef}|$ is the mass matrix and determinant of the Jacobian for a given element face, respectively

$$M_{ij}^{ef} = \int_{-1}^{+1} \int_{-1}^{+1} \phi_i \phi_j |J_{ef}| d\xi d\eta \quad (3.1.5.34)$$

The FACT code requires the user to generate the global RHS vector in Eq. (3.1.5.32) and to input the volumetric flows, F_i , at each required global boundary node. A recommendation would be to return to the traditional finite formulation of specifying the normal component of the Darcy velocity to avoid confusion.

Finally, if point sinks or sources are present in the flow region, the sink or source term in Eq. (3.1.1.6c) depends on the type of sink or source function. For the case involving point sources and sinks, the general expression for q is

$$q = q_s \delta(\mathbf{x} - \mathbf{x}_\beta) \quad (3.1.5.35)$$

where

\mathbf{x}_β location of point source/sink

q_s elemental volumetric flow rate at source/sink per unit volume

When Eq. (3.1.5.35) is used, the elemental source (or sink) term in Eq. (3.1.1.6c) becomes

$$F_{s_i}^e = \int_{\Omega_e} \phi_i q_s \delta(\mathbf{x} - \mathbf{x}_\beta) d\Omega_e = Q_{\beta i}^e \phi_i(\bar{\xi}_\beta) \quad (3.1.5.36)$$

where

$\phi_i(\bar{\xi}_\beta)$ basis function at node i evaluated at $\bar{\xi}_\beta$

$Q_{\beta i}^e$ volume flowrate contribution at node i in element e from point sink/source located at $\bar{\xi}_{\beta}$

If the point source (or sink) is at a given node, then only that node has a contribution. Let the node number where the point source exists be denoted as ig^* (a global index) (and i^* the local index). If we evaluate Eq. (3.1.5.36) for each element within the mesh (note that only those elements in contact with this global node contribute and only one non-zero contribution results from the elemental matrices) and assemble the global source/sink term matrix, we obtain for an elemental vector the members

$$F_{s_i}^e = \begin{cases} Q_{\beta i}^e & i = i^* \\ 0 & i \neq i^* \end{cases} \quad \text{for element } e \quad (3.1.5.37)$$

and for the overall global (point source/sink) vector

$$F_s = \begin{bmatrix} Q_{\beta_1} & \cdots & Q_{\beta_{ig}} & \cdots & Q_{\beta_{np}} \end{bmatrix}^T \quad (3.1.5.38)$$

where

$Q_{\beta ig^*}$ total volumetric flow rate at global node ig^* for point source/sink

Thus, as expressed by Eq. (3.1.5.38), the global source/sink term vector has members that are non-zero only for those nodes containing a point source/sink.

For the case involving distributed volume sinks (e.g. the case of water uptake by plant roots), q is a continuous function that can be represented using linear interpolation functions as

$$q = \sum_j \phi_j q_j \quad (3.1.5.39)$$

The integral term in Eq. (3.1.5.36) can be evaluated as

$$F_{s_i} = \int_{\Omega} \phi_i q d\Omega = \sum_j \left\{ \int_{-1}^{+1} \int_{-1}^{+1} \int_{-1}^{+1} \phi_i \phi_j |J| d\xi d\eta d\zeta \right\} q_j \quad (3.1.5.40)$$

As before, it can be shown that the triple integral above becomes the mass matrix \mathbf{M} . Thus,

$$F_{s_i} = \sum_j M_{ij} q_j \quad (3.1.5.41)$$

If we assume q to be a constant over the domain then

$$F_{s_i} = \left\{ \sum_j M_{ij} \right\} q = \left\{ \int_{-1}^{+1} \int_{-1}^{+1} \int_{-1}^{+1} \phi_i \delta_{ij} |J| d\xi d\eta d\zeta \right\} q = M_{ij}^L q \quad (3.1.5.42)$$

FACT CODE MANUAL

Equation (3.1.5.42) can be integrated using influence matrix coefficients or two-point Gauss-Legendre quadrature to obtain

$$F_{s_i} = \frac{\ell m H}{8} \delta_{ij} q \quad (\text{IM}) \quad (3.1.5.43a)$$

$$F_{s_i} = \left\{ \sum_{k=1}^8 \phi_i^k \delta_{ij} w_k |J_k| \right\} q \quad (\text{GL}) \quad (3.1.5.43b)$$

The FACT code does not internally support distributed volume sinks. The user must perform the necessary quadratures outside the code and allocate the computed volumetric flowrates to the global nodes.

3.1.6 Line Source/Sink within 3D Element

If distributed sources/sinks are present in the flow region, the source/sink term in Eq. (3.1.1.6c) depends on the type of source/sink applied. Above point sources/sinks were addressed. Here distributed sources/sinks are addressed. FACT currently only handles line sources/sinks of the following two types: (1) flux specified line strengths that are ultimately allocated to individual nodes and appear as a line of point sources/sinks (looks similar to type 2 BC's) and (2) head-dependent line strengths that are a function of a specified flow resistance and external hydraulic head (looks similar to type 3 BC's). Each of these cases is discussed in the following two sections. The second type of line source/sink is restricted to a vertical orientation and to extraction only from an aquifer unit. Type 1, 2, and 3 BC's are commonly referred to as Dirichlet, Neumann, and Cauchy BC's, respectively.

3.1.6.1 Flux Specified Line Source within 3D Element

For the case involving a "vertical" line source/sink where the line strength is specified directly, the general expression for q becomes (horizontal line sources/sinks are handled in an identical manner and are not presented below):

$$q = q_\beta \delta(x - x_\beta, y - y_\beta) \quad (3.1.6.1)$$

where

(x_β, y_β) areal location where vertical line source is applied

q_β volumetric flow rate per unit length (line strength)

In FACT this type of line source/sink is not handled automatically; but rather, indirectly through user input of a series of point sources/sinks that lie along the line source/sink. The user (external to FACT) must allocate the appropriate amount of the line source/sink (i.e., flow rate) consistent with their assumptions as to how the line strength varies over the line source/sink (typically assumed to be uniformly distributed) and mesh spacing. Line source/sinks involve two or more point sources/sinks. For the examples to be presented below we shall always assume that the source strength is uniform over each

FACT CODE MANUAL

active portion of its line segment (note that a line segment corresponds to an edge of an element).

Instead of taking the approach of generating the general expressions for the source/sink term, we shall focus on particular examples that can be easily extended to the more arbitrary cases. In this example we shall focus on a single rectangular prism element where a vertical line source is applied to one of its vertical edges (active over its entire length) as illustrated in Fig. 3.1.2.

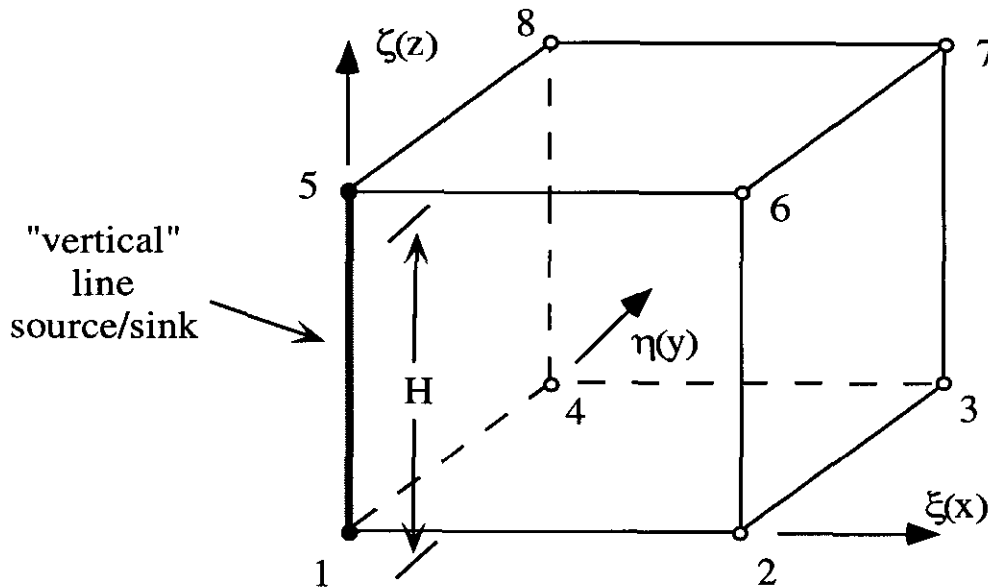


Fig. 3.1.2. 3-D Rectangular Prism Element with Vertical Line Source Along its Line Segment between Nodes 1 and 5.

Assume a line source (or sink) with a specified source strength (assumed to be uniform over the line segment) from node number 1 to node 5. Then, Eq. (3.1.6.1) applies over the vertical heights $z_1 \leq z \leq z_5$ (if the line source/sink partially extended into this element, then the limits of integration would reflect this). When Eq. (3.1.6.1) is used, the source (or sink) term for node 1 in Eq. (3.1.1.6c) becomes

$$\begin{aligned}
 F_{s_1} &= \int_{\Omega^e} \varphi_1 q d\Omega^e = \int_{\Omega^e} \varphi_1 q_\beta \delta(x - x_1, y - y_1) d\Omega^e \\
 &= q_\beta \int_{z_1}^{z_5} \varphi_1 \delta(x - x_1, y - y_1) dz = q_\beta \left[\frac{H}{2} \right] \int_{-1}^{+1} \varphi_1(\xi_1, \eta_1, \zeta) d\zeta
 \end{aligned}
 \tag{3.1.6.2}$$

Integration of Eq. (3.1.6.2) can be performed once the basis function for node 1 is evaluated at the local point $(\xi_1, \eta_1) = (-1, -1)$ from Eq. (3.1.2.2)

$$\varphi_1(-1, -1, \zeta) = \frac{1}{8} (2)(2)(1 - \zeta) = \frac{1}{2} (1 - \zeta)
 \tag{3.1.6.3}$$

Performing the integration for node 1 and a similar integration for node 5 yields

$$F_{s_1} = F_{s_5} = \frac{Hq_\beta}{2} = \frac{Q_\beta}{2} \quad (3.1.6.4)$$

where Q_β is the total volumetric flow of the source/sink over this element height, H , and contained within this element. In the global sense, when there are up to four neighboring elements having a common edge, Eq. (3.1.6.2) still applies where the node numbers become the global node numbers and the source strength is the total source strength.

Application of the above example, given by Eq. (3.1.6.2), to multiple elements (or other directions) is straightforward. The following is an example where a vertical line source extends over two neighboring elements (e.g., a partially screened well within an aquifer unit whose active portion extends over two elements entirely) as illustrated in Fig. 3.1.3.

Assume the node numbers presented represent global node numbers, and based upon application of Eq. (3.1.6.2) for each line segment, we can compute the source/sink term contributions for global nodes 1, 2, and 3. Note that we are assuming that the source strength is uniform over both line segments (of varying lengths)

$$q_\beta = \frac{Q_\beta}{H_1 + H_2} = \frac{Q_1 + Q_2}{H_1 + H_2} \quad (3.1.6.5)$$

where $Q_i = H_i q_\beta$ is the total volumetric flow rate of the line source/sink contained within the i^{th} line segment (element height). Based on these definitions the source term contributions become:

$$F_{s_1} = \left[\frac{H_1}{2} \right] q_\beta = \frac{Q_1}{2} \quad (3.1.6.6a)$$

$$F_{s_2} = \left[\frac{H_1 + H_2}{2} \right] q_\beta = \frac{Q_1 + Q_2}{2} \quad (3.1.6.6b)$$

$$F_{s_3} = \left[\frac{H_2}{2} \right] q_\beta = \frac{Q_2}{2} \quad (3.1.6.6c)$$

It is seen that for a uniform line source the source is distributed to each global node based upon the distribution of line segment lengths.

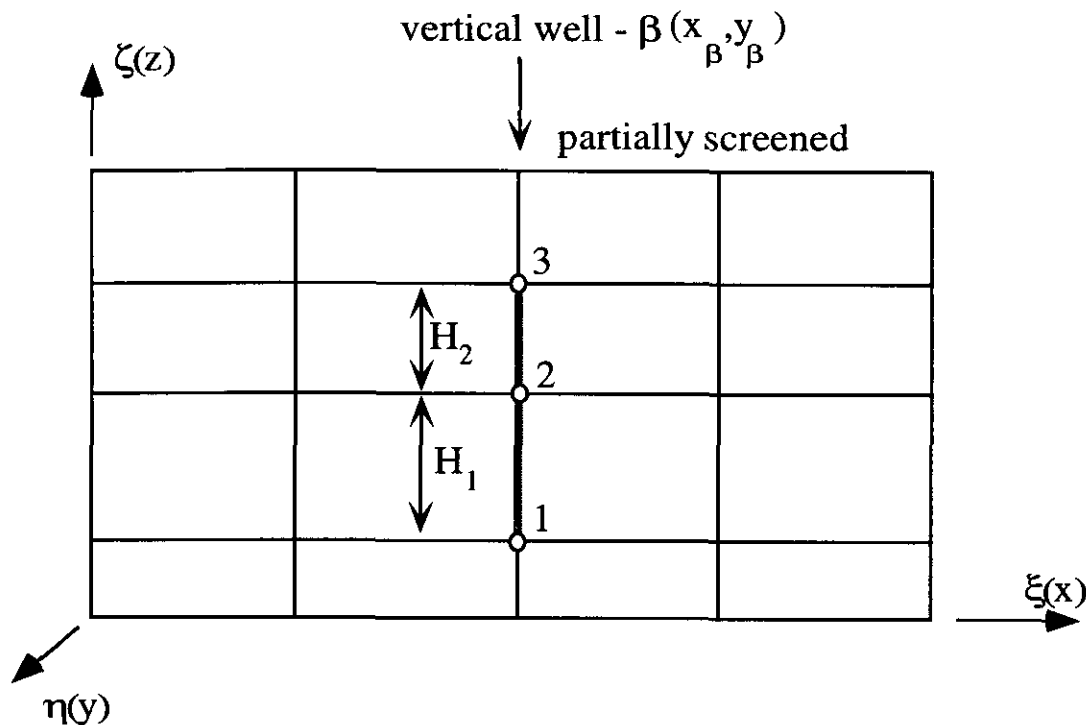


Fig. 3.1.3. Example of Vertical Line Source (specified strength) Extending over Two Elements.

In the above examples we have limited ourselves to vertical line sources/sinks of uniform strengths that extend over the entire length of those elements containing them. For more general applications, Eq. (3.1.6.2) will have to be cast into the direction of interest and the appropriate basis functions and source/sink functions must be chosen. Upon substitution, integration of Eq. (3.1.6.2) for the rectangular prism or constrained hexahedron element will establish the appropriate allocation of flow rate among the various nodes.

At this point we shall generate more general expressions for the vertical (or horizontal) source/sink term where the active portion of the line source/sink does not extend the entire length of the element edge. We shall focus on a single rectangular prism element where a vertical line source is applied to one of its vertical edges as illustrated in Fig. 3.1.4.

Again, assume a line source (or sink) with a specified source strength (assumed to be uniform over the active portion of the line segment and zero outside this portion) from node number 1 to node 5. Then, Eq. (3.1.6.1) applies over the vertical heights $z_1 \leq z \leq z_5$ (due to zero contributions outside the active portion, the limits of integration reduce to $z_B \leq z \leq z_T$). When Eq. (3.1.6.1) is used, the source (or sink) terms for nodes 1 and 5 in Eq. (3.1.1.6c) become

$$F_{s_i} = q_\beta \left[\frac{H}{2} \right] \int_{\zeta_B}^{\zeta_T} \phi_i(\xi_\beta, \eta_\beta, \zeta) d\zeta \quad (3.1.6.7a)$$

$$F_{s_5} = q_\beta \left[\frac{H}{2} \right] \int_{\zeta_B}^{\zeta_T} \varphi_5(\xi_\beta, \eta_\beta, \zeta) d\zeta \quad (3.1.6.7b)$$

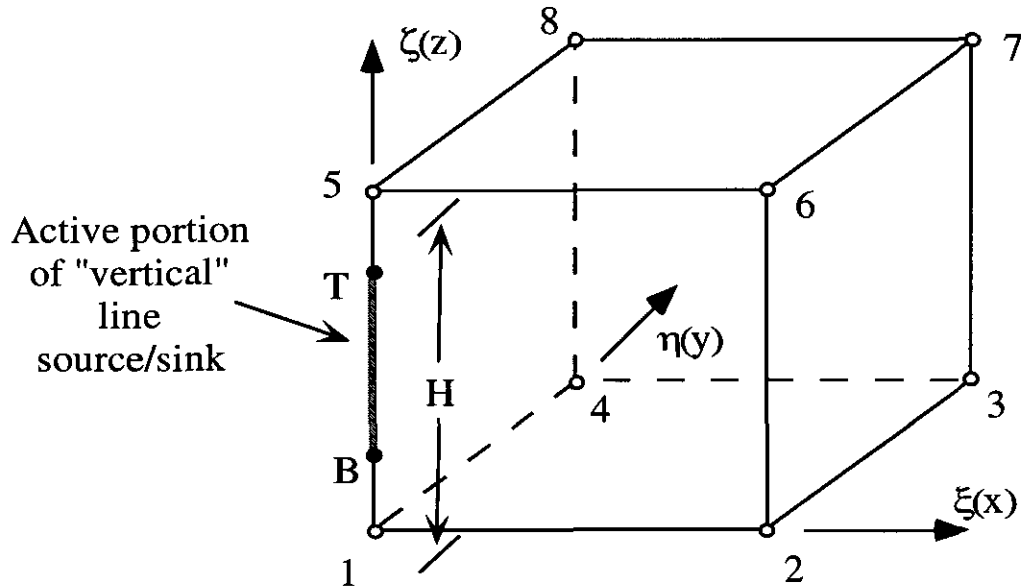


Fig. 3.1.4. 3-D Rectangular Prism Element with Vertical Line Source along a Portion of its Line Segment between Nodes 1 and 5.

where the normalized limits of integration are

$$\begin{aligned} \zeta_T &= 2 \left[\frac{z_T - z_1}{H} \right] - 1 \\ \zeta_B &= 2 \left[\frac{z_B - z_1}{H} \right] - 1 \end{aligned} \quad \text{where } H = z_5 - z_1 \quad (3.1.6.8)$$

and the source strength is uniform over the active portion of the line segment (zero outside it)

$$q_\beta = \frac{Q_\beta}{z_T - z_B} \quad (3.1.6.9)$$

Integration of Eqs. (3.1.6.7) can be performed once the basis functions for nodes 1 and 5 are evaluated at the local point $(\xi_\beta, \eta_\beta) = (-1, -1)$ from Eq. (3.1.2.2)

$$\varphi_1(-1, -1, \zeta) = \frac{1}{8}(2)(2)(1 - \zeta) = \frac{1}{2}(1 - \zeta) \quad (3.1.6.10a)$$

$$\varphi_5(-1, -1, \zeta) = \frac{1}{8}(2)(2)(1 + \zeta) = \frac{1}{2}(1 + \zeta) \quad (3.1.6.10b)$$

Performing the integrations for nodes 1 and 5 yield

$$F_{s_1} = \frac{Hq_\beta}{2} \left[\frac{1}{2}(\zeta_T - \zeta_B) - \frac{1}{4}(\zeta_T^2 - \zeta_B^2) \right] \quad (3.1.6.11a)$$

$$F_{s_5} = \frac{Hq_\beta}{2} \left[\frac{1}{2}(\zeta_T - \zeta_B) + \frac{1}{4}(\zeta_T^2 - \zeta_B^2) \right] \quad (3.1.6.11b)$$

In the global sense, when there are up to four neighboring elements having a common edge, Eqs. (3.1.6.11) still apply where the node numbers become the global node numbers and the source strength is the total source strength.

Application of the above example, given by Eqs. (3.1.6.11), to multiple elements (or other directions) is straightforward. The following is an example where a vertical line source extends over one element and into its nearest neighboring elements as illustrated in Fig. 3.1.5 (i.e., the entire active portion of the line source/sink is within the range $z_B \leq z \leq z_T$).

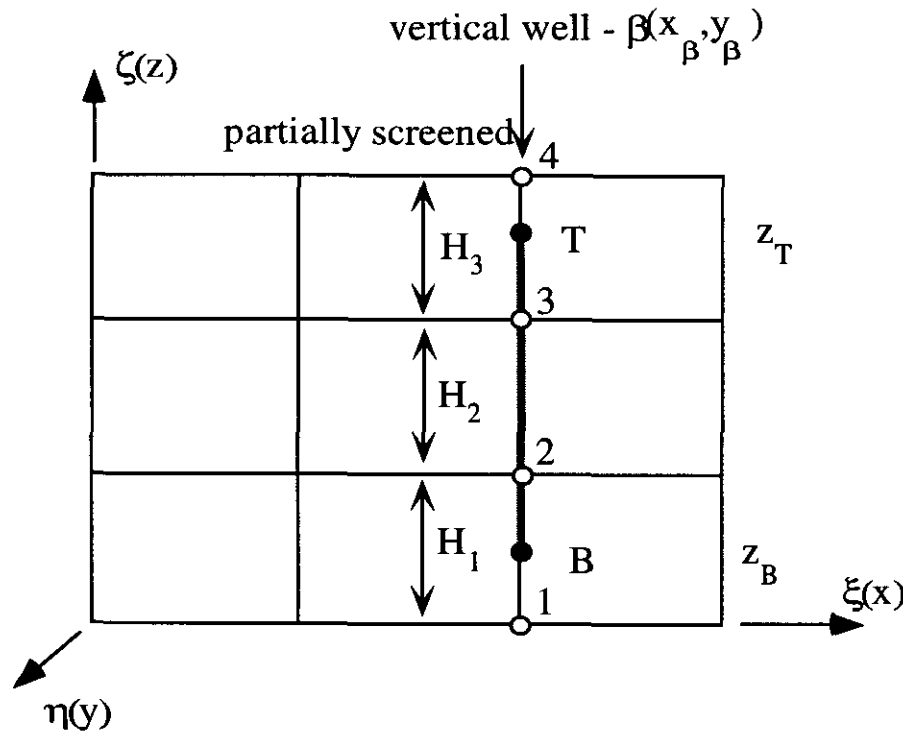


Fig. 3.1.5. Example of Vertical Line Source (specified strength) extending into Three Rectangular Prism Elements.

Assume the node numbers presented represent global node numbers and based upon application of Eq. (3.1.6.11) for each line segment we can compute the source/sink term contributions for global nodes 1, 2, 3, and 4. Note that we are assuming that the source strength (volumetric flow rate per active length of source within a given element) may differ between each elemental line segment but is uniform over each active portion within that line segment. The source term contributions become:

$$F_{s_1} = \frac{H_1 q_1}{2} \left[\frac{1}{2}(1 - \zeta_B) - \frac{1}{4}(1 - \zeta_B^2) \right] \quad (3.1.6.12a)$$

$$F_{s_2} = \frac{H_2 q_2}{2} + \frac{H_1 q_1}{2} \left[\frac{1}{2}(1 - \zeta_B) + \frac{1}{4}(1 - \zeta_B^2) \right] \quad (3.1.6.12b)$$

$$F_{s_3} = \frac{H_2 q_2}{2} + \frac{H_3 q_3}{2} \left[\frac{1}{2}(\zeta_T + 1) - \frac{1}{4}(\zeta_T^2 - 1) \right] \quad (3.1.6.12c)$$

$$F_{s_4} = \frac{H_3 q_3}{2} \left[\frac{1}{2}(\zeta_T + 1) + \frac{1}{4}(\zeta_T^2 - 1) \right] \quad (3.1.6.12d)$$

For the case where the active portions say extend half way into line segments 1 and 3, $\zeta_B = \zeta_T = 0$, and the source strength is uniform over all three line segments, Eqs. (3.1.6.12) reduce to

$$F_{s_1} = \frac{1}{8} [H_1 q_\beta] \quad (3.1.6.13a)$$

$$F_{s_2} = \frac{1}{2} [H_2 q_\beta] + \frac{3}{8} [H_1 q_\beta] \quad (3.1.6.13b)$$

$$F_{s_3} = \frac{1}{2} [H_2 q_\beta] + \frac{3}{8} [H_3 q_\beta] \quad (3.1.6.13c)$$

$$F_{s_4} = \frac{1}{8} [H_3 q_\beta] \quad (3.1.6.13d)$$

A more general application of the above example would be the positioning of the vertical line source not coincident with a set of areal nodes, but internal to a set of vertically stacked elements. At this point we shall generate these more general expressions focusing first on a single rectangular prism element where a vertical line source is applied (limited) to the internal areal region of an element as illustrated in Fig. 3.1.6. Application of these equations can be easily extended to the multiple element case. As discussed in a later section, these equations for an arbitrary located vertical line source (flux specified) have been automated within the FACT code as an input option.

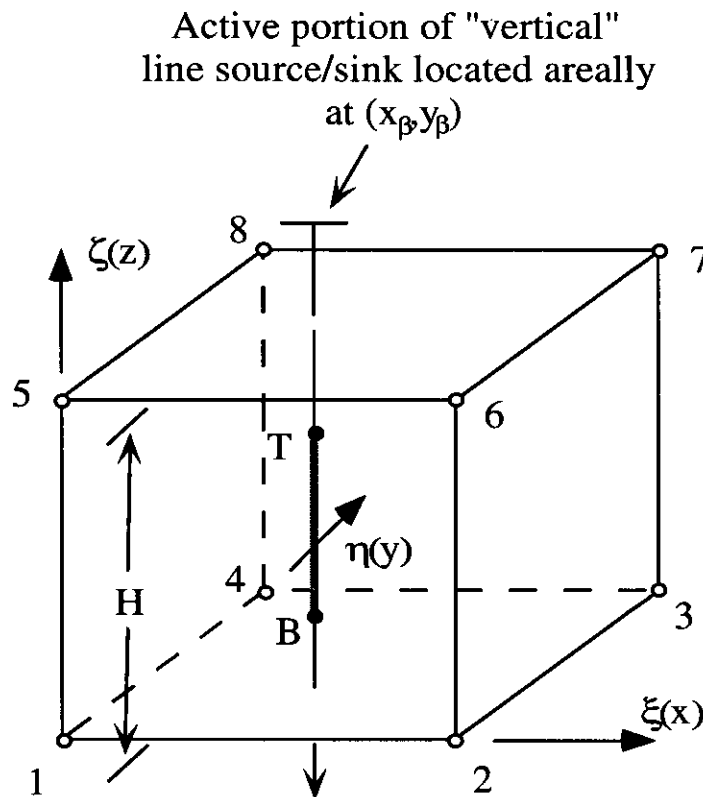


Fig. 3.1.6. 3-D Rectangular Prism Element with Vertical Line Source along a Portion of its Line Segment between Nodes 1 and 5.

Again, assume a line source (or sink) with a specified source strength (assumed to be uniform over the active portion of the line segment and zero outside this portion) is located arbitrarily within a specified rectangular prism element at the areal point (x_β, y_β) . Then, Eq. (3.1.6.1) applies over the vertical heights $z_B \leq z \leq z_T$. When Eq. (3.1.6.1) is used, the source (or sink) term for the i^{th} node in Eq. (3.1.1.6c) becomes

$$\begin{aligned}
 F_{s_i}^e &= \int_{\Omega^e} \varphi_i q^e d\Omega^e = \int_{\Omega^e} \varphi_i q_\beta^e \delta(x - x_\beta, y - y_\beta) d\Omega^e \\
 &= q_\beta^e \int_{z_B}^{z_T} \varphi_i \delta(x - x_\beta, y - y_\beta) dz = q_\beta^e \left[\frac{H_\beta^e}{2} \right] \int_{\zeta_B}^{\zeta_T} \varphi_i(\xi_\beta, \eta_\beta, \zeta) d\zeta
 \end{aligned}
 \tag{3.1.6.14a}$$

where

q_β^e source strength (flow rate per unit of active length) located at the areal point (x_β, y_β) and the allocated amount to element e .

H_β^e element height at areal point (x_β, y_β) .

$\varphi_i(\xi_\beta, \eta_\beta, \zeta)$... shape function evaluated at local point (ξ_β, η_β) .

and where the normalized limits of integration are evaluated from

$$\zeta = 2 \left[\frac{z - z_b}{H_\beta^e} \right] - 1 \quad (3.1.6.14b)$$

and z_b represents the z elevation of the lower element face defined in Eq. (3.1.4.5e) for a rectangular prism element.

Assuming the source strength is uniform over the active portion, Eq. (3.1.6.14a) reduces to

$$F_{s_i}^e = \left[\frac{q_\beta^e}{16} \right] \left[(1 + \xi_i \xi_\beta)(1 + \eta_i \eta_\beta) \right] \left[(\zeta_T - \zeta_B) + \frac{\zeta_i}{2} (\zeta_T^2 - \zeta_B^2) \right] \quad (3.1.6.15)$$

Equation (3.1.6.15) is to be applied to every element in contact with the active screen portion of a specified vertical well (i.e., line source). The elemental contributions are then distributed out to the eight global nodes associated with those elements.

3.1.6.2 Head-Dependent Line Sink within 3D Element

In general the volumetric flow rate per unit length (line strength), q_β , will vary vertically over a well's active screen height. Only under very special conditions will the line strength actually be uniform. In addition, the maximum total flow rate that an aquifer can deliver (i.e., maximum pumping rate from an extraction well) is typically unknown. The vertical variation in line strength and the maximum pumping rate result from the combined hydrogeologic properties of the aquifer (in the proximity of the well) and the extraction well's "well efficiency" (that comprises the choices made during its design and its actual construction). However, in many situations the assumption of either a uniform or spatially varying line strength is an adequate approximation and for those cases a flux specified line source is appropriate (see Section 3.1.6.1 for details). For the case involving a "vertical" line sink where the line strength's spatial variation and/or total strength is unknown a priori, a head-dependent line sink is required. To better handle these types of situations in an automated way, we have developed a special head-dependent line sink option in FACT. We have made it general enough to handle confined and unconfined aquifer units, but limited it to the process of only extracting from the aquifer (the option of injecting into the aquifer is a minor upgrade slated for the future). For an unconfined aquifer the potential existence of a seepage face at the well screen is accounted for. The head-dependent line sink is further restricted to areally coincide with the intersection of the x and y grid planes (i.e., coincides with the vertical edges of a stack of brick elements). A typical line segment of one such line sink is shown in Fig. 3.1.2. The general expression for q becomes (for a vertical head-dependent line sink located at the areal node location, β):

$$q = q_\beta \delta(x - x_\beta, y - y_\beta, z) \quad (3.1.6.16a)$$

$$q_\beta = \hat{S}_w K_{\text{well}} [h_{\text{well}}(z) - h(z)] \quad (3.1.6.16b)$$

where

FACT CODE MANUAL

- q_β volumetric flow rate per unit length (line strength)
 \hat{S}_w donored water saturation at aquifer/well screen interface
 K_{well} overall hydraulic conductivity of well skin, screen, and casing
 $h_{well}(z)$ hydraulic head distribution within well casing
 $h(z)$ hydraulic head distribution within aquifer at well screen

Note that Eq. (3.1.4.16b) expresses the overall resistance to flow (resulting from the serial composite of head losses due to skin, screen, and casing frictional processes). Also the strength of the sink can vary over and within each of its line segments. The dominant (limiting) process is assumed to be occurring within a laminar flow regime and thus the overall process can be approximated as a linear process. The overall ("effective") hydraulic conductivity factor is a function to some degree of well efficiency. The factors contributing to excessive drawdown in wells (inefficiency) can be grouped into two classes: (1) design factors such as inadequate well screen flow areas and (2) construction factors such as poor removal of fine particles resulting in reduced aquifer permeabilities near well screens. One standard approach to estimating well efficiency for an extraction well contained within an unconfined aquifer (see Fig. 3.1.7) is based on the formula:

$$eff_{well} = 100 \left[\frac{\text{drawdown outside casing}}{\text{drawdown inside casing}} \right] \quad (3.1.6.17)$$

where drawdown is computed based upon the initial (static) water level prior to pump operations. Making use of Eq. (3.1.6.17) and the results from FACT in an iterative manner, the user can establish an overall hydraulic conductivity factor for the well (that quantifies its skin resistance and screen losses) that is consistent with a specified well efficiency. Note that for large values of K_{well} , say greater than 100-1000 ft/day, the well behaves ideally; while, for extremely low values the well essentially quits pumping. The maximum pumping capacity of an aquifer unit occurs when the well is assumed to be 100% efficient (very large K_{well}) and the water level within the well is set at or below the bottom of the active screen.

The donored water saturation becomes the water saturation value of either the local aquifer or the well depending upon the direction of flow. Since we have limited this option to extraction wells only, the donored water saturation is set to the local value in the aquifer.

In FACT this type of line sink is handled automatically through user input of a series of line segments (i.e., node point pairs that define and lie along the line sink). FACT internally allocates the appropriate amount of flow rate per line segment over the entire line sink consistent with the modeling assumptions listed above. Each line sink involves user specification of: (1) one or more line sink segments, (2) a single overall hydraulic conductivity for the line sink, and (3) a single time invariant hydraulic head for the line sink (extraction well).

Note that no use of the Dupuit approximation (as illustrated in Fig. 3.1.7) can be taken advantage of here. The Dupuit approximation is only valid for conditions where vertical

FACT CODE MANUAL

velocity components are insignificant. As shown in Fig. 3.1.7, the Dupuit approximation eliminates the presence of a seepage face at the well casing. To determine the maximum flow rate capacity of an extraction well, the hydraulic head within the well casing must be dropped to the bottom of the active portion of the screen. Thus, all flow being delivered to the well crosses the well screen within a seepage face.

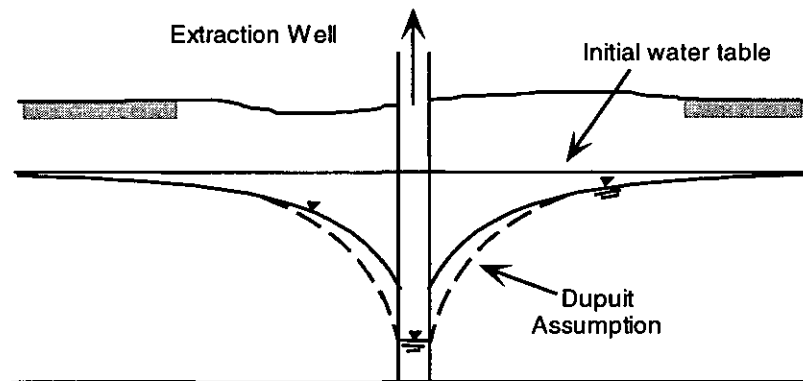


Fig. 3.1.7. Extraction Well Contained within an Unconfined Aquifer Unit.

In deriving our head-dependent line sink equations, we shall focus on a single element where a vertical line sink is applied to one of its vertical edges (a line segment over its entire length) as illustrated in Fig. 3.1.2. To further assist us, a modification is made to Fig. 3.1.7, and shown in Fig. 3.1.8, where half of this figure is replaced with a vertical FACT grid along with some additional helpful annotations.

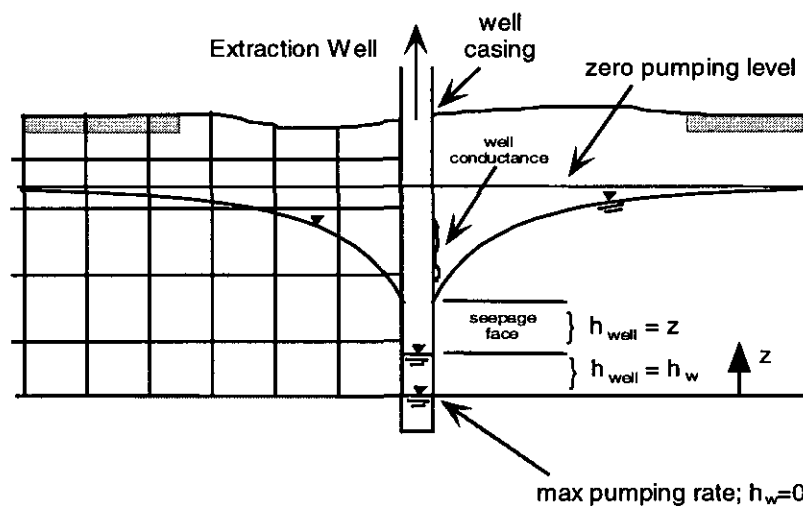


Fig. 3.1.8. Notation Used for Head-dependent Line Sink Model.

As before, substituting Eqs. (3.1.6.16) into (3.1.5.23) results in the line sink contribution to the source term, F_s , for the i 'th node:

$$\begin{aligned}
 F_{s_i} &= \int_{\Omega} \varphi_i q_{\beta} \delta(x - x_{\beta}, y - y_{\beta}, z) d\Omega \\
 &= K_{\text{well}} \int_{z_1}^{z_5} \varphi_i(\xi_{\beta}, \eta_{\beta}, z) \hat{S}_w [h_{\text{well}} - h] dz
 \end{aligned}
 \quad (3.1.6.18)$$

We shall restrict our derivation to only vertical line sinks that coincide with areal node locations. Therefore, our local basis functions reduce to their one-dimensional form. For convenience we shall re-normalize these basis functions such that their independent variable, ζ , ranges from zero to one:

$$\varphi_i(\xi_{\beta}, \eta_{\beta}, z) = \varphi_{\beta i}(\zeta) = \begin{bmatrix} 1 - \zeta \\ \zeta \end{bmatrix} \quad (3.1.6.19a)$$

where

$$z = z_1 + H\zeta \quad \text{and} \quad H = z_5 - z_1 \quad (3.1.6.19b)$$

We also assume (valid approximation in majority of situations) that the water contribution to the well from flow crossing the screen in the vadose zone is negligible. This can be accomplished by assuming that the water saturation becomes zero just above the surface of the water table. The integral expressed by Eq. (3.1.4.18) now reduces to

$$F_{s_i} = HK_{\text{well}} \int_0^{S_{\text{aq}}} \varphi_{\beta i}(\zeta) h_{\text{well}} d\zeta - HK_{\text{well}} \int_0^{S_{\text{aq}}} \varphi_{\beta i}(\zeta) h d\zeta \quad (3.1.6.20)$$

where the limits of integration correspond only to the saturated region of the aquifer and S_{aq} represents the fraction of vertical height within the line segment containing saturated aquifer conditions. For later purposes we also define a fractional saturation term, S_{well} , that represents the fraction of vertical height within the line segment containing saturated well casing conditions. Both saturation fractions are defined as:

$$S_{\text{aq}} \equiv \zeta_{\text{aq}} = \frac{z_{\text{wt}} - z_1}{H} \quad \text{and} \quad S_{\text{well}} \equiv \zeta_{\text{well}} = \frac{h_w - z_1}{H} \quad (3.1.6.21)$$

where for an extraction well case S_{aq} always exceeds S_{well} and where

h_w height of water within well casing.

z_w location of water table within aquifer at the well casing surface.

z_1 lower elevation of element edge where well is specified.

H height of element edge where well is specified.

In order to evaluate the first integral term in Eq. (3.1.6.20), the spatial variation of hydraulic head within the well casing must be specified. It is assumed that frictional losses associated with vertical flow within the well casing is negligible and the well casing is vented to the atmosphere. Thus, a hydrostatic pressure profile exists within the well casing and can be expressed as

$$\Psi_{\text{well}}(z)=0 \Rightarrow h_{\text{well}} = \begin{cases} h_w & \text{for } z \leq h_w \\ z & \text{for } z > h_w \end{cases} \quad (3.1.6.22)$$

Setting up for the integration of the first term yields

$$F_{s_i}^{(1)} = HK_{\text{well}} \left[h_w \int_0^{S_{\text{well}}} \phi_{\beta i}(\zeta) d\zeta + \sum_j \left\{ \int_{S_{\text{well}}}^{S_{\text{aq}}} \phi_{\beta i}(\zeta) \phi_{\beta j}(\zeta) d\zeta \right\} z_j \right] \quad (3.1.6.23)$$

Performing the integrations of Eq. (3.1.6.23), making use of the local basis functions expressed above results in the contributions to nodes 1 and 5 as

$$\begin{bmatrix} F_{s_1} \\ F_{s_5} \end{bmatrix}^{(1)} = \frac{HK_{\text{well}}}{2} \left\{ h_w \begin{bmatrix} 2S_{\text{well}} - S_{\text{well}}^2 \\ S_{\text{well}}^2 \end{bmatrix} + 2 \sum_j \left\{ L_{ij}(S_{\text{aq}}) - L_{ij}(S_{\text{well}}) \right\} z_j \right\} \quad (3.1.6.24)$$

where

$$L_{ij}(x) \equiv \begin{bmatrix} x - x^2 + \frac{1}{3}x^3 & \frac{1}{2}x^2 - \frac{1}{3}x^3 \\ \frac{1}{2}x^2 - \frac{1}{3}x^3 & \frac{1}{3}x^3 \end{bmatrix} \quad (3.1.6.25)$$

Similarly for the second term, integration results in

$$F_{s_i}^{(2)} = \frac{HK_{\text{well}}}{2} \left\{ 2 \sum_j L_{ij}(S_{\text{aq}}) h_j \right\} \quad (3.1.6.26)$$

The total contributions to nodes 1 and 5 are obtained by adding the two terms together as

$$\begin{aligned} \begin{bmatrix} F_{s_1} \\ F_{s_5} \end{bmatrix} &= \frac{HK_{\text{well}}}{2} \left\{ h_w \begin{bmatrix} 2S_{\text{well}} - S_{\text{well}}^2 \\ S_{\text{well}}^2 \end{bmatrix} + 2 \sum_j \left\{ L_{ij}(S_{\text{aq}}) - L_{ij}(S_{\text{well}}) \right\} z_j \right\} \quad (\text{RHS}) \\ &\quad - HK_{\text{well}} \left\{ \sum_j L_{ij}(S_{\text{aq}}) h_j \right\} \quad (\text{LHS}) \end{aligned} \quad (3.1.6.27)$$

The first grouping of terms in Eq. (3.1.6.27) are loaded into the RHS forcing vector of the governing equations, while the second grouping of terms are loaded into the LSH global matrix. Both groups being loaded at their appropriate global number locations. Since the actual surface level of the water table is unknown prior to its solution, the application of a head-dependent vertical line sink introduces additional non-linearity in the same manner as a unconfined aquifer does.

FACT CODE MANUAL

Once FACT converges, the resulting hydraulic head solution can then be used to perform post-iteration computations for determining the line sink flow rates across each of its line segments. These calculations are performed automatically by FACT and are then printed out.

The integrated (total) volumetric flow rate into the extraction well is obtained by summing up the integrated contributions from all of the line segments corresponding to a given line sink. The general expression for the integrated flow rate for each line segment becomes

$$Q_{\text{seg}} = HK_{\text{well}} \left[\int_0^{S_{\text{aq}}} h_{\text{well}} d\zeta - \int_0^{S_{\text{aq}}} h d\zeta \right] \quad (3.1.6.28)$$

Applying the same set of assumptions as employed above, Eq. (3.1.6.28) becomes

$$Q_{\text{seg}} = HK_{\text{well}} \left[h_w \int_0^{S_{\text{well}}} d\zeta + \int_{S_{\text{well}}}^{S_{\text{aq}}} \zeta d\zeta - \int_0^{S_{\text{aq}}} h d\zeta \right] \quad (3.1.6.29)$$

Expanding and performing the integration of Eq. (3.1.4.23) results in the integrated flow rate

$$Q_{\text{seg}} = \frac{HK_{\text{well}}}{2} [T_1 - T_2] \quad (3.1.6.30a)$$

where

$$T_1 = 2h_w S_{\text{well}} + \left[2S_{\text{aq}} - S_{\text{aq}}^2 - 2S_{\text{well}} + S_{\text{well}}^2 \right] z_1 + \left[S_{\text{aq}}^2 - S_{\text{well}}^2 \right] z_5 \quad (3.1.6.30b)$$

$$T_2 = \left[2S_{\text{aq}} - S_{\text{aq}}^2 \right] h_1 + \left[S_{\text{aq}}^2 \right] h_5 \quad (3.1.6.30c)$$

The total flow rate into the line sink (i.e., extraction well) then is computed by

$$Q_w = \sum_{\text{seg}} Q_{\text{seg}} \quad (3.1.6.31)$$

3.1.6.3 Uniform Flux Specified Vertical Well Option

In groundwater modeling it is very common to have the need to place one or more vertical wells within the mesh domain. And in many cases, it is inconvenient for the user to be forced to limit their placement to only areal node locations, as well as, tedious for the user to have to externally compute the appropriate amount of a line source/sink to be allocated out to its surrounding nodes. In addition, these vertical wells are often approximated as having a uniform strength over each aquifer unit that is in contact with the active portion of the well screen.

Since uniform strength injection/extraction wells are so common place in groundwater modeling, we have added a feature to FACT that automatically handles vertical wells

FACT CODE MANUAL

whose source strengths are uniform and time-dependent. Given as input a vertical well's areal location (not limited to areal node locations), the top and bottom elevations of its active screen (not limited to vertical grid surfaces), and its total volumetric flow rate (positive for injection and negative for extraction), spline index of pumping time series, FACT automatically performs the following input pre-processing:

- Limited input error checking is performed to ensure supplied input is valid and consistent. For example, execution is terminated with a written error message if a well location is specified outside of the areal or vertical grid domain.
- If a well is areally within a specified tolerance of either the x or y gridlines then the well is moved such that it resides on that gridline.
- If a well is vertically within a specified tolerance of a z grid surface, then the well's active screen elevation (top or bottom) is moved such that it coincides with that grid surface.
- The global node numbers who are in contact with those active elements spanned by the active portion of the well screen are computed and stored.
- Steady-state or temporal flux BC's (type 2 BC's) are generated for each global node number associated with this line source/sink. The flow rate contribution for each element associated with these global node numbers is computed based on Eq. (3.1.6.14a) and added to the flux BC array at the global node number.

The above pre-processing sequence is performed sequentially on each user specified vertical well. For each well appropriately allocated flow contributions are computed that are ultimately loaded into the flux BC array. These contributions are added to the array locations corresponding to those global nodes associated with each 3D element that the active screen resides within. Based on this strategy, the user can specify as many vertical wells as desired that are all co-located at the same areal location. In fact, the vertical extents of each well can overlap each other. The net effect of having multiple wells specified at the same areal and vertical locations is the specification of a composite well at that location whose source strength is the sum of the individual source strengths.

In many situations a well's source strength can vary significantly over its vertical extent and as such can not be approximated as uniform over its entire length. In some cases this variation is limited to a finite number of step changes in strength. For example, a well screen that extends over multiple aquifer units. In such cases, to a good approximation one can assume that its strength is uniform, but a different value, over a finite number of line segments. Under such situations the user can specify several vertical wells at the same areal location whose screen elevations coincide with the tops and bottoms of the uniform segments. Each well would have its own unique value for source strength.

In most cases, the user probably knows the total flow rate for the well but not its variation over these line segments (or aquifer units in the stated example). The following discussion presents an iterative technique for obtaining estimates of these flow rates (i.e., the flow fractions) for each line segment of a vertical well whose source strength varies in a step-wise fashion. By means of an example, we will consider a vertical extraction well whose active screen height extents over three aquifer units (aquifer A, aquitard B, and

FACT CODE MANUAL

aquifer C). The more general case of an arbitrary number of line segments is a straightforward extension. The example chosen is depicted in Fig. 3.1.9 where it is assumed that the user knows the horizontal conductivity and screen height for all three units, as well as, the total flow rate extracted from the well. Estimates of hydraulic heads within each unit may not be available.

During the iterative process we want to estimate (allocate) the source strength on a segment basis (i.e., flow rate per segment) over several aquifer units. Starting with the aquifer system depicted in Fig. 3.1.9, we want to estimate the volumetric flow rates occurring in each segment (Q_a , Q_b , and Q_c) where

$$Q_{\text{tot}} = \sum_{i=1}^{\text{nseg}} Q_i \quad (3.1.6.31)$$

and

Q_{tot} specified total volumetric flow rate over entire well

Q_i volumetric flow rate for i^{th} segment

nseg number line segments within vertical well (3 for current example)

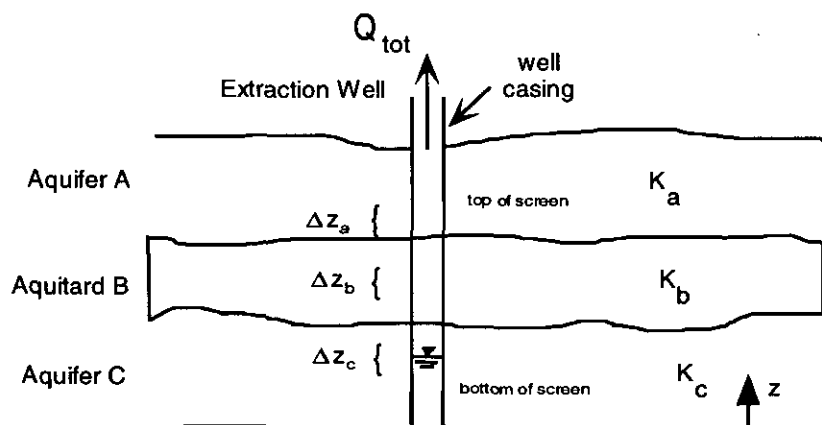


Fig. 3.1.9. A Vertical Well whose Screen Extends across Several Aquifer Units.

The local flow rate within a given line segment can be expressed in the form

$$Q_i = 2\pi R \Delta z_i q_i = \frac{2\pi R}{\Delta r} \Delta z_i K_{hi} (\bar{h}_i - h_w) \quad (3.1.6.32)$$

where

R arbitrary radial distance from well centerline

Q_i volumetric flow rate of i^{th} segment

q_i volumetric flow rate per unit length (line strength)

Δz_i vertical height of i^{th} segment

Δr radial distance, $R - r_w$

r_w radial distance to outside surface of well screen

FACT CODE MANUAL

K_{hi} horizontal hydraulic conductivity for i^{th} segment

h_w hydraulic head within well casing

\bar{h}_i average hydraulic head for i^{th} segment

Based on Eq. (3.1.6.32) we can define a volumetric flow rate at the perimeter as

$$\hat{Q}_i = \frac{Q_i}{\left(\frac{2\pi R}{\Delta r} \right)} = \Delta z_i K_{hi} \Delta h_i \quad (3.1.6.33)$$

where $\Delta h_i = \bar{h}_i - h_w$ is the average driving head for the i^{th} segment.

A total volumetric flow rate at the perimeter, \hat{Q}_{tot} , can be defined in a similar fashion as was done in Eq. (3.1.6.31) resulting in

$$\hat{Q}_{\text{tot}} = \sum_{i=1}^{\text{nseg}} \hat{Q}_i = \sum_{i=1}^{\text{nseg}} \Delta z_i K_{hi} \Delta h_i \quad (3.1.6.34)$$

Thus, the fraction of total volumetric flow allocated to the i^{th} segment becomes

$$f_i = \frac{Q_i}{Q_{\text{tot}}} = \frac{\hat{Q}_i}{\hat{Q}_{\text{tot}}} = \frac{\Delta z_i K_{hi} \Delta h_i}{\sum_{i=1}^{\text{nseg}} \Delta z_i K_{hi} \Delta h_i} \quad (3.1.6.35)$$

If the user has no prior information on hydraulic head within the segments, then the following initial estimate (to be updated or verified once a FACT calculation is complete) should be assumed for the first FACT run (i.e., uniform driving heads for all segments)

$$\Delta h = \Delta h_a = \Delta h_b = \Delta h_c = \Delta h_i \quad (3.1.6.36)$$

Only a few iterations should be necessary to achieve converged values for the flow rates to each segment. Note that this approach is restricted to steady-state flow conditions only. Fortunately, most cases of interest conform to the limitation imposed by the above approach and should be useful to most FACT users.

3.1.6.4 Uniform Flux Specified Vertical Recirculation Well Option

Vertical recirculation wells are an innovative technology for the in-situ clean up of groundwater contaminated with volatile compounds, most notably dissolved chlorinated volatile organic compounds (CVOC). The vertical recirculation well is a pump and treat system that uses a combination of existing technologies, including air stripping, air lift pumping, and groundwater wells in on complete in-site assembly (Jackson and Looney, 1996). The system consists of an upper and lower screen zone, an air injection blower having an associated eductor placed at the lower well screen, an optional submersible type well pump to reinforce the pumping effect, and vacuum removal of the off-gas at the well head. The conventional design calls for placement of the lower screen near the

FACT CODE MANUAL

bottom of the aquifer and the placement of the upper screen near the top of the aquifer, just below the confining zone. During operation, air is injected using an eductor lowered inside the well bore to the lower screen zone. As the air rises to the surface in the well, the CVOCs are removed by air stripping. As the air bubbles rise with the well-bore, the density of the water is decreased and an upward flow field is developed with the well-bore. The naturally induced upward flow is often enhanced via a mechanical pump to increase performance and capture zone. The groundwater flow pattern into the lower screen and out of the upper screen causes development of a recirculation pattern around the well screens. Figure 3.1.10 presents a schematic representation of a vertical recirculation well and the resultant flow field.

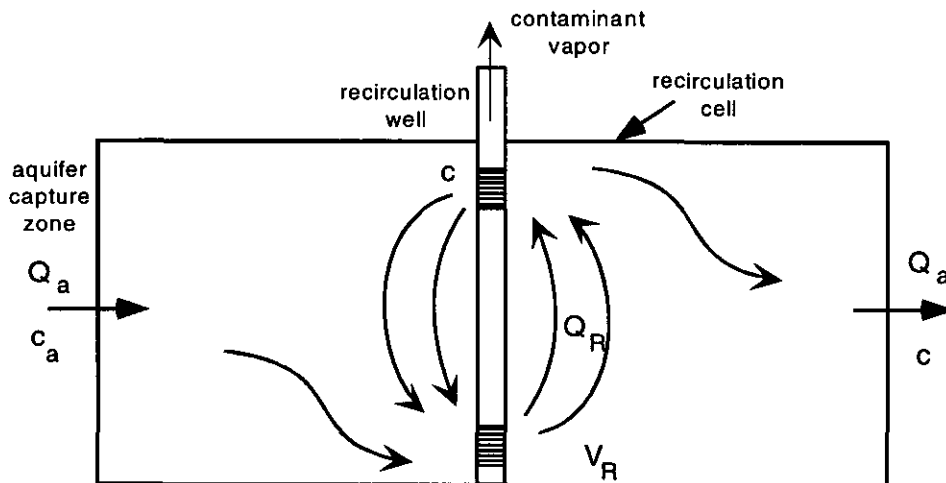


Fig. 3.1.10. Schematic of Basic Flow Pattern Under Vertical Recirculation Well Operation

Groundwater flow modeling of vertical recirculation wells can be performed analytically under certain limiting conditions and useful parametric curves can be generated for certain numerical solutions. Classical results addressing vertical recirculation flows can be found in the literature (Herrling et al., 1990). Application of the classical solutions to the design of a vertical recirculation well system for the A/M Area Southern Sector has been performed by (Jackson and Looney, 1996). These idealized solutions typically assume the aquifer to be subject to: (1) a uniform one-dimensional head gradient field upstream and downstream, (2) a uniform and planar confining unit, (3) a homogeneous isotopic aquifer, and (4) well networks being perpendicular to natural groundwater flow. These approaches provide relatively quick and typically adequate accuracy in determining the lateral width of capture zones for simple well networks.

To eliminate many of the limiting assumptions mentioned above, assess previous calculations, and to incorporate new hydrogeological data, the FACT code has been modified to accommodate vertical recirculation wells consisting of two screen zones; an extraction screen zone and an injection screen zone.

The vertical recirculation well is modeled as a vertical uniform flux specified line sink (extraction) and line source (injection) located at the same areal location. The extracted volumetric flow is re-injected into the injection screen zone instantaneously. The

FACT CODE MANUAL

volumetric flowrate for each line sink/source is partitioned to the respective global nodes using the same methodology applied to the uniform flux specied vertical well. The recirculation well pumping rate can be time-dependent.

3.1.7 Head-Dependent Flux Boundary Conditions

FACT has the capability to accommodate a third-type boundary condition known as "head-dependent flux condition." Physically, this may correspond to induced infiltration or vertical leakage conditions where fluxes transmitted through a semi-permeable bed are head-dependent. These fluxes are controlled by the difference between the hydraulic head at the top of the bed and the hydraulic head in the underlying aquifer. A typical situation is illustrated in Fig. 3.1.11.

If, at the bottom of the semi-permeable bed the aquifer head h_B is less than the bed elevation z_B , it is assumed that $\psi_B \approx 0$ and locally the water table is below the point z_B . Thus the nodal leakage flux becomes

$$q_i \equiv \frac{Q_i}{A_i} = \left(\frac{K}{b} \right)_{\text{bed}} \Delta h_i \quad (3.1.7.1)$$

$$\Delta h_i = \begin{cases} h_T - h_i & \text{for } h_i \geq z_B \\ h_T - h_B & \text{for } h_i < z_B \end{cases} \quad (3.1.7.2)$$

where

Q_i volumetric flowrate of source bed

A_i flow area of source bed

$(K/b)_{\text{bed}}$ leakance coefficient of source bed

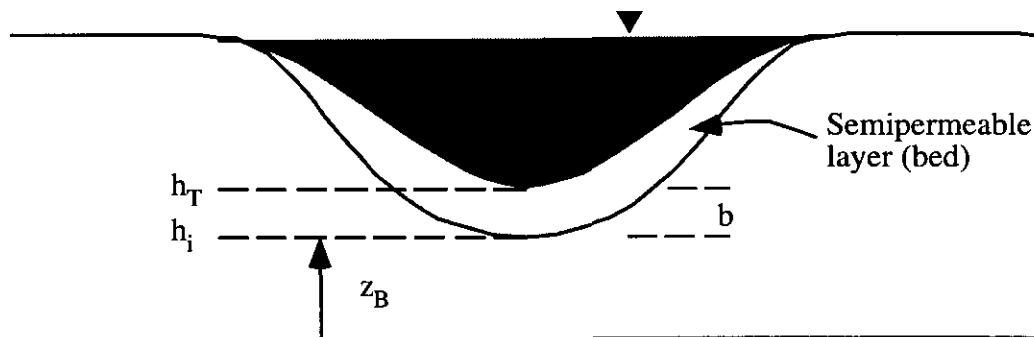


Fig. 3.1.11. Typical Head-Dependent Flux Boundary Condition (River or Stream).

In the Galerkin approximation we shall assume this nodal leakage flux to be a point source at a given node i . Thus

$$F_{sb_i} = \int_{\sigma} \phi_i q_i d\sigma \quad (3.1.7.3)$$

Assuming a point source on a given surface

$$q_i = \frac{Q_i}{A_i} \delta(\mathbf{x} - \mathbf{x}_i) \quad (3.1.7.4)$$

we get by substituting into Eq. (3.1.7.3)

$$F_{sb_i} = \int_{\sigma} \varphi_i \frac{Q_i}{A_i} \delta(\mathbf{x} - \mathbf{x}_i) d\sigma = Q_i = \left[A \left(\frac{K}{b} \right)_{bed} \right]_i \Delta h_i \quad (3.1.7.5)$$

The FACT code supports four types of head-dependent boundary conditions. They are for a given source bed (note that for each source bed multiple nodal locations can exist in contact with each source bed):

isbtyp	Source bed type
0	Aquitard
1	River
2	Drain
3	General Head

Given the table of head-dependent boundary conditions above, the flow area A and driving head term Δh_i in Eq. (3.1.7.5) are given as

$$A = \begin{cases} A_i & \text{for isbtyp} = 0 \\ A_{eff} & \text{for isbtyp} \neq 0 \end{cases} \quad (3.1.7.6)$$

$$\Delta h_i = \begin{cases} h_T - h_i & \text{for } h_i > z_B & \text{isbtyp} = 0,1 \\ h_T - z_B & \text{for } h_i \leq z_B \\ 0 & \text{for } h_T - h_i \geq 0 & \text{isbtyp} = 2 \\ h_T - h_i & \text{for } h_T - h_i < 0 \\ h_T - h_i & \text{all conditions} & \text{isbtyp} = 3 \end{cases} \quad (3.1.7.7)$$

where A_i is the nodal flow area computed in FACT and A_{eff} is an effective flow area of the source bed provided through user input.

Equation (3.1.7.5) is computed for each global head-dependent source bed node and partitioned into the LHS global system array and RHS load vector depending on the driving head term in Eq. (3.1.7.7) and whether the Picard or Newton-Raphson scheme is used to solve Eq. (3.1.1.7). In the Picard scheme, Eq. (3.1.7.5) is linearized as

$$F_{sb_i} \rightarrow F_{sb_i}^m + \left(\frac{\partial F_{sb_i}}{\partial h_i} \right)^m (h_i^{m+1} - h_i^m) \quad (3.1.7.8)$$

where m is the Picard iteration number. It turns out that Eq. (3.1.1.7) is solved in terms of the change in the hydraulic head vector, therefore, $(\partial F_{sb_i} / \partial h_i)^m$ is added to the LHS

array **A** and $F_{sb_i}^m$ is added the RHS load vector **F** for each source bed global node. The following table is a summary of the contributions to the LHS and RHS global arrays.

isbtyp	Condition	Δh_i	RHS	LHS
0	$h_i > z_B$	$h_T - h_i$	$A_i \left(\frac{K}{b} \right) (h_T - h_i)$	$A_i \left(\frac{K}{b} \right)$
0	$h_i \leq z_B$	$h_T - z_B$	$A_i \left(\frac{K}{b} \right) (h_T - z_B)$	0
1	$h_i > z_B$	$h_T - h_i$	$A_{eff} \left(\frac{K}{b} \right) (h_T - h_i)$	$A_{eff} \left(\frac{K}{b} \right)$
1	$h_i \leq z_B$	$h_T - z_B$	$A_{eff} \left(\frac{K}{b} \right) (h_T - z_B)$	0
2	$h_T \geq h_i$	0	0	0
2	$h_T < h_i$	$h_T - h_i$	$A_{eff} \left(\frac{K}{b} \right) (h_T - h_i)$	$A_{eff} \left(\frac{K}{b} \right)$
3	all	$h_T - h_i$	$A_{eff} \left(\frac{K}{b} \right) (h_T - h_i)$	$A_{eff} \left(\frac{K}{b} \right)$

The Newton-Raphson contributions to the LHS and RHS arrays are identical to the Picard scheme due to the linearization in Eq. (3.1.7.8).

3.1.7.1 Head-Dependent Recharge & Drain Boundary Conditions

The basic idea is to combine recharge and drainage and into a single Type 3 (Cauchy) boundary condition. Justification for this combined boundary condition is based on the assumption of minimal ponding of surface water. Physically, minimal ponding of surface water should occur when one assumes that most rainfall runs off. When low permeability zones are present at (i.e., cropout) or near the ground surface, recharge specified uniformly over the surface can produce non-physical results in the form of very high hydraulic heads at the points of low conductivity. In these situations, hydraulic head should not significantly exceed the surface elevation (i.e., near zero pressure head where pressure head is defined as hydraulic head minus elevation) and local infiltration should be only a fraction of the regional recharge rate. In addition, the existence and location of seepines (i.e., contours of zero pressure head along the ground surface) are generally unknown or unspecified a priori to a flow solution. For elevations above the seepines infiltration (along with negative pressure heads) can exist, while below the seepines seepage faces exist where drainage occurs (along with non-negative pressure heads). For variably saturated ground water flow modeling, these features (1) complicate implementation of surface recharge (infiltration) and drainage conditions and (2) are typically observed for terrain with heterogeneous hillsides or engineered ground surfaces.

For a flow model with conventional "layer cake" conductivity fields, the conductivities of the top layer of elements are relatively large because the entire layer corresponds to a transmissive aquifer unit. In this case, recharge can be specified uniformly over the top surface without difficulty. Simultaneously, drain boundary conditions can then be added wherever the uppermost aquifer is known or suspected to discharge at the surface (excess

FACT CODE MANUAL

recharge removed by drain boundary conditions). Unfortunately, this approach typically leads to artificially inflated overall recharge/drain volumetric flowrates and for complex terrain the locations of seepage faces are seldom known.

When seepage faces are present, Neuman et al. (1974), and later modified by Rulon (1984) and then implemented by Huyakorn et al. (1986), adopted a procedure whereby the locations of seepines and the non-linear flow equations were iteratively solved using a Picard iteration strategy. Surface boundary conditions were switched from prescribed zero pressure head (below the seepines) to prescribed surface flux (above the seepines) during the iterative process. Infiltration (or evaporation) rates were limited to a maximum potential flux rate whose value diminished to zero as the seepage line was approached (resulting in better estimates of overall regional recharge). Overall drainage rates were then obtained by post-processing of the flow solution over the seepage faces. To enhance overall convergence of the solution various criteria for transitioning between boundary condition types were employed. With this method convergence difficulties may occur for complex terrain, as well as, the additional overhead required to update boundary conditions during the iteration process.

The difficulties expressed above can be eliminated by combining the concepts of recharge and drainage into a single boundary condition. The basic idea is that locally the surface is either recharging or draining the subsurface, and there should be a continuous transition between these conditions. Infiltration should occur for negative pressure head (water level below the ground surface) and aquifer discharge should occur for positive pressure head. Also, to be consistent with the continuity needs of the Newton-Raphson iterative solver employed in FACT, the overall function representing this "combined" recharge/drain boundary condition should also be continuous in its first derivative. Figure 3.1.12 presents a combined recharge/drain boundary condition that meets the above criteria and is used in the present version of FACT.

Locally, when the water level is well below the ground surface, recharge occurs at the maximum rate permitted. As the pressure head approaches zero, recharge is smoothly reduced to zero. For positive pressure head, the surface drains the aquifer at a rate proportional to the pressure head. To the left of the transition zone, the combined recharge/drain boundary condition is exactly the same as the conventional recharge boundary condition. To the right of the transition zone, the combined recharge/drain boundary condition is identical to a typical drain boundary condition. The transition zone reflects a non-linear region connecting two limiting linear boundary conditions.

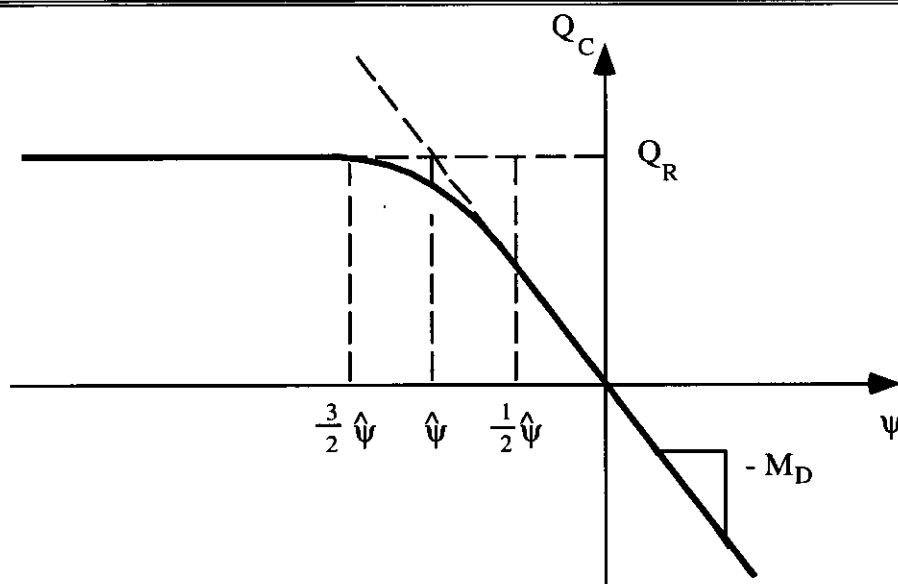


Fig. 3.1.12. Source Bed Boundary Condition for Simultaneous Treatment of Surface Recharge and Drainage.

The mathematical formulation chosen for this function, as shown in Fig. 3.1.12 is

$$Q_c(x) = \frac{Q_R}{8} [7 - 2x - x^2] \quad (3.1.7.9)$$

where

$$\psi = h - z_c \quad (3.1.7.9a)$$

$$Q_R = A_D R_{\max} \quad (3.1.7.9b)$$

$$M_D \equiv A_D \left(\frac{K}{b} \right)_D \quad (3.1.7.9c)$$

$$x \equiv 2 \frac{\hat{\psi} - \psi}{\hat{\psi}} \quad (3.1.7.9d)$$

$$\hat{\psi} = -\frac{Q_R}{M_D} \quad (3.1.7.9e)$$

and

h hydraulic head

z_c elevation of combination boundary condition

ψ pressure head

Q_c volumetric source or sink from combined effects of recharge and drainage

R_{\max} maximum localized recharge (input)

A_D area available for recharge and drainage (geometric area)

FACT CODE MANUAL

$(K/b)_D$ leakance coefficient (input)

Equation (3.1.7.9) is our Cauchy (type 3) boundary condition that is C^1 continuous from $\psi = \frac{3}{2}\hat{\psi}$ to $\psi = \frac{1}{2}\hat{\psi}$ (which corresponds to $x = -1$ to $x = 1$). It is a quadratic equation in x that satisfies the constraints

$$Q_c = Q_R \quad \text{and} \quad \frac{dQ_c}{dx} = 0 \quad \text{at } x = -1 \quad (3.1.7.10a)$$

$$Q_c = -\frac{M_D \hat{\psi}}{2} = \frac{Q_R}{2} \quad \text{and} \quad \frac{dQ_c}{dx} = -\frac{Q_R}{2} \quad \text{at } x = 1 \quad (3.1.7.10b)$$

Note that in general the four constraints expressed above would result in a cubic equation in x . The quadratic results from our choice of locations for the two transition points.

Over the entire range of pressure head the Picard and Newton-Raphson terms are given as

$$Q_c = \begin{cases} Q_R & \text{for } \psi \leq \frac{3}{2}\hat{\psi} \\ \frac{Q_R}{8} [7 - 2x - x^2] & \text{for } \frac{3}{2}\hat{\psi} < \psi < \frac{1}{2}\hat{\psi} \\ -M_D \psi & \text{for } \frac{1}{2}\hat{\psi} \leq \psi \end{cases} \quad (3.1.7.11)$$

for the RHS global load vector and

$$\frac{dQ_c}{d\psi} = \frac{dQ_c}{dh} = \begin{cases} 0 & \text{for } \psi \leq \frac{3}{2}\hat{\psi} \\ \frac{Q_R}{2\hat{\psi}} (1+x) & \text{for } \frac{3}{2}\hat{\psi} < \psi < \frac{1}{2}\hat{\psi} \\ -M_D & \text{for } \frac{1}{2}\hat{\psi} \leq \psi \end{cases} \quad (3.1.7.12)$$

for the LHS global system matrix.

Equation (3.1.7.11) represents a two-parameter model requiring the specification of the maximum localized recharge rate and the surface leakance coefficient. The level of ponding that occurs along a seepage face can be adjusted by varying the magnitude of the surface leakance coefficient. This leakance coefficient represents how conductive the flow of water normal to the surface is. It is a measure only of the ground surface's skin resistance (not the aquifer unit itself) and generally the head solution from FACT is not overly sensitive to its magnitude. Typically Eq. (3.1.7.11) is applied to every node over the entire top surface of a flow model. The locations where seepelines result are automatically established during the iterative solution of the non-linear flow and boundary conditions. Since average recharge over the entire region and total drainage are very common quantities of interest, they are computed in a post-processing fashion and written to output files.

3.1.8 Numerical Solution of Flow Equation

For stability considerations the flow equation, Eq. (3.1.1.7), will be time differenced using backward Euler (i.e., fully implicit) differencing to yield the new (n+1)th time solution. Equation (3.1.1.7) becomes

$$G_i^{n+1} = \frac{B_{ij}^{n+1}}{\Delta t_n} \left(h_j^{n+1} - h_j^n \right) + A_{ij}^{n+1} h_j^{n+1} - F_i^{n+1} \quad (3.1.8.1)$$

where G_i^{n+1} is the residual vector at the new time level.

Note that superscripts denote time levels and will be omitted for the new time level in the derivations to follow. Since matrices **B** and **A**, as well as vector **F**, are in general dependent upon hydraulic heads, Eq. (3.1.8.1) is a system of non-linear algebraic equations that must be solved by use of an iterative strategy (sometimes referred to as our outer iteration loop). Note that under certain limiting conditions (such as a confined aquifer with simple boundary conditions) Eq. (3.1.8.1) reduces to a linear set of algebraic equations whose solution is obtained during the first iteration pass.

Two basic options for solving Eq. (3.1.8.1) are currently available in FACT: (1) a Picard iteration scheme and (2) a full (including a modified option as well) Newton-Raphson (N-R) technique. The optimum choice of which iteration strategy to use is problem dependent. However, a general rule of thumb is to use the more expensive per iteration N-R technique for the more complex and difficult to converge problems. Such problems naturally arise when the porous media becomes highly heterogeneous and/or significant recharge through the vadose zone is occurring. Abrupt changes in the relative permeability or boundary conditions, which occur when the soil characteristic curves have steep gradients or the leakage coefficient is large, may result in slow convergence. Convergence difficulties may also occur when the residual water saturation is near zero. The rate of convergence for a complex flow problem is very sensitive to the initial conditions. For these types of problems making use of the upstream weighting option for relative permeability generally improves convergence.

The following is a general derivation of our iteration strategy employing a N-R formulation. This formulation results in an asymmetrical global coefficient matrix due to the asymmetrical contributions coming from certain terms. The Picard scheme results when these terms (as indicated) are omitted, thus producing a symmetrical global coefficient matrix. It is these terms that make each iteration of the N-R technique more expensive than that of the Picard scheme.

Application of the N-R procedure to Eq. (3.1.8.1) yields

$$G_i^{m+1} \equiv G_i^m + \left(\frac{\partial G_i}{\partial h_k} \right)^m \Delta h_k^{m+1} = 0 \quad (3.1.8.2)$$

FACT CODE MANUAL

where superscripts now denote iteration levels and Δh_k^{m+1} is a displacement vector, defined as

$$\Delta h_k^{m+1} = h_k^{m+1} - h_k^m \quad (3.1.8.3)$$

The leading term of the Taylor series expansion in Eq. (3.1.8.2) is

$$G_i^m = \frac{B_{ij}^m}{\Delta t_n} (h_j^m - h_j^n) + A_{ij}^m h_j^m - F_i^m \quad (3.1.8.4)$$

and the Jacobian is given by

$$\left(\frac{\partial G_i}{\partial h_k} \right)^m = \frac{B_{ij}^m \delta_{jk}}{\Delta t_n} + \left(\frac{\partial B_{ij}}{\partial h_k} \right)^m \frac{h_j^m - h_j^n}{\Delta t_n} + A_{ij}^m \delta_{jk} + \left(\frac{\partial A_{ij}}{\partial h_k} \right)^m h_j^m - \left(\frac{\partial F_i}{\partial h_k} \right)^m \quad (3.1.8.5)$$

Substituting Eqs. (3.1.8.5) and (3.1.8.1) into (3.1.8.2) yields the following linear algebra problem at each iteration

$$S_{ik}^m x_k = y_i^m \quad (3.1.8.6a)$$

where the current iterate of change in hydraulic head at the new time step is defined as

$$x_k \equiv \Delta h_k^{m+1} = h_k^{m+1} - h_k^m \quad (3.1.8.6b)$$

and S_{ik}^m is a symmetric diagonally dominant matrix for the Picard scheme and an asymmetric matrix (whose diagonal dominance may have diminished) for the full N-R technique defined as

$$S_{ik}^m = \begin{cases} \frac{B_{ik}^m}{\Delta t_n} + \left(\frac{\partial B_{ij}}{\partial h_k} \right)^m \frac{h_j^m - h_j^n}{\Delta t_n} + A_{ik}^m + \left(\frac{\partial A_{ij}}{\partial h_k} \right)^m h_j^m - \left(\frac{\partial F_i}{\partial h_k} \right)^m & (N-R) \\ \frac{B_{ik}^m}{\Delta t_n} + A_{ik}^m - \left(\frac{\partial F_i}{\partial h_k} \right)^m & (\text{Picard}) \end{cases} \quad (3.1.8.6c)$$

and y_i^m is the RHS vector

$$y_i^m = -\frac{B_{ij}^m}{\Delta t_n} (h_j^m - h_j^n) - A_{ij}^m h_j^m + F_i^m \quad (3.1.8.6d)$$

Note that for the Picard scheme the general forcing function, F , is put in a linearized form as well.

The derivative of the storage matrix, B_{ij} , with respect to hydraulic head is computed as

$$\left(\frac{\partial B_{ij}}{\partial h_k} \right)^m = \frac{\partial}{\partial h_k} \left\langle \phi_e \frac{dS_w}{d\psi} + S_w S_s \right\rangle M_{ij}^L \quad (3.1.8.7)$$

The coefficients to the mass matrix in Eq. (3.1.8.7) are evaluated as

$$\frac{\partial}{\partial h_k} \left\langle \phi_e \frac{dS_w}{d\psi} \right\rangle = \phi_e \sum_{p=1}^8 \varphi_p(0) \left(\frac{d^2 S_w}{d\psi^2} \right)_p \varphi_k(\xi_p) = \frac{\phi_e}{8} \left(\frac{d^2 S_w}{d\psi^2} \right)_k \quad (3.1.8.7a)$$

$$\frac{\partial}{\partial h_k} \langle S_w S_s \rangle = S_s \sum_{p=1}^8 \varphi_p(0) \left(\frac{dS_w}{d\psi} \right)_p \varphi_k(\xi_p) = \frac{S_s}{8} \left(\frac{dS_w}{d\psi} \right)_k \quad (3.1.8.7b)$$

The derivative of the storage matrix becomes

$$\left(\frac{\partial B_{ij}}{\partial h_k} \right)^m = \frac{1}{8} \left\{ \phi_e \left(\frac{d^2 S_w}{d\psi^2} \right)_k^m + S_s \left(\frac{dS_w}{d\psi} \right)_k^m \right\} M_{ij}^L \quad (3.1.8.8)$$

and the contribution to the Jacobian matrix is

$$\left(\frac{\partial B_{ij}}{\partial h_k} \right)^m \frac{h_j^m - h_j^n}{\Delta t_n} = \frac{1}{8} \left\{ \phi_e \left(\frac{d^2 S_w}{d\psi^2} \right)_k^m + S_s \left(\frac{dS_w}{d\psi} \right)_k^m \right\} M_{ij}^L \frac{h_j^m - h_j^n}{\Delta t_n} \quad (3.1.8.9)$$

The lumped mass matrix, M_{ij}^L is computed using Eq. (3.1.5.27) for the influence coefficient method or Eq. (3.1.5.28) for two-point Gauss Legendre quadrature.

The derivative of the seepage matrix, A_{ij} , with respect to hydraulic head is computed as

$$\left(\frac{\partial A_{ij}}{\partial h_k} \right)^m = \int_{-1}^{+1} \int_{-1}^{+1} \int_{-1}^{+1} \left(\mathbf{J}^{-1} \nabla_{\xi} \varphi_i \right)^T \cdot \left(\frac{\partial k_{rw} \mathbf{K}}{\partial h_k} \right)^m \left(\mathbf{J}^{-1} \nabla_{\xi} \varphi_j \right) \mathbf{J} d\xi d\eta d\zeta \quad (3.1.8.10)$$

The derivative of $k_{rw} \mathbf{K}$ with respect to hydraulic head with no upstream weighting of the relative permeability is

$$\left(\frac{\partial k_{rw} \mathbf{K}}{\partial h_k} \right)^m = \frac{\partial}{\partial h_k} \langle k_{rw} \rangle \begin{bmatrix} K_{xx} & K_{xy} & K_{xz} \\ K_{xy} & K_{yy} & K_{yz} \\ K_{xz} & K_{yz} & K_{zz} \end{bmatrix} \quad (3.1.8.11a)$$

where

$$\frac{\partial}{\partial h_k} \langle k_{rw} \rangle = \frac{1}{8} \sum_{p=1}^8 \left(\frac{dk_{rw}}{dS_w} \right)_p \left(\frac{dS_w}{d\psi} \right)_p \phi_k(\xi_p) = \frac{1}{8} \left(\frac{dk_{rw}}{dS_w} \right)_k \left(\frac{dS_w}{d\psi} \right)_k \quad (3.1.8.11b)$$

FACT has an upstream weighting of relative permeabilities option which enhances convergence of the Picard and N-R iterations. The upstream weighting affects the centroidal approximations, $\langle k_{rw}^x \rangle K_{xx}$, $\langle k_{rw}^y \rangle K_{yy}$, $\langle k_{rw}^z \rangle K_{zz}$ in seepage matrix **A**. The derivative of $k_{rw} \mathbf{K}$ with respect to hydraulic head with upstream weighting of the relative permeability is

$$\left(\frac{\partial k_{rw} \mathbf{K}}{\partial h_k} \right)^m = \begin{bmatrix} \frac{\partial}{\partial h_k} \langle k_{rw}^x \rangle K_{xx} & \frac{\partial}{\partial h_k} \langle k_{rw} \rangle K_{xy} & \frac{\partial}{\partial h_k} \langle k_{rw} \rangle K_{xz} \\ \frac{\partial}{\partial h_k} \langle k_{rw} \rangle K_{xy} & \frac{\partial}{\partial h_k} \langle k_{rw}^y \rangle K_{yy} & \frac{\partial}{\partial h_k} \langle k_{rw} \rangle K_{yz} \\ \frac{\partial}{\partial h_k} \langle k_{rw} \rangle K_{xz} & \frac{\partial}{\partial h_k} \langle k_{rw} \rangle K_{yz} & \frac{\partial}{\partial h_k} \langle k_{rw}^z \rangle K_{zz} \end{bmatrix} \quad (3.1.8.12a)$$

and

$$\frac{\partial}{\partial h_k} \langle k_{rw}^d \rangle = \sum_{p=1}^8 w_p^d \left(\frac{dk_{rw}}{dS_w} \right)_p \left(\frac{dS_w}{d\psi} \right)_p \phi_k(\xi_p) = w_k^d \left(\frac{dk_{rw}}{dS_w} \right)_k \left(\frac{dS_w}{d\psi} \right)_k \quad (3.1.8.12b)$$

where

d x,y or z direction

w_p^x, w_p^y, w_p^z ... upstream weighting factors in the x, y and z direction, respectively

In order to compute w_p^x , the average hydraulic head for face 1 (the region bound by nodes 1,4,5,8) and face 2 (the region bound by nodes 2,3,6,7) are computed

$$h_{1458} = (h_1 + h_4 + h_5 + h_8) / 4 \quad (3.1.8.13a)$$

$$h_{2367} = (h_2 + h_3 + h_6 + h_7) / 4 \quad (3.1.8.13b)$$

where h_p is the hydraulic head at node p. The weighting factor w_p^x is defined as

$$w_p^x = \begin{cases} (1-\mu)/8 & \text{if } h_{1458} < h_{2367} \\ (1+\mu)/8 & \text{if } h_{1458} \geq h_{2367} \end{cases} \quad \text{for } p = 1,4,5,8 \quad (3.1.8.14a)$$

$$w_p^x = \begin{cases} (1+\mu)/8 & \text{if } h_{1458} < h_{2367} \\ (1-\mu)/8 & \text{if } h_{1458} \geq h_{2367} \end{cases} \quad \text{for } p = 2,3,6,7 \quad (3.1.8.14b)$$

where $0 \leq \mu \leq 1$ is a user defined weighting parameter. The weighting factors w_p^y and w_p^z are constructed in a similar manner. Upstream weighting is not used when $\mu = 0$ and full upstream weighting is used when $\mu = 1$.

Finally, the contribution to the Jacobian matrix by $(\partial A_{ij}/\partial h_k)^m h_j^m$ is

$$\begin{aligned} \left(\frac{\partial A_{ij}}{\partial h_k} \right)^m h_j^m = & \left\{ \frac{mH}{2\ell} w_k^x K_{xx} A_{ij}^{xx} + \frac{\ell H}{2m} w_k^y K_{yy} A_{ij}^{yy} + \frac{\ell m}{2H} w_k^z K_{zz} A_{ij}^{zz} \right. \\ & \left. + \frac{H}{16} K_{xy} A_{ij}^{xy} + \frac{m}{16} K_{xz} A_{ij}^{xz} + \frac{\ell}{16} K_{yz} A_{ij}^{yz} \right\} \left(\frac{dk_{rw}}{dS_w} \right)_k \left(\frac{dS_w}{d\psi} \right)_k h_j^m \end{aligned} \quad (3.1.8.15)$$

based on the influence matrix formulation and

$$\left(\frac{\partial A_{ij}}{\partial h_k} \right)^m h_j^m = \left\{ \sum_{g=1}^8 \left(\mathbf{J}_g^{-1} \nabla_{\xi}^g \phi_i \right)^T \left(\frac{\partial k_{rw} \mathbf{K}}{\partial h_k} \right)^m \left(\mathbf{J}_g^{-1} \nabla_{\xi}^g \phi_j \right) w_g \mathbf{J}_g \right\} h_j^m \quad (3.1.8.16)$$

using two-point Gauss-Legendre quadrature.

The derivative of the RHS load vector, $(\partial F_i/\partial h_k)^m$, is computed for head-dependent vertical line sinks, head-dependent source beds and combination recharge/drain boundary conditions in Sections 3.1.6.2, 3.1.7 and 3.1.7.1, respectively.

Further enhancement in convergence of the N-R method can be achieved through the use of backtracking along the N-R direction. For some flow problems both Picard and N-R iterations fail to converge. If the initial guess is not close to the root of

$$\mathbf{G}^{n+1} = 0 \quad (3.1.8.17)$$

the N-R iteration will wander or enter a cycle. Since the N-R method has rapid local convergence, it is reasonable to require the residual

$$\|\mathbf{G}^m\| = \left(\mathbf{G}^m \right)^T \mathbf{G}^m \quad (3.1.8.18)$$

to decrease for each N-R iteration. After solving equation (3.1.8.2) for $\Delta \mathbf{h}^{m+1}$ the full N-R iteration is given by

$$\mathbf{h}^{m+1} = \mathbf{h}^m + \Delta \mathbf{h}^{m+1} \quad (3.1.8.19)$$

If $\|\mathbf{G}^{m+1}\|^2 < \|\mathbf{G}^m\|^2$ the N-R iteration is accepted and $\Delta \mathbf{h}^{m+2}$ is computed. Otherwise,

we backtrack along the N-R direction $\Delta \mathbf{h}^{m+1}$ until $\|\mathbf{G}_\gamma^{m+1}\|^2 < \|\mathbf{G}^m\|^2$ where

$$\mathbf{h}_\gamma^{m+1} = \mathbf{h}^m + \gamma \Delta \mathbf{h}^{m+1}, \quad 0 < \gamma < 1 \quad (3.1.8.20)$$

and \mathbf{G}_γ^{m+1} is the nonlinear system (3.1.8.1) evaluated at \mathbf{h}_γ^{m+1} . The parameter γ is decreased until the residual is less than the previous iteration residual. Then the backtracking is accepted and $\mathbf{h}^{m+1} = \mathbf{h}_\gamma^{m+1}$. The backtracking strategy in FACT performs at most n backtracks for each iteration with

$$\mathbf{h}_i^{m+1} = \mathbf{h}^m + 2^{-i} \Delta \mathbf{h}^{m+1}, \quad i = 1, \dots, n \quad (3.1.8.21)$$

If $\|\mathbf{G}^{m+1}\|^2 < \|\mathbf{G}^m\|^2$ we accept the N-R iteration and backtracking is not performed.

Otherwise, FACT computes $\mathbf{h}_i^{m+1}, i = 1, \dots, k$ until $\|\mathbf{G}_k^{m+1}\|^2 < \|\mathbf{G}^m\|^2$ and the k^{th} backtrack is accepted and $\mathbf{h}^{m+1} = \mathbf{h}_\gamma^{m+1}$. If

$$\|\mathbf{G}_i^{m+1}\|^2 \geq \|\mathbf{G}^m\|^2, \quad i = 1, \dots, n \quad (3.1.8.22)$$

then the n^{th} backtrack is accepted and $\mathbf{h}^{m+1} = \mathbf{h}_n^{m+1}$. Experience suggests that the full N-R method should be used first. If FACT fails to converge then backtracking should be used with $n \leq 8$.

The above outer iteration scheme (Picard or N-R) is repeated until either: (1) the magnitude of the maximum nodal iterate value is less than a prescribed tolerance criterion, ϵ_{outer} , or (2) the maximum allowable number of iterations is reached, nitmax. The error criteria placed on hydraulic head is given as

$$\max_{i=1, np} |x_i| = \max |h_i^{m+1} - h_i^m| < \epsilon_{\text{outer}} \quad (3.1.8.23)$$

where the error tolerance placed upon the equation solver (sometimes referred to as our inner iteration loop) is computed based on

$$\epsilon_{\text{outer}} = \max \left(10^{-6}, 10^{-4} \epsilon_{\text{htol}} \right) \quad (3.1.8.24)$$

and ϵ_{htol} is an input convergence tolerance for hydraulic head. The maximum number of outer loop iterations is determined by

$$\text{nitmax} = \begin{cases} 1 & \text{for a linear flow problem} \\ 2 \rightarrow 200 & \text{for a non-linear flow problem} \end{cases} \quad (3.1.8.25)$$

Based on type of aquifer/aquitard units and boundary conditions to be analyzed, FACT internally determines if the current flow problem constitutes a linear problem. If so,

FACT sets the maximum number of outer loop iterations to unity and bypasses convergence checking.

3.1.9 Darcy and Phasic Velocity Computation

After convergence of the Picard scheme or Newton-Raphson iteration technique has been achieved, velocity components can be evaluated for output or when a subsequent analysis of a related solute transport problem is required. For transient flow simulations, the velocities may also have to be calculated for many time steps. Thus, it is desirable to use algorithms that permit the velocity computations to be achieved in as cost-effective a manner as possible. For transport calculations we require velocity components at the element centroids; while, for graphical purposes we prefer velocity components at the global node locations. We shall express our Darcy (or phasic) component velocities in formulas that result in a minimum of computational effort, while maintaining consistencies with transport and graphical requirements. The Darcy velocity vector is related to the phasic velocity vector by

$$\mathbf{U} = \theta_m \mathbf{u} \quad (3.1.9.1)$$

The following derivations are based on Darcy velocities. For phasic velocities divide through each equation by the liquid void fraction (i.e., mobile water content).

In FACT there are basically three coordinate systems that must be addressed:

- the local cube (ξ, η, ζ) that is (2 by 2 by 2) in size,
- the element brick (x', y', z') that is (l by m by H) in size where H is the arithmetic average height of the element, and
- the actual distorted element (x, y, z) whose top and bottom faces are allowed to be non-perpendicular to the z axis.

We need a means by which we can convert from one coordinate system to another in terms of velocity vectors, that is, a method to perform coordinate transformations from the local cube to the element brick and then (if necessary) to the actual distorted element. Recall that the Darcy velocity vector can be expressed as

$$\mathbf{U} = -k_{rw} \mathbf{K} \nabla_x h \quad (3.1.9.2a)$$

in global (brick or actual distorted) coordinates and as

$$\mathbf{U}' = -k_{rw} \mathbf{K}_\xi \nabla_\xi h \quad (3.1.9.2b)$$

in local (cube) elemental coordinates (note that the ∇ operator, as well as the conductivity tensor, are subscripted). Knowing the Darcy velocity components with respect to the local coordinate system, global Darcy velocity components can be determined using the following coordinate transformation rule:

$$\mathbf{U} = \mathbf{J}^T \mathbf{U}' \quad (3.1.9.3)$$

FACT CODE MANUAL

where \mathbf{J}^T is the transpose of the coordinate transformation (Jacobian) tensor for either the brick or actual distorted element. Equation (3.1.9.3) can be obtained from the following derivation:

$$\mathbf{U} = -k_{rw} \mathbf{K} \nabla_x h = -k_{rw} \left[\mathbf{J}^T \mathbf{K}_\xi \mathbf{J} \right] \mathbf{J}^{-1} \nabla_\xi h = \mathbf{J}^T \left[-k_{rw} \mathbf{K}_\xi \nabla_\xi h \right] = \mathbf{J}^T \mathbf{U}' \quad (3.1.9.4)$$

where use has been made of identities presented in Sections 3.1.2 and 3.1.5 above.

For a constrained trilinear hexahedron element, the centroidal values of the Darcy velocity components along the global coordinate axes can be computed by

$$\langle \mathbf{U} \rangle = \mathbf{J}^T \langle \mathbf{U}' \rangle = -k_{rw} \mathbf{K} \mathbf{J}^{-1} \sum_{j=1}^8 \nabla_\xi \varphi_j(0) h_j = -k_{rw} \mathbf{K} \mathbf{J}^{-1} \begin{bmatrix} h_\xi \\ h_\eta \\ h_\zeta \end{bmatrix} \quad (3.1.9.5)$$

where $\langle \rangle$ implies evaluation at the elemental centroid. The inverse of the Jacobian and the gradient of the hydraulic head are also evaluated at the element centroid. Substituting expressions for the permeability tensor and the inverse of the Jacobian matrix from Eqs. (3.1.5.11) and (3.1.4.9), respectively, into Eq. (3.1.9.5) yields

$$\begin{aligned} \langle U_x \rangle = & - \left\langle k_{rw}^x K_{xx} \right\rangle \left(\frac{h_\xi}{x_\xi} - \frac{z_\xi h_\zeta}{x_\xi z_\zeta} \right) - \left\langle k_{rw} K_{xy} \right\rangle \left(\frac{h_\eta}{y_\eta} - \frac{z_\eta h_\zeta}{y_\eta z_\zeta} \right) \\ & - \left\langle k_{rw} K_{xz} \right\rangle \frac{h_\zeta}{z_\zeta} \end{aligned} \quad (3.1.9.6a)$$

$$\begin{aligned} \langle U_y \rangle = & - \left\langle k_{rw} K_{yx} \right\rangle \left(\frac{h_\xi}{x_\xi} - \frac{z_\xi h_\zeta}{x_\xi z_\zeta} \right) - \left\langle k_{rw}^y K_{yy} \right\rangle \left(\frac{h_\eta}{y_\eta} - \frac{z_\eta h_\zeta}{y_\eta z_\zeta} \right) \\ & - \left\langle k_{rw} K_{yz} \right\rangle \frac{h_\zeta}{z_\zeta} \end{aligned} \quad (3.1.9.6b)$$

$$\begin{aligned} \langle U_z \rangle = & - \left\langle k_{rw} K_{zx} \right\rangle \left(\frac{h_\xi}{x_\xi} - \frac{z_\xi h_\zeta}{x_\xi z_\zeta} \right) - \left\langle k_{rw} K_{zy} \right\rangle \left(\frac{h_\eta}{y_\eta} - \frac{z_\eta h_\zeta}{y_\eta z_\zeta} \right) \\ & - \left\langle k_{rw}^z K_{zz} \right\rangle \frac{h_\zeta}{z_\zeta} \end{aligned} \quad (3.1.9.6c)$$

For the rectangular prism element, the Jacobian matrix becomes diagonal and Eqs. (3.1.9.6) reduce to a simpler form as

$$\begin{aligned} \langle U_x \rangle = & \left\langle k_{rw}^x K_{xx} \right\rangle \frac{h_{1458} - h_{2367}}{\ell} + \left\langle k_{rw} K_{xy} \right\rangle \frac{h_{1256} - h_{3478}}{m} \\ & + \left\langle k_{rw} K_{xz} \right\rangle \frac{h_{1234} - h_{5678}}{H} \end{aligned} \quad (3.1.9.7a)$$

$$\begin{aligned} \langle U_y \rangle = & \left\langle k_{rw} K_{yx} \right\rangle \frac{h_{1458} - h_{2367}}{\ell} + \left\langle k_{rw}^y K_{yy} \right\rangle \frac{h_{1256} - h_{3478}}{m} \\ & + \left\langle k_{rw} K_{yz} \right\rangle \frac{h_{1234} - h_{5678}}{H} \end{aligned} \quad (3.1.9.7b)$$

$$\begin{aligned} \langle U_z \rangle = & \left\langle k_{rw} K_{zx} \right\rangle \frac{h_{1458} - h_{2367}}{\ell} + \left\langle k_{rw} K_{zy} \right\rangle \frac{h_{1256} - h_{3478}}{m} \\ & + \left\langle k_{rw}^z K_{zz} \right\rangle \frac{h_{1234} - h_{5678}}{H} \end{aligned} \quad (3.1.9.7c)$$

where the notation h_{IJKL} is used to denote the arithmetic average of hydraulic head values at the nodes that belong to a particular face of the rectangular prism (e.g., $h_{IJKL} = (h_I + h_J + h_K + h_L)/4$). In addition, when the principal directions of the saturated hydraulic conductivity tensor in the global coordinate system are aligned with the global coordinate axes in the FACT code, then Eqs. (3.1.9.7) reduce further to

$$\langle U_x \rangle = \left\langle k_{rw}^x K_{xx} \right\rangle \frac{h_{1458} - h_{2367}}{\ell} \quad (3.1.9.8a)$$

$$\langle U_y \rangle = \left\langle k_{rw}^y K_{yy} \right\rangle \frac{h_{1256} - h_{3478}}{m} \quad (3.1.9.8b)$$

$$\langle U_z \rangle = \left\langle k_{rw}^z K_{zz} \right\rangle \frac{h_{1234} - h_{5678}}{H} \quad (3.1.9.8c)$$

Equations (3.1.9.6) and (3.1.9.7) represent the centroidal velocity components relative to the global coordinate system of the constrained hexahedron and rectangular prism element, respectively. Both transport and flow modeling employ the same constrained hexahedron or rectangular prism element representation in the computation of their elemental matrix contributions. Therefore, these velocity components are the appropriate (i.e., consistent formalism) values to be used in any corresponding transport calculations.

For graphical purposes the Darcy (and also phasic) velocity vector at the nodes is more desirable. By having velocity vectors at the nodes coincident with the head and concentration results, a single mesh reflecting the actual outline of the elements is achieved. Overlaying of velocity vectors, streamlines, and head (or concentration) profiles is straightforward. To estimate the velocity vectors at the nodes, the Galerkin approximation is applied to Eq. (3.1.9.2a) with Darcy velocity vectors replaced by phasic velocity vectors using Eq. (3.1.9.1) as

$$\int_{\Omega} \phi_i \theta_m \mathbf{u} d\Omega = - \int_{\Omega} \phi_i k_{rw} \mathbf{K} \nabla_x h d\Omega \quad (3.1.9.9)$$

As usual, Eq. (3.1.9.9) applies to each node within the mesh and is created by the sum of the elemental contributions from every neighboring element to that node (excluding inactive elements). Transforming from global to local coordinates and assuming the phasic velocity vector varies linearly across an element, the left hand side of Eq. (3.1.9.9) at the element level can be evaluated as

$$\begin{aligned} \int_{\Omega_e} \phi_i \theta_m \mathbf{u} d\Omega_e &= \langle \theta_m \rangle_e \sum_{j=1}^8 \left\{ \int_{-1}^{+1} \int_{-1}^{+1} \int_{-1}^{+1} \phi_i \phi_j |\mathbf{J}| d\xi d\eta d\zeta \right\} \mathbf{u}_j \\ &= \langle \theta_m \rangle_e \sum_{j=1}^8 [\mathbf{M}_{ij}]_e \mathbf{u}_j \end{aligned} \quad (3.1.9.10)$$

where \mathbf{M}_{ij} represents the mass matrix given by Eq. (3.1.5.23) and \mathbf{u}_j represents the unknown nodal velocity vector at global node j . If we assume mass lumping for \mathbf{M}_{ij} then Eq. (3.1.9.10) simplifies to

$$\int_{\Omega_e} \phi_i \theta_m \mathbf{u} d\Omega_e = \langle \theta_m \rangle_e [\mathbf{M}_{ii}^L]_e \mathbf{u}_i \quad (3.1.9.11)$$

where

$$[\mathbf{M}_{ii}^L]_e = \begin{cases} \left(\frac{\ell m H}{8} \right)_e & (\text{IM}) \\ \sum_{g=1}^8 \phi_i^g w_g |\mathbf{J}_g| & (\text{GL}) \end{cases} \quad (3.1.9.11a)$$

making the left hand side of Eq. (3.1.9.9) a diagonal matrix and this results in a set of decoupled algebraic equations that are very quick to solve. The lumping approximation is quite adequate for our graphical purposes here. The right hand side of Eq. (3.1.9.9) at the element level becomes

$$\begin{aligned} \int_{\Omega_e} \phi_i k_{rw} \mathbf{K} \nabla_x h d\Omega_e &= \sum_{j=1}^8 \left\{ \int_{-1}^{+1} \int_{-1}^{+1} \int_{-1}^{+1} \phi_i k_{rw} \mathbf{K} \mathbf{J}^{-1} \nabla_{\xi} \phi_j |\mathbf{J}| d\xi d\eta d\zeta \right\} h_j \\ &= \sum_{j=1}^8 [\mathbf{D}_{ij}]_e h_j \end{aligned} \quad (3.1.9.12)$$

Each (i,j) member of the \mathbf{D}_{ij} matrix represents a column vector with x , y and z components as

$$[D_{ij}]_e = \begin{bmatrix} D_{ij}^x \\ D_{ij}^y \\ D_{ij}^z \end{bmatrix}_e \quad (3.1.9.13)$$

where

$$D_{ij}^x = \int_{-1}^{+1} \int_{-1}^{+1} \int_{-1}^{+1} \varphi_i \mathbf{i} \cdot (\mathbf{k}_{rw} \mathbf{K}) \mathbf{J}^{-1} \nabla_{\xi} \varphi_j |\mathbf{J}| d\xi d\eta d\zeta \quad (3.1.9.14a)$$

$$D_{ij}^y = \int_{-1}^{+1} \int_{-1}^{+1} \int_{-1}^{+1} \varphi_i \mathbf{j} \cdot (\mathbf{k}_{rw} \mathbf{K}) \mathbf{J}^{-1} \nabla_{\xi} \varphi_j |\mathbf{J}| d\xi d\eta d\zeta \quad (3.1.9.14b)$$

$$D_{ij}^z = \int_{-1}^{+1} \int_{-1}^{+1} \int_{-1}^{+1} \varphi_i \mathbf{k} \cdot (\mathbf{k}_{rw} \mathbf{K}) \mathbf{J}^{-1} \nabla_{\xi} \varphi_j |\mathbf{J}| d\xi d\eta d\zeta \quad (3.1.9.14c)$$

and \mathbf{i} , \mathbf{j} , and \mathbf{k} are the unit vectors along the x-, y-, and z-coordinates, respectively.

The integrals in Eq. (3.1.9.9) are now replaced by sums over all active elements as

$$\int_{\Omega} \varphi_i \theta_m \mathbf{u} d\Omega \rightarrow \sum_{e=1}^{ne} \int_{\Omega_e} \varphi_i \theta_m \mathbf{u} d\Omega_e = \sum_{e=1}^{ne} \langle \theta_m \rangle_e [M_{ii}^L]_e \mathbf{u}_i \quad (3.1.9.15a)$$

$$-\int_{\Omega} \varphi_i \mathbf{k}_{rw} \mathbf{K} \nabla_x h d\Omega \rightarrow -\sum_{e=1}^{ne} \int_{\Omega_e} \varphi_i \mathbf{k}_{rw} \mathbf{K} \nabla_x h d\Omega_e = -\sum_{e=1}^{ne} \sum_{j=1}^8 [D_{ij}]_e h_j \quad (3.1.9.15b)$$

The summations in Eqs. (3.1.9.15) are stored for each global node i which is a member of element e . More specifically, we solve for the nodal phasic velocity vector as

$$\mathbf{u}_i = \frac{-\sum_{e=1}^{ne} \sum_{j=1}^8 [D_{ij}]_e h_j}{\sum_{e=1}^{ne} \langle \theta_m \rangle_e [M_{ii}^L]_e} \quad i \in e \quad (3.1.9.16)$$

where components of the nodal phasic velocity vector (u, v, w) are

$$u_i = \frac{-\sum_{e=1}^{ne} \sum_{j=1}^8 [D_{ij}^x]_e h_j}{\sum_{e=1}^{ne} \langle \theta_m \rangle_e [M_{ii}^L]_e}, \quad v_i = \frac{-\sum_{e=1}^{ne} \sum_{j=1}^8 [D_{ij}^y]_e h_j}{\sum_{e=1}^{ne} \langle \theta_m \rangle_e [M_{ii}^L]_e} \quad i \in e \quad (3.1.9.17a)$$

$$w_i = \frac{- \sum_{e=1}^{ne} \sum_{j=1}^8 \left[D_{ij}^z \right]_e h_j}{\sum_{e=1}^{ne} \langle \theta_m \rangle_e \left[M_{ii}^L \right]_e} \quad i \in e \quad (3.1.9.17b)$$

3.1.10 Vertical Observation Well Option

In groundwater modeling it is very common to have the need to compare the computed hydraulic (or pressure) head results with some sort of desired target values. The difference between the computed hydraulic head (results from FACT) and their targets values (e.g., monitoring data) is typically referred to as a residual. The magnitude and spatial variation of the computed residuals lend guidance to the user as to how adequate the model represents an actual groundwater system and also provides information useful in improving that model. In FACT, when performing a flow analysis hydraulic head residuals are computed while for a transport analysis concentration residuals are computed.

The source for possible targets varies (monitoring or compliance wells, seepage faces, streams, drainage canals, retention basins, rainfall, etc.). However, the most common and dominant type of target comes in the form of in-situ vertical monitoring (or compliance) well measurements (hydraulic head or contaminant concentrations). Since this type of target (data base) is so commonplace, we have added a special feature to FACT that allows the user to specify a list of observation wells whose target values are used to compute residuals that are written out for viewing.

The areal and vertical locations of these observation wells are not limited to just nodal points. They can be placed anywhere within the model domain and FACT computes a vertically integrated average hydraulic head (or concentration) for each well based on the 3D elemental basis functions and computed nodal head values. These calculations are performed as a post-processing step after FACT completes its calculations at a given time step that corresponds to the user's requested frequency.

The vertical integration performed for an observation well ranges over the well's active screen height (i.e., from the bottom to the top of the well screen). Since many observation wells have their screens extending above the water table, this integration has been limited to only that portion of the screen below the water table. It is assumed that vadose zone contributions to the measured value taken from the well is negligible and that the well measurement reflects an average of the property's variation only over its saturated zones. Also if the user specifies an observation well that extends over or into an inactive element, the integration is limited to only those portions of the screen contained within active elements.

Observation points can also be defined by simply specifying the top and bottom screen elevations equal to the same location. In this case no integration is performed, only the interpolation process is required. Observation points that coincide with node points

(areally and vertically) are also handle; however, it may be more computationally efficient to place them in the observation node category as input if there are a large number of them and group statistics is not required. Note that for observation nodes (specified through user input) only the head or concentration values are computed and written to standard output.

For observation wells, steady-state overall statistical quantities such as the root mean square (rms), are also computed based on the residuals. Since such statistical quantities are often useful in assessing a model's accuracy in relation to a given aquifer unit, the user can define multiple observation well groups. In practice observation wells containing aquifer and aquitard units are generally broken up into separate groups. The overall statistics is performed on each group separately. In many cases the rms within one group (e.g., a single aquifer unit) will be quite different than in another group and can be altered without significantly effecting the other's rms. We typically see this when aquitards significantly decouple neighboring aquifer units.

For each observation well the user must specify its areal location, the elevation of the screen's top and bottom, a steady-state target value, and the group this well will be assigned to. Given this input, FACT automatically performs the following input pre-processing:

- If a well is areally within a specified tolerance of either the x or y grid lines then the well is moved such that it resides on that grid line. However, if the well is outside the areal extent of the mesh, then the computations for this particular well are disregarded.
- If a well is vertically within a specified tolerance of a z grid surface, then the well's active screen elevation (top or bottom) is moved such that it coincides with that grid surface. If the well's screen extends beyond the mesh domain, then its screen boundaries are adjusted such that it is confined to the mesh domain. In addition, the top elevation of the screen is not allowed to exceed the water table (if one exists).
- Only the active elements spanned by the active portion of the well screen are computed, stored, and written out to standard output.

The above pre-processing sequence is performed sequentially on each user-specified observation well. For steady-state simulations: (1) the observation well statistics file is written and (2) individual observation well residuals and target values are written to Tecplot™ zones within each observation well group. For transient simulations, the simulation time and computed screen-average values are written to Tecplot™ zones within each observation well group. Only those wells contained within active elements contribute to each group's overall statistics.

For each observation well the actual integration being performed within FACT is based upon the following assumptions. In general, the average value of a fluid property contained within a vertical segment of porous media can be computed from the volume integrals:

$$\bar{\rho} = \frac{\int_{\Omega} \rho d\Omega}{\int_{\Omega} d\Omega} \quad (3.1.10.1)$$

For the observation wells it is assumed that their areal extent is negligible when compared to element spacing and can therefore be approximated as vertical lines with zero areal area. Also the limits of integration are confined to only the saturated zones (i.e., excludes the vadose zone where water saturation is less than unity). Imposing these restrictions/assumptions on Eq. (3.1.10.1) results in the simpler expression

$$\bar{\rho} = \frac{\int_{z_{\text{lower}}}^{z_{\text{upper}}} \rho dz}{\int_{z_{\text{lower}}}^{z_{\text{upper}}} dz} \quad (3.1.10.2)$$

where the spatial variation of the fluid property over the vertical extent is based on the same basis functions employed in the Galerkin procedures and can be expressed as

$$\rho = \sum_i \varphi_i(x_{\beta}, y_{\beta}, z) p_i \quad (3.1.10.3)$$

and

z_{upper} upper elevation of well screen (not to exceed water table or domain)

z_{lower} lower elevation of well screen (limited to bottom elevation of domain)

ρ computed fluid property (head or concentration) within domain

$\bar{\rho}$ average fluid property (head or concentration) over well screen

$\varphi_i(x_{\beta}, y_{\beta}, z)$... basis function evaluated at the areal location of the well

(x_{β}, y_{β}) areal location specified for given observation well

The actual integration is performed over each active element the well spans and then each elemental contribution is summed resulting in the computed average property value for the well. Given the steady-state target value, a residual for each well is computed by

$$e_k^g = \begin{cases} \bar{h}_k^g - h_k^g & \text{flow analysis} \\ \bar{c}_k^g - c_k^g & \text{transport analysis} \end{cases} \quad 1 \leq k \leq n_g \quad (3.1.10.4)$$

where

e_k^g computed residual for k'th observation well of g'th well group

\bar{x}_k^g computed screen average value ($x = h$ or c) for k 'th observation well of g 'th well group

x_k^g target value ($x = h$ or c) for k 'th observation well of g 'th well group

For a steady-state simulation, several statistical parameters are computed for each well group based on the above computed residual values. For each well group the following parameters are computed by

- Root-mean-square (rms) error: $\sqrt{\frac{1}{n_g} \sum_k (e_k^g)^2}$

- Average error: $\frac{1}{n_g} \sum_k e_k^g$

- Average absolute error: $\frac{1}{n_g} \sum_k |e_k^g|$

- Maximum error: $\max_{1 \leq k \leq n_g} |e_k^g|$

In addition, an overall (all groups included) rms is computed by

- Overall root-mean-square error: $\sqrt{\frac{1}{\sum_g n_g} \sum_g n_g \text{rms}_g^2}$

3.2 Numerical Techniques for Variably Saturated Solute Transport

Numerical approximations of the solute transport equation (for a binary system) are performed in a similar manner to those of the groundwater flow equations. However, special consideration must be given to the numerical solution of this partial differential equation (PDE) when the first-order terms become significant (i.e., when the problem of interest is advection-dominated). It is well documented that numerical solutions to this equation are characterized by oscillations when the advection (convection) term is dominant. As a means of alleviating this numerical difficulty at the cost of smearing the solution profile, the traditional numerically symmetric techniques are modified to account for the fact that the advective process is inherently directional and one-sided in nature. One such modification known as upstream weighting, is well known when applied to finite difference schemes and has been extended to Galerkin-like finite element formulations by numerous authors (e.g., Huyakorn (1977, 1979) - Upstream-weighted residual method, Heinrich and Zienkiewicz (1977) - Petrov-Galerkin method, and Hughes and Brooks (1979) - Quadrature upwind method). Shapiro and Pinder (1979) applied a similar methodology to the finite element orthogonal collocation method through the use of an asymmetric basis function. Pinder and Shapiro (1981) also investigated the propagation characteristics of several of these modified schemes employing Fourier series

FACT CODE MANUAL

analysis. The Fourier series analysis provides quantitative insight into the role each upstream weighting method plays in the solution of this type of PDE.

Regardless of which numerical scheme that is chosen, the issue as to how to address the problem of excessive oscillations remains. There are basically two philosophies for solving the problem of excessive oscillations in the solution. Gresho and Lee (1979) argue that the oscillations tell the analyst that the model is somehow inadequate. In some important region the mesh is not refined enough, the boundary conditions are inappropriate, or the problem is simply too hard due to the parameter choices. If one employs an upwinding scheme, then both the solution and the physics are smoothed, and isolating the specific cause becomes difficult. They also point out that the traditional limitation on cell Peclet number is really a limitation on the product of the cell Peclet number times concentration gradient of the solution, since the cell Peclet number limit can be significantly exceeded without disastrous consequences provided the solution is not steep at the same location. They further point out that the mass matrix should not be lumped because that causes excessive phase errors (phase lag) and may further smooth the solution in time more than desired.

In contrast, Brooks and Hughes (1982) argue that central-difference (typical Bubnov-Galerkin formulations) methods provide under-diffusion (under-dispersion) while upwind methods provide over-diffusion, and the optimal method is one that combines the two ideas to provide just the right amount of diffusion to dampen the oscillations but not to change the solution (similar comments can be applied to finite difference and volume methods as well). They prefer to establish mesh refinement based upon other means, and not to depend on a "wiggle signal" to identify them.

The approach currently taken in FACT is to allow the user the option of specifying what level of upstream weighting is appropriate. A Petrov-Galerkin scheme is used where the magnitude of these weighting factors are user inputted or automatic weighting based upon optimum choices of these weighting factors at the element level. The optimal choice of weighting parameter is optimized for Courant number less than one. For sufficiently low flow rates no asymmetrical (biasing) weighting (the Bubnov-Galerkin formulation) is used. The current technique works quite well for many transport problems of interest in groundwater systems and is reasonably efficient in terms of overall computational effort. However, the user has the burden of determining what constituents an acceptable solution when faced with oscillatory behavior.

3.2.1 Upstream-Weighted Residual Formulation

To overcome/minimize the above mentioned (potential) numerical oscillations, FACT utilizes a simplified form of an upstream-weighted residual Petrov-Galerkin finite element method. In this technique, the weighted residual integral equations are obtained using asymmetric (upstream) weighting (test) functions (Pepper and Stephenson, 1995) to weight certain terms of the transport equation, and the standard basis (trial) functions to weight the remaining terms. The standard (symmetrical) basis functions are employed for approximating the dependent variable over each finite element. The choice as to which

terms in the PDE are to be upstream-weighted results in three basic variants: (1) all terms in the transport equation, (2) only spatial derivative terms (i.e., the total flux terms), and (3) only the first spatial derivative terms (i.e., the advective flux terms).

In FACT the third variant is chosen. Investigations by Pinder and Shapiro (1981) (error analyses) suggest that the third approach out performs the first approach. When the asymmetric weighting functions chosen are applied to the dispersive terms (as in the second variant), to obtain satisfactory solutions it was necessary to evaluate the multi-dimensional weighting functions and their derivatives setting certain weighting factors to zero (i.e., those factors in the transverse directions; see Huyakorn, P.S. and G.R. Pinder, 1983, pp. 208). It can be shown that by setting these weighting factors to zero is equivalent to making the original choice of the third variant. Since the second variant must ultimately be reduced to the more direct third variant to achieve satisfactory solutions, we shall limit ourselves to the third variant and describe its derivation below.

Equation (2.2.28) is solved by the upstream-weighted residual finite element method. In this procedure, the solute concentration function is approximated as a finite linear combination of symmetric basis (trial) functions of the form

$$c(\mathbf{x}, t) = \sum_{J=1}^{np} \varphi_J(\mathbf{x}) c_J(t) \quad (3.2.1.1)$$

where $\varphi_J(\mathbf{x})$ and $c_J(t)$ are the basis functions and the nodal values of solute concentration at time t , respectively, np is the number of nodes in the finite element network. Note that the basis functions supply local support only (i.e., the basis function for any given node is non-zero only over those neighboring elements in contact with that node). The weighted residual integral equations are obtained by choosing weighting functions that are asymmetrical with respect to flow direction (i.e., upstream weighted), $\psi_I(\mathbf{x}, \mathbf{U})$, for the advective flux terms and symmetrical (i.e., standard trial functions), $\varphi_I(\mathbf{x})$, for the remaining terms.

Rearranging and applying the upstream-weighted residual criterion to Eq. (2.2.28) yields

$$\begin{aligned} \int_{\Omega} \varphi_I \left\{ \theta_m R \frac{\partial c}{\partial t} + \theta_m (R \lambda_r + \lambda_m) c + q(c - c^*) - \nabla \cdot (\mathbf{D} \nabla c) \right\} d\Omega \\ + \int_{\Omega} \psi_I \{ \mathbf{U} \cdot \nabla c \} d\Omega = 0 \quad \text{for } I = 1, 2, \dots, np \end{aligned} \quad (3.2.1.2)$$

Since we shall choose C^0 continuous basis and weighting functions, φ_I and ψ_I , the dispersion integral is evaluated by applying the divergence theorem (actually, Green's first identity, the multidimensional equivalent of integration by parts) to obtain

$$\begin{aligned}
\int_{\Omega} \phi_I \nabla \cdot (\mathbf{D} \nabla c) d\Omega &= \int_{\Omega} \nabla \cdot (\phi_I \mathbf{D} \nabla c) d\Omega - \int_{\Omega} \nabla \phi_I \cdot (\mathbf{D} \nabla c) d\Omega \\
&= \int_{\sigma} \phi_I \mathbf{n} \cdot (\mathbf{D} \nabla c) d\sigma - \int_{\Omega} \nabla \phi_I \cdot (\mathbf{D} \nabla c) d\Omega \quad (3.2.1.3) \\
&= - \int_{\sigma} \phi_I (\mathbf{n} \cdot \mathbf{j}_a) d\sigma - \int_{\Omega} \nabla \phi_I \cdot (\mathbf{D} \nabla c) d\Omega
\end{aligned}$$

where Ω is the solution domain with boundary σ , and the dispersive flux is $\mathbf{j}_a = -\mathbf{D} \nabla c$.

Substituting Eqs. (3.2.1.1) and (3.2.1.3) into (3.2.1.2) gives the expression

$$\begin{aligned}
&\sum_{J=1}^{np} \left\{ \int_{\Omega} (\theta_m R) \phi_I \phi_J d\Omega \right\} \frac{dc_J}{dt} + \sum_{J=1}^{np} \left\{ \int_{\Omega} \theta_m (R\lambda_r + \lambda_m) \phi_I \phi_J d\Omega \right\} c_J \\
&+ \sum_{J=1}^{np} \left\{ \int_{\Omega} (q) \phi_I \phi_J d\Omega \right\} c_J + \sum_{J=1}^{np} \left\{ \int_{\Omega} [\nabla \phi_I \cdot \mathbf{D} \nabla \phi_J + \psi_I \mathbf{U} \cdot \nabla \phi_J] d\Omega \right\} c_J \quad (3.2.1.4) \\
&= \int_{\Omega} (qc^*) \phi_I d\Omega + \int_{\sigma} (\mathbf{j}_n) \phi_I d\sigma \quad \text{for } I = 1, 2, \dots, np
\end{aligned}$$

where the normal component of the dispersive flux (incoming is positive by convention) is $\mathbf{j}_n = -\mathbf{n} \cdot \mathbf{j}_a$.

Equation (3.2.1.4) can be written in the more concise form

$$B_{IJ} \frac{dc_J}{dt} + [E_{IJ} + G_{IJ} + P_{IJ}] c_J = F_I, \quad I = 1, 2, \dots, np \quad (3.2.1.5)$$

where

$$B_{IJ} = \int_{\Omega} (\theta_m R) \phi_I \phi_J d\Omega \quad (3.2.1.6a)$$

$$E_{IJ} = \int_{\Omega} [\nabla \phi_I \cdot \mathbf{D} \nabla \phi_J + \psi_I \mathbf{U} \cdot \nabla \phi_J] d\Omega \quad (3.2.1.6b)$$

$$G_{IJ} = \int_{\Omega} \theta_m (R\lambda_r + \lambda_m) \phi_I \phi_J d\Omega \quad (3.2.1.6c)$$

$$P_{IJ} = \int_{\Omega} (q) \phi_I \phi_J d\Omega \quad (3.2.1.6d)$$

$$F_I = \int_{\Omega} (qc^*) \phi_I d\Omega + \int_{\sigma} (\mathbf{j}_n) \phi_I d\sigma \quad (3.2.1.6e)$$

FACT CODE MANUAL

The set of time-dependent linear ordinary differential equations defined by Eq (3.2.1.4) can also be presented in its equivalent vector form as

$$\mathbf{B} \frac{d\mathbf{c}}{dt} + [\mathbf{E} + \mathbf{G} + \mathbf{P}] \mathbf{c} = \mathbf{F} \quad (3.2.1.7)$$

where

- B** storage (capacitance or mass) matrix
- E** advection-dispersion matrix
- G** radioactive and first-order decay matrix
- P** source/sink matrix
- F** RHS forcing function vector
- c** solute (contaminant) concentration vector
- t** time

Equation (3.2.1.7) represents the upstream-weighted residual Petrov-Galerkin approximation to Eq. (2.2.28) and sometimes is referred to as the upstream-weighted residual Weak Statement to Eq. (2.2.28). This equation set applies to the global set of nodes contained within the mesh (including boundary nodes). Most of these global matrices and vectors are generated during an assemblage process whereby the creation of their elemental counter-parts are stuffed into their appropriate locations in the global matrices and vectors. For convenience, those terms containing point sources/sinks and boundary conditions are handled globally (i.e., the elemental assemblage process is bypassed and global quantities are created directly).

The elemental assemblage process mentioned above can be described as a summation of individual elemental matrices (over the number of elements within the mesh; excluding all inactive elements) into a single global matrix where the connectivity matrix of the finite element mesh is employed (i.e., local node numbers within a specific element are associated with specific global node numbers). Assume that the elemental matrices are 8 by 8 matrices whose (64) non-zero members represent those locations where a connection between the global nodes i_g and j_g (i.e., neighboring nodes) exists. For example, the global storage matrix then becomes

$$\mathbf{B} = \sum_{e=1}^{ne} \mathbf{B}^e \quad (3.2.1.8)$$

where

- B** n_p by n_p global storage matrix
- B^e** 8 by 8 elemental storage matrix
- ne** number of elements within finite element mesh

The sign convection for \mathbf{j}_n is the same as for q . That is, \mathbf{j}_n is positive for net inward dispersive transport and negative for net outward dispersive transport. F_i represents all sources, sinks, and other boundary conditions. The global coefficient matrices \mathbf{B}_{IJ} , \mathbf{E}_{IJ} , \mathbf{G}_{IJ} , \mathbf{P}_{IJ} , and \mathbf{F}_I are assembled as a sum of the element matrices for a general eight-noded constrained hexahedron or rectangular prism element. For those sources/sinks that

FACT CODE MANUAL

coincide with node locations, the elemental assemblage process for P_{IJ} and F_I can be omitted and these terms can then be created and inserted directly into the global equation set.

Influence coefficient techniques presented by Huyakorn et al. (1984) and Huyakorn et al. (1986) for linear basis functions along the coordinate axis, can be effectively used for assembling eight-noded rectangular prism elements in order to avoid costly numerical integration of each of the elemental matrices. Two-point Gauss-Legendre quadrature is also available for integration of the elemental matrices. The advection-dispersion coefficients provide the appropriate connectivity for transport between nodes of the element.

For the eight-noded constrained hexahedron or rectangular prism element, internal nodes within the mesh consist of a maximum of 27 nearest nodal neighbors (including itself). The dispersion "influence coefficient matrices" for the eight-noded rectangular prism element are provided by Huyakorn et al. (1986a) (note that the general seepage influence coefficient matrices presented in Huyakorn et al. (1986a) apply to dispersion as well). A consistent mass matrix approach is used for the eight-noded constrained hexahedron to rectangular prism element.

The transport equation is solved on the same geometric grid (and element type) as used for the flow equation. The basis (trial) functions chosen are the same linear functions employed for flow modeling and presented in Section 3.1.2 with the exception of the asymmetric weighting functions applied to the advection matrix. These three-dimensional basis functions are the result of a triple product of one-dimensional linear basis functions (sometimes referred to as 1-D linear Chapeau functions or hat functions) in each of the coordinate directions. Therefore, all the properties presented for the basis functions in Section 3.1.2 apply for the transport formulations.

3.2.2 Eight-noded Constrained Hexahedron Element

For the upstream-weighted residual finite element method, the weighting (test) functions are not in general equivalent to the symmetric basis functions. The chosen 1-D weighting functions represent the sum of a symmetric part (i.e., the original 1-D basis functions) and an asymmetric part which is a function of the dot product of the Darcy velocity and the gradient of the shape function. For linear 1-D isoparametric finite elements, the expressions of these asymmetric weighting functions and the general procedure for obtaining the sign of upstream parameters have been presented elsewhere (Huyakorn, 1977). For completeness, we shall summarize those features of the 1-D weighting functions of interest here and then extend them to our 3-D element.

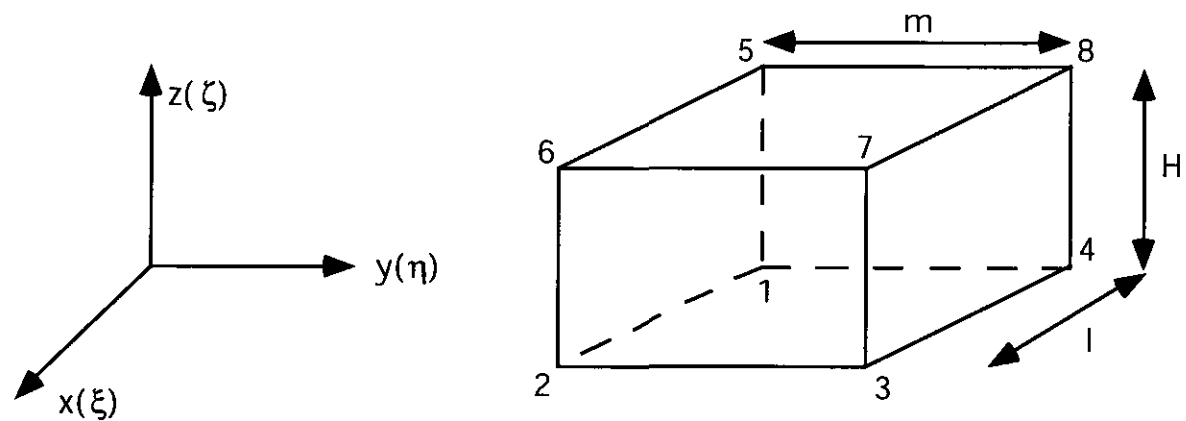


Fig. 3.2.1. Eight-noded Trilinear Hexahedron Element Showing Node Numbering in Local and Global Coordinate Systems.

3.2.3 1-D Asymmetric Weighting Functions

Consider two 1-D coordinate systems, a local isoparametric (ξ) system and a global Cartesian system (x) that are co-linear. The one-dimensional line elements in (x) are mapped onto a standard length element in local coordinates (size $\Delta\xi=2$) as shown in Fig. 3.2.2. Furthermore, let the local element in (ξ) be such that its end points are located at $\xi \pm 1$.

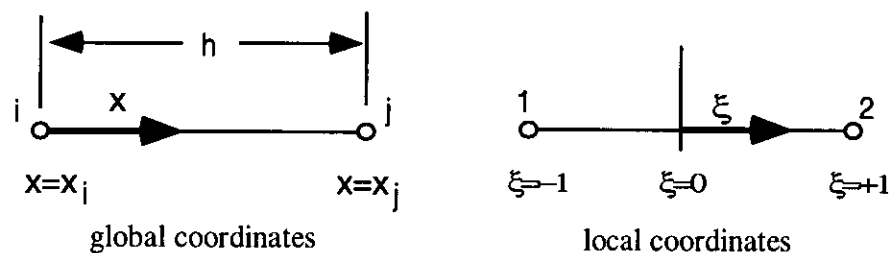


Fig. 3.2.2. Linear Line Element Showing Node Numbering in Local and Global Coordinate Systems.

A Petrov-Galerkin scheme (Brueckner and Heinrich, 1991; Yu and Heinrich, 1986) is used to generate a weighting function ψ_i which is different from the shape function ϕ_i . In 1-D the weighting functions are given by

$$\psi_i(x) = \phi_i(x) + \frac{\alpha \Delta x}{2|U_x|} U_x \frac{d\phi_i}{dx} \quad (3.2.3.1)$$

where

ϕ_i linear basis function

α parameter obtained for each element as a function of the cell Peclet number, $0 \leq \alpha \leq 1$

Δx length of the element

The 1-D asymmetric weighting functions in local coordinates become

FACT CODE MANUAL

$$\psi_i(\xi) = \varphi_i(\xi) + \frac{\alpha \operatorname{sgn}(U_x) \xi_i}{2} = \frac{1}{2} [1 + \xi_i \xi + \alpha \operatorname{sgn}(U_x)] \quad (3.2.3.2)$$

where $\operatorname{sgn}(U_x) = U_x / |U_x|$, $\xi_1 = -1$ and $\xi_2 = +1$.

In order to establish numerical stability with a minimum lost of accuracy (i.e., reduce and perhaps eliminate solution wiggles without significantly smearing out local solution gradients), the value of α must be carefully chosen. An optimum value of α can be estimated based on the analytical solution from steady-state 1-D solute transport through a media with constant properties. Taking the 1-D form of Eq. (2.2.28) and assuming

- steady-state
- no point or line sources/sinks
- constant material properties
- no radioactive decay
- no first-order reactions
- no solid phase absorption

results in

$$D_L \frac{d^2 c}{dx^2} - u_x \frac{dc}{dx} = 0 \quad \text{for } 0 \leq x \leq L \quad (3.2.3.3)$$

where

D_L longitudinal dispersion coefficient, $\alpha_L u_x$

u_x phasic water velocity

and the boundary conditions are

$$c(0) = 0 \quad \text{and} \quad c(L) = 1 \quad (3.2.3.4)$$

Rearranging and integrating both sides of Eq. (3.2.3.3) as

$$\int \frac{d\left(\frac{dc}{dx}\right)}{\left(\frac{dc}{dx}\right)} = \int \frac{u_x}{D_L} dx \quad (3.2.3.5)$$

yields

$$\ln\left(\frac{dc}{dx}\right) = \operatorname{Pe}_x + c_1 \quad \text{where} \quad \operatorname{Pe}_x = \frac{u_x x}{D_L} \quad (3.2.3.6)$$

Taking the exponential of both sides of Eq. (3.2.3.6) gives

$$\frac{dc}{dx} = c_2 e^{Pe_x} \quad (3.2.3.7)$$

Performing the final integrations of Eq. (3.2.3.7) yields

$$c(x) = c_2 \frac{u_x}{D_L} e^{Pe_x} + c_3 \quad (3.2.3.8)$$

Applying the first boundary condition, $c(0) = 0$, to Eq. (3.2.3.8) gives

$$c_3 = -c_2 \frac{u_x}{D_L} \quad (3.2.3.9a)$$

Applying the second boundary condition, $c(L) = 1$, results in

$$c_2 = \frac{D_L}{u_x} \frac{1}{e^{Pe_L} - 1} \quad (3.2.3.9b)$$

Substituting Eqs. (3.2.3.9) into (3.2.3.8) gives the exact solution of this problem as

$$c(x) = \frac{e^{Pe_x} - 1}{e^{Pe_L} - 1} \quad (3.2.3.10)$$

Performing numerical results from an uniform mesh and computing its error using Eq. (3.2.3.10), a parametric study (varying the value of α) can be performed to locate the optimum α value (minimum error for a given local cell Peclet number). It can be shown that for each value of cell Peclet number tested, there exists an optimum value of α where complete accuracy can be achieved. An expression for this optimum α value was theoretically derived by Christie et. al. and can be written in the form

$$\alpha_{opt} = \coth\left(\frac{Pe_{\Delta x}}{2}\right) - \frac{2}{Pe_{\Delta x}} \quad \text{where} \quad Pe_{\Delta x} = \frac{u_x \Delta x}{D_L} \quad (3.2.3.11)$$

where for our purposes the cell Peclet number corresponds to the local elemental value (i.e. local phasic velocity, mesh spacing, and dispersion coefficient). The non-dimensional parameter in Eq. (3.2.3.11) is optimal in the sense that the exact solution is obtained at the nodes when using this value, provided the Peclet number is constant and a uniform mesh size is used. It can be demonstrated that use of Eq. (3.2.3.11) overcomes, to a large extent, the problem of accuracy loss inherent in the upwinding process. Indeed, accurate solutions can be obtained at high values of Peclet number using relatively coarse meshes.

Under transient conditions, Eq. (3.2.3.11) can still be applied. But, excessive dispersion may be experienced. To circumvent this problem, it is desirable to derive an optimal parameter α for the unsteady convective diffusive equation that is a function of cell Peclet and Courant numbers. An upwind finite element scheme using Petrov-Galerkin asymmetric weighting functions (Eq. 3.2.3.1) has been developed for FACT for cell Courant numbers less than one.

FACT CODE MANUAL

To select an optimal upwind parameter, comparisons between analytical and numerical transient one-dimensional concentration profiles are made. The one-dimensional unsteady advection-dispersion equation with a unit step change in concentration is solved

$$D_L \frac{d^2c}{dx^2} - u_x \frac{dc}{dx} = \frac{dc}{dt} \quad (3.2.3.12)$$

The boundary and initial conditions are given by

$$\left. \begin{array}{l} c(0, t) = 1 \quad t \geq 0 \\ c(\infty, t) = 0 \quad t \geq 0 \end{array} \right\} \text{BCs} \quad (3.2.3.13a)$$

$$c(x, 0) = 0 \quad x \geq 0 \quad \text{IC} \quad (3.2.3.13b)$$

The analytic solution to Eq. (3.2.3.12) for these conditions is (Ogata and Banks, 1961)

$$c(x, t) = \frac{1}{2} \left[\operatorname{erfc} \left(\frac{x - u_x t}{2\sqrt{D_L t}} \right) + \exp \left(\frac{u_x x}{D_L} \right) \operatorname{erfc} \left(\frac{x + u_x t}{2\sqrt{D_L t}} \right) \right] \quad (3.2.3.14)$$

Equation (3.2.3.14) may be expressed in dimensionless form as

$$c(Pe_x, t_r) = \frac{1}{2} \left\{ \operatorname{erfc} \left[\left(\frac{Pe_x}{4t_r} \right) (1 - t_r) \right] + \exp(Pe_x) \operatorname{erfc} \left[\left(\frac{Pe_x}{4t_r} \right) (1 + t_r) \right] \right\} \quad (3.2.3.15)$$

where $Pe_x = u_x x / D_L$ and $t_r = u_x t / x$.

The General Particle Tracking Model in 3-dimensions (GPT3) developed by Hydrogeologic, Inc was modified to include the 1-D Petrov-Galerkin weighting functions. GPT3 has the option to perform one-dimensional unsteady transport. The modified GPT3 and FACT numerically solved the same transport equation in one-dimension. Therefore, this version of GPT3 was used as the numerical solver to derive the optimal upwind parameter for Courant number less than one.

The test problem considered is that of one-dimensional, saturated, unsteady contaminant transport in a steady uniform flow field. Values of the basic physical parameters used in the GPT3 simulations are presented in Table 3.2.3.1. The grid chosen consists of 501 rectangular elements uniformly sized (2 ft in length) and stacked along the x-axis. At the column inlet boundary (left face) a first-type Dirichlet boundary condition, $c(0, t) = 1.0$, is applied to the solute concentration at the two nodes. Due to the finite overall length of our mesh, at the outflow boundary (right face) the dispersive flux is set to zero, while the advective flux is calculated as part of the solution. Since this is a 1-D problem, solute concentrations do not exist in the transverse direction (y direction). Therefore, the dispersive fluxes along these two faces (top and bottom) are set to zero. The column is modeled as being fully saturated at a water content of 0.25 (total porosity of 0.25). For each simulation a transient calculation was performed for 200 days utilizing 400 time

steps of 0.50 days. The mesh spacing and time step size were chosen to keep the cell Courant numbers equal to 1. The longitudinal dispersivity was varied to produce cell Peclet numbers from 5 to 100000. Computed column concentration profile for each GPT3 simulation were stored every 10 days.

Table 3.2. Input and Key Computed Parameters for GPT3 Simulations

Physical parameters	Value
Darcy velocity, U_x	1.0 ft/day
Water saturation, S_w	1.0
Total porosity, ϕ	0.25
Longitudinal dispersivity, α_L	0.4 to 0.00002
Retardation coefficient, R	1.0
Retardation coefficient, R	1.0
First-order decay coefficient, λ	0.0 day ⁻¹
Boundary solute concentration, $c(0, t)$	1.0
Grid specifics	
Element length, δx	2.0 ft
Element length, δy	10.0 ft
Number nodes in x-direction	501
Number nodes in y-direction	2
Time steps	
Time duration	200 days
number time-steps	400
time-step size, δt	0.5 day
Key computed parameters	
Phasic velocity, u_x	4.0 ft/day
Dispersion coefficient, D_L	1.6 to 0.00008
Cell Peclet number, Pe_x	5 to 100,000
Cell Courant number, Co_x	1.0

The methodology by Ramakrishnan (1979) was used to derive the optimal upwind parameter for the Petrov-Galerkin finite element scheme in FACT. The results by the finite element method (GPT3) for each run (fixed α , Pe and t) is compared with the analytical solution for the computation of errors and the presence of overshooting.

A simple measure of the error involved in the upwinding procedure is necessary. The analytical solution, Eq. (3.2.3.14), is programmed to give very accurate values for various ranges of the parameters u_x and D_L and the variables x and t . Thus the quantity

$$E(\alpha, t) = \sqrt{\frac{1}{L} \int_0^L \{c(\xi, t) - c_e(\xi, t)\}^2 d\xi} \quad (3.2.3.16)$$

is taken as a measure of the root-mean-square (rms) numerical error. $c(\xi, t)$ is the numerical solution obtained by the finite element method and $c_e(\xi, t)$ is the analytic (exact) solution obtained by Eq. (3.2.3.14). The integrated error, Eq (3.2.3.16), is computed from $t = 0$ to 200 days, every 10 days for each finite element simulation. The optimal choice of upwind parameter for fixed Pe must satisfy the restriction imposed on the integrated error as

$$\max_{0 \leq t \leq 200} E(\alpha_{opt}, t) \leq 1.03 \quad (3.2.3.17)$$

A second measure is used to quantify the extent of overshoot both upstream and downstream of the concentration front. The maximum ratio of the crest and trough values of the magnitude of concentration is limited to lie below a specified value. A limiting ratio of $r_\ell = 1.001$ was used. This is the same value used by Ramakrishnan. Thus, the optimal choice of upwind parameter for fixed Pe must also satisfy the restriction imposed on overshoot as

$$r = c_c/c_t \leq 1.001 \quad 0 \leq t \leq 200 \quad (3.2.3.18)$$

where c_c is the magnitude of concentration at the crest and c_t is the magnitude of the concentration at the trough.

Table 3.3 is a summary of the optimal upwind parameter as a function of Peclet number for Courant number equal to one. The computed overshoot ratio and the integrated error at 200 days is also tabulated.

Table 3.3. Optimal Upwind Parameters as a Function of Peclet Number

Pe	α_{opt}	r	$E(\alpha, 200)$
5	0.000	1.00011	0.03419
7	0.000	1.00898	0.02542
8	0.030	1.00991	0.02492
9	0.060	1.00952	0.02511
10	0.080	1.00991	0.02492
12	0.120	1.00875	0.02550
14	0.140	1.00939	0.02517
16	0.160	1.00911	0.02535
18	0.170	1.00976	0.02502
20	0.180	1.00991	0.02492
24	0.200	1.00938	0.02521
28	0.210	1.00965	0.02504
40	0.230	1.00991	0.02492
50	0.240	1.00991	0.02492
60	0.250	1.00937	0.02521
80	0.255	1.00991	0.02492
100	0.260	1.00991	0.02492

Pe	α_{opt}	r	E($\alpha, 200$)
150	0.267	1.00989	0.02494
200	0.270	1.00991	0.02492
300	0.274	1.00978	0.02497
400	0.275	1.00991	0.02492
500	0.276	1.00991	0.02492
1000	0.278	1.00991	0.02492
2000	0.280	1.00977	0.02500
4000	0.280	1.00979	0.02496
10000	0.280	1.00990	0.02493
100000	0.280	1.00991	0.02492

A maximum likelihood fit of the optimal upwind parameters in Table 3.3 is

$$\alpha_{opt} = \begin{cases} 0 & \text{Pe}_{\Delta x} \leq 7 \\ \frac{a(\text{Pe}_{\Delta x} - 7)}{1 + b(\text{Pe}_{\Delta x} - 7)} & \text{Pe}_{\Delta x} > 7 \end{cases} \quad a = 0.04016, b = a/0.28 \quad (3.2.3.19)$$

where $\text{Pe}_{\Delta x} = u_x \Delta x / D_L$. The shape of Eq. (3.2.3.19) is shown in Fig. 3.2.3.

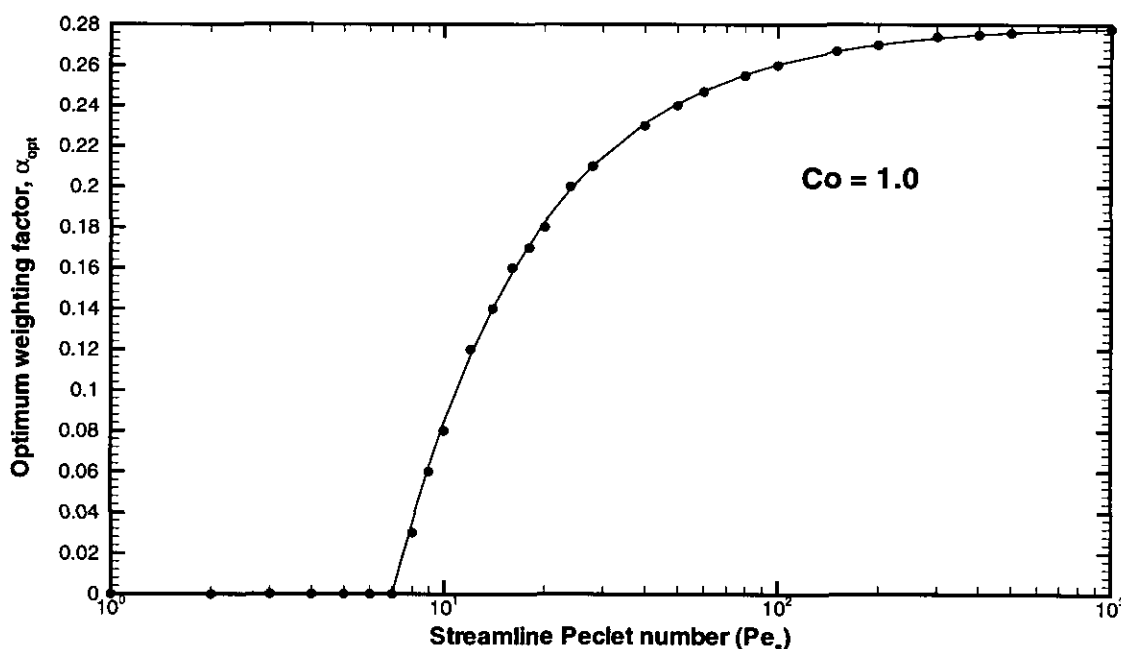


Fig. 3.2.3. Optimal Weighting Factor for the One-Dimensional Unsteady Convection-Diffusion Equation using Petrov-Galerkin Weighting Functions.

3.2.4 3-D Asymmetric Weighting Functions

In Section 3.2.3 we described the 1-D weighting functions. In this section we shall extend these weighting functions to the constrained hexahedron or rectangular prism elements (see Section 3.1.2 for more details). The Petrov-Galerkin scheme can be

FACT CODE MANUAL

formulated in a way similar to the one-dimensional case if trilinear shape functions are used, i.e.,

$$\psi_i = \varphi_i + \frac{\alpha h_e}{2|\mathbf{U}|} \left(\mathbf{U}^T \mathbf{J}^{-1} \nabla_{\xi} \varphi_i \right) \quad (3.2.4.1)$$

where $|\mathbf{U}| = \sqrt{U_x^2 + U_y^2 + U_z^2}$ is the magnitude of the Darcy velocity vector at the element centroid and h_e is a length scale given for a general trilinear hexahedron element as

$$h_e = |h_1| + |h_2| + |h_3| \quad (3.2.4.2)$$

with

$$h_1 = \frac{1}{|\mathbf{U}|} (U_x h_{\xi x} + U_y h_{\xi y} + U_z h_{\xi z}) \quad (3.2.4.3a)$$

$$h_2 = \frac{1}{|\mathbf{U}|} (U_x h_{\eta x} + U_y h_{\eta y} + U_z h_{\eta z}) \quad (3.2.4.3b)$$

$$h_3 = \frac{1}{|\mathbf{U}|} (U_x h_{\zeta x} + U_y h_{\zeta y} + U_z h_{\zeta z}) \quad (3.2.4.3c)$$

and

$$h_{\xi x} = \frac{1}{4} \sum_{i=1}^8 \xi_i x_i, \quad h_{\xi y} = 0, \quad h_{\xi z} = \frac{1}{4} \sum_{i=1}^8 \xi_i z_i \quad (3.2.4.3d)$$

$$h_{\eta x} = 0, \quad h_{\eta y} = \frac{1}{4} \sum_{i=1}^8 \eta_i y_i, \quad h_{\eta z} = \frac{1}{4} \sum_{i=1}^8 \eta_i z_i \quad (3.2.4.3e)$$

$$h_{\zeta x} = 0, \quad h_{\zeta y} = 0, \quad h_{\zeta z} = \frac{1}{4} \sum_{i=1}^8 \zeta_i z_i \quad (3.2.4.3f)$$

The upwind parameter is provided through input or computed for each element as a function of cell streamline Peclet number as

$$\alpha_{\text{opt}} = \begin{cases} 0 & \text{Pe}_{\text{sl}} \leq 7 \\ \frac{a(\text{Pe}_{\text{sl}} - 7)}{1 + b(\text{Pe}_{\text{sl}} - 7)} & \text{Pe}_{\text{sl}} > 7 \end{cases} \quad a = 0.04016, b = a/0.28 \quad (3.2.4.4)$$

where the cell streamline Peclet number is computed as $\text{Pe}_{\text{sl}} = |\mathbf{U}| h_e / D_e$.

The diffusion coefficient D_e is an effective diffusion in the direction of the local Darcy velocity vector and is calculated using the components of \mathbf{D} as

$$D_e = \frac{\mathbf{U}^T \mathbf{D} \mathbf{U}}{|\mathbf{U}|^2} \quad (3.2.4.5)$$

The Petrov-Galerkin weighting functions in Eq. (3.2.4.1) have the effect of introducing a form of anisotropic balancing diffusion into the numerical scheme which acts along the local streamline.

3.2.5 Transport Equation Elemental Matrix Computation

The elemental matrices B_{ij} , E_{ij} , G_{ij} , P_{ij} , and vector F_i resulting from the Bubnov and Petrov-Galerkin approximations to the transport equation can be computed using influence coefficient matrices or Gauss-Legendre quadrature for the rectangular prism or constrained hexahedron element, respectively.

3.2.5.1 The Elemental Storage (Capacitance) Matrix

From Eq. (3.2.1.6a) the expression for the elemental storage coefficient matrix is obtained as

$$B_{ij} = \int_{\Omega_e} \langle \theta_m R \rangle \phi_i \phi_j d\Omega_e \quad (3.2.5.1)$$

where $\langle \theta_m R \rangle$ is the centroidal value of $\theta_m R$, θ_m is the mobile water content, and R is the retardation coefficient. Transforming the storage matrix, B_{ij} , from global to local coordinates yields

$$B_{ij} = \langle \theta_m R \rangle M_{ij} \quad (3.2.5.2)$$

where

$$M_{ij} = \int_{-1}^{+1} \int_{-1}^{+1} \int_{-1}^{+1} \phi_i \phi_j |\mathbf{J}| d\xi d\eta d\zeta \quad (3.2.5.3)$$

is the familiar consistent mass matrix.

One can (row sum) lump the mass matrix \mathbf{M} by adding all elements in each row of \mathbf{M} and putting the sum on the diagonal. This is done in many algorithms (e.g., in fully explicit routines) to take advantage of the computational speedup available (effectively decoupling the equation set). However, based on error analysis it has been shown that mass lumping of Eq. (3.2.5.3) can degrade the solution. Therefore, in general mass lumping of the solute transport equations is not recommended and in our case no off-setting improvement in computational efficiency exist to warrant it. Therefore, the current version of FACT does not give the user a lumping option.

The consistent mass matrix is computed using influence coefficient matrices or two-point Gauss-Legendre quadrature. The elemental mass matrix of the rectangular prism element can be evaluated using influence coefficient matrices as

$$M_{ij} = \frac{\ell m H}{8} m_{ij} \quad (3.2.5.4)$$

where

$$m_{ij} = \frac{1}{27} \left[\begin{array}{c|c} 2\mathbf{a}^{zz} & \mathbf{a}^{zz} \\ \hline \mathbf{a}^{zz} & 2\mathbf{a}^{zz} \end{array} \right] \quad (3.2.5.5)$$

The \mathbf{a}^{zz} matrix has already been computed in Eq. (3.1.5.18c) for the element seepage matrix for flow.

For the constrained hexahedron element, the consistent mass matrix is computed using two-point Gauss-Legendre quadrature as

$$M_{ij} = \sum_{g=1}^8 \phi_i^g \phi_j^g w_g |\mathbf{J}_g| \quad (3.2.5.6)$$

3.2.5.2 The Elemental Advection-Dispersion Matrix

From Eq. (3.2.1.6b) the expression for the elemental advection-dispersion coefficient matrix is obtained as

$$E_{ij} = \int_{\Omega_e} \left\{ \nabla_x \phi_i \cdot \mathbf{D} \nabla_x \phi_j + \psi_i \mathbf{U} \cdot \nabla_x \phi_j \right\} d\Omega_e \quad (3.2.5.7)$$

where the components of the elemental dispersion tensor, \mathbf{D} , and elemental Darcy velocity vector, \mathbf{U} , are specified with respect to the global coordinate system. Transforming the advection-dispersion matrix, E_{ij} , from a global to local coordinate system yields

$$E_{ij} = E_{Dij} + E_{Uij} \quad (3.2.5.8a)$$

where

$$E_{Dij} = \int_{-1}^{+1} \int_{-1}^{+1} \int_{-1}^{+1} \left(\mathbf{J}^{-1} \nabla_{\xi} \phi_i \right)^T \mathbf{D} \left(\mathbf{J}^{-1} \nabla_{\xi} \phi_j \right) \mathbf{J} d\xi d\eta d\zeta \quad (3.2.5.8b)$$

$$E_{Uij} = \int_{-1}^{+1} \int_{-1}^{+1} \int_{-1}^{+1} \psi_i \mathbf{U} \cdot \left(\mathbf{J}^{-1} \nabla_{\xi} \phi_j \right) \mathbf{J} d\xi d\eta d\zeta \quad (3.2.5.8c)$$

Substituting the expression for the 3-D asymmetric weighting functions from Eq. (3.2.4.1) in (3.2.5.8c) yields

$$E_{Uij} = \int_{-1}^{+1} \int_{-1}^{+1} \int_{-1}^{+1} \phi_i \mathbf{U} \cdot \left(\mathbf{J}^{-1} \nabla_{\xi} \phi_j \right) \mathbf{J} |d\xi d\eta d\zeta$$

$$+ \frac{\alpha h_e}{2|\mathbf{U}|} \int_{-1}^{+1} \int_{-1}^{+1} \int_{-1}^{+1} \mathbf{U} \cdot \left(\mathbf{J}^{-1} \nabla_{\xi} \phi_i \right) \mathbf{U} \cdot \left(\mathbf{J}^{-1} \nabla_{\xi} \phi_j \right) \mathbf{J} |d\xi d\eta d\zeta \quad (3.2.5.8d)$$

Equations (3.2.5.8b) and (3.2.5.8d) represent the dispersive and advective components, respectively. Note that \mathbf{E}_D is invariant with respect to coordinate transformations. The overall dispersion tensor (shown here in the global coordinate system) is symmetric

$$\mathbf{D} = \begin{bmatrix} D_{xx} & D_{xy} & D_{xz} \\ D_{yx} & D_{yy} & D_{yz} \\ D_{zx} & D_{zy} & D_{zz} \end{bmatrix} \quad (3.2.5.9)$$

Influence Coefficient Matrices

The dispersive component, Eq. (3.2.5.8b), of the advection-dispersion tensor can be rearranged as

$$E_{Dij} = \int_{-1}^{+1} \int_{-1}^{+1} \int_{-1}^{+1} \left(\nabla_{\xi} \phi_i \right)^T \left(\mathbf{J}^{-1} \right)^T \mathbf{D} \mathbf{J}^{-1} \nabla_{\xi} \phi_j | \mathbf{J} | d\xi d\eta d\zeta \quad (3.2.5.10)$$

Note that the Jacobian transformation matrix, Eq. (3.1.2.4), for the rectangular prism element is symmetric. Therefore, its inverse is also symmetric. Performing the matrix multiplications of the inverse Jacobian matrices and the dispersion tensor within Eq. (3.2.5.10) results in

$$\left(\mathbf{J}^{-1} \right)^T \mathbf{D} \mathbf{J}^{-1} = \begin{bmatrix} \frac{4}{\ell^2} D_{xx} & \frac{4}{\ell m} D_{xy} & \frac{4}{\ell H} D_{xz} \\ \frac{4}{\ell m} D_{xy} & \frac{4}{m^2} D_{yy} & \frac{4}{\ell^2} D_{yz} \\ \frac{4}{\ell H} D_{xz} & \frac{4}{m H} D_{yz} & \frac{4}{H^2} D_{zz} \end{bmatrix} \quad (3.2.5.11)$$

We can evaluate the dispersion matrix terms by expanding the right-hand side of Eq. (3.2.5.10) and using the determinant of the Jacobian. The resulting equation can be written in matrix notation and the integration over the element sub-domain can be evaluated simply by introducing centroidal approximations to the binary dispersion coefficients (D_{xx} , D_{yy} , D_{zz} , D_{xy} , D_{xz} , and D_{yz}). The resulting expression for E_{Dij} is given by

$$E_{Dij} = \frac{mH}{2\ell} \langle D_{xx} \rangle A_{ij}^{xx} + \frac{\ell H}{2m} \langle D_{yy} \rangle A_{ij}^{yy} + \frac{\ell m}{2H} \langle D_{zz} \rangle A_{ij}^{zz}$$

$$+ \frac{H}{2} \langle D_{xy} \rangle A_{ij}^{xy} + \frac{m}{2} \langle D_{xz} \rangle A_{ij}^{xz} + \frac{\ell}{2} \langle D_{yz} \rangle A_{ij}^{yz} \quad (3.2.5.12)$$

where the quantities in angle brackets correspond to centroidal component values of the dispersion tensor within an element; while A_{ij}^{xx} , A_{ij}^{yy} , A_{ij}^{zz} , A_{ij}^{xy} , A_{ij}^{xz} , and A_{ij}^{yz} are

FACT CODE MANUAL

influence coefficient matrices with matrix elements computed in Eqs. (3.1.5.16a) to (3.1.5.16f)

The Darcy velocity vector (shown here in the global coordinate system) is

$$\mathbf{U} = [U_x \quad U_y \quad U_z]^T \quad (3.2.5.13)$$

Performing the matrix multiplication of the Darcy velocity vector, the inverse of the Jacobian and the gradient of the shape function in Eq. (3.2.5.8d) results in

$$\mathbf{U} \cdot \mathbf{J}^{-1} \nabla_{\xi} \phi_i = \frac{2}{\ell} \langle U_x \rangle \phi_{i,\xi} + \frac{2}{m} \langle U_y \rangle \phi_{i,\eta} + \frac{2}{H} \langle U_z \rangle \phi_{i,\zeta} \quad (3.2.5.14)$$

We can evaluate the advection matrix terms by expanding the right-hand side of Eq. (3.2.5.8d) and using the determinant of the Jacobian. The resulting equation can be written in matrix notation and the integration over the element sub-domain can be evaluated simply by introducing centroidal approximations to the Darcy velocity components (U_x , U_y , and U_z). The resulting expression for E_{Uij} is given by

$$E_{Uij} = \left(E_{Uij} \right)^{BG} + \left(E_{Uij} \right)^{PG} \quad (3.2.5.15)$$

where BG represents the Bubnov-Galerkin component and PG the Petrov-Galerkin component of the element advection matrix. The Bubnov-Galerkin term is computed as

$$\left(E_{Uij} \right)^{BG} = \frac{mH}{4} \langle U_x \rangle E_{ij}^{vx} + \frac{\ell H}{4} \langle U_y \rangle E_{ij}^{vy} + \frac{\ell m}{4} \langle U_z \rangle E_{ij}^{vz} \quad (3.2.5.16)$$

where the quantities in angle brackets correspond to centroidal component values of the Darcy velocity vector within an element; while E_{ij}^{vx} , E_{ij}^{vy} and E_{ij}^{vz} are influence coefficient matrices with matrix components computed as

$$E_{ij}^{vx} = \int_{-1}^{+1} \int_{-1}^{+1} \int_{-1}^{+1} \phi_i \phi_{j,\xi} d\xi d\eta d\zeta \quad (3.2.5.17a)$$

$$E_{ij}^{vy} = \int_{-1}^{+1} \int_{-1}^{+1} \int_{-1}^{+1} \phi_i \phi_{j,\eta} d\xi d\eta d\zeta \quad (3.2.5.17b)$$

$$E_{ij}^{vz} = \int_{-1}^{+1} \int_{-1}^{+1} \int_{-1}^{+1} \phi_i \phi_{j,\zeta} d\xi d\eta d\zeta \quad (3.2.5.17c)$$

Substituting the expressions for the derivatives of the basis functions from Eqs. (3.1.2.3) into Eqs. (3.2.5.17) and performing the triple integration for each matrix element yields

$$E^{vx} = \frac{1}{18} \begin{bmatrix} 2e^{vx} & e^{vx} \\ e^{vx} & 2e^{vx} \end{bmatrix} \quad E^{vy} = \frac{1}{18} \begin{bmatrix} 2e^{vy} & e^{vy} \\ e^{vy} & 2e^{vy} \end{bmatrix} \quad (3.2.5.18a,b)$$

$$\mathbf{E}^{vz} = \frac{1}{18} \begin{bmatrix} -\mathbf{e}^{vz} & \mathbf{e}^{vz} \\ -\mathbf{e}^{vz} & \mathbf{e}^{vz} \end{bmatrix} \quad (3.2.5.18c)$$

where

$$\mathbf{e}^{vx} = \begin{bmatrix} -2 & 2 & 1 & -1 \\ -2 & 2 & 1 & -1 \\ -1 & 1 & 2 & -2 \\ -1 & 1 & 2 & -2 \end{bmatrix} \quad \mathbf{e}^{vy} = \begin{bmatrix} -2 & -1 & 1 & 2 \\ -1 & -2 & 2 & 1 \\ -1 & -2 & 2 & 1 \\ -2 & -1 & 1 & 2 \end{bmatrix} \quad (3.2.5.19a,b)$$

$$\mathbf{e}^{vz} = \mathbf{a}^{zz} = \begin{bmatrix} 4 & 2 & 1 & 2 \\ 2 & 4 & 2 & 1 \\ 1 & 2 & 4 & 2 \\ 2 & 1 & 2 & 4 \end{bmatrix} \quad (3.2.5.19c)$$

Note that each influence coefficient matrix is an 8 x 8 matrix partitioned into four (4 x 4) submatrices and that these integrals have been verified by evaluation of each using Mathematica™. As can be seen submatrices of any individual influence matrix differ from one another by a constant multiple. Furthermore, the submatrices are easy to evaluate and require virtually no computational effort.

The Petrov-Galerkin term is computed when the upwind parameter, α , is greater than zero. The Petrov-Galerkin term is computed as

$$\begin{aligned} \left(\mathbf{E}_{U_{ij}} \right)^{PG} = \frac{\alpha h_e}{2|\mathbf{U}|} & \left\{ \frac{mH}{2\ell} \langle U_x^2 \rangle A_{ij}^{xx} + \frac{\ell H}{2m} \langle U_y^2 \rangle A_{ij}^{yy} + \frac{\ell m}{2H} \langle U_z^2 \rangle A_{ij}^{zz} \right. \\ & \left. + \frac{H}{2} \langle U_x U_y \rangle A_{ij}^{xy} + \frac{m}{2} \langle U_x U_z \rangle A_{ij}^{xz} + \frac{\ell}{2} \langle U_y U_z \rangle A_{ij}^{yz} \right\} \end{aligned} \quad (3.2.5.20)$$

where the quantities in angle brackets correspond to centroidal component products of the Darcy velocity vector within an element; while A_{ij}^{xx} , A_{ij}^{yy} , A_{ij}^{zz} , A_{ij}^{xy} , A_{ij}^{xz} , and A_{ij}^{yz} are influence coefficient matrices with matrix elements computed in Eqs. (3.1.5.16a) to (3.1.5.16f)

Two-point Gauss-Legendre Quadrature

For the constrained trilinear hexahedron element, the components of the advection-dispersion elemental matrix is computed as

$$E_{Dij} = \sum_{g=1}^8 \left(\mathbf{J}_g^{-1} \nabla_{\xi}^g \phi_i \right)^T \mathbf{D} \left(\mathbf{J}_g^{-1} \nabla_{\xi}^g \phi_j \right) \mathbf{w}_g |\mathbf{J}_g| \quad (3.2.5.21a)$$

$$\left(E_{Uij}\right)^{BG} = \sum_{g=1}^8 \varphi_i^g \mathbf{U}^T \left(\mathbf{J}_g^{-1} \nabla_{\xi}^g \varphi_j \right) w_g |\mathbf{J}_g| \quad (3.2.5.21b)$$

$$\left(E_{Uij}\right)^{PG} = \frac{\alpha h_e}{2|\mathbf{U}|} \sum_{g=1}^8 \mathbf{U}^T \left(\mathbf{J}_g^{-1} \nabla_{\xi}^g \varphi_i \right) \mathbf{U}^T \left(\mathbf{J}_g^{-1} \nabla_{\xi}^g \varphi_j \right) w_g |\mathbf{J}_g| \quad (3.2.5.21c)$$

where

g number of the Gauss

φ_i^g local shape function evaluated at the g^{th} Gauss point

∇_{ξ}^g local gradient operator evaluated at the g^{th} Gauss point

\mathbf{J}_g^{-1} inverse Jacobian matrix evaluated at the g^{th} Gauss point

$|\mathbf{J}_g|$ determinant of the Jacobian matrix at the g^{th} Gauss point

w_g weight of the g^{th} Gauss point

3.2.5.3 The Elemental Radioactive and First-Order Decay Matrix

From Eq. (3.2.1.6c) the expression for the elemental radioactive and first-order decay storage matrix is obtained as

$$G_{ij} = \int_{\Omega_e} \theta_m (R\lambda_r + \lambda_m) \varphi_i \varphi_j d\Omega_e \quad (3.2.5.22)$$

where θ_m is the mobile water content, R is the retardation coefficient, λ_r is the radioactive decay constant and λ_m is the first-order decay constant. Transforming the element radioactive and first-order decay matrix, G_{ij} , from global to local coordinates yields

$$G_{ij} = \langle \theta_m R \lambda_r \rangle M_{ij} + \langle \theta_m \lambda_m \rangle M_{ij} \quad (3.2.5.23)$$

where $\langle \rangle$ represent centroidal values and

$$M_{ij} = \int_{-1}^{+1} \int_{-1}^{+1} \int_{-1}^{+1} \varphi_i \varphi_j |\mathbf{J}| d\xi d\eta d\zeta \quad (3.2.5.24)$$

is the familiar consistent mass matrix. Note that from Eq. (3.2.5.23), radioactivity and first-order decay are handled as uniformly distributed sinks within each element.

The consistent mass matrix is computed using influence coefficient matrices or two-point Gauss-Legendre quadrature. The elemental mass matrix of the rectangular prism element can be evaluated using influence coefficient matrices as

$$M_{ij} = \frac{\ell m H}{8} m_{ij} \quad (3.2.5.25)$$

where

$$m_{ij} = \frac{1}{27} \left[\begin{array}{c|c} 2\mathbf{a}^{zz} & \mathbf{a}^{zz} \\ \hline \mathbf{a}^{zz} & 2\mathbf{a}^{zz} \end{array} \right] \quad (3.2.5.26)$$

The \mathbf{a}^{zz} matrix has already been computed in Eq. (3.1.5.18c) for the element seepage matrix for flow.

For the constrained hexahedron element, the consistent mass matrix is computed using two-point Gauss-Legendre quadrature as

$$M_{ij} = \sum_{g=1}^8 \varphi_i^g \varphi_j^g w_g \left| \mathbf{J}_g \right| \quad (3.2.5.27)$$

3.2.5.4 The Elemental and Global Source/Sink Matrix

If sources or sinks are present within the domain, the source/sink terms, q , in Eqs. (3.2.1.6) depend on the type of source/sink function assumed. The source/sink term matrix and the RHS forcing function vector, Eqs. (3.2.1.6d,e), can also be evaluated in a simple manner: however, we must decide how the flow rate q is distributed over each element. In the current version of FACT it is assumed that q represents a point source/sink that resides at a global node location (line sources/sinks can also be handled by the appropriate allocation of source strength to each global node in contact with the line source). From the viewpoint of the flow equation, how point (or line) sources/sinks are handled in FACT is discussed in Sections 3.1.5 and 3.1.6. The first term of Eq. (3.2.1.6e) is handled in a very similar way as was presented in Sections 3.1.5 and 3.1.6.

For cases involving point sources and/or sinks, the general expression for q is given by Eq. (3.1.3.21). The point source/sink term matrix, Eq. (3.2.1.6d), can also be evaluated in a simple manner. When Eq. (3.1.5.35) is used, the source/sink term in (3.1.1.6d) at the element level becomes

$$P_{ij} = \int_{\Omega_e} (q) \varphi_i \varphi_j d\Omega_e = \int_{\Omega_e} q_s \delta(\mathbf{x} - \mathbf{x}_\beta) \varphi_i \varphi_j d\Omega_e = Q_\beta^e \varphi_i(\xi_\beta) \varphi_j(\xi_\beta) \quad (3.2.5.28)$$

where Q_β^e is the elemental volumetric flow rate contribution of the source/sink (that is associated with element e) distributed to each node of the element by the weight factor $\varphi_i(\xi_\beta) \varphi_j(\xi_\beta)$. In FACT, the point source (or sink) is limited to node locations only.

The total volumetric flow rate at the point source/sink is the sum of the Q_β^e over each element in contact with the particular global node located at the point source. Let the node number where the point source exists be denoted as ig^* (a global index) (and i^* the

FACT CODE MANUAL

local index), if we evaluate Eq. (3.2.5.28) for each element within the mesh (note that only those elements in contact with this global node contribute and only one non-zero contribution results from each elemental matrix) and assemble the global source/sink term matrix, we obtain for an elemental matrix the members

$$P_{ij} = \begin{cases} Q_{\beta i}^e & i = i^* = j \\ 0 & i \neq i^* \neq j \end{cases} \quad \text{for element } e \quad (3.2.5.29)$$

and for the overall global matrix

$$P_{IJ} = \begin{bmatrix} Q_{\beta_1} & \cdots & 0 & \cdots & 0 \\ \vdots & \ddots & 0 & \cdots & 0 \\ 0 & 0 & Q_{\beta_{ig}} & \cdots & 0 \\ \vdots & \vdots & \vdots & \ddots & 0 \\ 0 & 0 & 0 & 0 & Q_{\beta_{np}} \end{bmatrix} \quad (3.2.5.30)$$

where

$Q_{\beta_{ig}}$ total volumetric flow rate at global node ig (point source)

Thus, as expressed by Eq. (3.2.5.30), the global source/sink term matrix is a diagonal matrix whose diagonal members are non-zero only for those nodes containing a point source/sink.

3.2.5.5 The Elemental and Global RHS Forcing Function Vector

Next, we deal with the right-hand-side forcing function vector in Eq. (3.2.1.6e). The first term in Eq. (3.2.1.6e) represents a point source/sink of contaminant (i.e., mass flow rate of contaminant) and the approach taken here is identical to that employed for a volumetric flow point source/sink as presented in Section 3.1.5, Eqs. (3.1.5.35) to (3.1.5.37).

For the case involving a contaminant point source, the general expression for qc^* is

$$qc^* = q_s c^* \delta(\mathbf{x} - \mathbf{x}_\beta) \quad (3.2.5.31)$$

where as before

q_s elemental volumetric flow rate at source/sink per unit volume

c^* incoming contaminant concentration at mass point source/sink

\mathbf{x}_β location of point source/sink

When Eq. (3.2.5.31) is used, the elemental source (or sink) term in Eq. (3.1.1.6e) becomes

$$F_{s_i}^e = \int_{\Omega_e} \phi_i q_s c^* \delta(\mathbf{x} - \mathbf{x}_\beta) d\Omega_e = Q_{\beta i}^e c^* \phi_i(\xi_\beta) \quad (3.2.5.32)$$

Note that the actual value employed for the contaminant concentration depends upon whether we are looking at a mass source (i.e., incoming mass flow, positive Q_β^e) or a mass sink (i.e., outgoing mass flow, negative Q_β^e). The contaminant concentration becomes the user inputted value c^* for incoming flows while it becomes the local concentration value of the aquifer for outgoing flows.

Equations for the first term of Eq. (3.2.1.6e) can be obtained by simply replacing the volumetric flow rate with the contaminant mass flow rate in Eqs. (3.1.5.36) and (3.1.5.37) resulting in an elemental vector with members

$$F_{s_i}^e = \begin{cases} Q_{\beta i}^e c^* & i = i^* \\ 0 & i \neq i^* \end{cases} \quad \text{for element } e \quad (3.2.5.33)$$

and for the overall global (mass point source/sink) vector

$$\mathbf{F}_s = \left[Q_{\beta_1} c^* \quad \cdots \quad Q_{\beta_{ig}} c^* \quad \cdots \quad Q_{\beta_{np}} c^* \right]^T \quad (3.2.5.34)$$

where

$Q_{\beta_{ig}}^e$ total contaminant mass flow rate at global node ig for point source/sink

Recall that the governing solute transport equation chosen, Eq. (2.2.28), is in non-conservative form. One feature that results from this form is the cancellation of terms on the LHS and RHS of the global representation of Eq. (3.2.1.7) when a mass point sink (outgoing) is specified. Basically, the mass flow rate contribution at node ig expressed in Eq. (3.2.5.34) cancels with the same term created during the matrix multiplication of Eq. (3.2.5.30) with the aquifer concentration vector. Therefore, application of mass point sinks (during transport simulations) are not necessary since they are automatically handled.

3.2.6 Numerical Solution of Transport Equation

The set of time-dependent ordinary differential equations defined by Eq (3.2.1.7) are integrated through time employing finite differencing. Equation (3.2.1.7) is a linear set of equations since the coefficient matrices \mathbf{B} , \mathbf{E} , \mathbf{G} , \mathbf{P} and the forcing vector \mathbf{F} are limited to time dependency only. For example, FACT is currently limited to the use of a linear equilibrium sorption isotherm model (see Section 2.2). Applying variably weighted time differencing to Eq. (3.2.1.7) yields the new $(n+1)^{\text{th}}$ time solution for solute concentration:

$$\left[\frac{\mathbf{B}}{\Delta t} \right]^{n+\omega} (\mathbf{c}^{n+1} - \mathbf{c}^n) + [\mathbf{E} + \mathbf{G} + \mathbf{P}]^{n+\omega} (\omega \mathbf{c}^{n+1} + \{1 - \omega\} \mathbf{c}^n) = \mathbf{F}^{n+\omega} \quad (3.2.6.1)$$

where the coefficient matrices and forcing vector are evaluated at the intermediate point in time $(n+\omega)$. Two basic algorithmic choices as to their evaluation can be made

$$\mathbf{X}^{n+\omega} = \begin{cases} \omega \mathbf{X}(t^{n+1}) + \{1 - \omega\} \mathbf{X}(t^n) \\ \mathbf{X}(t^{n+1}) \end{cases} \quad \text{for } 0 \leq \omega \leq 1 \quad (3.2.6.2)$$

where \mathbf{X} can represent \mathbf{B} , \mathbf{E} , \mathbf{G} , \mathbf{P} , or \mathbf{F} . At each new time step a set of linear algebraic equations must be solved. Eq. (3.2.6.1) can be rearrange into the standard linear algebra form given as:

$$\left[\frac{\mathbf{B}}{\Delta t} + \omega(\mathbf{E} + \mathbf{G} + \mathbf{P}) \right]^{n+\omega} \mathbf{c}^{n+1} = \mathbf{F}^{n+\omega} + \left[\frac{\mathbf{B}}{\Delta t} + \{\omega - 1\}(\mathbf{E} + \mathbf{G} + \mathbf{P}) \right]^{n+\omega} \mathbf{c}^n \quad (3.2.6.3)$$

Due to the nature of the advection operator Eq. (3.2.6.3) represents an asymmetrical set of algebraic equations. Various common time-stepping schemes can be obtained by varying the magnitude of the time differencing parameter, ω . Three of the more notable ones are:

- $\omega = 0$, fully explicit (or forward Euler) method that is first order accurate in time and only conditionally stable (that is, the time step size is restricted below certain magnitudes),
- $\omega = 1/2$, centered-differencing (or Crank-Nicolson) method that is second order accurate in time and is unconditionally stable (no time step limitation due to stability required),
- $\omega = 1$, fully implicit (or backward Euler) method that is first order accurate in time and is unconditionally stable (no time step limitation due to stability required).

For ω less than one half the method is only conditionally stable. Generally, the explicit scheme requires less computational effort per time step. However, for typical groundwater transport problems the time step constraint associated with stability is significantly smaller than that required by accuracy considerations. As a result, the total computational effort required is significantly greater when employing the explicit method. Therefore, it is recommended for transient transport simulations that either the centered-differencing or fully implicit scheme be chosen. The differences in computational effort between these two options are negligible. FACT allows the user to specify the value of ω , $0 \leq \omega \leq 1$. Without specific reasons to the contrary, it is further recommended that the centered-differencing scheme be chosen to obtain second-order accuracy.

In the current version of FACT, we evaluate the various matrices and vector terms at the new time (i.e., new time velocity and water saturation are used). These simplifications reduce computational and storage demands associated with evaluation of the matrix and

vector terms without significant loss in accuracy. Thus, Eq. (3.2.6.3) can be further reduced to the form

$$\left[\frac{\mathbf{B}}{\Delta t} + \omega(\mathbf{E} + \mathbf{G} + \mathbf{P}) \right]^{n+1} \mathbf{c}^{n+1} = \mathbf{F}^{n+\omega} + \left[\frac{\mathbf{B}}{\Delta t} + \{\omega-1\}(\mathbf{E} + \mathbf{G} + \mathbf{P}) \right]^{n+1} \mathbf{c}^n \quad (3.2.6.4)$$

where

$$\begin{aligned} \mathbf{B}^{n+1} &\equiv \mathbf{B}(\theta_m^{n+1}), & \mathbf{E}^{n+1} &\equiv \mathbf{E}(\theta_m^{n+1}, \mathbf{U}^{n+1}), & \mathbf{G}^{n+1} &\equiv \mathbf{G}(\theta_m^{n+1}) \\ \mathbf{P}^{n+\omega} &\equiv \mathbf{P}(t^{n+\omega}), & \mathbf{F}^{n+\omega} &= \mathbf{F}(t^{n+\omega}) \end{aligned} \quad (3.2.6.5)$$

The computational effort required per time step in solving Eq. (3.2.6.4) can be greatly reduced for certain transient transport simulations. For conditions where the left hand side (LHS) of Eq. (3.2.6.4) is time-independent (e.g., for a steady-state flow field and source/sink terms with a constant time step size), if the decomposition (from a direct solver) of the LHS matrix is stored during the first time step further time steps require only the updating of the RHS vector and then the forward and backward sweep operations of a linear algebra solver. Since typically the major work load is in the decomposition step of a direct method's linear algebra solver, significant savings in run time can be achieved. For pre-conditioned conjugate gradient-like solvers (that are by their nature iterative), an incomplete decomposition of the LHS matrix is typically chosen as the pre-conditioner. For these cases, the incomplete decomposition is stored during the first time step and is reused during every iterative pass through the iterative solver. Sizable savings are still achievable. During the processing of the problem statement, FACT automatically determines if the conditions exist to take advantage of this speedup option. No external user input is required for this feature to be activated.

3.2.7 Treatment of Transport Boundary Conditions

As discussed in Section 2.2, boundary conditions must also be specified at all times for the transport simulation. The types of BCs of practical interest include the conditions of prescribed concentration, prescribed material dispersive flux, and prescribed material total flux. Application of these BC types for the nonconservative form of the transport equation, Eq. (2.2.28), requires some further explanations.

To assist us in this discussion we shall look at a simple example where the three BC types are considered. Eqs. (2.2.29b-d) are rewritten below for convenience:

$$\text{Dirichlet} \quad c(\mathbf{x}, t) = \bar{c} \text{ on boundary portion } B'_1 \quad (3.2.7.1a)$$

$$\text{Neumann} \quad \mathbf{n} \cdot \mathbf{D}\nabla c = \mathbf{j}_n \text{ on boundary portion } B'_2 \quad (3.2.7.1b)$$

$$\text{Cauchy} \quad \mathbf{n} \cdot (\mathbf{D}\nabla c - c\mathbf{U}) = \mathbf{N}_n \text{ on boundary portion } B'_3 \quad (3.2.7.1c)$$

where B'_1 is the portion of the boundary where concentration is prescribed as \bar{c} , and B'_2 and B'_3 are portions of the boundary where the dispersive and the total solute mass fluxes

FACT CODE MANUAL

are prescribed as j_n and N_n , respectively. These BCs are sometimes referred to as type 1, type 2, and type 3 BCs, respectively. By convention we assume that incoming solute material is positive. Also, specification of Dirichlet conditions is not limited to the boundary of the domain. Dirichlet conditions can be specified at any active grid node and application of it at a node supersedes any other type of BC type for that node. Application of multiple material flux BCs to a single node (excluding a Dirichlet specified node) is allowed and the contributions from each flux BC become additive. Note that the transport equation is linear when one assumes a linear isotherm adsorption model as is done in the current version of FACT.

The first-type BC, Eq. (3.2.7.1a), is treated by setting current concentration values at the boundary nodes to the prescribed concentration \tilde{c} . Physically, this BC may apply to inflow boundary surfaces where the solute concentration of the incoming fluid is known and can be assumed to be approximately the same as the resident nodal solute concentration in the porous media. Internal nodes, representing injection wells or contaminant sources for example, may also be subject to the type 1 BC if the above stated equilibrium assumption is adopted. However, in most cases specification of the material flux of solute due to sources is a more valid and practical approach.

The second-type BC, Eq. (3.2.7.1b), is treated by adding the integrated nodal value of the prescribed dispersive flux (i.e., a mass flowrate) to the right hand side of the discretized transport equations (F_i of Eq. (3.2.1.5)). This mass flowrate represents the second integral of Eq. (3.2.1.6e). Physically, this BC may apply to impermeable boundary surfaces where the dispersive flux is essentially zero. The resulting normal concentration gradients then become zero. It may also apply to certain contaminated buried sources that are placed in an undisturbed flow field, wherein the waste material is leaching solute at the prescribed rate, j_n . In order for the local flow field to be undisturbed, the net material entering the porous media must be zero (i.e., typically referred to as equimolar counter-diffusion transport). If the transport of material results in a net flux of material into (or out of) the porous media (i.e., a non-zero bulk average velocity at the boundary interface), the flow field is effected and the following BC type should be used.

The third-type BC, Eq. (3.2.7.1c), generally applies to inlet boundary surfaces or injection wells where the solute concentration of incoming or injected fluid c^* may be unequal to the resident nodal concentration values. In these cases, the integrated nodal value of the prescribed total flux (i.e., a mass flowrate) is added to the right hand side of the discretized transport equations (F_i of Eq. (3.2.1.5)). This mass flowrate represents the first integral of Eq. (3.2.1.6e) where for the case of an inlet boundary surface flux the volume integral becomes actually a surface integral of qc^* . In addition, an integrated nodal advective flux term (i.e., a volumetric flowrate) corresponding to the bulk (Darcy) velocity term in Eq. (3.2.7.1c) is added to the left hand side of the discretized transport equations (the diagonal term P_{II} of Eq. (3.2.1.5); incorporated into the coefficient matrix along its diagonal). This volumetric flowrate represents the integral of Eq. (3.2.1.6d) where for the case of an inlet boundary surface flux the volume integral becomes actually a surface integral of q .

FACT CODE MANUAL

For the special case of extraction wells (sinks), the outgoing solute concentration, c^* , takes on the same value as the resident nodal concentration, c . As noted earlier, the nonconservative form of the transport equation, Eq. (2.2.28), is being solved and as a result these special cases are handled automatically by the formulation used. Basically, the BC expressed by Eq. (3.2.7.1c) then reduces to that of Eq. (3.2.7.1b) with a zero dispersive flux value.

The case of an outflow boundary is similar to the extraction well case. Here the outflow boundary is handled automatically if a zero ("natural") dispersive flux assumption is adequate. This is the natural boundary condition within the finite element framework and requires no treatment for its bounding surfaces. If (but typically unlikely) dispersive information at an outflow boundary exists, then application of the second-type BC should be used. The advective transport contribution is handled based on the inputted flow field. The current version of FACT does not allow for a non-zero dispersive flux for this case.

Boundary conditions ultimately reside at specified nodes within the mesh. A temporal variation of a BC at any given node is accommodated in a convenient manner by specifying the BC to be a transient BC whose transient behavior is inputted as either a continuous piecewise cubic spline (or linear) approximation or a discontinuous (step function) approximation. These transient approximations represent the actual graph of solute concentration or solute flux (actually integrated nodal volumetric or mass flowrates) versus time. Steady-state BC values are inputted as constants.

By way of example, Fig. 3.2.4 illustrates a typical situation where the above three BC types are applied. Figure 3.2.4 represents a 2-D vertical cross-section through an aquifer unit containing both a saturated zone and a vadose zone. The upper boundary, B_a , coincides with the ground surface topography. The lower boundary, B_c , coincides with the top surface of an impermeable aquitard (i.e., the transport of solute, as well as water, being negligible). On the left boundary, B_b , groundwater flows into the domain carrying along a known concentration of the solute species of interest. On the right boundary, B_d , groundwater flows out of the domain carrying along an unknown amount of the solute.

In addition to these boundary conditions, two types of sources exist. The first source of solute results from the vertical injection well, while the second results from the leaching out of solute from buried waste. These source terms were added to this example to further illustrate how, in FACT, source/sinks and boundary fluxes are treated very similarly. In FACT, once source/sink strengths and boundary fluxes have been allocated out to their appropriate neighboring nodes, their contributions to the transport equation are handled identically.

Looking at Fig. 3.2.4 we see that the following nodal boundary conditions apply:

- Nodes on boundary surface B_a - Surface recharge containing a known solute concentration is handled as a type 3 BC where the dispersive flux is assumed to be zero.
- Nodes on boundary surface B_b - An inflow boundary whose solute concentration at this surface is known is handled as a type 1 BC.

FACT CODE MANUAL

- Nodes on boundary surface B_c - An impermeable boundary (both to bulk flow, as well as species diffusion) that is handled as a type 2 BC whose dispersive flux is assumed to be zero (i.e., this is a natural BC and it is handled automatically).
- Nodes on boundary surface B_d - An outflow boundary whose solute concentration at this surface is unknown is handled as a type 2 BC where the dispersive flux is assumed to be zero (i.e., this is a natural BC and it is handled automatically [the default BC]).
- Nodes on boundary surface B_c - An impermeable boundary (both to bulk flow, as well as species diffusion) that is handled as a type 2 BC whose dispersive flux is assumed to be zero (i.e., this is a natural BC and it is handled automatically).
- Nodes on boundary surface B_d - An outflow boundary whose solute concentration at this surface is unknown is handled as a type 2 BC where the dispersive flux is assumed to be zero (i.e., this is a natural BC and it is handled automatically).
- Nodes along vertical well screen - For an injection well the source term is handled similar to a type 3 BC where the dispersive flux is assumed to be zero. For an extraction well, no BC needs to be applied, since this case is handled by the formulation of the governing equation.

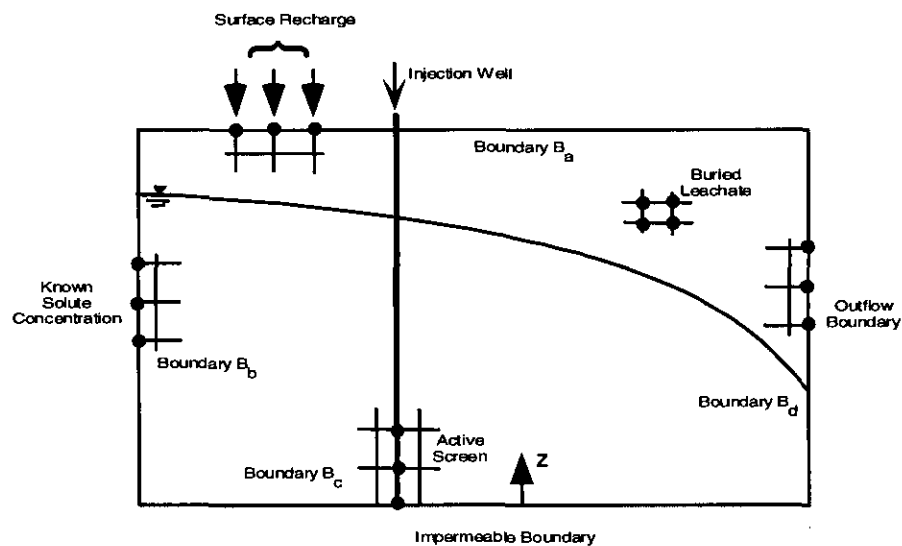


Fig. 3.2.4. An example for illustrating the treatment of transport boundary conditions and source terms.

- Nodes associated with buried waste - For a buried waste form that impacts the flow field the source term is handled similar to a type 3 BC where the dispersive flux is assumed to be zero; otherwise, for cases where the flow field can be assumed to be undisturbed, then a type 2 BC applies. This latter case arises for example when a small quantity of fluid highly concentrated with a solute is injected (or leached) into the subsurface. The impact on the flow field is negligible for transport calculational purposes and can be omitted. In this case the preliminary flow simulation would also assume a zero volumetric flowrate injected into the subsurface.

3.3 Numerical Techniques for Variably Saturated Mobile/Immobile Solute Transport

The standard weak formulation of the Petrov-Galerkin weighted residual technique (Section 3.2.1) is employed to cast the mobile-phase governing transport equation into integral form. The mobile-phase transport equation reduces to the contaminant transport equation in Section 3.2 when no interfacial mass transfer between mobile and immobile solute occurs. The immobile-phase transport equation does not include advection-dispersion terms, therefore, the standard formulation of the Bubnov-Galerkin weighted residual technique is employed to cast the equation into integral form.

3.3.1 Upstream-Weighted Residual Formulation of the Mobile-Phase Transport Equation

The mobile-phase governing equation for transport, Eq. (2.3.15), is solved by the upstream-weighted residual finite element method. The mobile and immobile solute concentrations are approximated as finite linear combinations of the symmetric basis (trial) functions of the form

$$c_m(\mathbf{x}, t) = \sum_{J=1}^{np} \varphi_J(\mathbf{x}) c_J(t) \quad \text{and} \quad c_{im}(\mathbf{x}, t) = \sum_{J=1}^{np} \varphi_J(\mathbf{x}) ci_J(t) \quad (3.3.1.1)$$

where $\varphi_J(\mathbf{x})$, $c_J(t)$ and $ci_J(t)$ are the basis functions, the nodal values of mobile solute concentration, and the nodal values of immobile solute concentration at time t , respectively.

Rearranging and applying the upstream-weighted residual criterion to Eq. (2.3.15) yields

$$\begin{aligned} \int_{\Omega} \varphi_I \left\{ \theta_m R_m \frac{\partial c_m}{\partial t} + \theta_m (R_m \lambda_r + \lambda_m) c_m + q(c_m - c^*) - \nabla \cdot (\mathbf{D} \nabla c_m) \right\} d\Omega \\ + \int_{\Omega} \psi_I \{ \mathbf{U} \cdot \nabla c_m \} d\Omega + \int_{\Omega} \varphi_I \{ \alpha(c_m - c_{im}) \} d\Omega = 0 \quad \text{for } I = 1, 2, \dots, np \end{aligned} \quad (3.3.1.2)$$

Since we shall choose C^0 continuous basis and weighting functions, φ_I and, ψ_I the dispersion integral is evaluated by applying the divergence theorem (actually, Green's first identity, the multidimensional equivalent of integration by parts) to obtain

$$\begin{aligned} \int_{\Omega} \varphi_I \nabla \cdot (\mathbf{D} \nabla c_m) d\Omega &= \int_{\Omega} \nabla \cdot (\varphi_I \mathbf{D} \nabla c_m) d\Omega - \int_{\Omega} \nabla \varphi_I \cdot (\mathbf{D} \nabla c_m) d\Omega \\ &= \int_{\sigma} \varphi_I \mathbf{n} \cdot (\mathbf{D} \nabla c_m) d\sigma - \int_{\Omega} \nabla \varphi_I \cdot (\mathbf{D} \nabla c_m) d\Omega \\ &= - \int_{\sigma} \varphi_I (\mathbf{n} \cdot \mathbf{j}_a) d\sigma - \int_{\Omega} \nabla \varphi_I \cdot (\mathbf{D} \nabla c_m) d\Omega \end{aligned} \quad (3.3.1.3)$$

FACT CODE MANUAL

where Ω is the solution domain with boundary σ , and the dispersive flux is $\mathbf{j}_a = -\mathbf{D}\nabla c_m$.

Substituting Eqs. (3.3.1.1) and (3.3.1.3) into (3.3.1.2) gives the expression

$$\begin{aligned}
 & \sum_{J=1}^{np} \left\{ \int_{\Omega} (\theta_m R_m) \phi_I \phi_J d\Omega \right\} \frac{dc_J}{dt} + \sum_{J=1}^{np} \left\{ \int_{\Omega} \theta_m (R_m \lambda_r + \lambda_m) \phi_I \phi_J d\Omega \right\} c_J \\
 & + \sum_{J=1}^{np} \left\{ \int_{\Omega} (q) \phi_I \phi_J d\Omega \right\} c_J + \sum_{J=1}^{np} \left\{ \int_{\Omega} [\nabla \phi_I \cdot \mathbf{D} \nabla \phi_J + \psi_I \mathbf{U} \cdot \nabla \phi_J] d\Omega \right\} c_J \\
 & + \sum_{J=1}^{np} \left\{ \int_{\Omega} (\alpha) \phi_I \phi_J d\Omega \right\} c_J = \int_{\Omega} (qc^*) \phi_I d\Omega + \int_{\sigma} (\mathbf{j}_n) \phi_I d\sigma \\
 & + \sum_{J=1}^{np} \left\{ \int_{\Omega} (\alpha) \phi_I \phi_J d\Omega \right\} ci_J \quad \text{for } I = 1, 2, \dots, np
 \end{aligned} \tag{3.3.1.4}$$

where the normal component of the dispersive flux (incoming is positive by convention) is $\mathbf{j}_n = -\mathbf{n} \cdot \mathbf{j}_a$.

Equation (3.3.1.4) can be written in the more concise form

$$B_{IJ} \frac{dc_J}{dt} + [E_{IJ} + G_{IJ} + I_{IJ} + P_{IJ}] c_J = F_I + I_{IJ} ci_J, \quad I = 1, 2, \dots, np \tag{3.3.1.5}$$

where

$$B_{IJ} = \int_{\Omega} (\theta_m R_m) \phi_I \phi_J d\Omega \tag{3.3.1.6a}$$

$$E_{IJ} = \int_{\Omega} [\nabla \phi_I \cdot \mathbf{D} \nabla \phi_J + \psi_I \mathbf{U} \cdot \nabla \phi_J] d\Omega \tag{3.3.1.6b}$$

$$G_{IJ} = \int_{\Omega} \theta_m (R_m \lambda_r + \lambda_m) \phi_I \phi_J d\Omega \tag{3.3.1.6c}$$

$$P_{IJ} = \int_{\Omega} (q) \phi_I \phi_J d\Omega \tag{3.3.1.6d}$$

$$F_I = \int_{\Omega} (qc^*) \phi_I d\Omega + \int_{\sigma} (\mathbf{j}_n) \phi_I d\sigma \tag{3.3.1.6e}$$

$$I_{IJ} = \int_{\Omega} (\alpha) \phi_I \phi_J d\Omega \tag{3.3.1.6f}$$

FACT CODE MANUAL

The set of time-dependent linear ordinary differential equations defined by Eq (3.3.1.4) can also be presented in its equivalent vector form as

$$\mathbf{B} \frac{d\mathbf{c}}{dt} + [\mathbf{E} + \mathbf{G} + \mathbf{I} + \mathbf{P}] \mathbf{c} = \mathbf{F} + \mathbf{I} \mathbf{c}_i \quad (3.3.1.7)$$

where

- B** mobile-phase storage (capacitance or mass) matrix
E advection-dispersion matrix
G mobile-phase radioactive and first-order decay matrix
I interfacial mass transfer matrix
P mobile-phase source/sink matrix
F RHS forcing function vector
c mobile solute (contaminant) concentration vector
c_i immobile solute (contaminant) concentration vector
t time

3.3.2 Bubnov-Galerkin Weighted Residual Formulation of the Immobile-Phase Transport Equation

The standard formulation of the Bubnov-Galerkin weighted residual technique is employed to cast the immobile-phase governing equation into integral form. The Galerkin integral form of Eq. (2.3.21) is

$$\int_{\Omega} \varphi_I \left\{ \theta_{im} R_{im} \frac{\partial c_{im}}{\partial t} + \theta_{im} (R_{im} \lambda_r + \lambda_{im}) c_{im} - \alpha (c_m - c_{im}) \right\} d\Omega = 0, \quad (3.3.2.1)$$

$I = 1, 2, \dots, np$

Substituting Eqs. (3.3.1.1) into Eq. (3.3.2.1) yields

$$\begin{aligned} \sum_{J=1}^{np} \left\{ \int_{\Omega} (\theta_{im} R_{im}) \varphi_I \varphi_J d\Omega \right\} \frac{dc_{iJ}}{dt} + \sum_{J=1}^{np} \left\{ \int_{\Omega} \theta_{im} (R_{im} \lambda_r + \lambda_{im}) \varphi_I \varphi_J d\Omega \right\} c_{iJ} \\ + \sum_{J=1}^{np} \left\{ \int_{\Omega} (\alpha) \varphi_I \varphi_J d\Omega \right\} c_{iJ} = \sum_{J=1}^{np} \left\{ \int_{\Omega} (\alpha) \varphi_I \varphi_J d\Omega \right\} c_J \quad \text{for } I = 1, 2, \dots, np \end{aligned} \quad (3.3.2.2)$$

Equation (3.3.2.2) can be written in the more concise form

$$B_{IJ} \frac{dc_{iJ}}{dt} + [G_{IJ} + I_{IJ}] c_{iJ} = I_{IJ} c_J, \quad I = 1, 2, \dots, np \quad (3.3.2.3)$$

where

$$B_{IJ} = \int_{\Omega} (\theta_{im} R_{im}) \varphi_I \varphi_J d\Omega \quad (3.3.2.4a)$$

$$G_{iIJ} = \int_{\Omega} \theta_{im} (R_{im} \lambda_r + \lambda_{im}) \phi_i \phi_j d\Omega \quad (3.3.2.4b)$$

The set of time-dependent linear ordinary differential equations defined by Eq (3.3.2.2) can also be presented in its equivalent vector form as

$$B_i \frac{dc_i}{dt} + [G_i + I] c_i = I c \quad (3.3.2.5)$$

where

- B_i** immobile-phase storage (capacitance or mass) matrix
G_i immobile-phase radioactive and first-order decay matrix
I interfacial mass transfer matrix
c mobile solute (contaminant) concentration vector
c_i immobile solute (contaminant) concentration vector
t time

3.3.3 Mobile-Phase Transport Equation Elemental Matrix Computation

The elemental matrices B_{ij} , E_{ij} , G_{ij} , I_{ij} , P_{ij} , and vector F_j resulting from the Bubnov and Petrov-Galerkin approximations to the mobile-phase transport equation can be computed using influence coefficient matrices or Gauss-Legendre quadrature for the rectangular prism or constrained hexahedron element, respectively.

3.3.3.1 The Mobile-Phase Elemental Storage (Capacitance) Matrix

From Eq. (3.3.1.6a) the expression for the mobile-phase elemental storage coefficient matrix is obtained as

$$B_{ij} = \int_{\Omega_e} (\theta_m R_m) \phi_i \phi_j d\Omega_e \quad (3.3.3.1)$$

where θ_m is the mobile water content, and R_m is the mobile-phase retardation coefficient. Transforming the mobile-phase elemental storage matrix, B_{ij} , from global to local coordinates yields

$$B_{ij} = \langle \theta_m R_m \rangle M_{ij} \quad (3.3.3.2)$$

where $\langle \rangle$ represent centroidal values and M_{ij} is the consistent mass matrix.

3.3.3.2 The Elemental Advection-Dispersion Matrix

The elemental advection-dispersion matrix is unchanged from the discussion in Section 3.2.5.2.

3.3.3.3 The Mobile-Phase Elemental Radioactive and First-Order Decay Matrix

From Eq. (3.3.1.6c) the expression for the mobile-phase elemental radioactive and first-order decay storage matrix is obtained as

$$G_{ij} = \int_{\Omega_e} \theta_m (R_m \lambda_r + \lambda_m) \phi_i \phi_j d\Omega_e \quad (3.3.3.7)$$

where θ_m is the mobile water content, R_m is the mobile-phase retardation coefficient, λ_r is the radioactive decay constant and λ_m is the mobile-phase first-order decay constant. Transforming the mobile-phase elemental radioactive and first-order decay matrix, G_{ij} , from global to local coordinates yields

$$G_{ij} = \langle \theta_m R_m \lambda_r \rangle M_{ij} + \langle \theta_m \lambda_m \rangle M_{ij} \quad (3.3.3.8)$$

where $\langle \rangle$ represent centroidal values and M_{ij} is the consistent mass matrix.

3.3.3.4 The Mobile-Phase Elemental and Global Source/Sink Matrix

No change from Section 3.2.5.7.

3.3.3.5 The Mobile-Phase Elemental and Global RHS Forcing Function Vector

No change from Section 3.2.5.8

3.3.3.6 The Elemental Interfacial Mass Transfer Matrix

From Eq. (3.3.1.6f) the expression for the elemental interfacial mass transfer matrix is obtained as

$$I_{ij} = \int_{\Omega_e} (\alpha) \phi_i \phi_j d\Omega_e \quad (3.3.3.9)$$

where α is the mass transfer coefficient between mobile and immobile solute. Transforming the mobile-phase elemental interfacial mass transfer matrix, I_{ij} , from global to local coordinates yields

$$I_{ij} = \langle \alpha \rangle M_{ij} \quad (3.3.3.10)$$

where $\langle \rangle$ represent centroidal values. The mass matrix is lumped in Eq. (3.3.3.10) in order to solve a decoupled set of algebraic equations for the new time immobile solute concentrations. The lumped elemental interfacial mass transfer matrix becomes

$$I_{ij}^L = \langle \alpha \rangle M_{ij}^L \quad (3.3.3.11)$$

3.3.4 Immobile-Phase Transport Equation Elemental Matrix Computation

The elemental matrices B_{ij} , G_{ij} , and I_{ij} resulting from the Bubnov-Galerkin approximations to the immobile-phase transport equation can be computed using influence coefficient matrices or Gauss-Legendre quadrature for the rectangular prism or constrained hexahedron element, respectively.

3.3.4.1 The Immobile-Phase Elemental Storage (Capacitance) Matrix

From Eq. (3.3.2.4a) the expression for the immobile-phase elemental storage coefficient matrix is obtained as

$$B_{ij} = \int_{\Omega_e} (\theta_{im} R_{im}) \phi_i \phi_j d\Omega_e \quad (3.3.4.1)$$

where θ_{im} is the immobile water content, and R_{im} is the immobile-phase retardation coefficient. Transforming the immobile-phase elemental storage matrix, B_{ij} , from global to local coordinates yields

$$B_{ij} = \langle \theta_{im} R_{im} \rangle M_{ij} \quad (3.3.4.2)$$

where $\langle \rangle$ represent centroidal values. The mass matrix is lumped in Eq. (3.3.4.2) in order to solve a decoupled set of algebraic equations for the new time immobile solute concentrations. The lumped immobile-phase elemental storage matrix becomes

$$B_{ij}^L = \langle \theta_{im} R_{im} \rangle M_{ij}^L \quad (3.3.4.3)$$

3.3.4.2 The Immobile-Phase Elemental Radioactive and First-Order Decay Matrix

From Eq. (3.3.2.4b) the expression for the immobile-phase elemental radioactive and first-order decay storage matrix is obtained as

$$G_{ij} = \int_{\Omega_e} \theta_{im} (R_{im} \lambda_r + \lambda_{im}) \phi_i \phi_j d\Omega_e \quad (3.3.4.4)$$

where θ_{im} is the immobile water content, R_{im} is the immobile-phase retardation coefficient, λ_r is the radioactive decay constant and λ_{im} is the immobile-phase first-order decay constant. Transforming the immobile-phase elemental radioactive and first-order decay matrix, G_{ij} , from global to local coordinates yields

$$G_{ij} = \langle \theta_{im} R_{im} \lambda_r \rangle M_{ij} + \langle \theta_{im} \lambda_{im} \rangle M_{ij} \quad (3.3.4.5)$$

where $\langle \rangle$ represent centroidal values. The mass matrix is lumped in Eq. (3.3.4.5) in order to solve a decoupled set of algebraic equations for the new time immobile solute

concentrations. The lumped immobile-phase elemental radioactive and first-order decay matrix becomes

$$G_{ij}^L = \langle \theta_{im} R_{im} \lambda_r \rangle M_{ij}^L + \langle \theta_{im} \lambda_{im} \rangle M_{ij}^L \quad (3.3.4.6)$$

3.3.5 Numerical Solution of the Mobile/Immobile Transport Equations

The set of time-dependent ordinary differential equations defined by Eqs. (3.3.1.7) and (3.3.2.5) are integrated through time employing finite differencing. Applying variably weighted time differencing (see Section 3.2.6) to Eqs. (3.3.1.7) and (3.3.2.5) yields the new $(n+1)^{th}$ time solution for mobile and immobile solute concentration, respectively

$$\begin{aligned} & \left[\frac{\mathbf{B}}{\Delta t} \right]^{n+\omega} (\mathbf{c}^{n+1} - \mathbf{c}^n) + [\mathbf{E} + \mathbf{G} + \mathbf{I} + \mathbf{P}]^{n+\omega} (\omega \mathbf{c}^{n+1} + \{1 - \omega\} \mathbf{c}^n) \\ & = \mathbf{F}^{n+\omega} + [\mathbf{I}]^{n+\omega} (\omega \mathbf{ci}^{n+1} + \{1 - \omega\} \mathbf{ci}^n) \end{aligned} \quad (3.3.5.1)$$

$$\begin{aligned} & \left[\frac{\mathbf{Bi}}{\Delta t} \right]^{n+\omega} (\mathbf{ci}^{n+1} - \mathbf{ci}^n) + [\mathbf{Gi} + \mathbf{I}]^{n+\omega} (\omega \mathbf{ci}^{n+1} + \{1 - \omega\} \mathbf{ci}^n) \\ & = [\mathbf{I}]^{n+\omega} (\omega \mathbf{c}^{n+1} + \{1 - \omega\} \mathbf{c}^n) \end{aligned} \quad (3.3.5.2)$$

where the coefficient matrices and forcing vector are evaluated at the intermediate point in time $(n+\omega)$.

At each new time step a set of linear algebraic equations must be solved. Eqs. (3.3.5.1) and (3.3.5.2) can be rearranged into the standard linear algebra form given as, respectively

$$\begin{aligned} & \left[\frac{\mathbf{B}}{\Delta t} + \omega (\mathbf{E} + \mathbf{G} + \mathbf{I} + \mathbf{P}) \right]^{n+\omega} \mathbf{c}^{n+1} = \mathbf{F}^{n+\omega} \\ & + \left[\frac{\mathbf{B}}{\Delta t} + \{ \omega - 1 \} (\mathbf{E} + \mathbf{G} + \mathbf{I} + \mathbf{P}) \right]^{n+\omega} \mathbf{c}^n + [\mathbf{I}]^{n+\omega} (\omega \mathbf{ci}^{n+1} + \{1 - \omega\} \mathbf{ci}^n) \end{aligned} \quad (3.3.5.3)$$

$$\begin{aligned} & \left[\frac{\mathbf{Bi}}{\Delta t} + \omega (\mathbf{Gi} + \mathbf{I}) \right]^{n+\omega} \mathbf{ci}^{n+1} = \left[\frac{\mathbf{Bi}^L}{\Delta t} + \{ \omega - 1 \} (\mathbf{Gi} + \mathbf{I}) \right]^{n+\omega} \mathbf{ci}^n \\ & + [\mathbf{I}]^{n+\omega} (\omega \mathbf{c}^{n+1} + \{1 - \omega\} \mathbf{c}^n) \end{aligned} \quad (3.3.5.4)$$

To avoid having to solve a coupled linear algebra problem, we decouple the set of algebraic equations in Eq. (3.3.5.4) by lumping the mass matrix.

FACT CODE MANUAL

Summing over all active elements and substituting Eqs. (3.3.3.11), (3.3.4.4), and (3.3.4.6) into Eq. (3.3.5.4) yields the new time immobile solute concentration as

$$ci_J^{n+1} = [W_J]^{n+\omega} ci_J^n + [L_J]^{n+\omega} \left(\omega c_J^{n+1} + \{1 - \omega\} c_J^n \right) \quad (3.3.5.5)$$

where

$$[W_J]^{n+\omega} = \frac{\sum_{e=1}^{ne} \left[\frac{\langle \theta_{im} R_{im} \rangle_e}{\Delta t} + \{ \omega - 1 \} \left(\langle \theta_{im} (R_{im} \lambda_r + \lambda_{im}) \rangle_e + \langle \alpha \rangle_e \right) \right]^{n+\omega} [M_{JJ}^L]_e}{\sum_{e=1}^{ne} \left[\frac{\langle \theta_{im} R_{im} \rangle_e}{\Delta t} + \omega \left(\langle \theta_{im} (R_{im} \lambda_r + \lambda_{im}) \rangle_e + \langle \alpha \rangle_e \right) \right]^{n+\omega} [M_{JJ}^L]_e} \quad (3.3.5.6)$$

$$[L_J]^{n+\omega} = \frac{\sum_{e=1}^{ne} [\langle \alpha \rangle_e]^{n+\omega} [M_{JJ}^L]_e}{\sum_{e=1}^{ne} \left[\frac{\langle \theta_{im} R_{im} \rangle_e}{\Delta t} + \omega \left(\langle \theta_{im} (R_{im} \lambda_r + \lambda_{im}) \rangle_e + \langle \alpha \rangle_e \right) \right]^{n+\omega} [M_{JJ}^L]_e} \quad (3.3.5.7)$$

and $J \in e$.

Substituting Eq. (3.3.5.5) into the time-differenced mobile-phase transport equation, Eq. (3.3.5.3) and combining like terms gives

$$\begin{aligned} & \left[\frac{\mathbf{B}}{\Delta t} + \omega \left(\mathbf{E} + \mathbf{G} + \mathbf{I}^L - \omega \mathbf{I}^L \mathbf{L} + \mathbf{P} \right) \right]^{n+\omega} \mathbf{c}^{n+1} = \mathbf{F}^{n+\omega} \\ & + \left[\frac{\mathbf{B}}{\Delta t} + \{ \omega - 1 \} \left(\mathbf{E} + \mathbf{G} + \mathbf{I}^L - \omega \mathbf{I}^L \mathbf{L} + \mathbf{P} \right) \right]^{n+\omega} \mathbf{c}^n \\ & + \left[\mathbf{I}^L \right]^{n+\omega} \left(\omega [\mathbf{W}]^{n+\omega} + \{1 - \omega\} \right) \mathbf{c}^n \end{aligned} \quad (3.3.5.8)$$

In the current version of FACT, we evaluate the various matrices and vector terms at the new time (i.e., new time velocity and water saturation are used). These simplifications reduce computational and storage demands associated with evaluation of the matrix and vector terms without significant loss in accuracy. Thus, Eqs. (3.3.5.5) and (3.3.5.8) can be further reduced to the form

$$\mathbf{c}^{n+1} = [\mathbf{W}]^{n+1} \mathbf{c}^n + [\mathbf{L}]^{n+1} \left(\omega \mathbf{c}^{n+1} + \{1 - \omega\} \mathbf{c}^n \right) \quad (3.3.5.9)$$

$$\begin{aligned}
& \left[\frac{\mathbf{B}}{\Delta t} + \omega \left(\mathbf{E} + \mathbf{G} + \mathbf{I}^L - \omega \mathbf{I}^L \mathbf{L} + \mathbf{P} \right) \right]^{n+1} \mathbf{c}^{n+1} = \mathbf{F}^{n+\omega} \\
& + \left[\frac{\mathbf{B}}{\Delta t} + \{\omega - 1\} \left(\mathbf{E} + \mathbf{G} + \mathbf{I}^L - \omega \mathbf{I}^L \mathbf{L} + \mathbf{P} \right) \right]^{n+1} \mathbf{c}^n \\
& + \left[\mathbf{I}^L \right]^{n+1} \left(\omega [\mathbf{W}]^{n+1} + \{1 - \omega\} \right) \mathbf{c}^n
\end{aligned} \tag{3.3.5.10}$$

where

$$\begin{aligned}
\mathbf{W}^{n+1} & \equiv \mathbf{W} \left(\theta_{im}^{n+1}, \alpha^{n+1} \right), \quad \mathbf{L}^{n+1} \equiv \mathbf{L} \left(\theta_{im}^{n+1}, \alpha^{n+1} \right) \\
\mathbf{B}^{n+1} & \equiv \mathbf{B} \left(\theta_m^{n+1} \right), \quad \mathbf{E}^{n+1} \equiv \mathbf{E} \left(\theta_m^{n+1}, \mathbf{U}^{n+1} \right), \quad \mathbf{G}^{n+1} \equiv \mathbf{G} \left(\theta_m^{n+1} \right) \\
\mathbf{I}^{n+\omega} & \equiv \mathbf{I} \left(\alpha^{n+\omega} \right), \quad \mathbf{P}^{n+\omega} \equiv \mathbf{P} \left(t^{n+\omega} \right), \quad \mathbf{F}^{n+\omega} = \mathbf{F} \left(t^{n+\omega} \right)
\end{aligned} \tag{3.3.5.11}$$

The mobile-phase transport equation is solved first for the new time mobile solute concentrations based on the old time mobile and immobile solute concentrations using the asymmetric PCG/ORTHOMIN solver implemented in FACT. The immobile-phase transport equation is then solved based on the old time immobile solute concentrations and the new and old time mobile solute concentrations.

The computational effort required per time step in solving Eq. (3.3.5.10) can be greatly reduced for certain transient transport simulations. For conditions where the left hand side (LHS) of Eq. (3.3.5.10) is time-independent (e.g., for a steady-state flow field and source/sink terms with a constant time step size), if the decomposition (from a direct solver) of the LHS matrix is stored during the first time step further time steps require only the updating of the RHS vector and then the forward and backward sweep operations of a linear algebra solver. Similarly, the arrays \mathbf{W} and \mathbf{L} in Eq. (3.3.5.10) just have to be built and stored once for a steady-state flow field, constant mass transfer coefficients and time step size. During the processing of the problem statement, FACT automatically determines if the conditions exist to take advantage of this speedup option.

3.3.6 Treatment of Mobile/Immobile Transport Boundary Conditions

The treatment of mobile-phase transport boundary conditions are discussed in Section 3.2.7. The immobile-phase transport equation does not require specification of boundary conditions; only initial conditions.

3.4 Matrix Solution Techniques

The linear algebra problems expressed by Eq. (3.1.8.6a) for flow, Eq. (3.2.6.4) for contaminant transport, and Eq. (3.3.5.10) for mobile-phase transport are solved using efficient pre-conditioned conjugate gradient-like (PCG) iterative solvers. Large structurally sparse matrix equations are generated by the finite element (or finite

FACT CODE MANUAL

difference) approximations to multi-dimensional field problems. The PCG algorithms chosen were designed to accommodate a large number of nodal unknowns consistent with the needs imposed by many realistic 3D field problems (e.g., these methods do not alter the sparsity pattern of the coefficient matrix during the solution process, thus no additional allocation of memory is required).

3.4.1 Symmetric PCG Solver

For solving large sparse symmetric matrix equations, the class of Incomplete Cholesky Conjugate Gradient (ICCG) algorithms has emerged as one of the most promising. These methods are guaranteed to converge for a symmetric positive-definite matrix (sometimes referred to as a type M matrix). The symmetric PCG solver implemented into FACT is based on a two-step procedure developed by Meijerink and van der Vorst (1977), then extended and implemented by Kershaw (1978) and Anderson (1983). It is used in FACT to solve the system of algebraic equations resulting from the application of the Picard scheme to the finite element flow equations.

We wish to solve the linear algebraic problem

$$\mathbf{S}\mathbf{x} = \mathbf{y} \quad (3.4.1.1)$$

where the finite element coefficient matrix, \mathbf{S} , is a positive diagonally dominant symmetric matrix. The first step of this PCG algorithm involves preconditioning of \mathbf{S} by computing its incomplete Cholesky decomposition in the form

$$\mathbf{S} \rightarrow \mathbf{B} = \mathbf{L}\mathbf{D}\mathbf{L}^T \quad (3.4.1.2)$$

where in FACT the preconditioner matrix, \mathbf{B} , is also symmetric and employs the following storage scheme

$$\mathbf{B} = \begin{bmatrix} \frac{1}{d_1} & 0 & 0 & \dots \\ l_{21}d_1 & \frac{1}{d_2} & 0 & \dots \\ l_{31}d_1 & l_{32}d_1 & \frac{1}{d_3} & \dots \\ l_{41}d_1 & l_{42}d_1 & l_{43}d_1 & \frac{1}{d_4} & \dots \\ \vdots & \vdots & \vdots & \vdots & \ddots \end{bmatrix} \quad \begin{aligned} b_{ii} &= \frac{1}{d_i} & i = 1, np \\ b_{ij} &= l_{ij}d_j & i > j \end{aligned} \quad (3.4.1.3)$$

The actual decomposition is performed such that zero fill-in occurs yielding the incomplete decomposition referred to as ICCG(0). During the decomposition process no adjustments are made for pivoting; however, the process does incorporate Kershaw's modification to the diagonal to enhance convergence stability. The basic algorithm employed for performing this incomplete decomposition is

$$\begin{aligned}
 &\text{do } i = 1, np \\
 &\quad \text{do } j = 1, i \\
 &\quad \quad b_{ij} = s_{ij} - \sum_{k=1}^{i-1} \{b_{ik} b_{jk} b_{kk}\} \\
 &\quad \quad \text{if } (j=i) b_{ij} \equiv b_{ii} = \frac{1}{b_{ij}} \\
 &\quad \text{end do} \\
 &\text{end do}
 \end{aligned} \tag{3.4.1.3}$$

Since zero fill-in is assumed errors accumulate during the decomposition process. If the diagonal becomes too small, Kershaw alters the diagonal to stabilize the decomposition. The following adjustment is proposed by Kershaw and is currently implemented in FACT (with $\epsilon = 2 \times 10^{-48}$):

$$\begin{aligned}
 &\text{do } i = 1, np \\
 &\quad \text{sum}_i = s_{ii} - \sum_{k=1}^{i-1} \{b_{ik} b_{ik} b_{kk}\} \\
 &\quad \eta_i = \max_{i \neq k} |s_{ik}| \\
 &\quad \text{if } \left(\text{sum}_i^2 < \epsilon \eta_i^2 \right) \text{ then} \\
 &\quad \quad b_{ii} = \text{sgn} \left(\frac{1}{\sqrt{\epsilon \eta_i^2}}, \text{sum}_i \right) \\
 &\quad \text{else} \\
 &\quad \quad b_{ii} = \frac{1}{\text{sum}_i} \quad (\text{same as basic algorithm above}) \\
 &\quad \text{end if} \\
 &\text{end do}
 \end{aligned} \tag{3.4.1.4}$$

The second step involves Conjugate Gradient (CG) iterations starting with the initial guess of the solution vector set to $\mathbf{x} = \mathbf{x}_0 = \mathbf{0}$ (recall that the solution vector represents the change in hydraulic head at each outer iteration and as one approaches steady-state conditions the new time solution becomes invariant). The CG recursive equations are as follows:

FACT CODE MANUAL

$$\begin{aligned}
& \mathbf{x}_0 = \text{"initial guess"} \\
& \mathbf{r}_0 = \mathbf{y} - \mathbf{S}\mathbf{x}_0 \\
& \mathbf{p}_0 = \mathbf{B}^{-1}\mathbf{r}_0 \\
& \mathbf{q}_0 = \mathbf{S}\mathbf{p}_0 \\
& \text{do } k = 1, \dots, \\
& \quad \alpha_k = \frac{\langle \mathbf{r}_{k-1}, \mathbf{B}^{-1}\mathbf{r}_{k-1} \rangle}{\langle \mathbf{p}_{k-1}, \mathbf{q}_{k-1} \rangle} \\
& \quad \mathbf{x}_k = \mathbf{x}_{k-1} + \alpha_k \mathbf{p}_k \\
& \quad \mathbf{r}_k = \mathbf{r}_{k-1} - \alpha_k \mathbf{q}_k \\
& \quad \beta_k = \frac{\langle \mathbf{r}_{k+1}, \mathbf{B}^{-1}\mathbf{r}_{k+1} \rangle}{\langle \mathbf{r}_k, \mathbf{B}^{-1}\mathbf{r}_k \rangle} \\
& \quad \mathbf{p}_{k+1} = \mathbf{B}^{-1}\mathbf{r}_{k+1} + \beta_k \mathbf{p}_k \\
& \quad \mathbf{q}_{k+1} = \mathbf{S}\mathbf{p}_{k+1} \\
& \text{end do}
\end{aligned} \tag{3.4.1.5}$$

where

- k inner loop counter
- \mathbf{S} symmetric LHS coefficient matrix
- \mathbf{B} decomposed pre-conditioner matrix of \mathbf{S}
- \mathbf{x}_k solution vector at k^{th} iteration
- \mathbf{y} RHS vector
- \mathbf{r}_k residual vector k^{th} iteration
- \mathbf{p}_k search direction vector at k^{th} iteration
- \mathbf{q}_k conjugate direction vector at k^{th} iteration
- α_k minimization parameter for solution and residual vector at k^{th} iteration
- β_k conjugate parameter for search vector at k^{th} iteration

This scheme is repeated until either: (1) the L_2 norms of the solution and residual vectors are less than a prescribed tolerance criterion, ϵ_{inner} , or (2) the maximum allowable number of iterations is reached, maxit. The relative error criteria are given as:

$$\frac{\|\mathbf{x}_{i+1} - \mathbf{x}_i\|_2}{\|\mathbf{h}_m + \mathbf{x}_{i+1}\|_2} < \epsilon_{\text{inner}} \tag{3.4.1.6a}$$

$$\frac{\|\mathbf{r}_{i+1}\|_2}{\|\mathbf{h}_m + \mathbf{x}_{i+1}\|_2} = \frac{\|\mathbf{S}\mathbf{x}_{i+1} - \mathbf{y}_i\|_2}{\|\mathbf{h}_m + \mathbf{x}_{i+1}\|_2} < \epsilon_{\text{inner}} \tag{3.4.1.6b}$$

where the error tolerance placed upon the PCG solver (sometimes referred to as our inner iteration loop) is computed based on

$$\epsilon_{\text{inner}} = \max\left(10^{-6}, 10^{-4} \epsilon_{\text{outer}}\right) \quad (3.4.1.7)$$

and the maximum number of inner PCG iterations is determined by

$$\text{maxit} = 2 * \min(\text{np}, 400) \quad (3.4.1.8)$$

In theory the number of iterations required to achieve the exact solution will not exceed the number of unknowns (np). However, due to finite arithmetic some number greater than np may be required. In general, for large nodal problems the number of iterations required becomes significantly less than the maximum expressed by Eq. (3.4.1.8). As Eq. (3.4.1.7) indicates, we have placed a more stringent level of convergence (i.e., three orders of magnitude) on our PCG solver (the inner loop) than on our N-R/Picard non-linear solvers (the outer loop). The magnitude of this multiplier is somewhat arbitrary, but experience suggests that two to three orders of magnitude is optimal.

3.4.2 Asymmetric PCG Solver

For solving large sparse asymmetric matrix equations, the PCG/ORTHOMIN algorithm has emerged as one of the most promising. The ORTHOMIN scheme presented by Behie and Winsome (1982) is well suited for solving these matrices and also maintains the property of guaranteed convergence for type M matrices. This version may be considered as another variant of the standard PCG procedure described in Section (3.4.1). Indeed, their formulations are quite similar. The full ORTHOMIN procedure is given as follows.

The asymmetric PCG/ORTHOMIN solver implemented into FACT is based on a two-step procedure developed by Behie and Winsome (1982). It is used in FACT to solve the system of algebraic equations resulting from: (1) the application of the N-R technique to the finite element flow equations and (2) the direct application to the linear set of finite element solute transport equations.

We wish to solve the linear algebraic problem

$$\mathbf{Ax} = \mathbf{y} \quad (3.4.2.1)$$

where the finite element coefficient matrix, \mathbf{A} , is a asymmetric matrix that is diagonally dominant under most circumstances (e.g., for solute transport diagonal dominance becomes weak for high cell Peclet numbers). The first step of this PCG algorithm involves preconditioning of \mathbf{A} by computing its incomplete Crouts decomposition (i.e., the diagonal of the upper triangular matrix is assumed to be unity) in the form

$$\mathbf{A} \rightarrow \mathbf{B} = \mathbf{LU} \quad (3.4.2.2)$$

where in FACT the preconditioner matrix, \mathbf{B} , is also asymmetric and employs the following storage scheme

$$\mathbf{B} = \begin{bmatrix} \frac{1}{l_{11}} & u_{12} & u_{13} & u_{14} & \cdots \\ l_{21} & \frac{1}{l_{22}} & u_{23} & u_{24} & \cdots \\ l_{31} & l_{32} & \frac{1}{l_{33}} & u_{34} & \cdots \\ l_{41} & l_{42} & l_{43} & \frac{1}{l_{44}} & \cdots \\ \vdots & \vdots & \vdots & \vdots & \ddots \end{bmatrix} \quad (3.4.2.3)$$

The actual decomposition is performed such that zero fill-in occurs. During the decomposition process no adjustments are made for pivoting. It is assumed that the diagonal dominance of \mathbf{A} is sufficient enough such that no modification to the diagonal to enhance stability is warranted. The basic algorithm employed for performing this incomplete decomposition is:

$$\begin{aligned} &\text{do } i = 1, np \\ &\quad \text{do } j = 1, i-1 : \text{lower triangular portion of } i^{\text{th}} \text{ row} \\ &\quad \quad b_{ij} \equiv l_{ij} = a_{ij} - \sum_{k=1}^{j-1} \{l_{ik} u_{kj}\} = a_{ij} - \sum_{k=1}^{j-1} \{b_{ik} u_{kj}\} \\ &\quad \text{end do} \\ &\quad : \text{diagonal of } i^{\text{th}} \text{ row} \\ &\quad \quad l_{ii} = a_{ii} - \sum_{k=1}^{i-1} \{l_{ik} u_{ki}\} = a_{ii} - \sum_{k=1}^{i-1} \{b_{ik} u_{ki}\} \\ &\quad \quad b_{ii} = \frac{1}{l_{ii}} \\ &\quad \text{do } j = i+1, np : \text{upper triangular portion of } i^{\text{th}} \text{ row} \\ &\quad \quad b_{ij} = u_{ij} = \frac{1}{l_{ii}} \left[a_{ij} - \sum_{k=1}^{i-1} \{l_{ik} u_{kj}\} \right] = b_{ii} \left[a_{ij} - \sum_{k=1}^{i-1} \{b_{ik} u_{kj}\} \right] \\ &\quad \text{end do} \\ &\text{end do} \end{aligned} \quad (3.4.2.4)$$

The second step involves orthogonalization iterations starting with the initial guess of the solution vector set to $\mathbf{x} = \mathbf{x}_0 = \mathbf{0}$ (recall that the solution vector represents the change in hydraulic head or solute concentration at each outer iteration and as one approaches steady-state conditions the new time solution becomes invariant). The ORTHOMIN recursive equations are as follows

```

x0 = "initial guess"
r0 = y - Ax0
do k = 1, ...,
  vk = B-1rk-1
  if (k = 1) then
    pk = vk
  else
    do i = 1, k - 1
      βki =  $\frac{\langle \mathbf{q}_i, \mathbf{A} \mathbf{v}_k \rangle}{\langle \mathbf{q}_i, \mathbf{q}_i \rangle}$ 
    end do
    pk = vk -  $\sum_{i=1}^{k-1} \beta_k^i \mathbf{p}_i$ 
  end if
  qk = Apk
  αk =  $\frac{\langle \mathbf{q}_k, \mathbf{r}_{k-1} \rangle}{\langle \mathbf{q}_k, \mathbf{q}_k \rangle}$ 
  xk+1 = xk + αkpk
  rk+1 = rk - αkpk
end do

```

(3.4.2.5)

where

k inner loop counter
 i inner iteration index
 A LHS coefficient matrix
 B decomposed pre-conditioner matrix of $\overline{\mathbf{A}}$
 x_k solution vector at kth iteration
 y RHS vector
 r_k residual vector at kth iteration
 p_k search direction vector at kth iteration
 q_k conjugate direction vector at kth iteration
 v_k intermediate convenience vector for computational needs at kth iteration
 α_k minimization parameter for solution and residual vector at kth iteration
 β_kⁱ ith component conjugate parameter for search vector at kth iteration

This scheme relies on the same convergence criteria logic and maximum number of inner iterations as given above for the symmetric solver (see bottom part of Section (3.4.1))

The above algorithm requires core memory storage of arrays \mathbf{p}_i and \mathbf{q}_i for all previous iterations ($i=1,2,\dots,k-1$). The computational effort further increases with the number of iterations, as well. In addition, as the number of orthogonalizations increases, round-off errors can become unacceptable. These difficulties are circumvented by noting that in practice not all n_p orthogonalizations are required. In view of this, it is advantageous to limit the number of orthogonalizations to a prescribed value, n_{orth} . In this way, the orthogonalization procedure is restarted at every $(n_{orth}+1)$ iteration. The actual number of orthogonalizations required to achieve good convergence is problem dependent. Experience has shown that a value of $n_{orth}=40$ is adequate.

As mentioned earlier for transient calculations where the LHS matrix, \mathbf{A} , is time-independent, the incomplete decomposition of the pre-conditioner can be stored during the first time step/iteration and then reused during all subsequent iterations and time steps. Sizable savings in the computational effort results since the LHS matrix no longer must be recreated at each time step and the incomplete decomposition step has to only be performed once.

3.5 Spatial and Temporal Discretizations

Varying levels of spatial discretization of the solution domain are performed automatically in the FACT code. FACT uses a right-handed Cartesian coordinate system. In the areal view a rectangular grid is used to represent the 3D model domain. The vertical planes (i.e., the x and y planes) are constrained to be flat surfaces that are perpendicular to each other; therefore, the resulting elements are rectangular in shape areally and their shape remains invariant in the vertical direction. The overall 3D mesh is structured whereby each horizontal layer of elements spans the entire areal extent. However, the horizontal layers of nodes are not restricted to planar surfaces (i.e., vertically distorted elements are allowed). Each element is represented by a linear (8-noded) finite element that is rectangular in the horizontal direction. The vertical coordinate (z -axis) is in the opposite direction relative to the gravity vector.

As specified by the user, FACT will automatically generate a grid with nodes and elements numbered sequentially sweeping first along the x -axis and then along the y -axis to form a horizontal nodal/elemental plane. The first horizontal plane resides at the bottom of the model and subsequent planes are created sequentially one stacked on top of the next. The areal grid is specified by the user through inputting an array of x and y -axis grid line locations. If the distance between adjacent horizontal (x and y -axes) planes is uniform (i.e., flat planar surfaces of nodes), then the user can specify the vertical grid spacing by only having to input an array of z -axis coordinates. For vertically distorted meshes however, the user is required to input the entire set of nodal vertical coordinates. A minimum of one element in length (two grid planes) is required for each of the three (x,y,z) coordinate directions.

The 3-D model contains the entire system, which is considered as one unit where different materials are accommodated by assigning different sets of material properties for different elements. For example, aquifer and aquitard regions are handled by the use of

differing material properties specified at those elements whose centroids correspond to their locations, respectively.

An example of a vertically distorted mesh, illustrating the node and element numbering conventions, is presented in Figs. 3.5.1 and 3.5.2. This example consists of four elements in the x-direction, four in the y-direction, and two in the z-direction, for a total of 32 elements and 75 nodes representing the entire mesh. Figure 3.5.1 contains an areal view of the mesh corresponding to its first horizontal plane; while, Fig. 3.5.2 contains a vertical view of the meshing corresponding to its first y-axis plane. The actual system boundaries are shown overlaid on the areal mesh in Fig. 3.5.1. The irregular system boundary is accommodated by assigning a non-positive (usually set to zero) material number to elements outside the region of interest (i.e., inactive elements) also shown in both figures as shaded areas. Note that inactive elements can exist anywhere throughout the mesh and do not necessarily have to extend the entire vertical extent at any given areal location (e.g., see elements numbered 3 and 19 in Fig. 3.5.2). A more in depth example of mesh capabilities, including boundary condition specification, will be presented in Section 5.

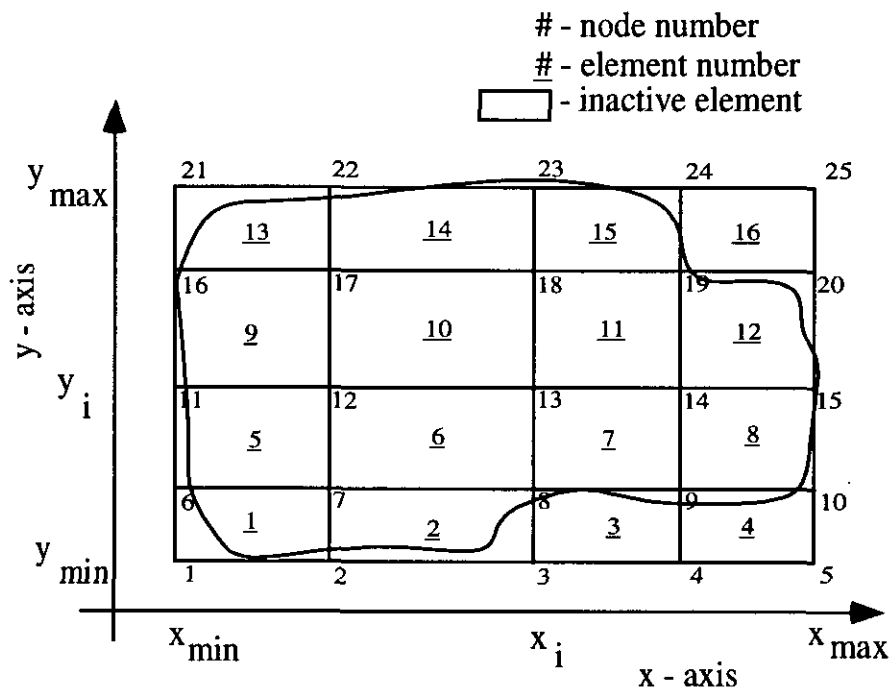


Fig. 3.5.1. Areal Slice through Example Mesh Illustrating Nodal and Elemental Numbering Conventions.

In FACT, temporal discretization can also be performed either manually or automatically if required. Under the manual option absolute time values (points) are inputted by the user. Internally FACT computes the appropriate time step size and then marches through time consistent with the inputted time table. Alternatively, the user can employ the automatic time step generation option in FACT. New time step sizes and time values are computed at the end of each time step by using the simple algorithm:

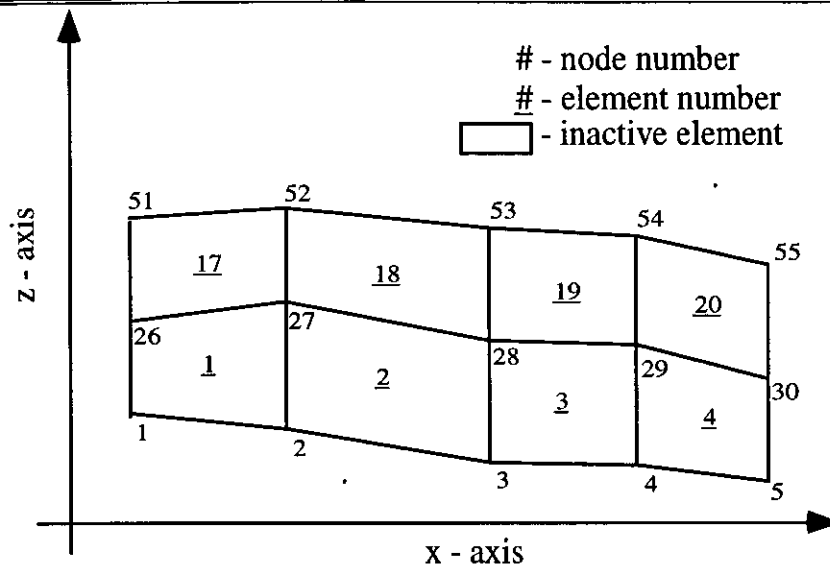


Fig. 3.5.2. Vertical Slice through Example Mesh Illustrating Nodal and Elemental Numbering Conventions.

$$\Delta t_n = \begin{cases} \frac{tmend(1) - tmst(1)}{nsti(1)} & 1 \leq n \leq nsti(1) \\ \frac{tmend(2) - tmst(2)}{nsti(2)} & nsti(1) + 1 \leq n \leq nsti(1)nsti(2) \\ \vdots & \vdots \\ \frac{tmend(nsi) - tmst(nsi)}{nsti(nsi)} & \prod_{i=1}^{nsi-1} nsti(i) + 1 \leq n \leq nts \end{cases} \quad (3.5.1)$$

where

nsi number of simulation intervals

tmst starting time of simulation interval

tmend ending time of simulation interval

nsti number of time steps between tmst and tmend

nts total number of time steps

and

$$t_n = t_{n-1} + \Delta t_n \quad (3.5.2)$$

3.6 Material Mass Balance Options

In groundwater modeling, as well as numerical modeling in general, several factors influence the numerical accuracy obtained. At several locations in previous sections some of these factors were alluded to and suggestions as to how to minimize them were given. In order to estimate the overall/relative accuracy (or error) of a given simulation, a material mass balance over the entire solution domain should be performed. In FACT there exists such a mass balance option for either a flow or transport simulation. It is

essential that the resulting mass balance errors be sufficiently small for the numerical solutions to the flow and transport equations. Sufficiently small is a relative term that may be better stated in the following way. It is desirable (a rule of thumb) to maintain numerical errors at least one-to-two orders of magnitude lower than those errors associated with modeling assumptions (e.g., conceptual model, source/sink terms, boundary conditions, material properties). In many cases modeling errors are unknown (or only known qualitatively) and under these conditions we typically try to minimize numerical errors as much as possible given the constraints of available computer resources and run time durations.

Since the accuracy of the numerical approximations to the flow and transport equations is mesh dependent (i.e., a mixture of first and second order convergence rates), the mass balance errors are affected by our choices in local/global spatial and temporal resolution. Computing mass balance errors at every individual node requires more CPU than is deemed necessary. Therefore, in FACT we employ a mass balance approach that estimates the overall mass error associated with the mesh domain that is computed each time step. This procedure generates an error norm that can be used as an indicator of the global accuracy of the numerical solution. It is conceivable that local error contributions from one region of the mesh could cancel out with contributions from other regions; thus, producing a greatly reduced "computed" error norm. The likelihood of such an occurrence is deemed to be remote and as such for efficiency we compute only a global indicator.

A derivation of this procedure, first for the flow equation and then for the more complicated transport equation, follows. The entire solution (mesh) domain is referred to as Ω_R , while its boundary is referred to as σ_B . Inactive elements are outside the domain and in many cases help in defining the domain's boundaries. Nodes completely surrounded by inactive elements are inactive, while any nodes adjacent to an active element become active. The scheme employed for performing material balance calculations is based upon the work of Huyakorn and Pinder (1983, see page 209 for additional information).

3.6.1 Flow Equation Mass Balance

An overall mass balance can be derived based on the flow equation, Eq. (2.1.17)

$$0 = (C + S_w S_s) \frac{\partial h}{\partial t} + \nabla \cdot \mathbf{U} - q \quad (3.6.1.1)$$

where the Darcy velocity vector is expressed as

$$\mathbf{U} = -k_{rw} \mathbf{K} \nabla h \quad (3.6.1.1a)$$

and the source term, q , has been included to take into account any contributions from point sources/sinks that may exist within the solution domain. Within FACT it is more convenient to consider specified surface recharge and surface fluxes as distributed sources. Note that distributed sources (e.g., line sources such as wells and surface

recharge) are ultimately allocated out to individual nodes and therefore, can for mass balance checking purposes be considered as point sources. Grouping together all nodes containing a point source, as well as those distributed sources that are converted, the following expression can be used to represent them

$$q = \sum_{P=1}^{n_w} q_P = \sum_{P=1}^{n_s} \left[\frac{Q_P}{V_P} \right] \delta(\mathbf{x} - \mathbf{x}_P) \quad (3.6.1.2)$$

where n_w represents the total number of nodes containing point sources/sinks.

The mass balance over the whole domain can be obtained by integrating Eq. (3.6.1.1) and applying Green's (divergence) theorem to the advective term. Thus, one obtains

$$\begin{aligned} 0 &= \int_{\Omega_R} \left\{ (C + S_w S_s) \frac{\partial h}{\partial t} + \nabla \cdot \mathbf{U} - q \right\} d\Omega_R \\ &= \int_{\Omega_R} \left\{ (C + S_w S_s) \frac{\partial h}{\partial t} \right\} d\Omega_R + \int_{\sigma_B} (\mathbf{n} \cdot \mathbf{U}) d\sigma_B - \int_{\Omega_R} q d\Omega_R \end{aligned} \quad (3.6.1.3)$$

The second integral in Eq. (3.6.1.3) represents the net material flux across the whole boundary. The first and third integrals represent, respectively, the net rate of mass storage and the net rate of mass production (owing to well injection or extraction, recharge, etc.) within the entire domain.

If the exact hydraulic head solution of Eq. (3.6.1.1), consistent with imposed boundary conditions, was known and then substituted into Eq. (3.6.1.3), that equation would be satisfied exactly (i.e., all three integrals would sum up to zero). However, if an approximate solution (such as the one obtained by FACT)

$$\tilde{h} = \sum_{J=1}^{np} \varphi_J(\mathbf{x}) h_J \quad (3.6.1.4)$$

is substituted into Eq. (3.6.1.3), the three integrals typically sum up to a non-zero result that corresponds to the rate of net material loss, $\dot{\epsilon}_F$, over the entire domain at that instant in time

$$\dot{\epsilon}_F = - \int_{\Omega_R} \left\{ (C + S_w S_s) \frac{\partial \tilde{h}}{\partial t} \right\} d\Omega_R + \int_{\sigma_B} U_n d\sigma_B + \int_{\Omega_R} q d\Omega_R \quad (3.6.1.5)$$

where the Darcy velocity normal to the boundary (incoming being positive by convention) can be estimated from

$$U_n = -\mathbf{n} \cdot \mathbf{U} = \mathbf{n} \cdot k_{rw} \mathbf{K} \nabla \tilde{h} \quad (3.6.1.5a)$$

The rate of net material loss, $\dot{\epsilon}_F$, represents our measure of overall numerical errors associated with the solution of the flow equation. The three integrals of Eq. (3.6.1.5) represent the overall mass accumulation within the domain, the net transport of material across the domain's boundaries, and the net production of material within the domain, respectively. Equation (3.6.1.5) expresses a global mass balance for the domain given the boundary conditions and source terms for a specific problem. However, the integrals in Eq. (3.6.1.5) are not in a convenient form for evaluation within the FACT framework. Ideally, we would like to transform these integrals into forms that take advantage of the Galerkin integrals already computed during the solution phase of FACT. Thereby, making the mass balance checking as computationally efficient as possible. This can be easily accomplished making use of certain properties of the basis functions.

The chosen nodal basis functions used in the Galerkin approximations have only local support (i.e., are non-zero only over the limited range of their neighboring nodes). The set of basis functions chosen are conformal and as such possess the following useful properties:

$$\sum_{K=1}^{n_B} \varphi_K(\mathbf{x}) = 1 \quad \text{for all } \mathbf{x} \text{ on boundary } \sigma_B \quad (3.6.1.6a)$$

$$\sum_{I=1}^{n_P} \varphi_I(\mathbf{x}) = 1 \quad \text{for all } \mathbf{x} \text{ within domain } \Omega_R \quad (3.6.1.6b)$$

where

n_B number of nodes on the whole boundary

n_P total number of nodes within whole solution domain

Making use of Eqs. (3.6.1.6), Eq. (3.6.1.5) can be re-expressed in the form

$$\dot{\epsilon}_F = - \sum_{I=1}^{n_P} F_I^S + \left[\sum_{K=1}^{n_B} F_K^B + \sum_{P=1}^{n_W} F_P^W \right] \quad (3.6.1.7)$$

where

$$F_I^S = \sum_{J=1}^{n_P} \left\{ \int_{\Omega_R} (C + S_w S_s) \varphi_I \varphi_J d\Omega_R \right\} \frac{dh_J}{dt} \quad (3.6.1.8a)$$

$$F_K^B = \int_{\sigma_B} \varphi_K U_n d\sigma_B \quad (3.6.1.8b)$$

$$F_P^W = \sum_{P=1}^{n_W} \int_{\Omega_R} \varphi_P \left[\frac{Q_P}{V_P} \right] \delta(\mathbf{x} - \mathbf{x}_P) d\Omega_R = \sum_{P=1}^{n_W} Q_P \quad (3.6.1.8c)$$

FACT CODE MANUAL

Note that the indices refer to specific nodes: **I** and **J** refer to the total set of active nodes making up the mesh domain; **K** refers to those nodes lying on the boundary (excluding nodes whose flux boundary conditions have been converted to point sources); and **P** refers to those nodes containing a point source or sink.

A considerable savings in CPU time can be achieved if the mass matrix in Eq. (3.6.1.8a) is lumped. Lumping of this mass matrix is also consistent with the formulation of the discretized set of flow equations solved by FACT. Following a similar derivation as was done in Section 3.1.5, Eq. (3.5.1.6a), the storage term, can be integrated and mass lumped to give the elemental contribution

$$F_i^S = \langle C + S_w S_s \rangle M_{ii}^L \frac{dh_i}{dt} \quad (3.6.1.9)$$

The global array associated with the storage term is already required for the setting up of the flow equations in FACT at each time step. This global storage array is saved for later mass balance calculations, if requested.

While the evaluation of the source term integral is straightforward, the evaluation of the boundary integral is more involved. Eq. (3.6.1.8b) is the boundary integral corresponding to the nodal fluid flux (actually a volumetric flow rate) at the *k*'th boundary node. In the finite element formulation a flux on a boundary, when allocated out to the appropriate boundary nodes, appears identical to a point source placed at that boundary node when viewing the discrete set of flow equations. Thus, from the viewpoint of the discrete set of flow equations, boundary fluxes and point sources (which include distributed/line sources and recharge) can be grouped together as implied by the brackets in Eq. (3.6.1.7). We shall refer to the entries of this combined group as nodal fluid fluxes that can reside either on the boundary or within the domain.

Each nodal fluid flux, say at the *k*'th node, can be computed by performing back substitution of the computed hydraulic head solution into the discrete finite element flow equation written for the *k*'th node. The back substitution is performed on discrete flow equations that have not been altered by boundary conditioning (i.e., type 1, 2, or 3 BC's). Boundary nodal fluid fluxes computed in this manner avoid the problems of discontinuities resulting from the potential discontinuities that arise when velocities at the boundary nodes of individual elements are computed. In FACT after the creation (i.e., elemental assemblage) of the global set of discrete flow equations and prior to application of boundary conditions we have the system of equations (see Section 3.1.1 for more details)

$$\mathbf{B}^F \frac{d\mathbf{h}}{dt} + \mathbf{A}^F \mathbf{h} - \mathbf{F}^F = \mathbf{0} \quad (3.6.1.10)$$

where

\mathbf{B}^F storage matrix prior to applying BC's

\mathbf{A}^F seepage matrix prior to applying BC's

\mathbf{F}^F nodal fluid flux array (actually nodal volumetric flow rates)

Only the matrix members associated with those global nodes where nodal fluid flux calculations are requested are stored.

Performing backward Euler (fully implicit) differencing on Eq. (3.6.1.10), as was done in Section 3.1.8, rearranging terms, and substituting in our approximate head solution, $\tilde{\mathbf{h}}$, we arrive at our working equation for computing the nodal fluid fluxes at time step (n+1)

$$\mathbf{F}^F = \left[\mathbf{A}^F + \frac{\mathbf{B}^F}{\Delta t} \right] \tilde{\mathbf{h}}^{n+1} - \left[\frac{\mathbf{B}^F}{\Delta t} \right] \tilde{\mathbf{h}}^n \quad (3.6.1.11)$$

Since the above matrices can be time varying, for transient applications these stored terms must be updated prior to mass balance computations. As pointed out above the nodal fluid flux array contains both the boundary nodes, as well as any other nodes within the domain that contains source contributions of any form. We can express this array by

$$\mathbf{F}^F \Rightarrow \left[\mathbf{F}^B, \mathbf{F}^W \right]^T \quad (3.6.1.12)$$

where B refers to boundary nodes and W refers to internal nodes with sources or sinks. This array contains nodal volumetric flow rates that are written to an output file for potential use in material balance checking for a subsequent transport simulation.

Upon the successful completion of a time step and if mass balance checking is requested, the nodal fluid fluxes are computed from Eq. (3.6.1.11) for all nodes. We now have an efficient method for computing the rate of net material loss defined by Eq. (3.6.1.7) and shown below in terms of nodal fluid fluxes as

$$\dot{\epsilon}_F = - \sum_{I=1}^{np} F_I^S + \sum_{K=1}^{np} F_K^F \quad (3.6.1.12)$$

In FACT, we compute nodal fluid fluxes for all active nodes. For those nodes which are not boundary flux nodes or internal point sinks or sources, the computed nodal fluid flux should be near zero.

For convenience, we also compute a normalized mass balance error defined as

$$\tilde{\epsilon}_F = \frac{\dot{\epsilon}_F}{\sum_{I=1}^{np} |F_I^S| + \sum_{K=1}^{np} |F_K^F|} \quad (3.6.1.13)$$

where the normalization factor is somewhat arbitrary but well behaved.

We also compute the cumulative mass balance error within the domain at each time level as

$$\epsilon_F^{n+1} = \sum_{k=1}^n \dot{\epsilon}_F^k \Delta t_k \quad (3.6.1.14)$$

3.6.2 Transport Equation Mass Balance

No transport equation mass balance performed. Mass balance algorithm not completed.

4 Verification Tests and Results

The numerical schemes of FACT were tested extensively using two groups of example problems selected to represent diversified field conditions. The main objectives of these tests are to verify the capability and demonstrate efficiency and robustness of the numerical schemes and modules used for various solution options offered by the code.

The first group of problems consist of ten groundwater flow problems covering a wide range of boundary conditions in the saturated and unsaturated zones of subsurface systems of various hydrogeologic configurations. The simulated results obtained from the flow modules of FACT were compared with the analytical solutions and/or with other well documented numerical codes. The test examples considered are described in Section 4.1 and listed as follows:

1. Steady-state, one-dimensional flow in a confined aquifer.
2. Steady-state, one-dimensional flow in an unconfined aquifer.
3. Steady-state flow through a heterogeneous subsurface system.
4. Unconfined aquifer subject to a combined recharge/drain boundary condition.
5. Radial flow to a well in a confined aquifer (Theis solution).
6. Radial flow to a well in an anisotropic confined aquifer.
7. Radial flow to a well in a leaky confined aquifer.
8. Radial flow to a well in an unconfined aquifer (Neuman solution).
9. Transient flow in an unconfined aquifer.
10. Unsaturated vertical soil column.

The second group of problems involves contaminant transport in the saturated zones of subsurface systems of various configurations. Five problem cases were used to test the transport modules of the FACT code. The following problem cases are described in Sections 4.2 and 4.3:

1. One-dimensional saturated solute transport in a uniform flow field.
2. Two-dimensional saturated solute transport in a uniform flow field.
3. Three-dimensional saturated solute transport in a uniform flow field.
4. One-dimensional saturated solute transport in a uniform flow field with first-order mobile/immobile mass transfer (van Genuchten and Wierenga analytical cases)
5. One-dimensional saturated solute transport in a uniform flow field with first-order mobile/immobile mass transfer (VERSE-LC comparison)

The results for these problems were verified against the analytical and numerical transport solutions.

In the following three sections, detailed descriptions of the test problems, physical configurations, and hydrogeologic properties of the groundwater systems, spatial and temporal discretizations, solution schemes used, and numerical results are presented.

FACT CODE MANUAL

The above test examples do not generally reflect large field-scale applications of FACT. However, FACT was designed and has been employed for numerous large field-scale applications typically ranging in node size from 50 to 100 thousand nodes (one 200 thousand node problem has also been solved). The details of these types of field-scale applications is too large to place in this report. The interested reader can view these types of applications in the following references (local chosen sites at the Savannah River Site):

- Old Burial Ground Application (OBG) - 63,600 nodes in size and models the flow and transport of tritium from buried tritiated waste forms to where it outcrops at the seepage faces of Fourmile Branch tributary. Local heterogeneity is handled by having each active finite element within the mesh domain a unique material type. Material type is based on detailed lithologic data in terms of mud fraction fitted over the entire mesh domain. Alternative remedial corrective actions plans are investigated (capping of the OBG). This model contained buried tritiated waste forms in the vadose zone that migrated downward into the underlying water table and then migrated somewhat horizontally in the saturated zones outcropping at Fourmile Branch. See reference: G. P. Flach, L. L. Hamm, M. K. Harris, P. A. Thayer, J. S. Haselow and A. D. Smits, "Groundwater Flow and Tritium Migration from the SRS Old Burial Ground to Fourmile Branch (U)," WSRC-TR-96-0037, 1996.
- TNX Area - 55,575 nodes in size and models groundwater flow throughout the TNX complex down to the Savannah River. A proposed recovery well network for capturing a 500 µg/L TCE plume is investigated. Vertical re-circulation well technology is also considered. This models included both the vadose and several saturated zones, with vertical mesh resolution in the vadose and water table zones to adequately predict the vertical velocity field near the vertical re-circulation well. See Reference: R. L. Nichols, L. L. Hamm and W. F. Jones, "Numerical Modeling of the TNX Area Hybrid Groundwater Corrective Action (U)," WSRC-RP-95-787, August 1995.
- A/M Area - 200,168 nodes in size and models the zone of capture for an existing recovery well network located within the central A/M Area and for a planned recovery well network to be located in the northern sector. A large number of individual wells were contained within the model. The model consisted of the water table and several underlying confining units and aquifers. The piezometric head profile for the surface of the water table was fixed as Dirichlet boundary conditions based on the fitting of available well data. See Reference: D. G. Jackson and S. E. Aleman, "Three Dimensional Zone of Capture Analysis for the A/M-Area (U)," WSRC-RP-95-0843, May 1995.
- A/M Area - 318,291 nodes in size and models the zone of capture and transient transport of TCE to assess the expected overall performance of two vertical recirculation wells located in the Southern Sector of A/M Area. The model consists of a 3000 ft by 3000 ft mesh of the "Lost Lake" aquifer zone. The recirculation well boundary condition in FACT was used to model the two wells. See Reference: S. E. Aleman and L. L. Hamm, "Capture Zone Analyses of Two Airlift Recirculation Wells in the Southern Sector of A/M Area (U)," WSRC-TR-99-00203, July 1999.

The above examples illustrate a variety of features that FACT performs and it is highly recommended that the user study these references for ideas when attempting to solve a field-scale problem with FACT.

4.1 Groundwater Flow Problems

4.1.1 Steady-state, One-Dimensional Flow in a Confined Aquifer

Figure 4.1.1.1 illustrates two confined aquifers experiencing steady, one-dimensional flow. The test cases are designed to confirm correct implementation of the general head and river bed boundary conditions. The problems can be easily solved analytically.

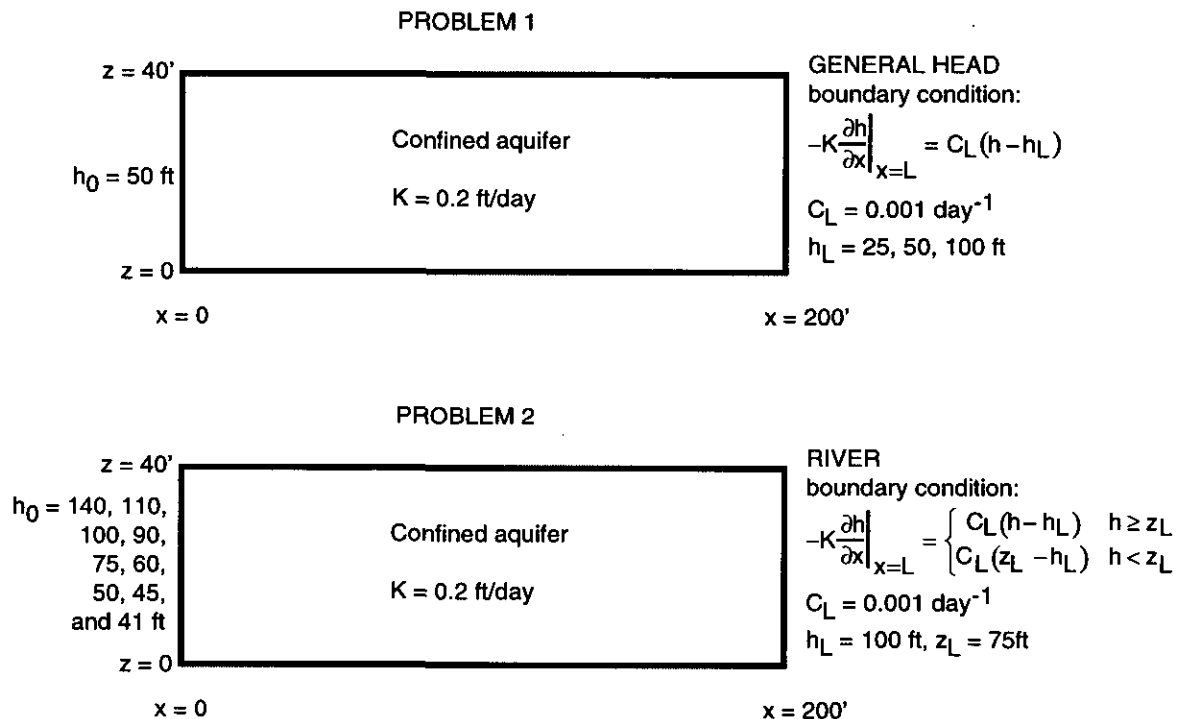


Fig. 4.1.1.1. Schematic diagram of a confined aquifer with a constant head boundary condition at $x = 0$ and either a general head (Problem 1) or river (Problem 2) boundary condition at $x = L$.

Analytic solution: Invoking the Dupuit assumption, the following governing equation can be developed for a confined aquifer (de Marsily, 1986, Eq. (5.3.11))

$$\nabla^2 h = \frac{\partial^2 h}{\partial x^2} + \frac{\partial^2 h}{\partial y^2} = \frac{S}{T} \frac{\partial h}{\partial t} + \frac{Q}{T} \quad (4.1.1.1)$$

For constant aquifer thickness, constant properties, one-dimensional steady flow and no recharge, Eq. (4.1.1.1) becomes

$$\frac{d^2 h}{dx^2} = 0 \quad (4.1.1.2)$$

FACT CODE MANUAL

For the boundary conditions of Problem 1

$$h = h_0 \quad @ \quad x = 0 \quad (4.1.1.3a)$$

$$-K \left. \frac{dh}{dx} \right|_{x=L} = C_L (h - h_L) \quad @ \quad x = L \quad (4.1.1.3b)$$

the solution can be derived using direct integration as

$$h = h_0 + \frac{h_L - h_0}{1 + \frac{K}{C_L L}} \frac{x}{L} \quad (4.1.1.4)$$

For the boundary conditions of Problem 2

$$h = h_0 \quad @ \quad x = 0 \quad (4.1.1.5a)$$

$$-K \left. \frac{dh}{dx} \right|_{x=L} = \begin{cases} C_L (h - h_L) & h \geq z_L \\ C_L (z_L - h_L) & h < z_L \end{cases} \quad @ \quad x = L \quad (4.1.1.5b)$$

the solution is

$$h = \begin{cases} h = h_0 + \frac{h_L - h_0}{1 + \frac{K}{C_L L}} \frac{x}{L} & h \geq z_L \\ h = h_0 + \frac{h_L - z_L}{1 + \frac{K}{C_L L}} \frac{x}{L} & h < z_L \end{cases} \quad (4.1.1.6)$$

FACT simulation and comparison: Figure 4.1.1.2 illustrates the FACT mesh chosen for both problems. Table 4.1.1.1 and Fig. 4.1.1.3 present the FACT results for Problem 1 in comparison with the analytic results. In order to test the river boundary condition the Darcy velocity is computed at node 11 ($x = 200'$, $y = 0'$, $z = 0'$) using the volumetric flow and the river boundary condition. The Darcy velocity is given by

$$U_x = \frac{Q}{A} \quad (4.1.1.7)$$

where the volumetric flow Q at node 11 is the result of the FACT mass balance computation (Group 11, IMBAL = 1) and the effective flow area A at node 11 is 400 ft². The Darcy velocity is also given by

$$U_x = \begin{cases} C_L (h - h_L) & h \geq z_L \\ C_L (z_L - h_L) & h < z_L \end{cases} \quad (4.1.1.8)$$

where h is hydraulic head at node 11 and $h_L = 100'$, $z_L = 75'$. Table 4.1.1.2 and Fig. 4.1.1.4 present the FACT results for Problem 2 which compares the two calculations of

Darcy velocity at node 11. FACT has excellent agreement with the analytic results for both problems.

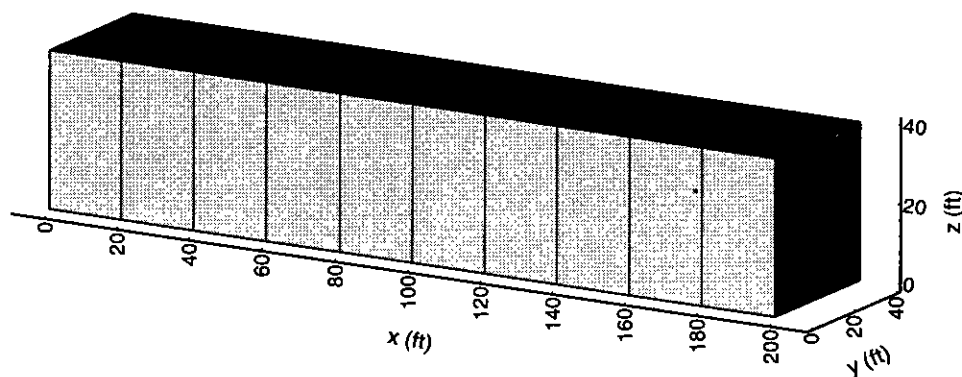


Fig. 4.1.1.2. FACT grid.

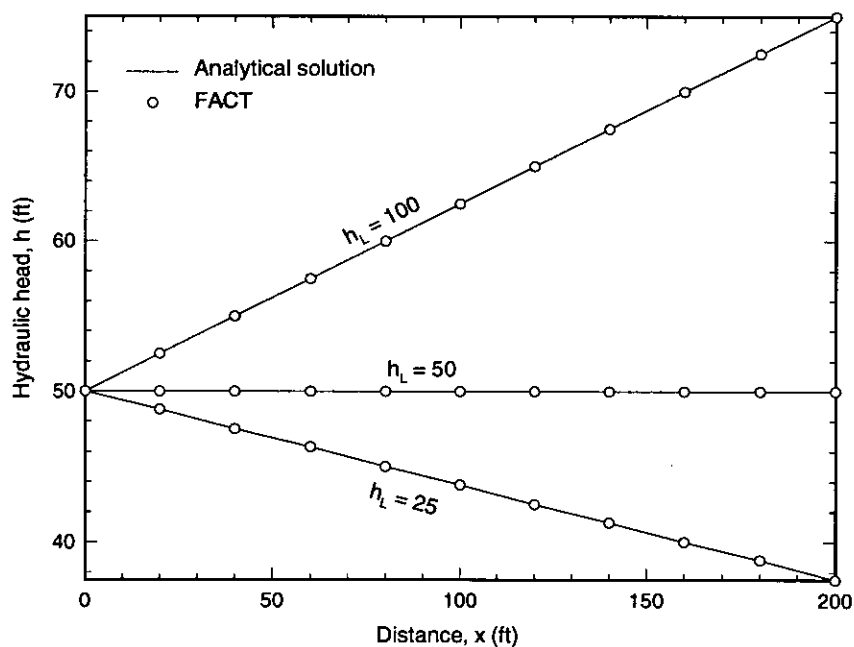


Fig. 4.1.1.3. Comparison of analytic solution to FACT numerical results for Problem 1.

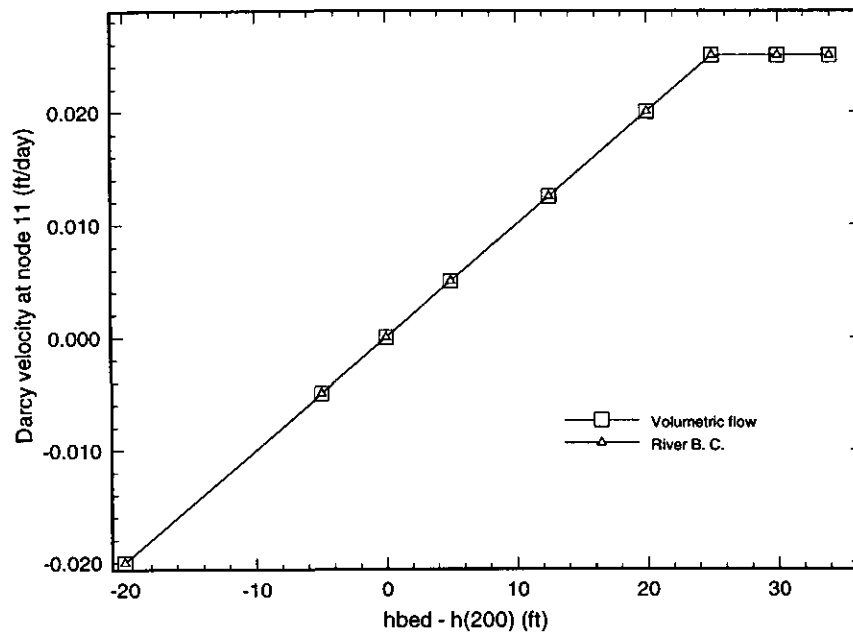


Fig. 4.1.1.4. FACT Darcy velocity for Problem 2.

Table 4.1.1.1

Comparison of analytic solution and FACT numerical results for Problem 1

x (ft)	$h_L = 25$ ft		$h_L = 50$ ft		$h_L = 100$ ft	
	Analytic (ft)	FACT (ft)	Analytic (ft)	FACT (ft)	Analytic (ft)	FACT (ft)
0	50.0	50.0	50.0	50.0	50.0	50.0
20	48.8	48.8	50.0	50.0	52.5	52.5
40	47.5	47.5	50.0	50.0	55.0	55.0
60	46.3	46.3	50.0	50.0	57.5	57.5
80	45.0	45.0	50.0	50.0	60.0	60.0
100	43.8	43.8	50.0	50.0	62.5	62.5
120	42.5	42.5	50.0	50.0	65.0	65.0
140	41.3	41.3	50.0	50.0	67.5	67.5
160	40.0	40.0	50.0	50.0	70.0	70.0
180	38.8	38.8	50.0	50.0	72.5	72.5
200	37.5	37.5	50.0	50.0	75.0	75.0

Table 4.1.1.2

FACT Darcy velocity at node 11 for Problem 2

h_0 (ft)	h_L (ft)	z_L (ft)	Volumetric flow		River bed B.C.	
			$h_{x=L}$ (ft)	U (ft/day)	$h_{x=L}$ (ft)	U (ft/day)
140	100	75	120	-0.02	120.0	-0.0200
110	100	75	105	-0.005	105.0	-0.0050
100	100	75	100	0	100.0	0.0000
90	100	75	95	0.005	95.0	0.0050
75	100	75	87.5	0.0125	87.5	0.0125
60	100	75	80	0.02	80.0	0.0200
50	100	75	75	0.025	75.0	0.0250
45	100	75	70	0.025	70.0	0.0250
41	100	75	66	0.025	66.0	0.0250

4.1.2 Steady-State, One-Dimensional Flow in an Unconfined Aquifer

Figures 4.1.2.1 and 4.1.2.2 illustrate a pair of unconfined aquifers experiencing steady, one-dimensional flow without and with recharge, respectively. The second problem is essentially FTWORK Problem 4.1.1 (GeoTrans, 1993). Both problems can be easily solved analytically.

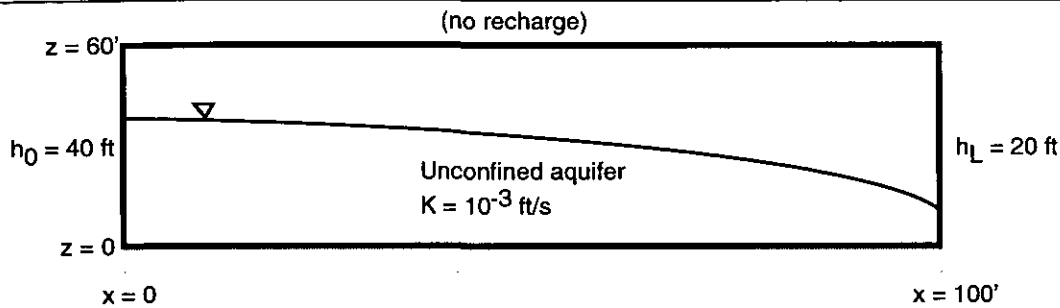


Fig. 4.1.2.1. Schematic diagram of an unconfined aquifer with no recharge and constant head boundary conditions (Problem 1).

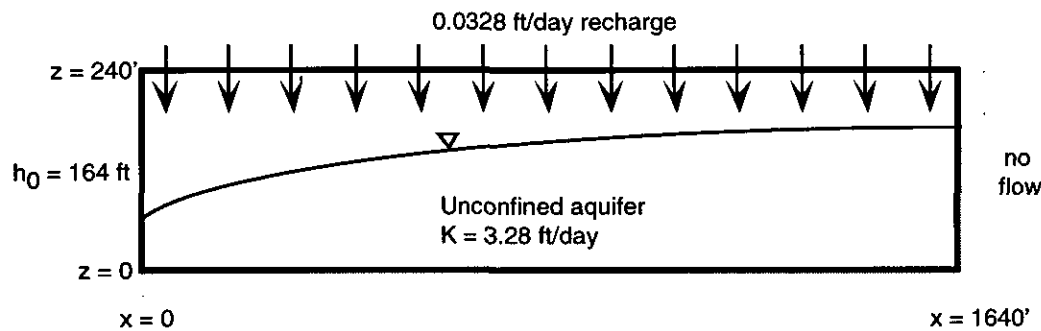


Fig. 4.1.2.2. Schematic diagram of an unconfined aquifer with recharge and mixed boundary conditions (Problem 2).

Analytic solutions: Invoking the Dupuit assumption (de Marsily, 1986, Eq. (5.1.1))) gives the following general expression for flow in an unconfined aquifer

$$\frac{\partial}{\partial x} \left[\int_{\sigma}^h K_{xx} dz \frac{\partial h}{\partial x} \right] + \frac{\partial}{\partial y} \left[\int_{\sigma}^h K_{yy} dz \frac{\partial h}{\partial y} \right] = \omega_d \frac{\partial h}{\partial t} + Q \quad (4.1.2.1)$$

For a horizontal confining unit ($\sigma = \text{constant}$), constant properties and one-dimensional steady flow, Eq. (4.1.2.1) becomes

$$\frac{d^2(h - \sigma)^2}{dx^2} = \frac{2Q}{K} \quad (4.1.2.2)$$

For the prescribed head boundary conditions

$$h = h_0 \quad @ \quad x = 0 \quad (4.1.2.3a)$$

$$h = h_L \quad @ \quad x = L \quad (4.1.2.3b)$$

the solution can be derived using direct integration as

$$(h - \sigma)^2 = (h_0 - \sigma)^2 + \left[(h_L - \sigma)^2 - (h_0 - \sigma)^2 \right] \frac{x}{L} + \frac{Q_{src} L^2}{K} \left(\frac{x}{L} \right) \left(1 - \frac{x}{L} \right) \quad (4.1.2.4)$$

where $Q_{src} = -Q$. For the boundary conditions

$$h = h_0 \quad @ \quad x = 0 \quad (4.1.2.5a)$$

$$\frac{dh}{dx} = 0 \quad @ \quad x = L \quad (4.1.2.5b)$$

the solution is

$$(h - \sigma)^2 = (h_0 - \sigma)^2 - \frac{Q_{src} L^2}{K} \left(\frac{x}{L} \right) \left(\frac{x}{L} - 2 \right) \quad (4.1.2.6)$$

FACT simulation and comparison: Figures 4.1.2.3 and 4.1.2.4 present the two grids chosen for FACT simulations. Each grid is one element thick in the y-direction. The mesh for problem 1 contains 10×6 elements in the x-z plane for a total of 60 elements. The corresponding number of nodes is $11 \times 2 \times 7 = 154$. The second mesh contains $20 \times 1 \times 1 = 20$ elements and $21 \times 2 \times 2 = 84$ nodes. Table 4.1.2.1 and Figs: 4.1.2.5 and 4.1.2.6 present the analytic and FACT results for an optimal selection of the pseudo-soil property parameters. The agreement is excellent for both problems. Figures 4.1.2.7 and 4.1.2.8 show the RMS head difference between the FACT and analytic results for other values of the pseudo-soil property parameters. Observe that the quality of the agreement is not strongly dependent on these parameters selections. Notice that the best results were obtained when UPSTR = 1.0 and S_{wr} is small.

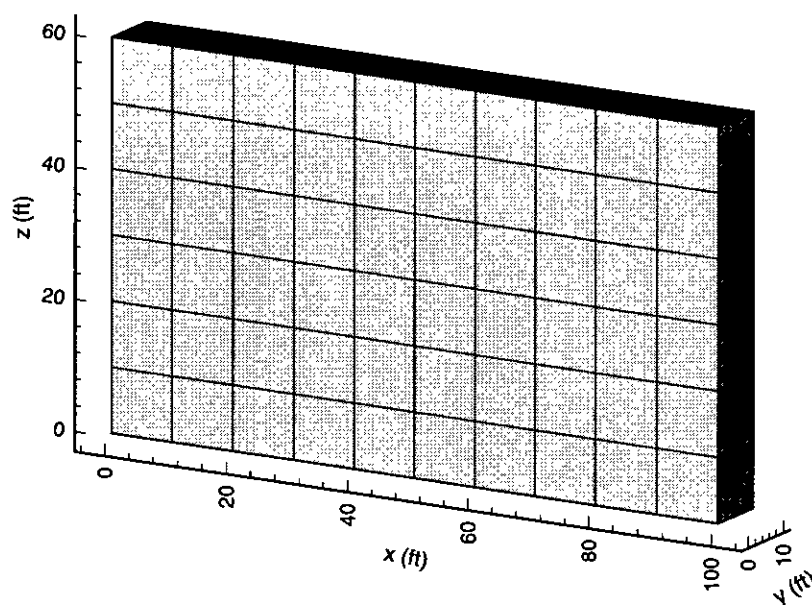


Fig. 4.1.2.3. FACT grid for Problem 1 shown in Fig. 4.1.2.1.

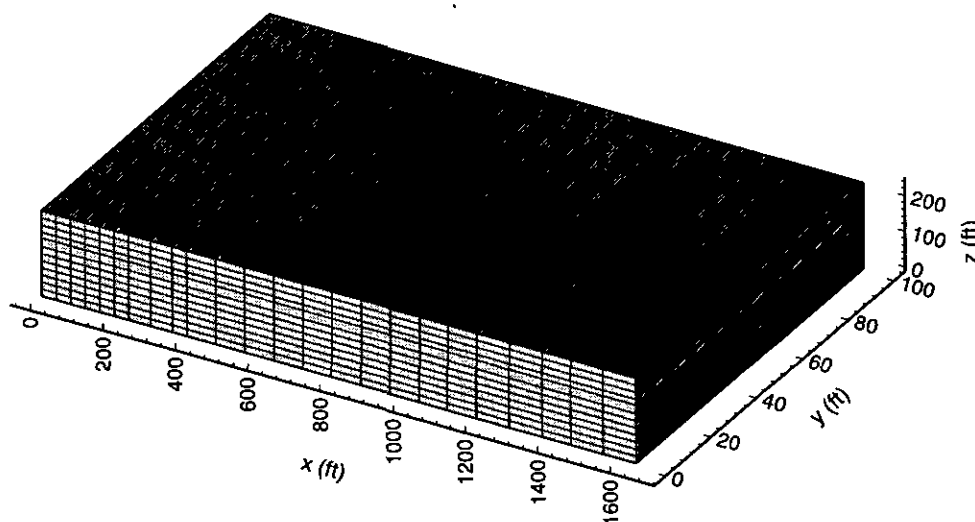


Fig. 4.1.2.4. FACT grid for Problem 2 shown in Fig. 4.1.2.2.

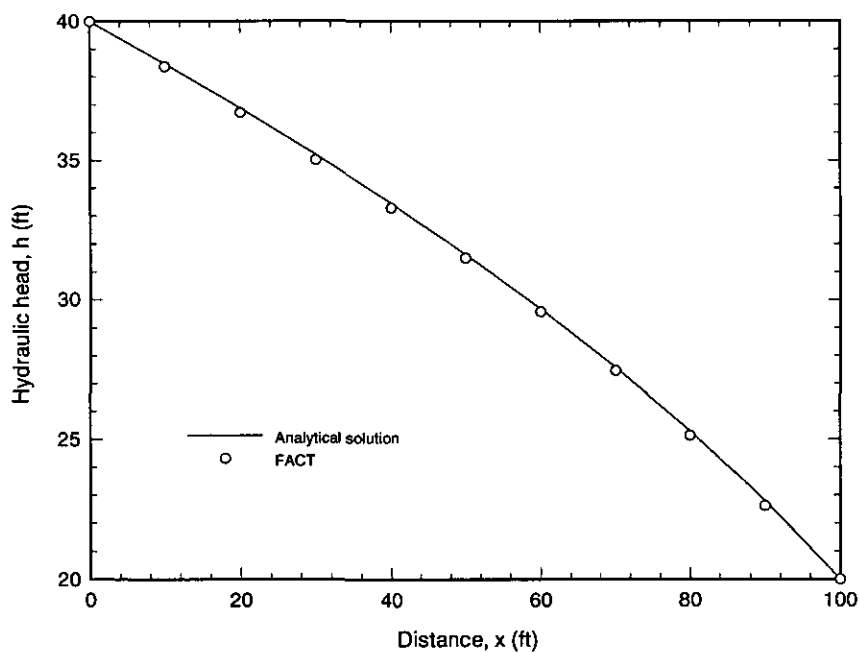


Fig. 4.1.2.5. Comparison of analytic solution and FACT results for Problem 1 shown in Fig. 4.1.2.1 with $\text{rampw} = 1.0$, $\text{upstr} = 1.0$ and $S_{WR} = 0.05$.

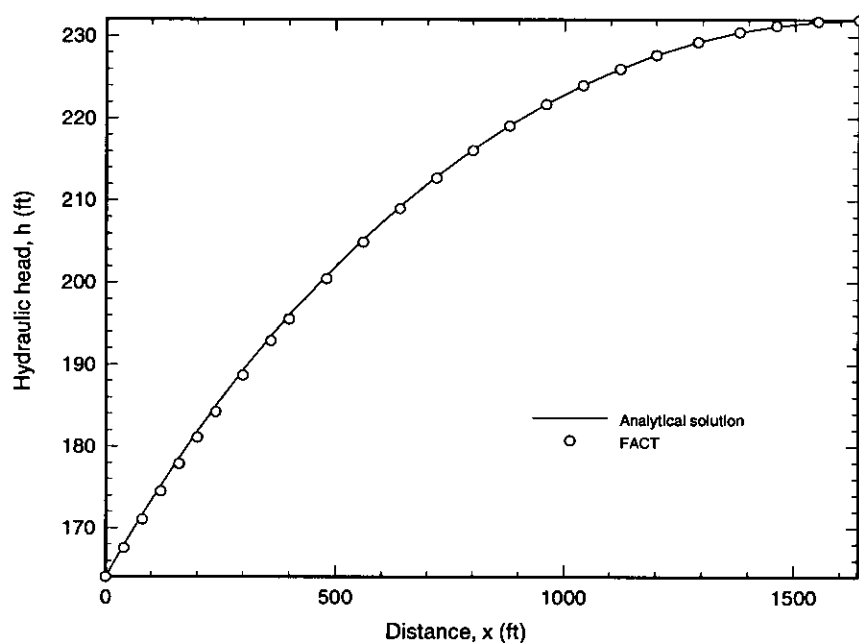


Fig. 4.1.2.6. Comparison of analytic solution and FACT results for Problem 2 shown in Fig. 4.1.2.2 with $\text{rampw} = 1.0$, $\text{upstr} = 1.0$ and $S_{wr} = 0.005$.

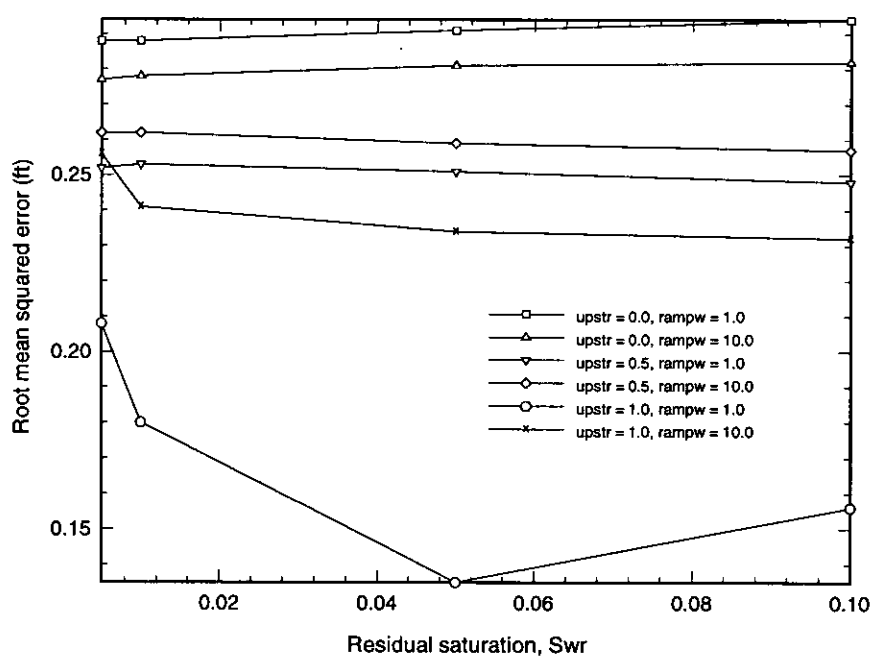


Fig. 4.1.2.7. Pseudo-soil property parameter study for Problem 1 shown in Fig. 4.1.2.1.

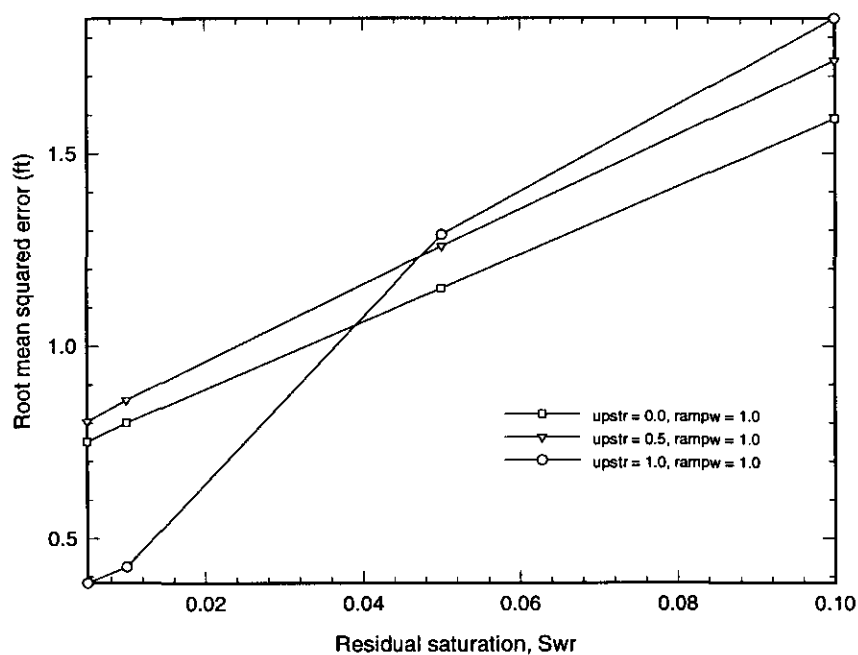


Fig. 4.1.2.8a. Pseudo-soil property parameter study for Problem 2 shown in Fig. 4.1.2.2.

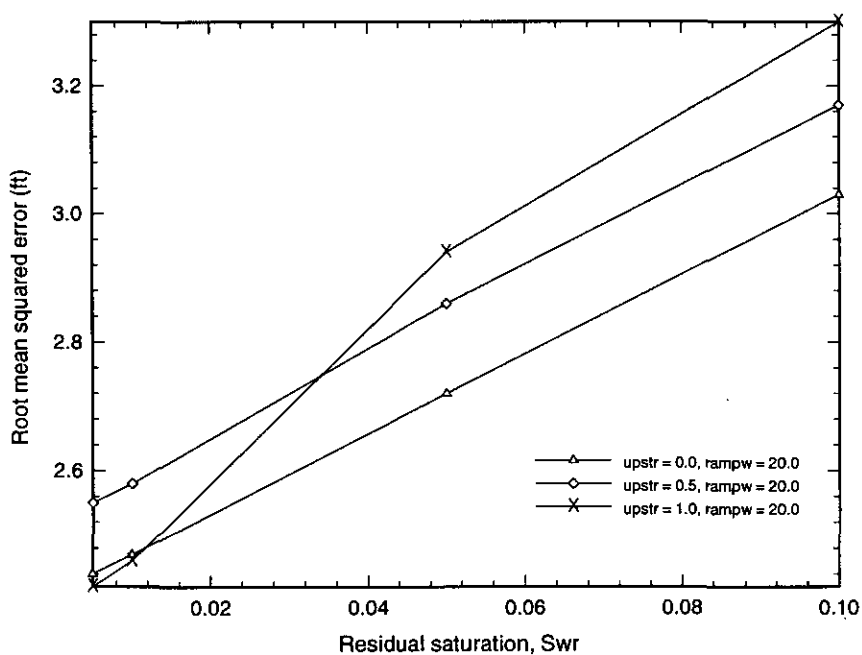


Fig. 4.1.2.8b. Pseudo-soil property parameter study for Problem 2 shown in Fig. 4.1.2.2.

Table 4.1.2.1

Comparison of analytic solution and FACT numerical results

Problem 1			Problem 2		
x (ft)	Analytic (ft)	FACT (ft)	x (ft)	Analytic (ft)	FACT (ft)
0.	40.000	40.000	0	164.000	164.000
10	38.471	38.365	40	167.905	167.545
20	36.878	36.712	80	171.628	171.058
30	35.214	35.025	120	175.180	174.506
40	33.466	33.293	160	178.572	177.861
50	31.623	31.491	200	181.813	181.102
60	29.665	29.567	240	184.911	184.222
70	27.568	27.462	300	189.304	188.682
80	25.298	25.139	360	193.411	192.878
90	22.804	22.626	400	196.000	195.524
100	20.000	20.000	480	200.838	200.448
			560	205.251	204.919
			640	209.265	208.999
			720	212.904	212.724
			800	216.185	216.086
			880	219.126	219.073
			960	221.739	221.701
			1040	224.036	224.001
			1120	226.027	225.999
			1200	227.719	227.708
			1290	229.275	229.288
			1380	230.469	230.507
			1460	231.231	231.289
			1550	231.756	231.829
			1640	231.931	232.008

4.1.3 Steady-State, Two-Dimensional Flow Through a Heterogeneous Aquifer System

Figure 4.1.3.1 schematically illustrates a particular problem involving steady-state groundwater flow through a heterogeneous subsurface system. The problem shown in Figure 4.1.3.1 was chosen as a test case to verify that FACT can correctly solve a groundwater flow problem involving a non-uniform hydraulic conductivity field. Problem parameters were carefully chosen to enable analytic solution. Specifically, the boundary conditions and conductivity field were chosen to create two aquifers with a constant head difference. A constant head difference coupled with a uniform conductivity in the confining unit yields a uniform leakance between the two aquifers. Assuming flow in the aquifers is essentially one-dimensional (Dupuit assumption; typically an excellent assumption), analytical solutions can be derived for both the unconfined and confined aquifers for a constant source/sink term. These analytical solutions are presented below followed by FACT simulation and comparison results.

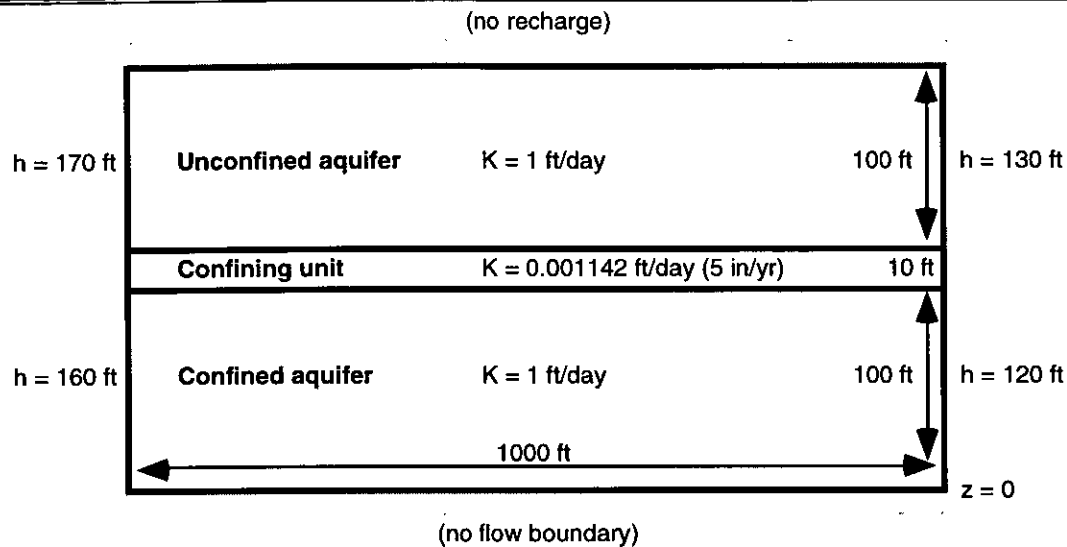


Fig. 4.1.3.1. A heterogeneous subsurface system consisting of an unconfined aquifer, confining unit and confined aquifer.

Unconfined aquifer analytical solution: Invoking the Dupuit assumption (de Marsily, 1986, Eq. (5.1.1)) gives the following general expression for flow in an unconfined aquifer

$$\frac{\partial}{\partial x} \left[\int_{\sigma}^h K_{xx} dz \frac{\partial h}{\partial x} \right] + \frac{\partial}{\partial y} \left[\int_{\sigma}^h K_{yy} dz \frac{\partial h}{\partial y} \right] = \omega_d \frac{\partial h}{\partial t} + Q \quad (4.1.3.1)$$

For a horizontal confining unit ($\sigma = \text{constant}$), constant properties and one-dimensional steady flow, Eq. (4.1.3.1) becomes

$$\frac{d^2(h - \sigma)^2}{dx^2} = \frac{2Q}{K} \quad (4.1.3.2)$$

For the prescribed head boundary conditions

$$h = h_0 \quad @ \quad x = 0 \quad (4.1.3.3a)$$

$$h = h_L \quad @ \quad x = L \quad (4.1.3.3b)$$

the solution can be derived using direct integration as

$$(h - \sigma)^2 = (h_0 - \sigma)^2 + \left[(h_L - \sigma)^2 - (h_0 - \sigma)^2 \right] \frac{x}{L} + \frac{Q_{src} L^2}{K} \left(\frac{x}{L} \right) \left(1 - \frac{x}{L} \right) \quad (4.1.3.4)$$

where $Q_{src} = -Q$.

Confined aquifer analytical solution: Invoking the Dupuit assumption, the following governing equation can be developed for a confined aquifer (de Marsily, 1986, Eq. (5.3.11))

$$\nabla^2 h = \frac{\partial^2 h}{\partial x^2} + \frac{\partial^2 h}{\partial y^2} = \frac{S}{T} \frac{\partial h}{\partial t} + \frac{Q}{T} \quad (4.1.3.5)$$

For constant aquifer thickness, constant properties and one-dimensional steady flow, Eq. (4.1.3.5) becomes

$$\frac{\partial^2 h}{\partial x^2} = \frac{Q}{Ke} \quad (4.1.3.6)$$

For the prescribed head boundary conditions

$$h = h_0 \quad @ \quad x = 0 \quad (4.1.3.7a)$$

$$h = h_L \quad @ \quad x = L \quad (4.1.3.7b)$$

the solution can be derived using direct integration as

$$h = h_0 \left(1 - \frac{x}{L} \right) + h_L \left(\frac{x}{L} \right) + \frac{Q_{src} L^2}{2Ke} \left(\frac{x}{L} \right) \left(1 - \frac{x}{L} \right) \quad (4.1.3.8)$$

where $Q_{src} = -Q$ as before.

FACT numerical simulation and comparison: Figure 4.1.3.2 illustrates the finite element mesh chosen for the simulation. The grid is 20×20 elements in the x-z plane and one element thick along the y axis. The number of nodes is (20+1)×(20+1)×(1+1) = 882. There are 8 elements vertically in each aquifer portion of the mesh and 4 elements in the confining unit. Table 4.1.3.1 and Fig. 4.1.3.3 present the FACT results alongside the approximate analytical results. Note that the head difference across the aquifers is indeed constant as desired. The agreement between code and analytical solution is excellent.

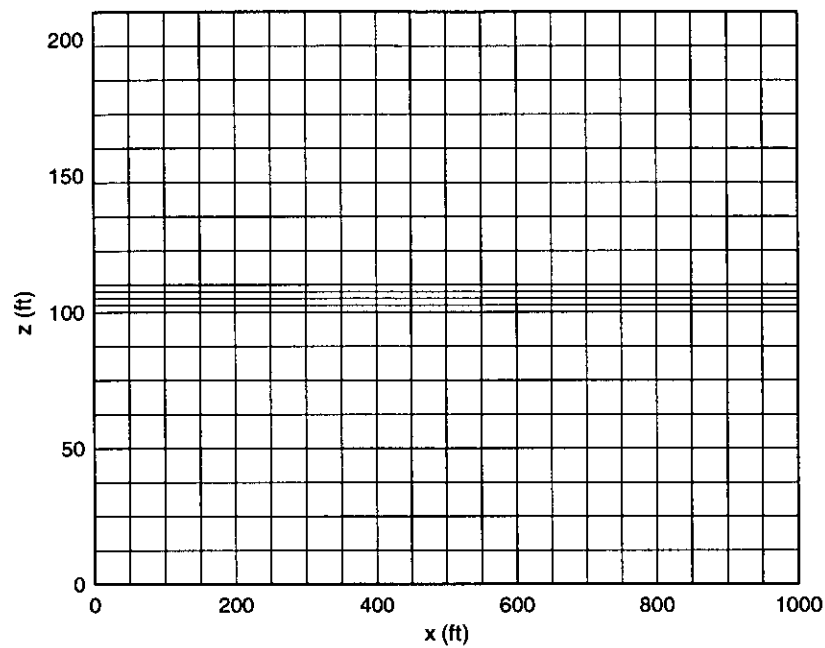


Fig. 4.1.3.2 Finite element mesh from x-z view (20×1×20 elements).

Table 4.1.3.1

Approximate analytical and FACT hydraulic head values for the unconfined and confined aquifer portions of the heterogeneous subsurface system shown in Fig. 4.1.1.

x/L	x (ft)	Unconfined aquifer head		Confined aquifer head	
		Analytical (ft)	FACT @ z=160' (ft)	Analytical (ft)	FACT @ z=50' (ft)
0.00	0	170.000	170.000	160.000	160.000
0.05	50	168.187	168.093	158.271	158.260
0.10	100	166.367	166.224	156.514	156.498
0.15	150	164.539	164.405	154.728	154.707
0.20	200	162.701	162.631	152.913	152.889
0.25	250	160.852	160.955	151.070	151.044
0.30	300	158.993	159.145	149.199	149.170
0.35	350	157.120	157.011	147.299	147.269
0.40	400	155.233	154.990	145.370	145.340
0.45	450	153.330	153.037	143.413	143.384
0.50	500	151.408	151.146	141.427	141.401
0.55	550	149.465	149.310	139.413	139.389
0.60	600	147.497	147.606	137.370	137.350
0.65	650	145.501	145.779	135.299	135.281
0.70	700	143.470	143.273	133.199	133.184
0.75	750	141.400	141.128	131.070	131.059
0.80	800	139.281	139.028	128.913	128.904
0.85	850	137.101	137.017	126.728	126.721
0.90	900	134.845	135.072	124.514	124.509
0.95	950	132.489	132.870	122.271	122.266
1.00	1000	130.000	130.000	120.000	120.000

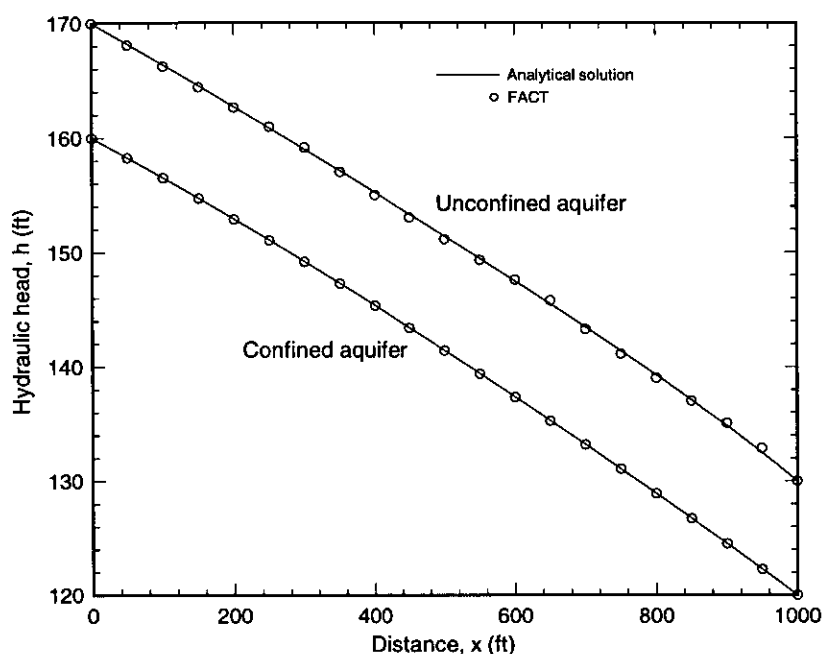


Fig. 4.1.3.3. Approximate analytical and FACT hydraulic head profiles for the unconfined and confined aquifer portions of the heterogeneous subsurface system shown in Fig. 4.1.3.1.

4.1.4 Unconfined Aquifer Subject to a Combined Recharge/Drain BC

Figure 4.1.4.1 schematically illustrates an unconfined aquifer experiencing both recharge and drainage at the ground surface. The position of the seepage line is unknown a priori. This test case is designed to test the combined recharge/drain boundary condition option.

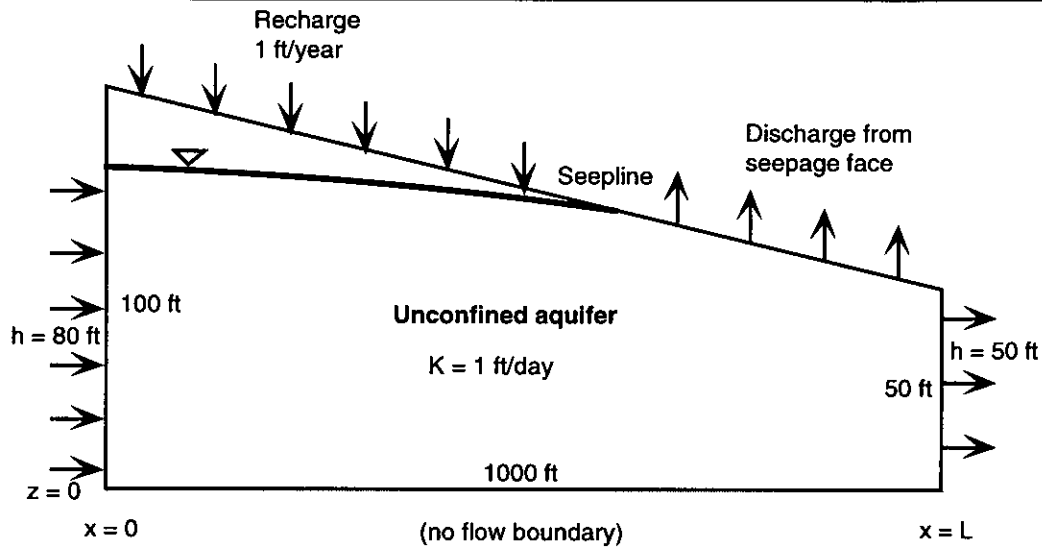


Fig. 4.1.4.1. Schematic illustration of an unconfined aquifer experiencing both recharge and drainage at the ground surface; seepage line unknown a priori.

Analytical solution: With the Dupuit assumption, an analytical solution can be derived for the problem. Between the left boundary and the seepage line, is an unconfined aquifer subject to a recharge rate of 1 ft/yr. From inspection of Eq. (4.1.3.4), the analytical solution for head is

$$h^2 = h_0^2 + \left(h_s^2 - h_0^2 \right) \frac{x}{L_s} + \frac{Q_{src} L^2}{K} \left(\frac{x}{L_s} \right) \left(1 - \frac{x}{L_s} \right) \quad 0 \leq x \leq L_s \quad (4.1.4.1)$$

where the seepage line is positioned at $x = L_s$, the head at the seepage line is h_s and $\sigma = 0$. The other symbols are defined as before. Along the seepage face the drain coefficient is assumed to be sufficiently large that the head is the same as the ground elevation. That is,

$$h = 50 \left(2 - \frac{x}{L} \right) \quad L_s \leq x \leq L \quad (4.1.4.2)$$

The location of the seepage line is obtained by simultaneous solution of the following nonlinear equation set:

$$h = 50 \left(2 - \frac{L_s}{L} \right) \quad (4.1.4.3)$$

$$\left. \frac{dh}{dx} \right|_{x=L_s^-} = \frac{1}{h_s} \left(\frac{h_s^2 - h_0^2}{2L_s} - \frac{Q_{src} L_s}{2K} \right) = \frac{h_L - h_s}{L - L_s} = \left. \frac{dh}{dx} \right|_{x=L_s^+} \quad (4.1.4.4)$$

For the parameter values indicated in Fig. 4.1.4.1, the location of the seepage line is $L_s = 829$ ft. The composite head solution is plotted in Fig. 4.1.4.2 and listed in Table 4.1.4.1.

FACT CODE MANUAL

FACT numerical simulation and comparison: Also shown in Fig. 4.1.4.2 is the FACT finite element mesh chosen for the simulation. The grid is 20×20 elements in the x-z plane and one element thick along the y axis. The number of nodes is $(20+1) \times (20+1) \times (1+1) = 882$. Figure 4.1.4.2 and Table 4.1.4.1 present the FACT solution in comparison to the analytical solution. The agreement is excellent.

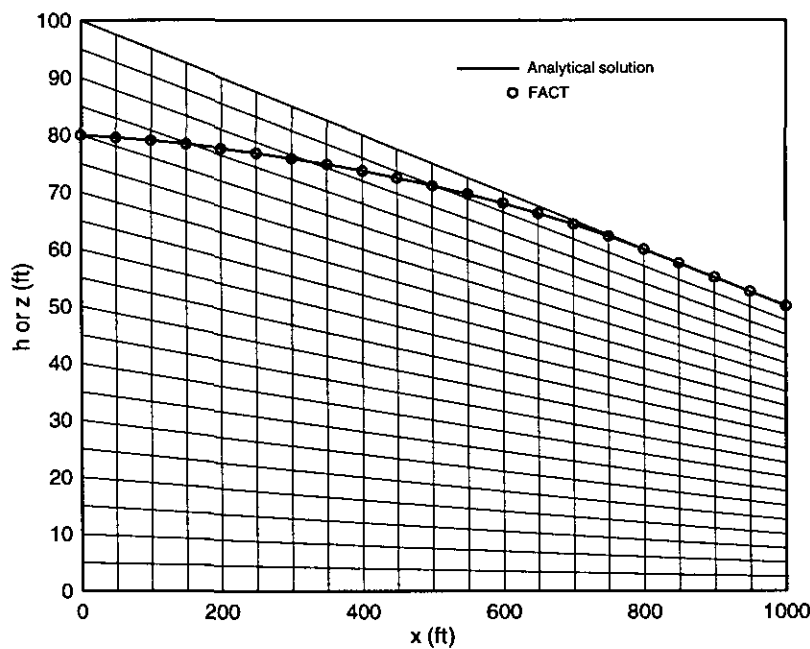


Fig. 4.1.4.2. FACT finite element mesh with FACT and analytical water table overlain.

Table 4.1.4.1

FACT and analytical water table comparison

Horizontal distance, x (ft)	Analytical head (ft)	FACT head (ft)
0	80.000	80.000
50	79.594	79.616
100	79.099	79.067
150	78.513	78.425
200	77.835	77.717
250	77.063	76.892
300	76.193	75.950
350	75.222	74.939
400	74.145	73.828
450	72.959	72.547
500	71.658	71.182
550	70.236	69.740
600	68.684	68.129
650	66.995	66.350
700	65.000	64.403
750	62.500	62.303
800	60.000	59.999
850	57.500	57.500
900	55.000	55.000
950	52.500	52.500
1000	50.000	50.000

4.1.5 Transient, One-Dimensional Flow to a Well in a Confined Aquifer (Theis, 1935)

This problem involves radial flow to well in a confined aquifer whose well-known solution is given by Theis (1935). The problem is illustrated in Fig. 4.1.5.1. Specifically we consider an aquifer with the following attributes:

- horizontal
- fully confined
- infinite in horizontal extent
- uniform thickness
- homogeneous and isotropic properties
- uniform head at $t = 0$
- water is removed instantaneously from storage with a fall in head
- flow is effectively horizontal (Dupuit assumption)

A single extraction well is assumed to be present with the following characteristics:

- fully penetrates aquifer
- constant pumping rate for $t > 0$
- infinitesimally small well diameter

The parameter values chosen for FACT simulations are given in Fig. 4.1.5.1 and are equivalent to those chosen by Anderson (1993, Problem 1) for MODFLOW simulations.

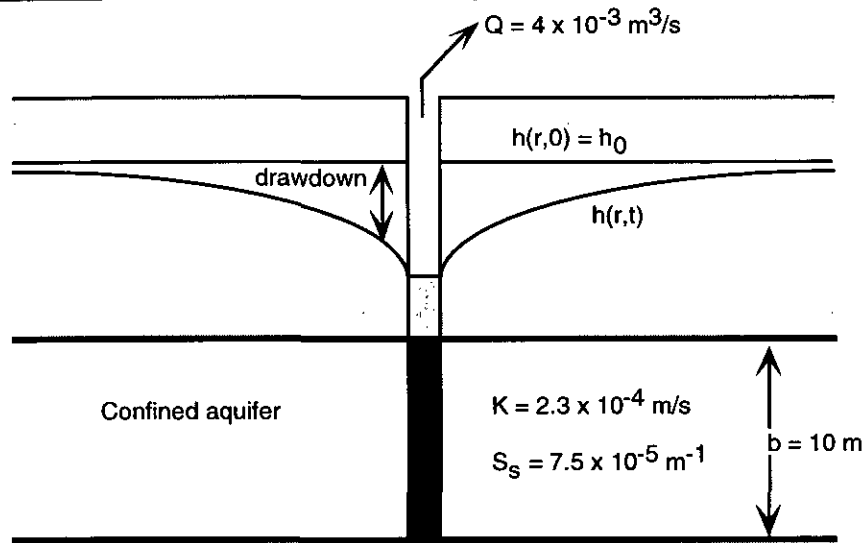


Fig. 4.1.5.1. Radial flow to a pumping well in a confined aquifer.

Theis analytic solution: The governing equation for the flow problem described above is (Freeze and Cherry, 1979, Section 8.3)

$$\frac{1}{r} \frac{\partial}{\partial r} \left(r \frac{\partial h}{\partial r} \right) = \frac{S}{T} \frac{\partial h}{\partial t} \quad (4.1.5.1)$$

The initial condition is

$$h(r,0) = h_0 \quad (4.1.5.2)$$

where h_0 is the constant initial hydraulic head.

The boundary conditions assume no drawdown in hydraulic head at the infinite boundary:

$$h(\infty, t) = h_0 \quad (4.1.5.3)$$

and a constant pumping rate Q at the well:

$$\lim_{r \rightarrow 0} \left(r \frac{\partial h}{\partial r} \right) = \frac{Q}{2\pi T} \quad \text{for } t > 0 \quad (4.1.5.4)$$

Because the aquifer properties are homogeneous

$$S = S_s b \quad (4.1.5.5)$$

$$T = Kb \quad (4.1.5.6)$$

An analytical solution to Eq. (4.1.5.1) subject to the initial and boundary conditions of Eqs. (4.1.5.2) through (4.1.5.4) is given by Theis (1935) in terms of drawdown as

$$s = h_0 - h(r,t) = \frac{Q}{4\pi T} \int_{1/u}^{\infty} \frac{e^{-\tau}}{\tau} d\tau = \frac{Q}{4\pi T} W(u) \quad (4.1.5.7)$$

where

$$u = \frac{4Tt}{r^2S} \quad (4.1.5.8)$$

and $W(u)$ is known as the Theis well function.

Evaluations of the Theis solution for the parameter values specified in Fig. 4.1.5.1 and a radial position of 55 meters from the well are presented in Table 4.1.5.1 for various times (Anderson, 1993, Table 1.4).

FACT simulation and comparison: Figure 4.1.5.2 illustrates the first grid chosen for FACT simulations. The mesh is 20 by 20 elements in the horizontal plane and 1 element thick vertically for a total of 400 elements. The number of nodes is $21 \times 21 \times 2 = 882$. The mesh is non-uniform with refinement near the pumping well because steep head gradients are expected there. Time steps were chosen to yield the same time increments given in Table 4.1.5.1. Figure 4.1.5.3 illustrates the FACT transient results at $r = 55$ m compared to the Theis solution, and Table 4.1.5.1 presents numerical values. The FACT results are observed to agree approximately with the Theis solution. The discrepancy is due to a relatively coarse grid and large time steps. Figure 4.1.5.4 presents drawdown at the final time step (86,400 seconds or 1 day).

Before refining the mesh and time steps, we first recognize that radial symmetry enables a smaller FACT grid domain. Specifically, a single quadrant of the mesh shown in Fig. 4.1.5.2 is adequate. Figure 4.1.5.5 illustrates such a mesh. Note that the mesh spacing is the same in Figs. 4.1.5.2 and 4.1.5.5. The number of elements is $10 \times 10 \times 1 = 100$ and there are $11 \times 11 \times 2 = 242$ nodes. Figure 4.1.5.6 and Table 4.1.5.1 present the FACT solution for this quadrant mesh. The numerical results for both grids are seen to be identical to three decimal places.

Next we refine the coarse quadrant mesh as illustrated in Fig. 4.1.5.7. The number of elements is $18 \times 18 \times 1 = 324$ and there are $19 \times 19 \times 2 = 722$ nodes. In addition, an intermediate time step is added to each time step indicated in Table 4.1.5.1 essentially doubling the number of time steps. The FACT results are presented in Fig. 4.1.5.6 and Table 4.1.5.1. The agreement between the code and Theis solution is significantly improved. Further grid and time step refinement would continue to improve agreement.

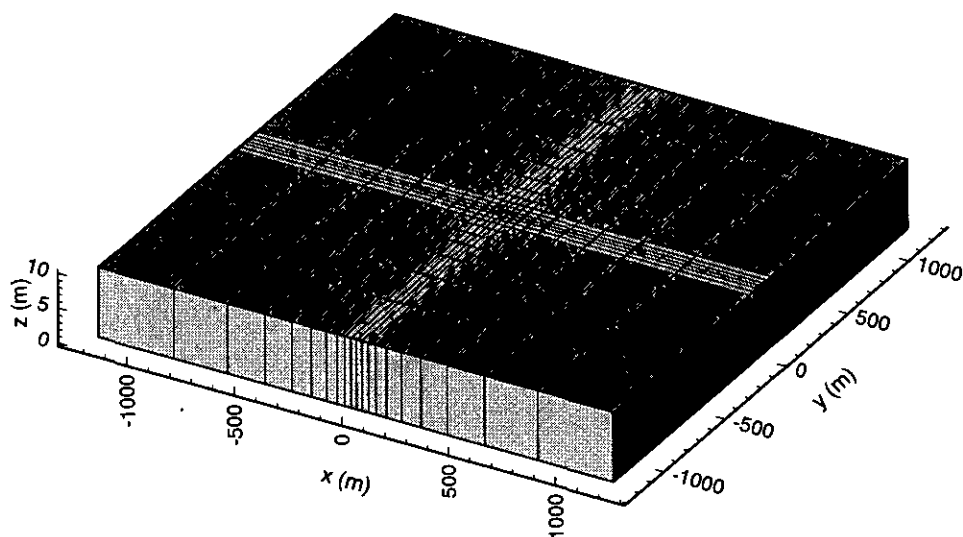


Fig. 4.1.5.2. FACT coarse full grid.

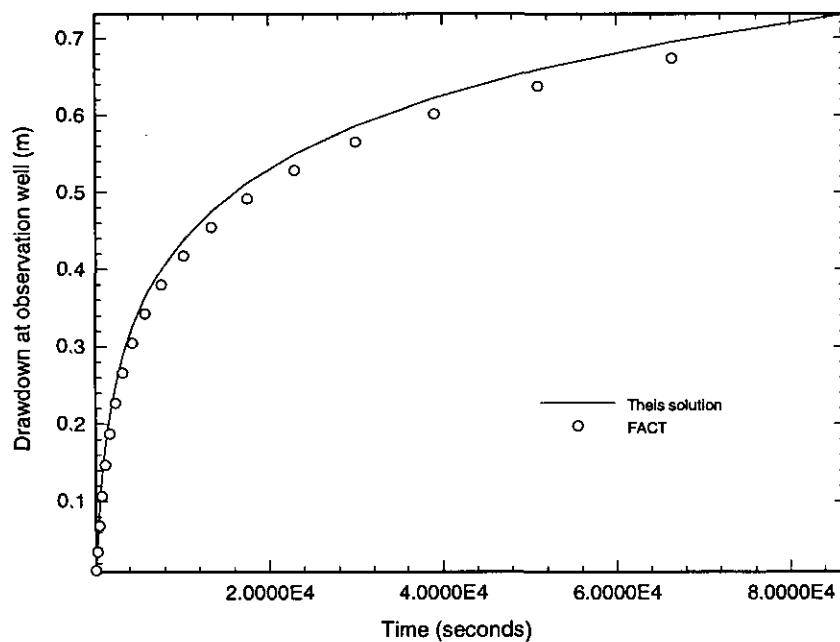


Fig. 4.1.5.3. Theis solution and FACT coarse full grid transient results at $r = 55$ meters.

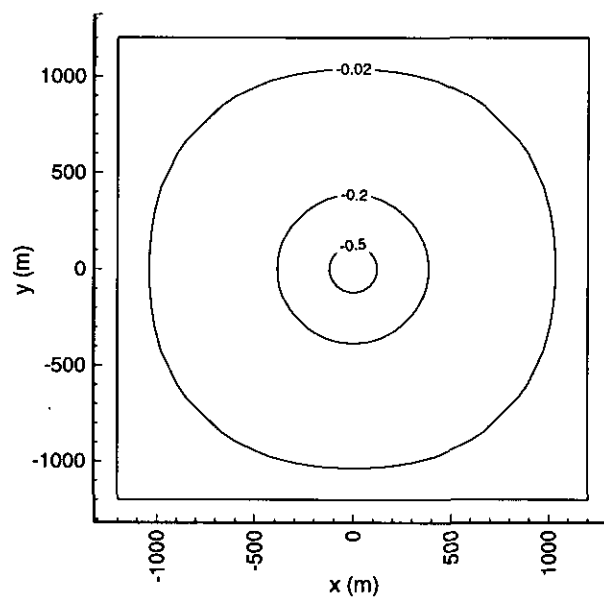


Fig. 4.1.5.4. FACT drawdown at 1 day for coarse full grid.

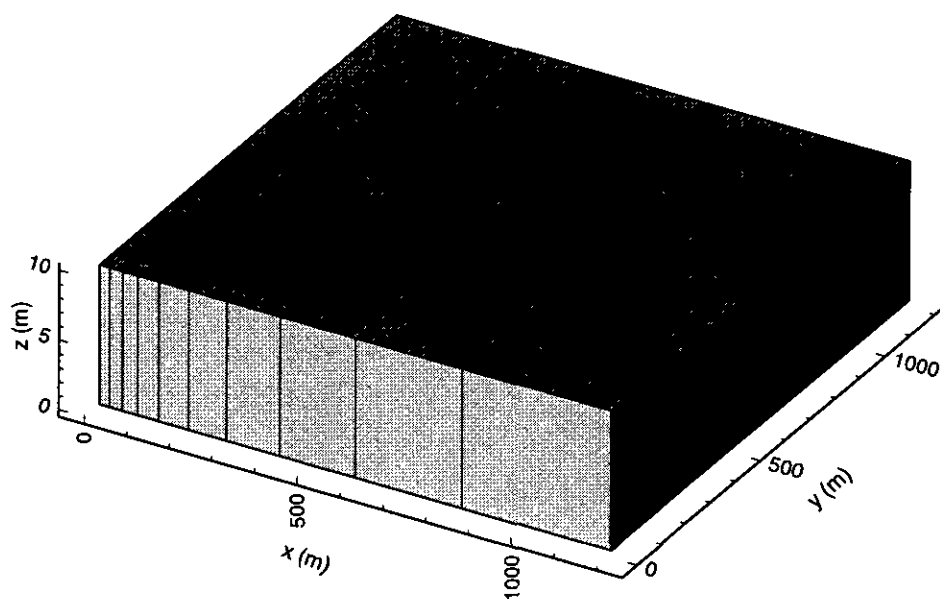


Fig. 4.1.5.5. FACT coarse quadrant grid.

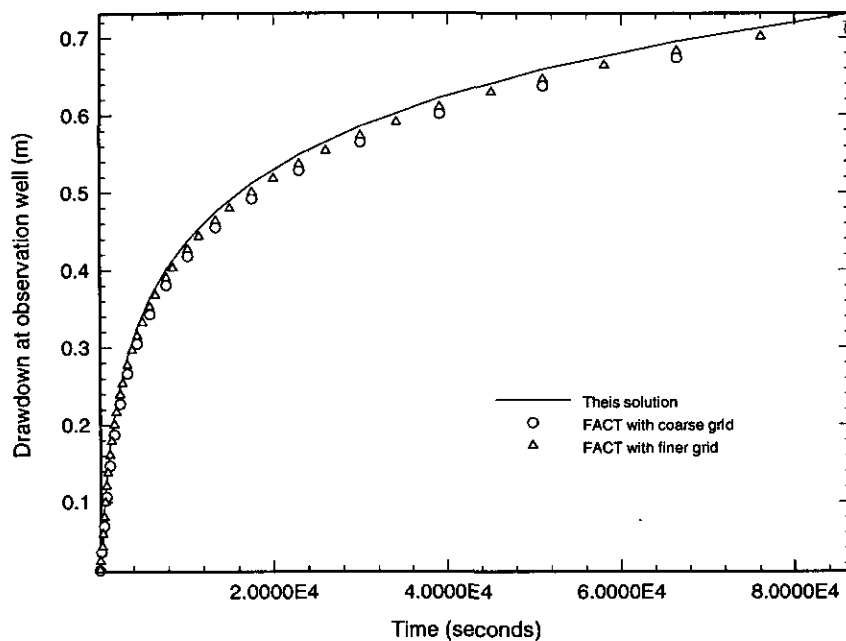


Fig. 4.1.5.6. Theis solution and FACT quadrant grid transient results at $r = 55$ meters.

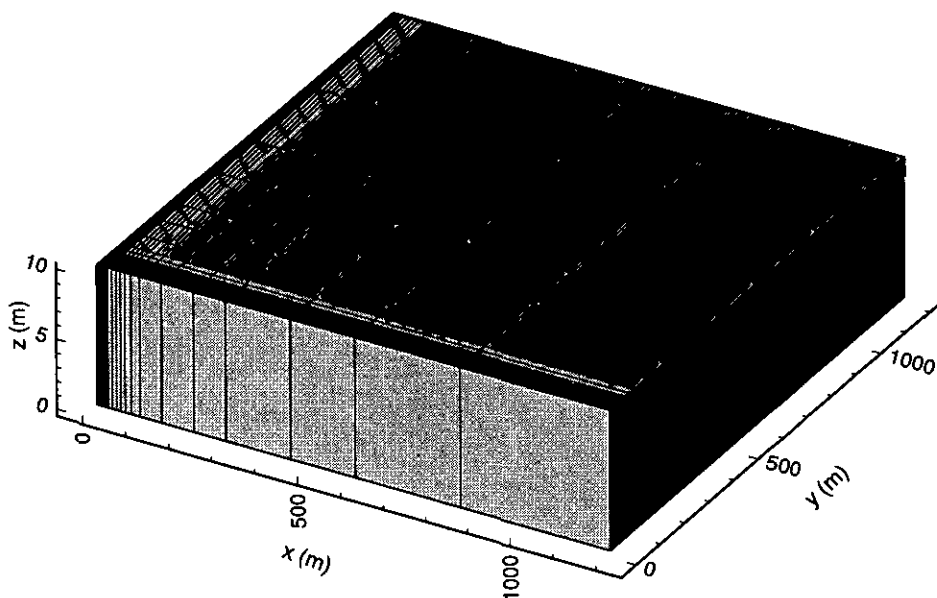


Fig. 4.1.5.7. FACT fine quadrant grid.

Table 4.1.5.1

Comparison of Theis solution and FACT numerical results

Time (sec)	Theis Solution (m)	FACT Coarse Full Grid (m)	FACT Coarse Quadrant Grid (m)	FACT Fine Quadrant Grid (m)
0.1371E+03	0.009	0.011	0.011	0.012
0.3153E+03	0.044	0.035	0.035	0.042
0.5471E+03	0.086	0.068	0.068	0.080
0.8486E+03	0.129	0.107	0.107	0.121
0.1240E+04	0.170	0.147	0.147	0.161
0.1749E+04	0.210	0.187	0.187	0.200
0.2411E+04	0.249	0.227	0.227	0.239
0.3271E+04	0.288	0.266	0.266	0.277
0.4389E+04	0.326	0.305	0.305	0.315
0.5843E+04	0.364	0.343	0.343	0.353
0.7734E+04	0.401	0.380	0.380	0.390
0.1019E+05	0.438	0.418	0.418	0.427
0.1339E+05	0.475	0.455	0.455	0.464
0.1754E+05	0.512	0.492	0.492	0.500
0.2294E+05	0.549	0.528	0.528	0.537
0.2995E+05	0.586	0.565	0.565	0.573
0.3908E+05	0.622	0.601	0.601	0.610
0.5094E+05	0.659	0.638	0.638	0.646
0.6636E+05	0.695	0.674	0.674	0.683
0.8640E+05	0.731	0.709	0.709	0.718

4.1.6 Transient, One-Dimensional Flow to a Well in an Anisotropic Confined Aquifer (Hantush and Thomas, 1966)

We next consider a confined aquifer identical to Problem 4.1.5 except that the hydraulic conductivity is anisotropic as shown in Fig. 4.1.6.1. The principal axes of the conductivity tensor are assumed to be aligned with the coordinate axes.

Analytic solution: The governing equation for the flow problem described above can be written as

$$\frac{\partial}{\partial x} \left(T_x \frac{\partial h}{\partial x} \right) + \frac{\partial}{\partial y} \left(T_y \frac{\partial h}{\partial y} \right) = S \frac{\partial h}{\partial t} + Q \delta(x) \delta(y) \quad -\infty < x < \infty, -\infty < y < \infty \quad (4.1.6.1)$$

The initial condition is

$$h(x, y, 0) = h_0 \quad (4.1.6.2)$$

Because the aquifer properties are homogeneous, Eq. (4.1.5.5) holds and

$$T_i = K_i b \quad (4.1.6.3)$$

The solution to the governing equation is given by Hantush and Thomas (1966) as

$$s = h_o - h(r, t) = \frac{Q}{4\pi\sqrt{T_x T_y}} \int_{1/u'}^{\infty} \frac{e^{-\tau}}{\tau} d\tau = \frac{Q}{4\pi\sqrt{T_x T_y}} W(u') \quad (4.1.6.4)$$

where

$$u = \frac{4T_x T_y t}{(x^2 T_y + y^2 T_x) S} \quad (4.1.6.5)$$

and $W(u')$ is the well function. Note that for $T_x = T_y$, the above solution reduces to the Theis solution presented in Section 4.1.5.

Evaluations of the analytic solution for the parameter values specified in Fig. 4.1.6.1 and (x,y) coordinate positions of (55 m, 0), (0, 55 m) and (55 m, 55m) are presented in Tables 4.1.6.1 through 4.1.6.3 for various times (Anderson, 1993, Tables 2.3-2.5).

FACT simulation and comparison: The same three grids considered in Section 4.1.5 are used for FACT simulations in this problem. These are termed the 'full' (Fig. 4.1.5.2), 'coarse quadrant' (Fig. 4.1.5.5) and 'fine quadrant' (Fig. 4.1.5.7) grids as before. Figure 4.1.6.2 illustrates the drawdown at 1 day computed using the FACT full grid. The effect of anisotropy in transmissivity is clear from inspection of its counterpart, Fig. 4.1.5.4. Figures 4.1.6.3 through 4.1.6.8 and Tables 4.1.6.1 through 4.1.6.3 summarize the transient analytic solution and FACT numerical results.

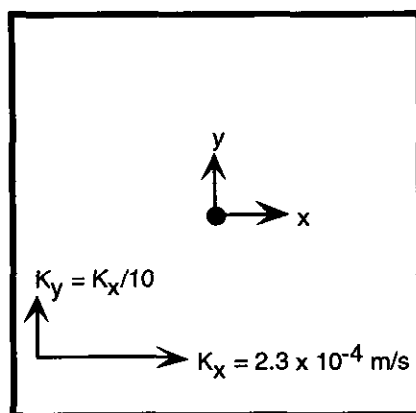


Fig. 4.1.6.1. Anisotropic confined aquifer with $K_x/K_y = 10$.

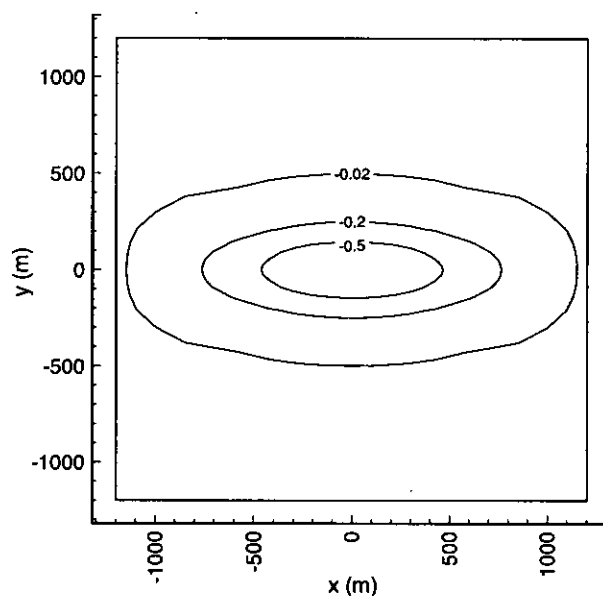


Fig. 4.1.6.2. FACT drawdown at 1 day for full grid.

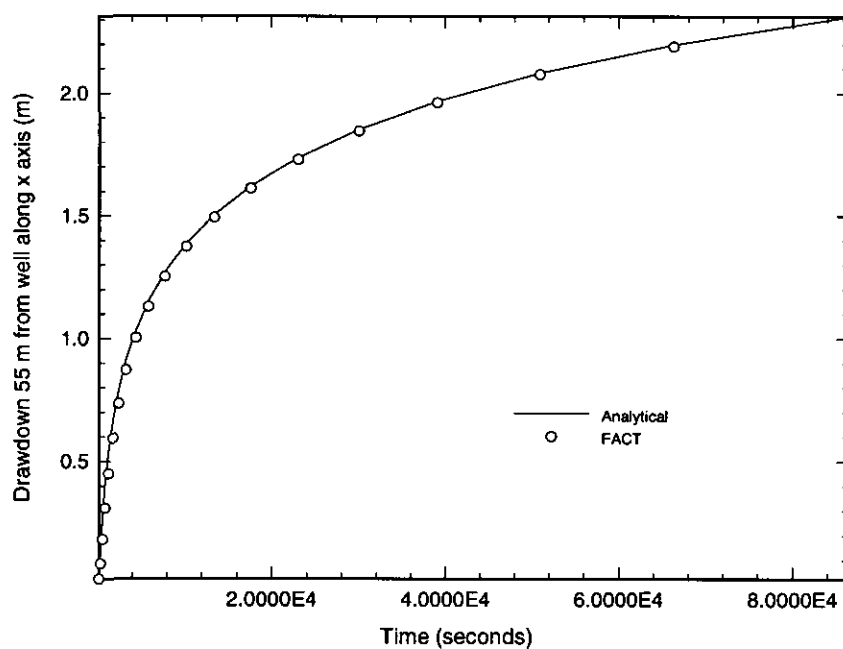


Fig. 4.1.6.3. Analytic solution and FACT full grid results at $x = 55$ m.

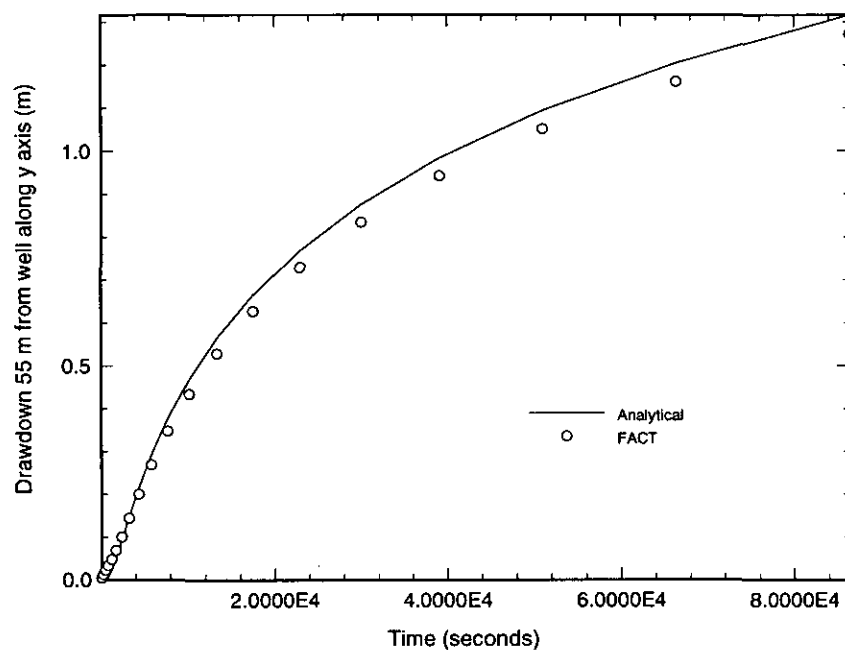


Fig. 4.1.6.4. Analytic solution and FACT full grid results at $y = 55$ m.

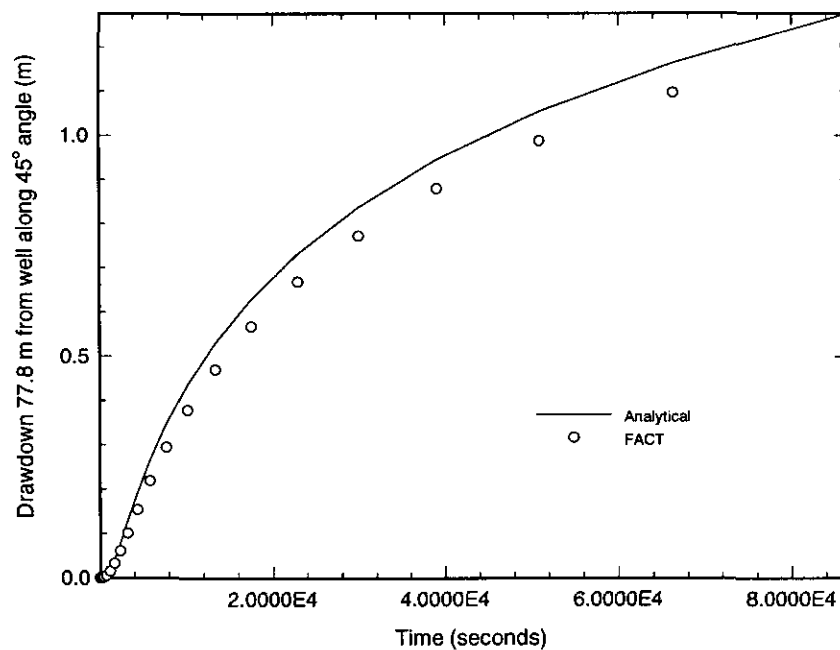


Fig. 4.1.6.5. Analytic solution and FACT full grid results at $x = 55$ m, $y = 55$ m.

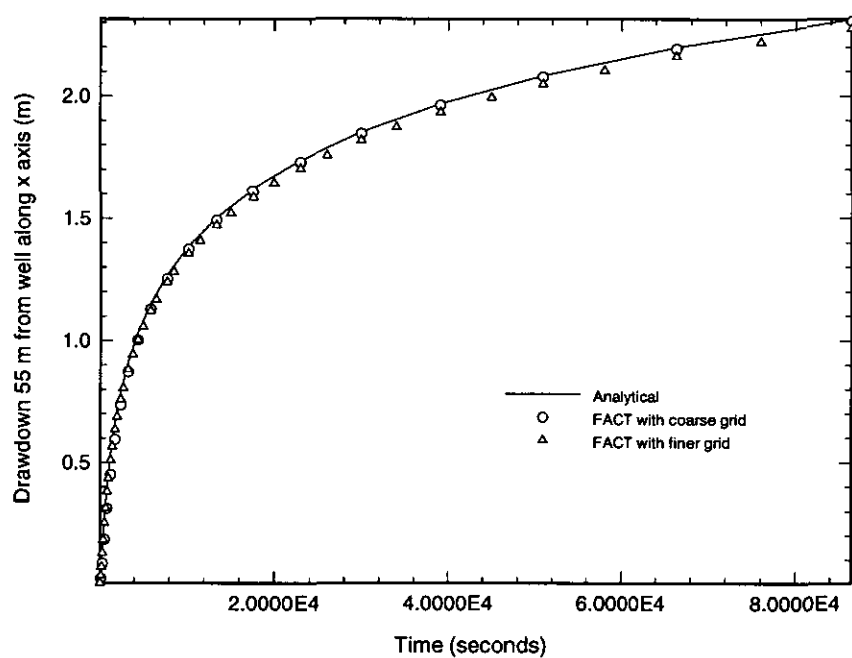


Fig. 4.1.6.6. Analytic solution and FACT quadrant grid results at $x = 55$ m.

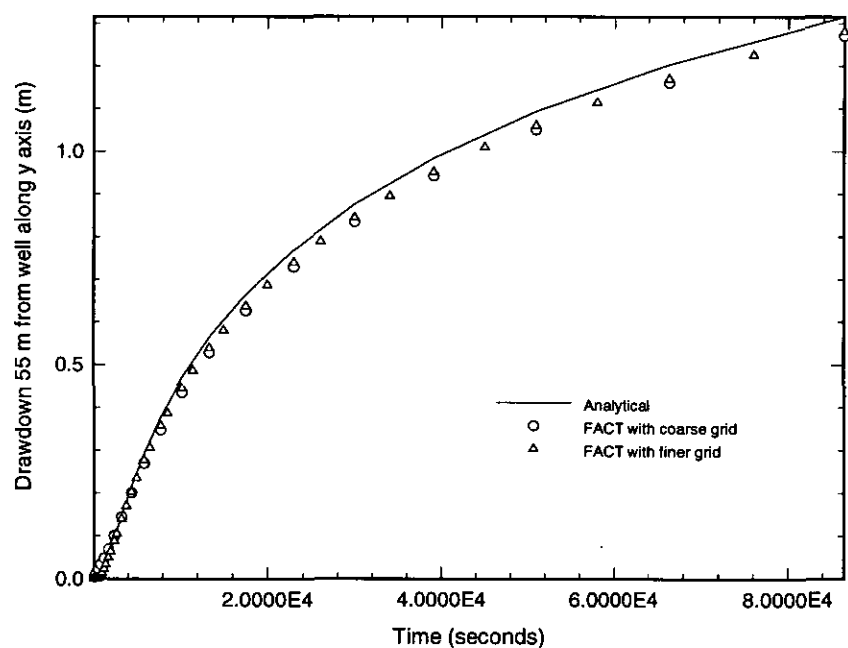


Fig. 4.1.6.7. Analytic solution and FACT quadrant grid results at $y = 55$ m.

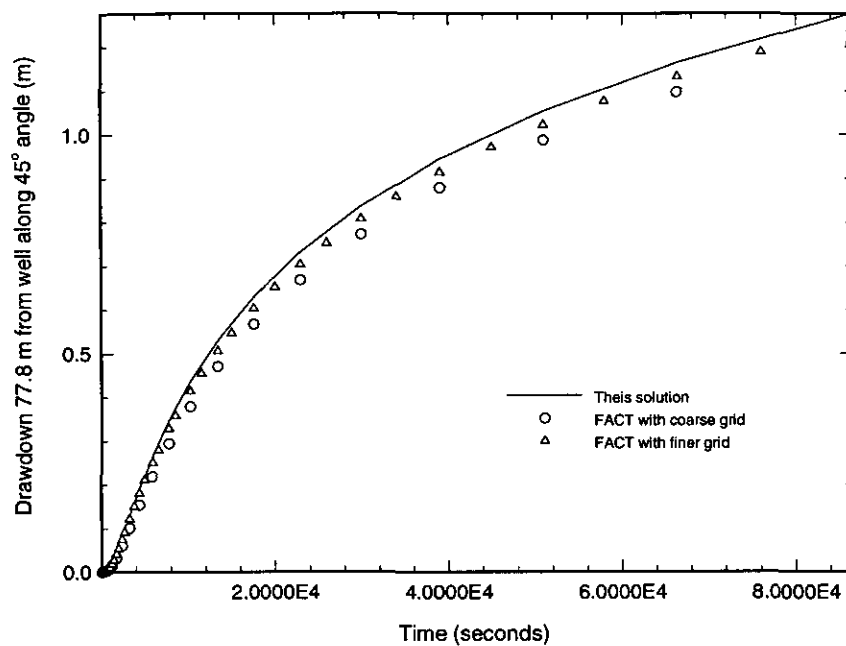


Fig. 4.1.6.8. Analytic solution and FACT quadrant grid results at $x = 55$ m, $y = 55$ m.

Table 4.1.6.1Comparison of analytic solution and FACT numerical results at $x = 55$ m

Time (sec)	Analytic Solution (m)	FACT Coarse Full Grid (m)	FACT Coarse Quadrant Grid (m)	FACT Fine Quadrant Grid (m)
0.1371E+03	0.028	0.025	0.025	0.036
0.3153E+03	0.140	0.086	0.086	0.130
0.5471E+03	0.273	0.185	0.185	0.253
0.8486E+03	0.407	0.311	0.311	0.382
0.1240E+04	0.537	0.451	0.451	0.510
0.1749E+04	0.664	0.595	0.595	0.636
0.2411E+04	0.789	0.736	0.736	0.760
0.3271E+04	0.911	0.872	0.872	0.882
0.4389E+04	1.032	1.003	1.003	1.003
0.5843E+04	1.151	1.129	1.129	1.122
0.7734E+04	1.269	1.253	1.253	1.240
0.1019E+05	1.387	1.374	1.374	1.356
0.1339E+05	1.503	1.494	1.494	1.472
0.1754E+05	1.620	1.612	1.612	1.587
0.2294E+05	1.736	1.729	1.729	1.702
0.2995E+05	1.852	1.845	1.845	1.817
0.3908E+05	1.967	1.961	1.961	1.932
0.5094E+05	2.082	2.077	2.077	2.047
0.6636E+05	2.198	2.192	2.192	2.161
0.8640E+05	2.313	2.306	2.306	2.275

Table 4.1.6.2Comparison of analytic solution and FACT numerical results at $y = 55$ m

Time (sec)	Analytic Solution (m)	FACT Coarse Full Grid (m)	FACT Coarse Quadrant Grid (m)	FACT Fine Quadrant Grid (m)
0.1371E+03	0.000	0.005	0.005	0.000
0.3153E+03	0.000	0.013	0.013	0.000
0.5471E+03	0.001	0.022	0.022	0.003
0.8486E+03	0.006	0.033	0.033	0.009
0.1240E+04	0.022	0.048	0.048	0.024
0.1749E+04	0.050	0.069	0.069	0.050
0.2411E+04	0.092	0.101	0.101	0.088
0.3271E+04	0.148	0.144	0.144	0.140
0.4389E+04	0.215	0.201	0.201	0.203
0.5843E+04	0.292	0.269	0.269	0.276
0.7734E+04	0.377	0.348	0.348	0.357
0.1019E+05	0.468	0.435	0.435	0.445
0.1339E+05	0.565	0.528	0.528	0.539
0.1754E+05	0.665	0.627	0.627	0.637
0.2294E+05	0.769	0.729	0.729	0.740
0.2995E+05	0.876	0.835	0.835	0.844
0.3908E+05	0.984	0.942	0.942	0.952
0.5094E+05	1.094	1.051	1.051	1.061
0.6636E+05	1.204	1.161	1.161	1.171
0.8640E+05	1.316	1.271	1.271	1.281

Table 4.1.6.3Comparison of analytic solution and FACT numerical results at $x = y = 55$ m

Time (sec)	Analytic Solution (m)	FACT Coarse Full Grid (m)	FACT Coarse Quadrant Grid (m)	FACT Fine Quadrant Grid (m)
0.1371E+03	0.000	0.000	0.000	0.000
0.3153E+03	0.000	0.001	0.001	0.000
0.5471E+03	0.001	0.002	0.002	0.002
0.8486E+03	0.004	0.006	0.006	0.007
0.1240E+04	0.017	0.016	0.016	0.019
0.1749E+04	0.041	0.033	0.033	0.041
0.2411E+04	0.078	0.062	0.062	0.075
0.3271E+04	0.129	0.101	0.101	0.122
0.4389E+04	0.192	0.154	0.154	0.181
0.5843E+04	0.265	0.219	0.219	0.251
0.7734E+04	0.347	0.295	0.295	0.329
0.1019E+05	0.436	0.379	0.379	0.415
0.1339E+05	0.530	0.471	0.471	0.506
0.1754E+05	0.629	0.568	0.568	0.603
0.2294E+05	0.732	0.669	0.669	0.704
0.2995E+05	0.837	0.773	0.773	0.808
0.3908E+05	0.945	0.879	0.879	0.914
0.5094E+05	1.054	0.988	0.988	1.022
0.6636E+05	1.164	1.097	1.097	1.132
0.8640E+05	1.276	1.207	1.207	1.242

4.1.7 Transient, One-Dimensional Flow to a Well in a Leaky Confined Aquifer (Hantush and Jacob, 1955)

We next consider a confined aquifer identical to Problem 4.1.5 except that the aquifer is recharged from an overlying constant head aquifer through an aquitard separating them, as shown in Fig. 4.1.7.1. The aquitard is assumed to have uniform thickness and vertical conductivity. Flow through the aquitard is assumed to be vertical and proportional to the head difference between the adjoining aquifers (storage capacity assumed to be zero). Parameter values are taken from a GeoTrans (1993) problem.

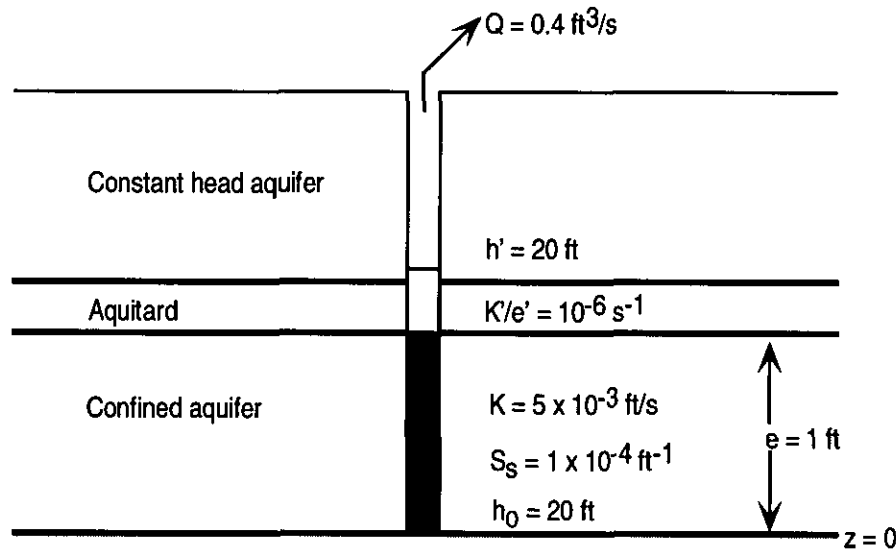


Fig. 4.1.7.1. Schematic diagram of a leaky confined aquifer with constant discharge from a single, fully-penetrating well.

Analytic solution: The governing equation for the flow problem described above is

$$\frac{1}{r} \frac{\partial}{\partial r} \left(r \frac{\partial h}{\partial r} \right) = \frac{S}{T} \frac{\partial h}{\partial t} + F_t \quad (4.1.7.1)$$

The initial condition is

$$h(r, 0) = h_0 \quad (4.1.7.2)$$

The boundary conditions assume no drawdown in hydraulic head at the infinite boundary:

$$h(\infty, t) = h_0 \quad (4.1.7.3)$$

and a constant pumping rate Q at the well:

$$\lim_{r \rightarrow 0} \left(r \frac{\partial h}{\partial r} \right) = \frac{Q}{2\pi T} \quad \text{for } t > 0 \quad (4.1.7.4)$$

where F_t represents leakage from the overlying aquifer. The leakage flux is given by

$$F_t = -\frac{K'}{e'} (h' - h) \quad (4.1.7.5)$$

where K'/e' is the aquitard leakage coefficient. The solution to Eq. (4.1.7.1) is given by Hantush and Jacob (1955) as

$$s = h_0 - h(r, t) = \frac{Q}{4\pi T} \int_{u/u}^{\infty} \frac{e^{-\tau - r^2/4B^2\tau}}{\tau} d\tau = \frac{Q}{4\pi T} W \left(u, \frac{r}{B} \right) \quad (4.1.7.6)$$

where the Hantush leakage factor $B = \sqrt{Te'/K'}$

FACT CODE MANUAL

Note that for $B = \infty$ (no leakance) the above solution reduces to the Theis solution presented in Section 4.1.5.

Evaluations of the analytic solution for the parameter values specified in Fig. 4.1.7.1 and $r = 60$ ft are presented in Table 4.1.7.1 and Fig. 4.1.7.2 for various times (GeoTrans, 1993, Table 4.8).

FACT simulation and comparison: Figures 4.1.7.3 and 4.1.7.4 present the two grids chosen for FACT simulations. Only one quadrant has been modeled because of azimuthal symmetry. The coarse mesh contains 14×14 elements in the x-y plane and is 1 element thick vertically for a total of 196 elements. The corresponding number of nodes is $15 \times 15 \times 2 = 450$. The fine mesh contains $23 \times 23 \times 1 = 529$ elements and $24 \times 24 \times 2 = 1152$ nodes. Table 4.1.7.1 and Fig. 4.1.7.2 present the FACT numerical drawdown predictions.

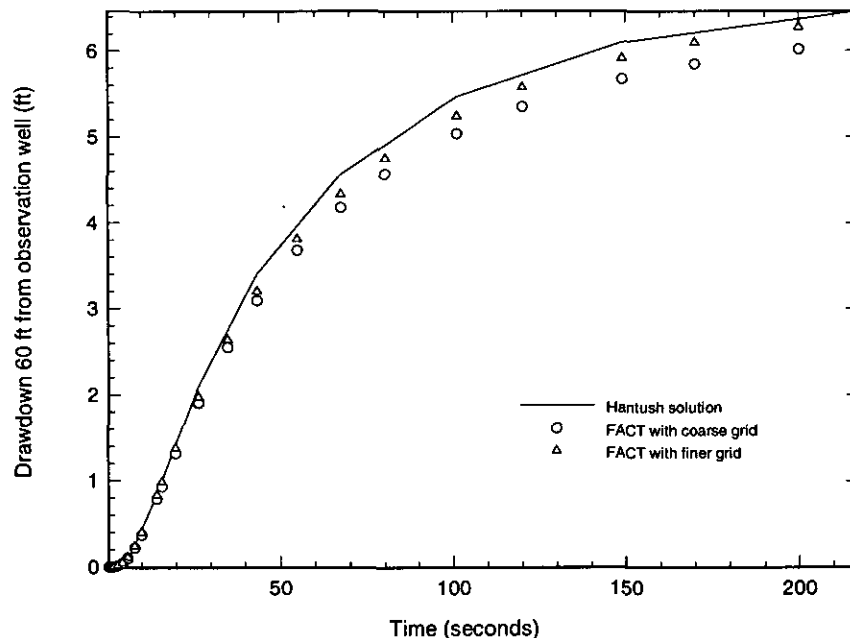


Fig. 4.1.7.2. Comparison of Hantush and Jacob (1955) analytic drawdown solution and FACT numerical results for two grids.

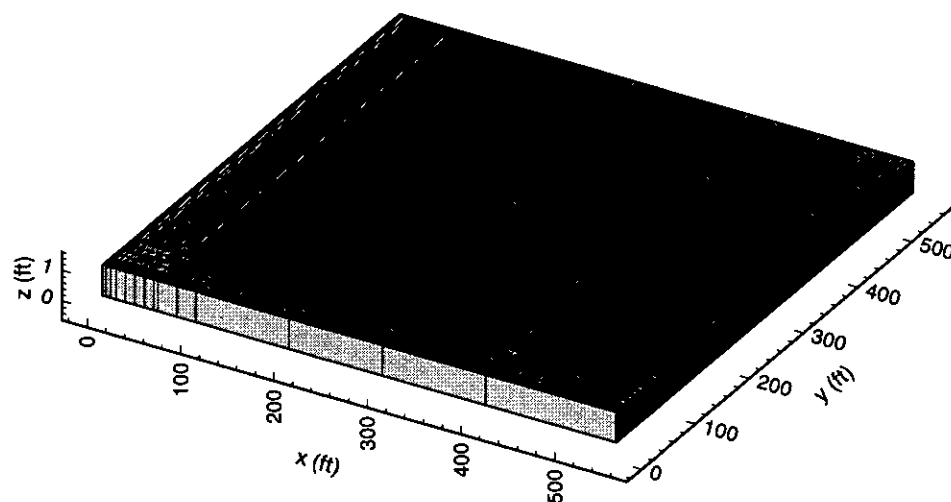


Fig. 4.1.7.3. FACT coarse grid.

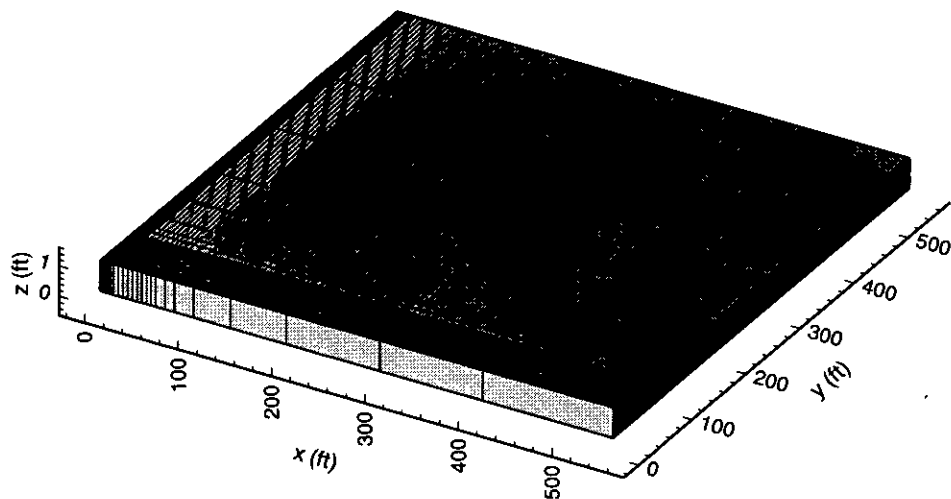


Fig. 4.1.7.4. FACT fine grid.

Table 4.1.7.1Comparison of analytic solution and FACT numerical results at $r = 60$ ft

Time (sec)	Analytic Solution (ft)	FACT Coarse Grid (ft)	FACT Fine Grid (ft)
0.5	-	0.00004	0.00003
1.0	-	0.0003	0.0002
1.5	-	0.0009	0.0008
2.0	-	0.002	0.002
3.0	-	0.012	0.012
4.4	-	0.043	0.047
6.0	0.08	0.108	0.118
8.0	-	0.229	0.248
10.0	-	0.381	0.411
14.5	0.85	0.796	0.842
16.0	-	0.939	0.991
20.0	-	1.326	1.387
26.5	2.1	1.906	1.980
35.0	-	2.556	2.646
43.5	3.41	3.100	3.208
55.0	-	3.683	3.816
67.5	4.57	4.179	4.337
80.0	-	4.571	4.751
101.0	5.47	5.039	5.246
120.0	-	5.353	5.578
149.0	6.1	5.675	5.917
170.0	-	5.849	6.100
200.0	-	6.021	6.277
217.0	6.46	6.099	6.357

4.1.8 Transient, Two-Dimensional Flow to a Well in an Unconfined Aquifer (Neuman, 1975)

We consider a problem involving radial flow to well in an unconfined aquifer whose solution is given by Neuman (1975). The problem is illustrated in Fig. 4.1.8.1. Specifically we consider an aquifer with the following attributes:

- horizontal
- unconfined
- infinite in horizontal extent
- initial uniform thickness
- homogeneous properties
- uniform head at $t = 0$

A single extraction well is assumed to be present with the following characteristics:

- constant pumping rate for $t > 0$
- infinitesimally small well diameter

The parameter values chosen for the FACT simulation are given in Fig. 4.1.8.1. These parameter values were chosen to match the unconfined pumping tests performed by Nichols (1992).

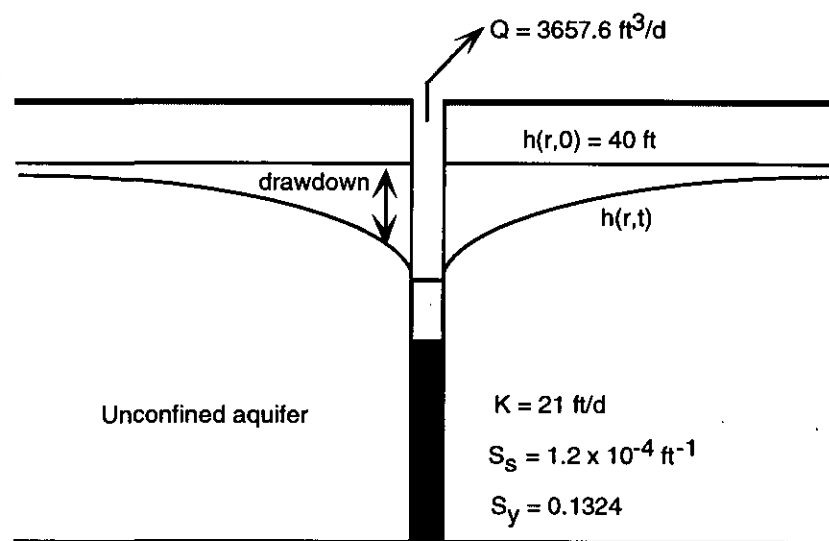


Fig. 4.1.8.1. Radial flow to a pumping well in an unconfined aquifer.

Analytic solution: The equations and boundary conditions used are, see (Fig. 4.1.8.1) in the aquifer,

$$K_r \frac{\partial^2 s}{\partial r^2} + \frac{K_r}{r} \frac{\partial s}{\partial r} + K_z \frac{\partial^2 s}{\partial z^2} = S_s \frac{\partial s}{\partial t}, \quad 0 < z < b \quad (4.1.8.1)$$

drawdown at the water table

$$K_z \frac{\partial s}{\partial z}(r, b, t) = -\omega_d \frac{\partial s}{\partial t}(r, b, t) \quad (4.1.8.2)$$

at the impervious bottom

$$\frac{\partial s}{\partial z}(r, 0, t) = 0 \quad (4.1.8.3)$$

along the well

$$\lim_{r \rightarrow 0} \left(r \frac{\partial s}{\partial r} \right) = -\frac{Q}{2\pi K_r b} \quad (4.1.8.4)$$

at infinity

$$s(\infty, z, t) = 0 \quad (4.1.8.5)$$

initial condition

$$s(r, z, 0) = 0 \quad (4.1.8.6)$$

FACT CODE MANUAL

with K_r , K_z the horizontal and vertical hydraulic conductivity in the aquifer.

The drawdown in the aquifer is given by

$$s = \frac{Q}{4\pi T} \int_0^\infty 4yJ_0(y\beta^{1/2})[u_0(y) + \sum_{n=1}^{\infty} u_n(y)]dy \quad (4.1.8.7)$$

where

$$u_0(y) = \frac{\{1 - \exp[-t_s\beta(y^2 - \gamma_0^2)]\} \cosh(\gamma_0 z / b)}{\{y^2 + (1 + \sigma)\gamma_0^2 - (y^2 - \gamma_0^2)^2 / \sigma\} \cosh(\gamma_0)}$$

$$u_n(y) = \frac{\{1 - \exp[-t_s\beta(y^2 + \gamma_n^2)]\} \cos(\gamma_n z / b)}{\{y^2 - (1 + \sigma)\gamma_n^2 - (y^2 + \gamma_n^2)^2 / \sigma\} \cosh(\gamma_0)}$$

and

$$T = K_r b$$

$$t_s = Tt / Sr^2$$

$$\beta = (K_r / K_z)(r^2 / b^2)$$

$$\sigma = S / \omega_d$$

The terms γ_0 and γ_n are roots of the following

$$\sigma\gamma_0 \sinh(\gamma_0) - (y^2 - \gamma_0^2) \cosh(\gamma_0) = 0 \quad \gamma_0^2 < y^2 \quad (4.1.8.8)$$

$$\sigma\gamma_n \sin(\gamma_n) + (y^2 + \gamma_n^2) \cos(\gamma_n) = 0 \quad (4.1.8.9)$$

$$(2n-1)(\pi/2) < \gamma_n < n\pi \quad n \geq 1$$

FACT simulation and comparison: Figure 4.1.8.2 illustrates the grid chosen for FACT simulations. The mesh is 24 by 24 elements in the horizontal plane and 26 elements thick vertically for a total of 14976 elements. The number of nodes is $25 \times 25 \times 27 = 16875$. The mesh is non-uniform with refinement near the pumping well, because steep head gradients are expected there. For water movement above the water table, the pseudo-soil is used. Pumping in an unconfined aquifer results in an unsaturated region near the well. Since FACT simulates an extraction well with nodal sinks in a saturated region, the nodal sinks must remain below the water table throughout the simulation. In order to determine the maximum water table drawdown at the well, FACT is used solve a steady state problem with a vertical line sink at the well location. After assigning the appropriate nodal sinks at the well location, FACT is used to solve the transient problem. Figure 4.1.8.3 illustrates the FACT transient results at $r = 31$ ft, $z = 23$ ft compared to the Neuman solution and pump test data, and Tables 4.1.8.1 - 4.1.8.3 present numerical values. Figure 4.1.8.4 presents drawdown at $z = 23$ ft, $t = 6.94$ days, and Tables 4.1.8.4 -

4.1.8.5 present numerical values. The FACT results are observed to agree approximately with the Neuman solution.

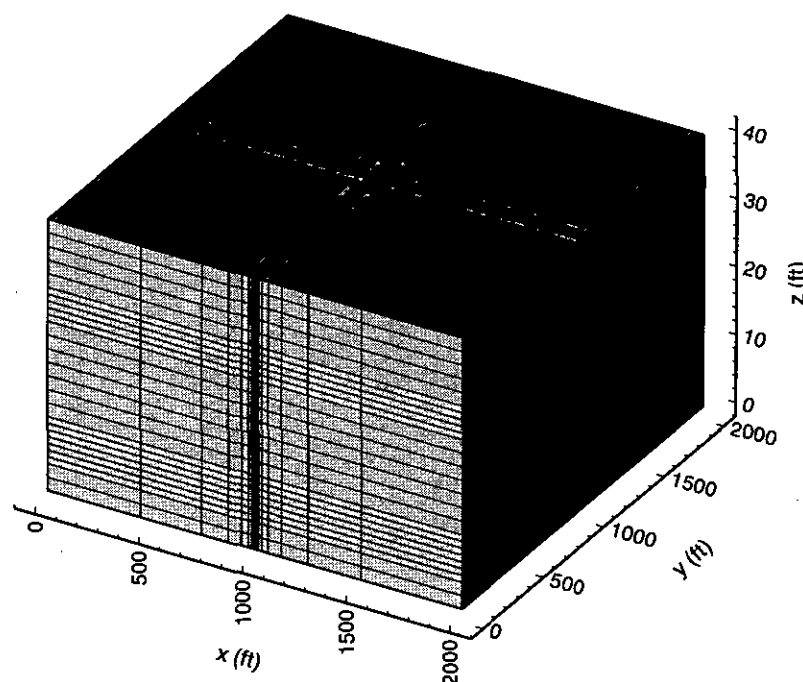


Fig. 4.1.8.2. FACT grid.

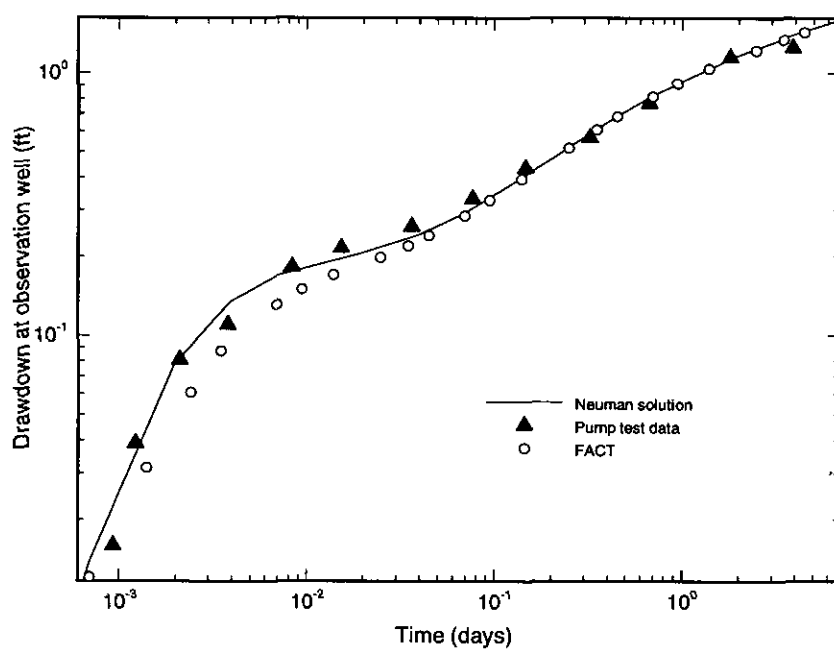


Fig. 4.1.8.3. Neuman solution, pump test data and FACT results at $r = 31$ ft, $z = 23$ ft.

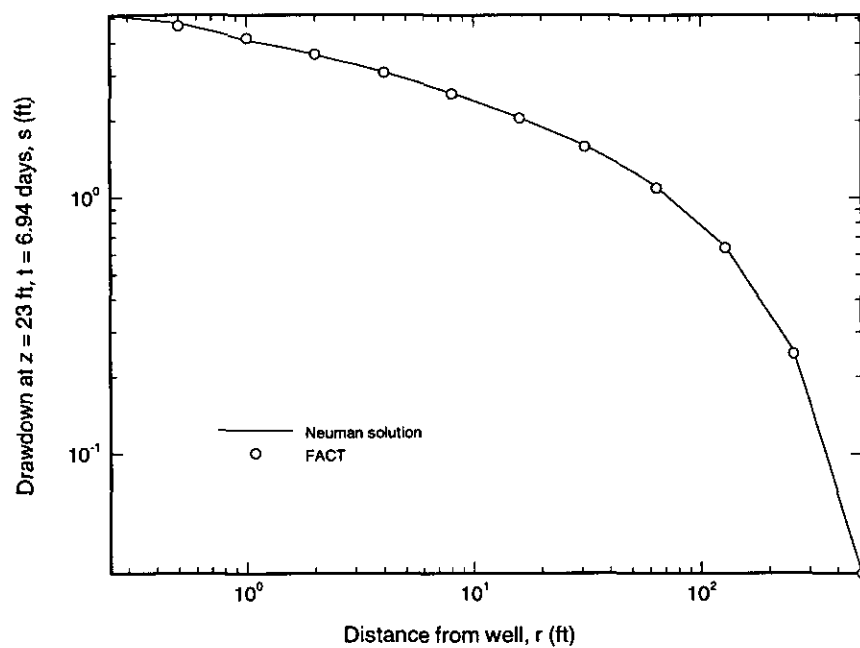


Fig. 4.1.8.4. Neuman solution and FACT results at $z = 23$ ft, $t = 6.94$ days.

Table 4.1.8.1Neuman solution at $r = 31$ ft, $z = 23$ ft

Time (days)	Neuman solution (ft)
.494E-03	.529E-02
.694E-03	.139E-01
.194E-02	.777E-01
.394E-02	.135
.694E-02	.169
.194E-01	.205
.394E-01	.241
.694E-01	.292
.194	.464
.394	.648
.694	.822
1.94	1.16
3.94	1.40
6.94	1.60

Table 4.1.8.2

Pump test data

Time (days)	Pump test data (ft)
9.259E-04	1.600E-02
1.215E-03	3.900E-02
2.083E-03	8.100E-02
3.819E-03	0.1100
8.333E-03	0.1820
1.527E-02	0.2150
3.611E-02	0.2600
7.638E-02	0.3320
0.1458	0.4330
0.3194	0.5659
0.6666	0.7670
1.805	1.149
3.888	1.250

Table 4.1.8.3

FACT numerical results

Time (days)	FACT drawdown (ft)
.694E-03	.123E-01
.139E-02	.322E-01
.239E-02	.622E-01
.347E-02	.896E-01
.694E-02	.135
.939E-02	.154
.139E-01	.174
.247E-01	.201
.347E-01	.222
.447E-01	.242
.694E-01	.287
.939E-01	.329
.139	.396
.247	.519
.347	.611
.447	.686
.694	.817
.939	.916
1.39	1.04
2.47	1.23
3.47	1.35
4.47	1.44
6.94	1.59

Table 4.1.8.4Neuman solution at $z = 23$ ft, $t = 6.94$ days

r (ft)	Neuman solution (ft)
.250	5.14
.500	4.79
.750	4.40
1.00	4.10
1.50	3.83
2.00	3.61
2.50	3.42
3.00	3.30
4.00	3.08
5.00	2.90
7.00	2.65
9.00	2.47
11.0	2.32
16.0	2.05
31.0	1.60
51.0	1.26
64.0	1.10
128.	.644
256.	.253
512.	.340E-01

Table 4.1.8.5

FACT numerical results

r (ft)	FACT drawdown (ft)
.500	4.75
1.00	4.26
2.00	3.72
4.00	3.17
8.00	2.63
16.0	2.09
31.0	1.60
64.0	1.09
128.	.641
256.	.253
512.	.420E-01

4.1.9 Transient, Two-Dimensional Flow in an Unconfined Aquifer

Figure 4.1.9.1 illustrates an unconfined aquifer experiencing transient, two-dimensional flow. The test problem is designed to confirm correct implementation of the drain boundary condition. The drain boundary condition is examined at

$$(x, z) = (20, 30) \quad (4.1.9.1)$$

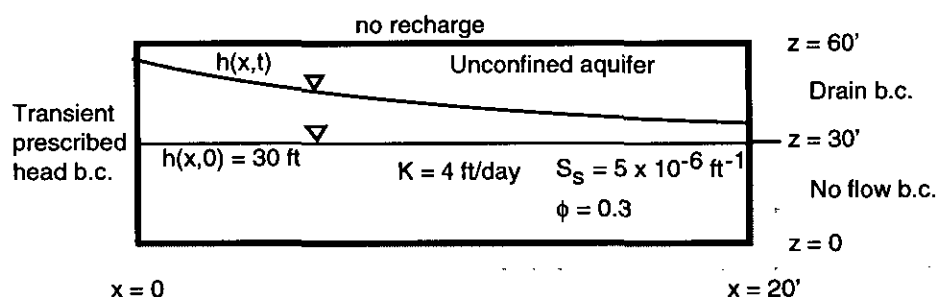


Fig. 4.1.9.1. Schematic diagram of an unconfined aquifer with a transient prescribed head boundary condition at $x = 0$ and a combination of drain and no flow boundary conditions at $x = 20$.

Problem description: The variably saturated flow equation is solved with the prescribed head boundary conditions,

$$h = h(t) \quad @ \quad x = 0, \quad 0 \leq y \leq 10, \quad 0 \leq z \leq 60 \quad (4.1.9.2)$$

the drain boundary condition,

$$-K \frac{\partial h}{\partial x} = \begin{cases} C_L (h - h_L) & h \geq h_L \\ 0 & h < h_L \end{cases} \quad (4.1.9.3)$$

$$@ \quad x = 20, \quad 0 \leq y \leq 10, \quad 30 \leq z \leq 60, \quad \text{and} \quad C_L = 2.5, \quad h_L = z$$

and the no flow boundary condition elsewhere.

FACT CODE MANUAL

FACT simulation and comparison: Figure 4.1.9.2 illustrates the FACT mesh chosen. The grid is 10×12 elements in the x-z plane and one element thick along the y axis. The number of nodes is $(10+1) \times (12+1) \times (1+1) = 286$. The transient prescribed head at $x=0$ rapidly increases from 30 ft to 50 ft during the simulation. Figure 4.1.9.3 presents the FACT transient water table height. In order to test the drain boundary condition the Darcy velocity is computed at node 143 ($x = 20'$, $y = 0'$, $z = 30'$) using the volumetric flow and the drain boundary condition. The Darcy velocity is given by

$$U_x = \frac{Q}{A} \quad (4.1.9.4)$$

where the volumetric flow Q at node 143 is the result of the FACT mass balance computation (Group 11, IMBAL = 1) and the effective flow area A at node 143 is 12.5 ft². The Darcy velocity is also given by

$$U_x = \begin{cases} C_L(h - h_L) & h \geq h_L \\ 0 & h < h_L \end{cases} \quad (4.1.9.5)$$

where h is hydraulic head at node 143 and $h_L = 30'$. Table 4.1.9.1 and Fig. 4.1.9.4 present the two calculations of Darcy velocity at node 143.

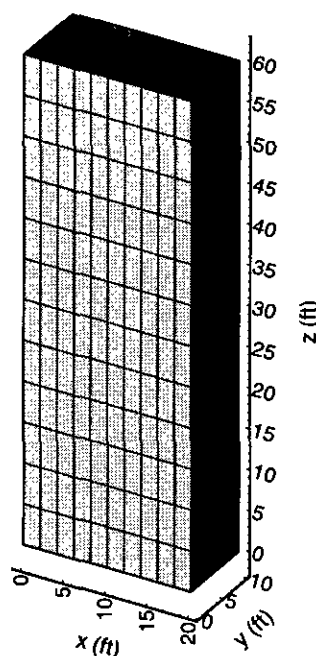


Fig. 4.1.9.2. FACT grid.

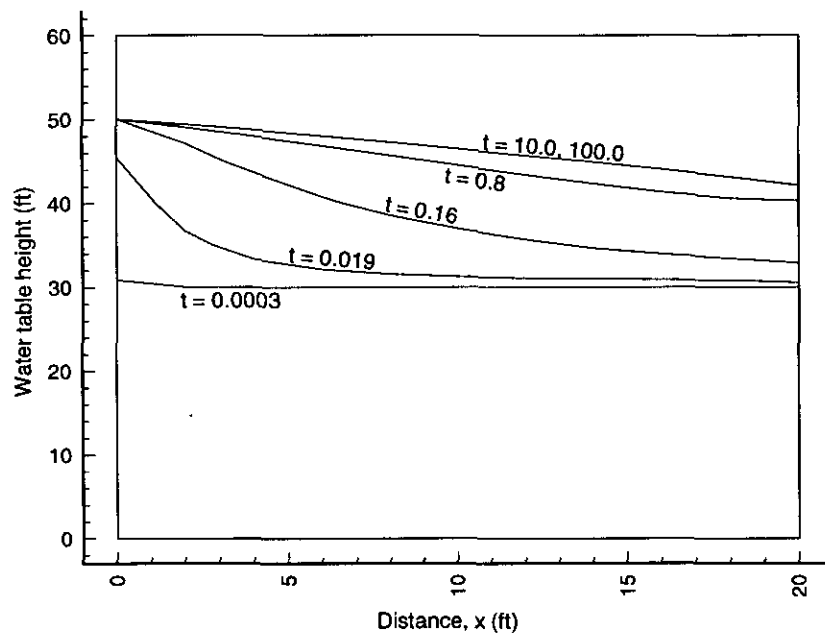
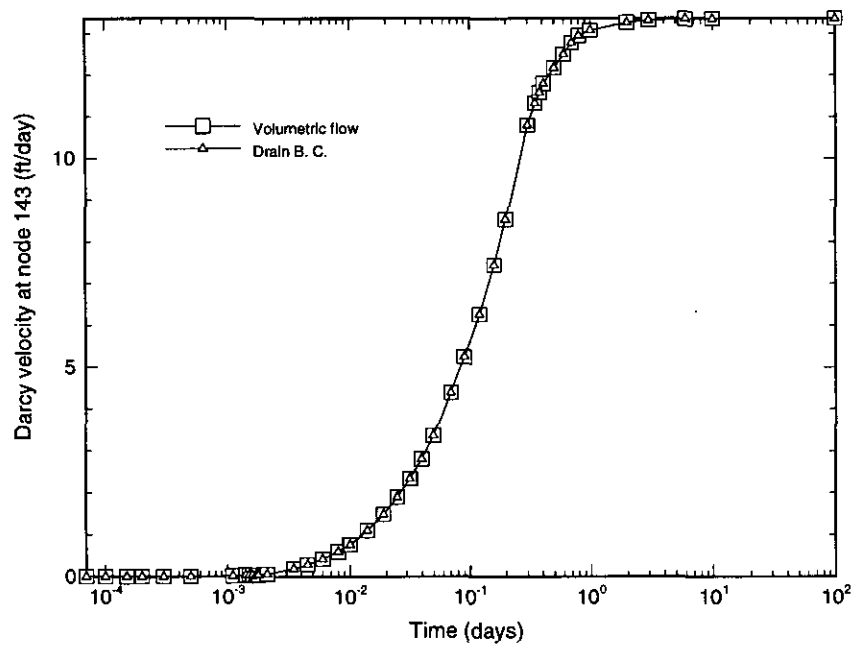
**Fig. 4.1.9.3.** FACT water table height.**Fig. 4.1.9.4.** FACT Darcy velocity at $x = 20'$, $z = 30'$.

Table 4.1.9.1FACT Darcy velocity at $x = 20'$, $z = 30'$

Time (day)	Volumetric flux (ft/day)	Drain Flux (ft/day)
0.00006944	0.00000007	0.00000007
0.00010000	0.00000012	0.00000012
0.00015000	0.00000031	0.00000031
0.00020000	0.00000067	0.00000067
0.00030000	0.00000272	0.00000272
0.00050000	0.00001773	0.00001773
0.00110000	0.00033194	0.00033192
0.00140000	0.00058052	0.00058053
0.00150000	0.00067454	0.00067454
0.00160000	0.00078063	0.00078063
0.00170000	0.00089978	0.00089978
0.00175000	0.00096272	0.00096275
0.00177000	0.00098848	0.00098848
0.00210000	0.00160783	0.00160774
0.00347222	0.13836838	0.13836833
0.00450000	0.24007208	0.24007204
0.00600000	0.37976824	0.37976822
0.00800000	0.55747641	0.55747641
0.01000000	0.73170317	0.73170314
0.01388889	1.07367627	1.07367603
0.01900000	1.46455484	1.46455482
0.02500000	1.87545203	1.87545202
0.03200000	2.31563815	2.31563803
0.04000000	2.79200611	2.79200609
0.05000000	3.35594935	3.35593853
0.06944444	4.38032886	4.38032884
0.09000000	5.23714952	5.23714956
0.12000000	6.25780281	6.25779629
0.16000000	7.43950587	7.43950621
0.20000000	8.53664630	8.53667607
0.30000000	10.80022826	10.80022805
0.34722222	11.32561859	11.32561852
0.38000000	11.58367136	11.58366935
0.41000000	11.79758758	11.79758694
0.50000000	12.17662248	12.17662198
0.60000000	12.50513109	12.50513099
0.70000000	12.77659993	12.77659907
0.80000000	12.94880157	12.94880421
1.00000000	13.07833772	13.07833568
2.00000000	13.26144369	13.26144338
3.00000000	13.31916598	13.31916712
6.00000000	13.34981163	13.34981354
10.00000000	13.35694070	13.35694326
100.00000000	13.35857379	13.35857354

FACT CODE MANUAL

4.1.10 Unsaturated Vertical Soil Column

Figure 4.1.10.1 illustrates the FACT mesh chosen for two unsaturated test cases also shown in the figure. The test cases are designed to confirm correct implementation of soil characteristic curves and Richard's equation. The first test case essentially reproduces the water retention curve in the FACT output. The second case involves steady-state unsaturated flow which invokes relative permeability. The soil characteristic curves chosen are for "Silt Loam G.E. 3" and taken from van Genuchten (1980). Figure 4.1.10.2 shows the characteristic curves. The van Genuchten models for capillary suction-water retention and relative permeability are

$$S_e = \frac{1}{\left[1 + (\alpha P_c)^{\frac{1}{1-m}}\right]^m} \quad (4.1.10.1)$$

$$k_{rw} = S_e^{1/2} \left[1 - \left(1 - S_e^{1/m}\right)^m\right]^2 \quad (4.1.10.2)$$

where S_e is the 'effective saturation' defined by

$$S_e = \frac{S_w - S_{wr}}{1 - S_{wr}} \quad (4.1.10.3)$$

with empirical parameters α and m .

For Silt Loam G.E. 3 the empirical parameters take on the values

$$S_{wr} = 0.331$$

$$\alpha = 0.129 \text{ ft}^{-1}$$

$$m = 0.515$$

The saturated conductivity is $K = 0.163 \text{ ft/day}$ (van Genuchten, 1980).

Water retention profile case: Because the steady-state head is zero along the column, there is no flow in the column. Figure 4.1.10.2 and Table 4.1.10.1 show the exact and code predicted saturation profile within the column. The agreement is excellent.

Steady-state unsaturated flow at constant saturation case: For a saturation of 75%, the capillary pressure is 0.005125952 ft and the relative permeability is 0.043098523. For boundary conditions of 75% saturation applied to both ends of the column, the Darcy velocity should be

$$U = k_{rw} K \frac{\Delta h}{\Delta z} = (0.043098523)(0.163 \frac{\text{ft}}{\text{day}}) \frac{50 \text{ ft}}{50 \text{ ft}} = 0.007025 \frac{\text{ft}}{\text{day}} \quad (4.1.10.4)$$

The FACT code reproduces this value as expected.

FACT CODE MANUAL

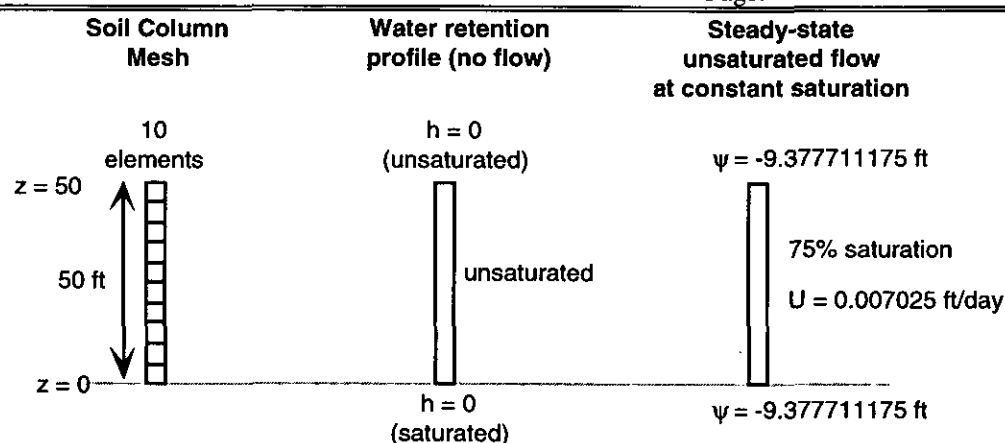


Fig. 4.1.10.1. Schematic illustration of FACT mesh and unsaturated test cases.

Soil Characteristic Curves for Silt Loam G.E. 3 (van Genuchten, 1980)

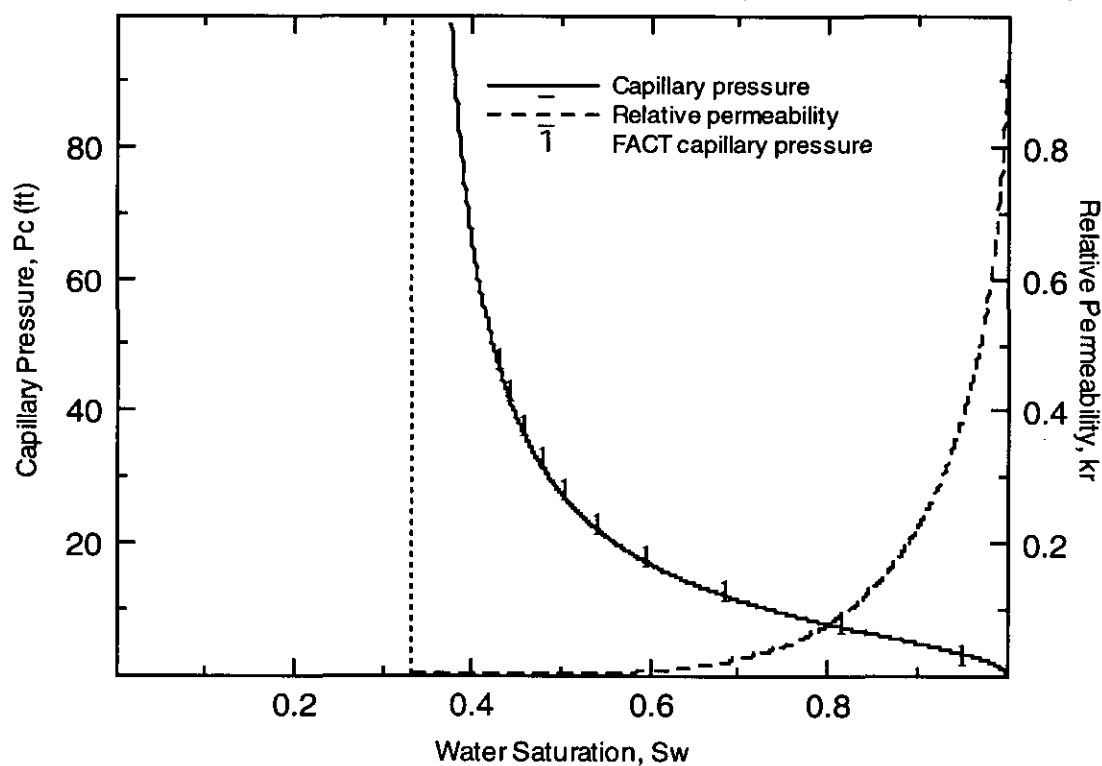


Fig. 4.1.10.2. Soil characteristic curves for Silt Loam G.E. 3 (van Genuchten, 1980) with FACT code results overlain.

Table 4.1.10.1*Water retention curve and FACT comparison of saturation*

Element No.	Elevation z (ft)	Analytical pressure head ψ (ft)	Water Retention Curve Saturation S_w	FACT Saturation (10 elem) S_w	Element No.	FACT Saturation (250 elem) S_w
1	2.5	-2.5	0.9689	0.9463	13	0.9688
2	7.5	-7.5	0.8073	0.8127	38	0.8073
3	12.5	-12.5	0.6731	0.6795	63	0.6731
4	17.5	-17.5	0.5890	0.5928	88	0.5891
5	22.5	-22.5	0.5354	0.5375	113	0.5354
6	27.5	-27.5	0.4991	0.5004	138	0.4991
7	32.5	-32.5	0.4733	0.4741	163	0.4733
8	37.5	-37.5	0.4540	0.4546	188	0.4540
9	42.5	-42.5	0.4392	0.4396	213	0.4392
10	47.5	-47.5	0.4274	0.4277	238	0.4275

4.2 Solute Transport Problems

In the following three sections we present one, two, and three dimensional solute transport examples, respectively. They are classical cases ideal for studying the basic behavior of an advection-dispersion equation solver. In the one-dimensional case we shall test the equation solver in various ways by varying its control parameters over a wide range of values. This enables users to see the inherent weaknesses of this solver and hopefully will help the users to minimize such weaknesses in their own problems. The majority of behaviors presented below are observed in all advection-dispersion solvers. Ultimately, the users must rely on their own experience and it is highly recommended that several transport simulations of the same problem be performed. Comparisons to these simulations will provide excellent insight into how adequate and optimal their solution is. The test cases selected all have analytic solutions for a clear picture as to how well FACT handles these transport conditions. As the users will see, oscillations about a point source typically occurs; however, in many field-scale applications such limited oscillations can have negligible effects beyond the close proximity of point sources.

4.2.1 One-Dimensional Saturated Solute Transport in a Uniform Flow Field

This problem deals with one-dimensional advection-dispersion of a non-conservative solute species through a semi-infinite porous medium and is used to demonstrate the impact that various FACT options (i.e., numerical approximations) have on its solution. The 1D advection-dispersion equation is ideal for testing an algorithm's behavior over a wide range of conditions. A physical schematic of this problem is shown in Fig. 4.2.1.1. As illustrated, a non-conservative contaminant is continuously released from a fully penetrating channel into a shallow confined aquifer unit whose groundwater flow is assumed to be uniform. Both hydrodynamic dispersion and molecular diffusion are allowed, as well as, the possibility of radioactive decay and/or adsorption of the species. It is assumed that the contaminant concentration level in the neighboring reservoir remains constant, the aquifer's flow rate is uniform and constant, and the homogeneous aquifer's properties (such as porosity, soil type, water saturation) are uniform and constant.

Analytic solution: Equation (2.2.28) represents the non-conservative form of the multi-dimensional advection-dispersion equation for solute transport through a variably saturated porous media. Taking the 1-D form of Eq. (2.2.28) and assuming that no point or line sources/sinks exist within the domain, constant water saturation level, and that material coefficients are constants, results in

$$\frac{\partial c}{\partial t} = D'_{xx} \frac{\partial^2 c}{\partial x^2} - u'_x \frac{\partial c}{\partial x} - \lambda_r c \quad (4.2.1.1)$$

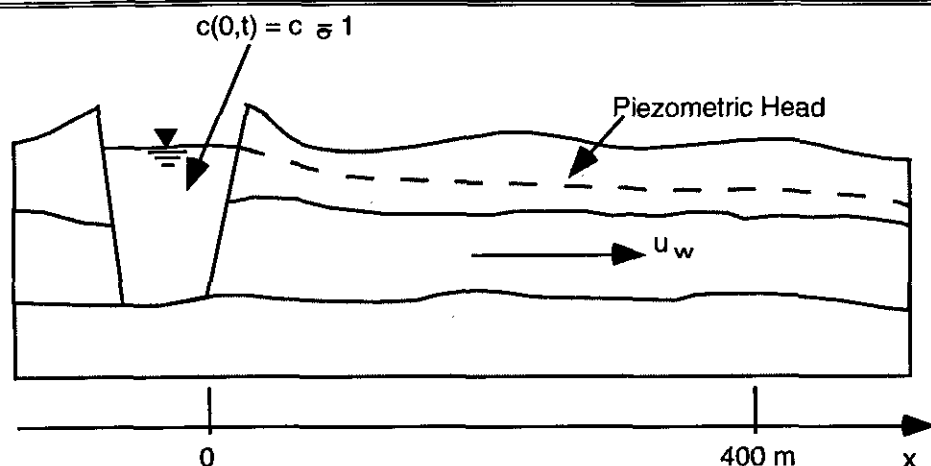


Fig. 4.2.1.1. Schematic diagram for 1D solute transport in a confined aquifer.

where

$$D_{xx} = \alpha_{LH} u_x + \theta_m \tau D^* \quad (\text{hydrodynamic dispersion coef.})$$

$$D'_{xx} = \frac{D_{xx}}{R} \quad (\text{retarded longitudinal dispersion coef.})$$

$$u'_x = \frac{u_x}{R} \quad (\text{retarded phasic water velocity})$$

$$u_x = \frac{U_x}{\theta_m} \quad (\text{phasic water velocity})$$

$$R = 1 + \frac{\rho_b k_d}{\theta_m} \quad (\text{retardation factor})$$

$$\rho_b = \rho_s (1 - \phi) \quad (\text{bulk soil density})$$

For our semi-infinite confined aquifer the initial conditions are:

$$c(x,0) = 0 \quad (4.2.1.2a)$$

and the boundary conditions are:

$$c(0,t) = c_0 \quad (4.2.1.2b)$$

$$c(\infty,t) = 0 \quad (4.2.1.2c)$$

For the first boundary condition we are assuming that at $x=0$ the contaminant concentration reaches its ultimate value c_0 immediately upon commencement of flow and remains at that value throughout all positive times ($x=0$ boundary represents an inflow boundary). The second boundary condition is equivalent to assuming that the dispersive flux of solute is zero at plus infinity or

$$\lim_{x \rightarrow \infty} \left(\frac{\partial c}{\partial x} \right) = 0 \quad (4.2.1.2d)$$

FACT CODE MANUAL

For finite times there exists a finite value of x where Eq. (4.2.1.2d) remains valid.

Equation (4.2.1.1), a linear partial differential equation subject to the initial and boundary conditions given by Eqs. (4.2.1.2a,b,c), can be solved by applying the Laplace transform technique. The general solution has been derived by Grobner and Hofreiter (1950) and takes the form:

$$c(x, t) = \frac{1}{2} c_0 \exp\left(\frac{u'_x x}{2D'_{xx}}\right) \left[\exp(-x\beta) \operatorname{erfc}\left(\frac{x - \sigma t}{2\sqrt{D'_{xx} t}}\right) + \exp(x\beta) \operatorname{erfc}\left(\frac{x + \sigma t}{2\sqrt{D'_{xx} t}}\right) \right] \quad (4.2.1.3)$$

where

$$\beta^2 = \left(\frac{u'_x}{2D'_{xx}}\right)^2 + \frac{\lambda_r}{D'_{xx}} \quad \text{and} \quad \sigma^2 = (u'_x)^2 + 4\lambda_r D'_{xx} \quad (4.2.1.3a)$$

When there is no radioactive decay ($\lambda_r = 0$) present Eq. (4.2.1.3) reduces to

$$c(x, t) = \frac{1}{2} c_0 \left[\operatorname{erfc}\left(\frac{x - u'_x t}{2\sqrt{D'_{xx} t}}\right) + \exp\left(\frac{u'_x x}{D'_{xx}}\right) \operatorname{erfc}\left(\frac{x + u'_x t}{2\sqrt{D'_{xx} t}}\right) \right] \quad (4.2.1.4)$$

derived also by Ogata and Banks (1961). The absence of adsorption is achieved by setting the retardation factor to unity ($R = 1$). Note that the original derivation by Grobner and Hofreiter was performed on the limited case of a saturated media in the absence of adsorption. The more general case presented here results in the same solution but are based upon retarded material coefficients (highlighted with carrots). The evaluation of the analytic expression Eq. (4.2.1.3) for a specific problem is performed numerically and has been placed in an algorithm named AT1D.

FACT numerical simulation and comparison: Values of the physical parameters used in the verification simulations are presented in Table 4.2.1.1. The base case grid chosen for this problem consists of 40 rectangular brick elements uniformly sized (10 m in length) and stacked along the x -axis. Figure 4.2.1.2 illustrates the finite element mesh chosen and the boundary conditions applied along the six outer domain surfaces. At the channel inlet boundary (left face), the concentration of solute in the incoming water is set to 1.0 kg/m^3 . Due to the finite overall length of our mesh, at the outflow boundary (right face) the dispersive flux is set to zero, while the advective flux is calculated as part of the solution. Since this is a 1-D problem, solute concentration gradients do not exist in the transverse directions (y and z directions). Therefore, the dispersive fluxes along these four faces (top, bottom, front, and back) are set to zero. By default, in the standard finite element formulation zero dispersive fluxes are automatically applied to all outer domain surfaces unless otherwise specified. The aquifer is assumed to be completely saturated.

Table 4.2.1.1

Values of the physical parameters, the finite element grid, time-step data, and some key parameters used in the one-dimensional transport problem (base case and its variations)

Physical parameters	Base case	Range tested
Darcy velocity, U_x	1.0 m/d	-
Porosity, ϕ	0.25	-
Longitudinal horizontal dispersivity, α_{LH}	5.0 m	0.01,5.0
Apparent molecular dispersion coefficient, $\theta_m \tau D^*$	0.0 m ² /d	-
Water saturation, S_w	1.0	-
radioactive decay coef., λ_T	0.0 d ⁻¹	0.0,0.01
Soil density, ρ_s	1.0 kg/m ³	-
Solute distribution coefficient, k_d	0.0 m ³ /kg	0.0,0.3333
Boundary solute concentration, c_0	1.0 kg/m ³	-
Grid specifics		
Element length, Δx	2 m	2,20,40,80
Element width, Δy	2 m	-
Element height, Δz	2 m	-
Number nodes in x-dir	201	201,21,11,6
Number nodes in y-dir	2	-
Number nodes in z-dir	2	-
Longitudinal length	400 m	-
Time steps		
Time duration	50 d	-
number time-steps	500	20,10,5,2
time-step size, Δt	0.1 d	2.5,5,10,25
Key computed parameters		
Retardation factor, R	1.0	1.0,2.0
Bulk soil density, ρ_b	0.75 kg/m ³	-
Phasic velocity, u_x	4.0 m/d	-
Retarded phasic velocity, u'_x	4.0 m/d	4.0,2.0
Retarded longitudinal dispersion coefficient, D'_{xx}	20.0 m ² /d	20.0,10.0
Cell Fourier number, $ Fo_x$	0.5	0.5,0.0078125, 0.03125,0.125,0.5, 1.0,2.0,5.0
Cell Courant number, $ Co_x$	0.2	0.2,0.125,0.25,0.5, 10,20,50
Cell Peclet number, $ Pe_x$	0.4	0.4,4.0,8.0,16.0, 1000.0

For this problem several simulations were performed. As summarized in Table 4.2.1.2, simulations were performed for a base case and then fifteen runs were made varying

certain key physical parameters and FACT options to demonstrate their impact on the final results. For each simulation a transient calculation was performed for a 50 day duration and the results from FACT at two points in time (25 and 50 days) are compared to the analytical solution given by Eq. (4.2.1.3). As shown in Table 4.2.1.1, a broad range of cell Peclet, cell material Courant, and cell Fourier numbers were tested. For understanding behavior, stability, and accuracy issues, these are very important quantities to consider.

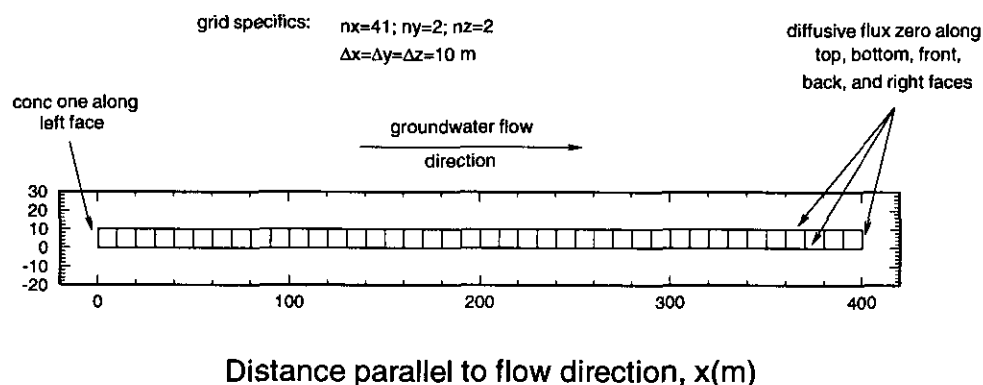


Fig. 4.2.1.2. FACT mesh and boundary conditions for 1D transport.

The results of all the simulations (both numerical and analytical) are shown in Figs. 4.2.1.3 through 4.2.1.14. Each figure corresponds to a different combination of parameters (e.g., spatial and temporal approximations). These results are also presented in tabular form for comparison in Tables 4.2.1.3 through 4.2.1.14. The analytical results were computed from the computer code AT1D. The FACT numerical results are labeled "FACT" for the base case and have additional nomenclature for the other runs (e.g., "FACT ($\lambda_r=0.01$)" represents the run where all parameters were at their base case values except for the radioactive decay parameter that was set to 0.01).

The results presented in Fig. 4.2.1.3 represent our base case. The concentration profiles at both time shots compare very close to the analytical profiles. Once the simulation time has reached 50 days, sufficient time has elapsed such that the concentration profile's shape is unaffected by the inlet boundary condition and the mean transport distance (location of 50% of the solute) corresponds to the retarded velocity times elapsed time. For the base case at 50 days the mean distance is 200 m (i.e., 4.0 m/d x 50 d). Characteristic oscillatory overshoot or undershoot, exhibited by second-order accurate centered spatial differencing, is not observed for the base case due to the fact that the local cell Peclet number does not exceed two.

FACT CODE MANUAL

By adjusting the solute distribution coefficient such that the retardation factor becomes 2.0 (case A), the retarded dispersion and velocity are halved. These results can be seen in Fig. 4.2.1.4 where (1) the mean transport distance at 50 days is now 100 m and (2) the spread of the plume has been greatly reduced. Compare the results in Fig. 4.2.1.4 to 4.2.1.3.

Table 4.2.1.2

Summary of simulations performed (base case and its variations) on the one-dimensional transport problem

FACT Options	Base case	A	B	C	D	E	F	G	H	I	J	K	L	M	N	O
temporal differencing central [Crank-Nicolson], $\omega=0.5$ backward [Euler] $\omega=1.0$	x	x	x	x	x	x	x	x	x	x	x			x	x	x
spatial differencing [Bubnov], $\alpha = 0$ optimum, $\alpha = 0.27$ full upstream, $\alpha = 1.0$	x	x	x	x	x	x	x	x	x	x		x		x		
Mesh Sizes																
Element length, $\Delta x = 2$ m	x	x	x	x				x	x	x	x	x	x	x	x	x
$\Delta x = 20$ m					x											
$\Delta x = 40$ m						x										
$\Delta x = 80$ m							x									
time-step size, $\Delta t = 0.1$ d	x	x	x	x	x	x	x				x	x	x	x	x	x
$\Delta t = 5$ d								x								
$\Delta t = 10$ d									x							
$\Delta t = 25$ d										x						
Physical Parameters																
Longitudinal horizontal dispersivity, $\alpha_{LH} = 5$ m	x	x	x	x	x	x	x	x	x	x	x	x	x			
$\alpha_{LH} = 0.01$ m														x	x	x
radioactive decay coef., $\lambda_T = 0.0$ d ⁻¹	x	x			x	x	x	x	x	x	x	x	x	x	x	x
$\lambda_T = 0.01$ d ⁻¹			x	x												
Solute distribution coef., $k_d = 0.0$ m ³ /kg	x		x		x	x	x	x	x	x	x	x	x	x	x	x
$k_d = 0.3333$ m ³ /kg		x		x												

By employing a non-zero radioactive decay coefficient such that the solute now becomes a non-conservative transport species (case B), the solute concentration profiles are reduced especially at the higher concentration levels. These results can be seen in Fig. 4.2.1.5 when compared to Fig. 4.2.1.3.

By applying both retardation and radioactive decay coefficients simultaneously (case C), we observe the composite effect as shown in Fig. 4.2.1.6. These results show (1) the

FACT CODE MANUAL

mean transport distance at 50 days is now less than 100 m and (2) the concentration profile has been reduced at the higher concentration levels.

The effect of varying the grid size (cases D, E, and F) can be seen in Fig. 4.2.1.7. As shown, the "effective" (i.e., artificial plus actual) dispersion coefficient continues to increase as the grid spacing increases. Thus, resolution of the concentration front diminishes. At the grid spacing $\Delta x = 80$ m, the cell Peclet number is 16 and we can begin to see overshoot and undershoot occurring.

The effect of varying the time-step size (cases G, H, and I) can be seen in Fig. 4.2.1.8. As shown, the "effective" (i.e., artificial plus actual) dispersion coefficient continues to increase as the time-step size increases. Thus, resolution of the concentration front diminishes. At the time-step sizes $\Delta t = 10$ and 25 days, the cell material Courant and Fourier numbers are exceeding unity and we can begin to see significant overshoot and undershoot occurring.

The effect of upstream spatial weighting (case J) can be seen in Fig. 4.2.1.9 when compared to Fig. 4.2.1.3. As shown, the "effective" (i.e., artificial plus actual) dispersion coefficient increases when full upstream weighting is applied. Note that the full upstream weighting scheme employed is only first-order accurate. In theory when the cell Peclet number is less than two, second-order accurate central spatial differencing (Bubnov-Galerkin scheme) is preferable. In practice this cutoff point can generally be raised to approximately ten. Beyond this value, some level of upstream weighting (Petrov-Galerkin scheme) is recommended to minimize overshoot and undershoot near steep concentration gradients. In FACT the degree of upstream weighting is control by input parameters or computed optimally (assuming streamline Courant number less than one) for each element as a function of streamline Peclet number.

The effect of temporal differencing (case K) can be seen in Fig. 4.2.1.10 when compared to Fig. 4.2.1.3. As shown, the "effective" (i.e., artificial plus actual) dispersion coefficient increases when backward (Euler) differencing is applied. Note that the backward (Euler) differencing scheme employed is only first-order accurate. The second-order accurate central (Crank-Nicolson) differencing is preferable. In FACT the option of temporal differencing for solute transport is control by an input parameter that is applied throughout the entire computational domain. The combined effect of spatial and temporal differencing (case L) can be seen in Fig. 4.2.1.11 when compared to Fig. 4.2.1.3. further increase in the "effective" dispersion coefficient occurs.

The above cases all were at a cell Peclet number of two. To see a strong effect of oscillation near the concentration front several case runs (cases M, N, and O) were performed at a cell Peclet number of a thousand. This high a cell Peclet number results in the transport of nearly square wave (i.e., plug flow) over the time and distance ranges of interest here. Using the optimum spatial and temporal differencing settings for our base case (case M) we see significant oscillatory behavior illustrated in Fig. 4.2.12. The central spatial differencing scheme attempt to capture the very steep concentration resulted in upstream oscillations. These oscillations can be minimized or eliminated by: (1) varying the degree of upstream weighting employed and/or (2) refining the grid

FACT CODE MANUAL

spacing. We will restrict ourselves to the grid spacing use in the base case. Applying full upstream weighting (case N) eliminates the oscillations but results in a significant increase in artificial dispersion. We can minimize the oscillations and artificial dispersion by appropriately setting the partial upstream weighting factor to $\alpha = 0.27$ (case O).

Based upon these calculations, some general guidance can be given for performing solute transport with FACT:

- Use the second-order accurate central temporal differencing (Crank-Nicolson) scheme.
- Apply the second-order accurate central spatial differencing (Bubnov-Galerkin) scheme.
- Estimate from the results the maximum cell Peclet number within the computational grid. Refine the grid such that the maximum value in each direction is less than ten (preferably less than two).
- If meeting the Peclet number constraint results in too fine of a grid for your current hardware (storage limits or run-times), then apply increasing amounts of upstream weighting until the oscillatory behavior becomes acceptable.
- In some cases grid refinement will be mandatory to meet acceptable results.

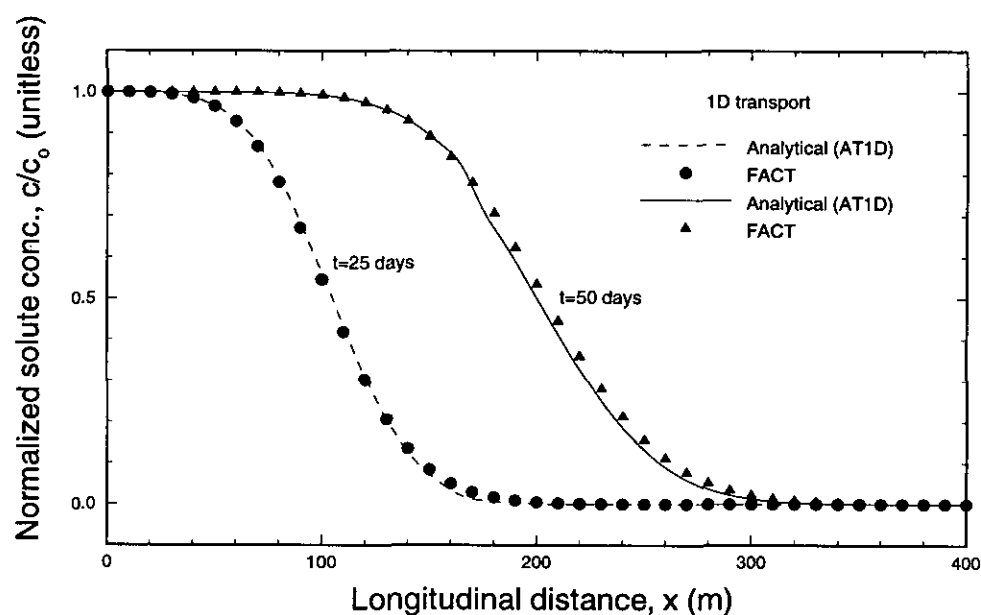


Fig. 4.2.1.3. Concentration profiles for 1D transport of the base case.

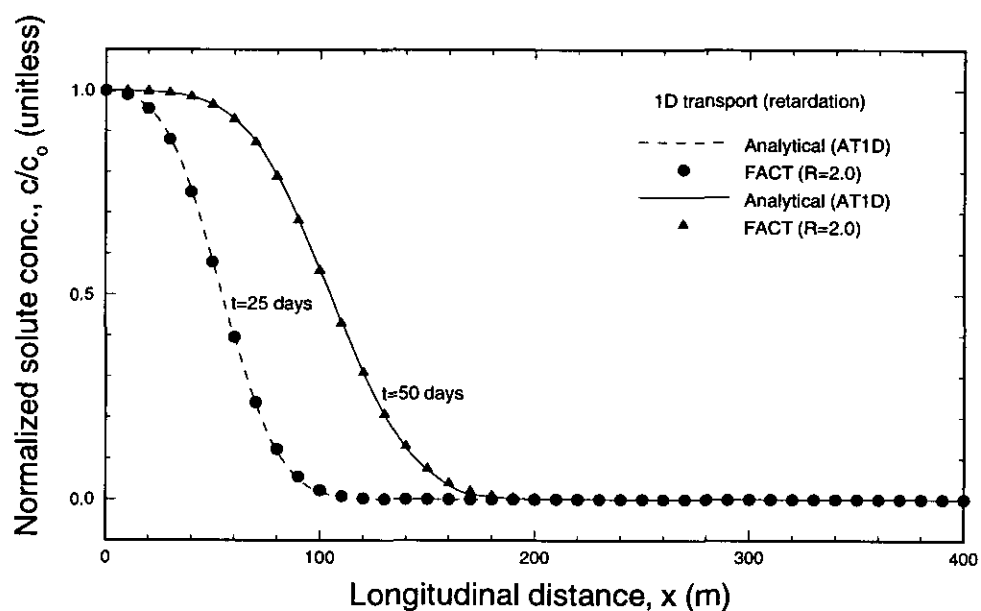


Fig. 4.2.1.4. Concentration profiles for 1D transport showing effect of retardation.

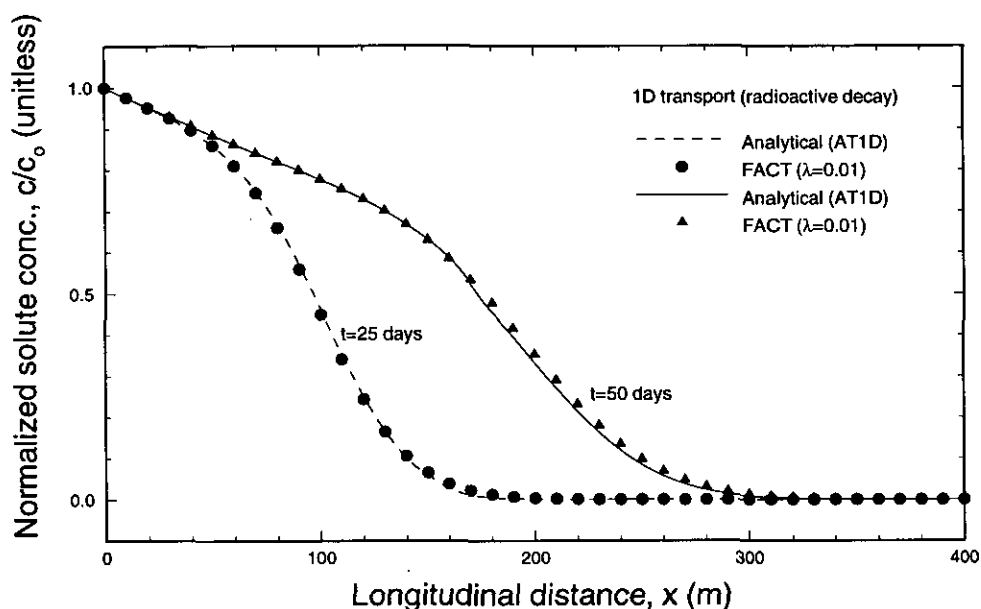


Fig. 4.2.1.5. Concentration profiles for 1D transport showing effect of radioactive decay.

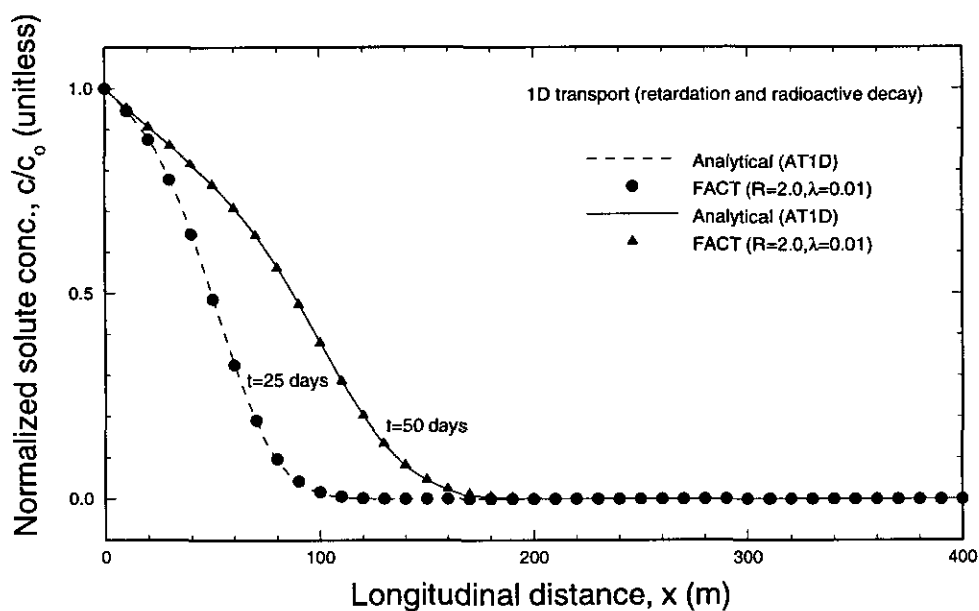


Fig. 4.2.1.6. Concentration profiles for 1D transport showing combined effect of retardation and radioactive decay.

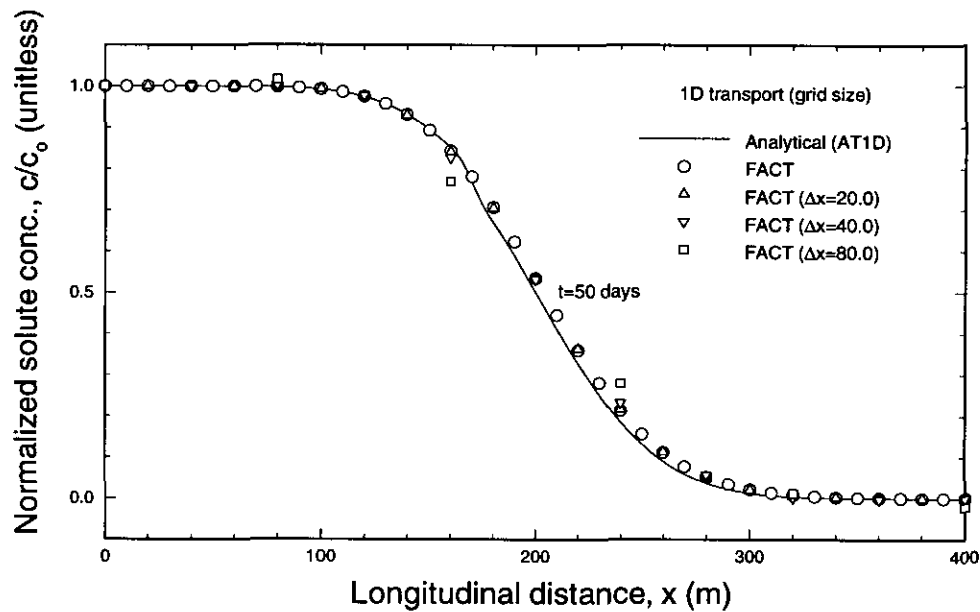


Fig. 4.2.1.7. Concentration profiles for 1D transport showing effect of grid size.

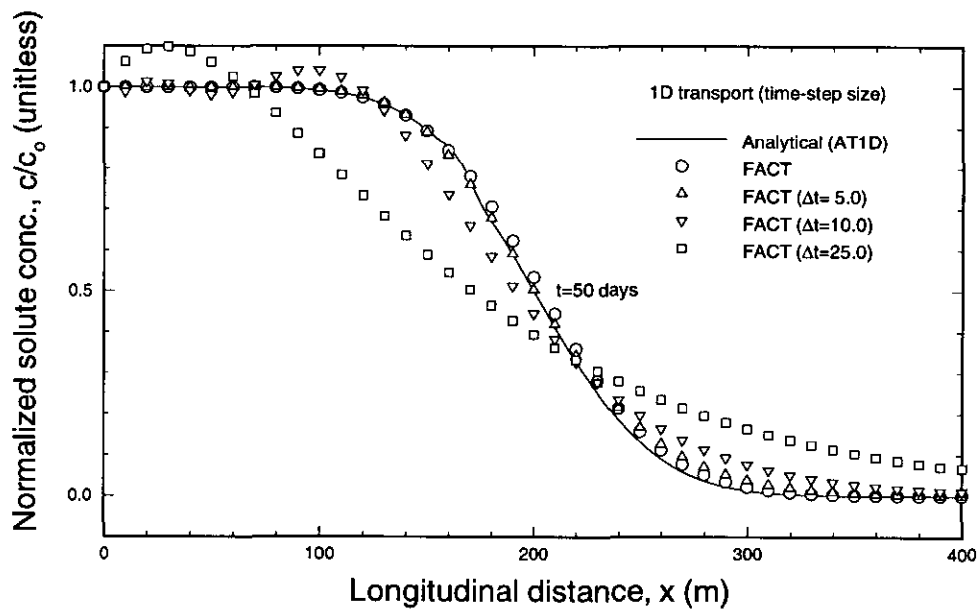


Fig. 4.2.1.8. Concentration profiles for 1D transport showing effect of time-step size.

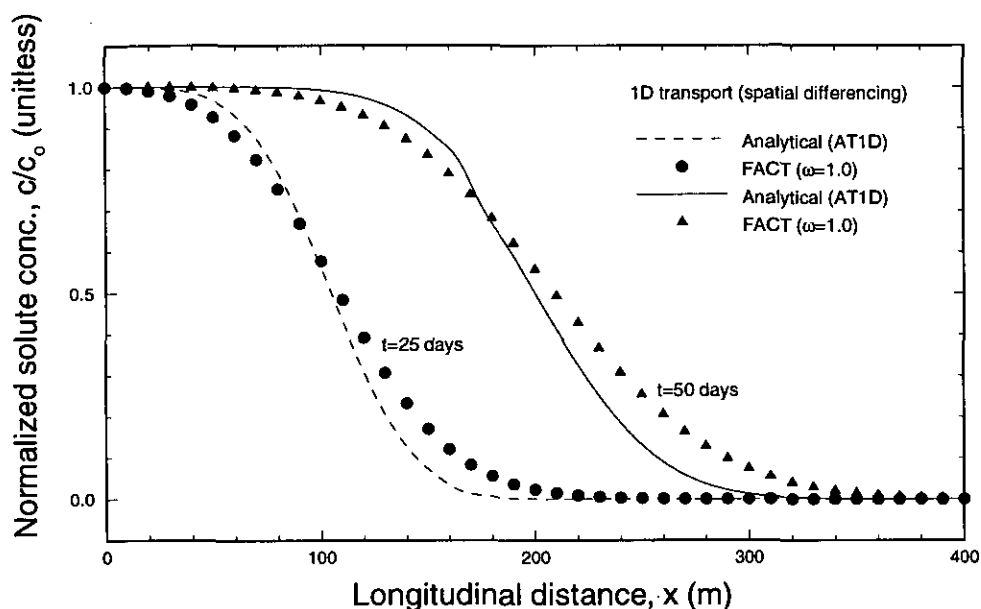


Fig. 4.2.1.9. Concentration profiles for 1D transport showing effect of spatial differencing.

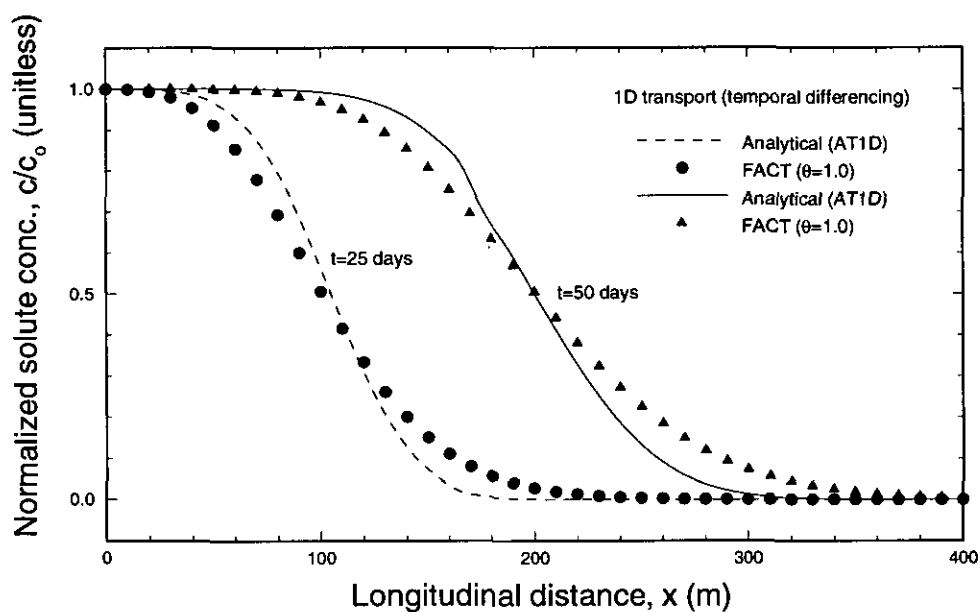


Fig. 4.2.1.10. Concentration profiles for 1D transport showing effect of temporal differencing.

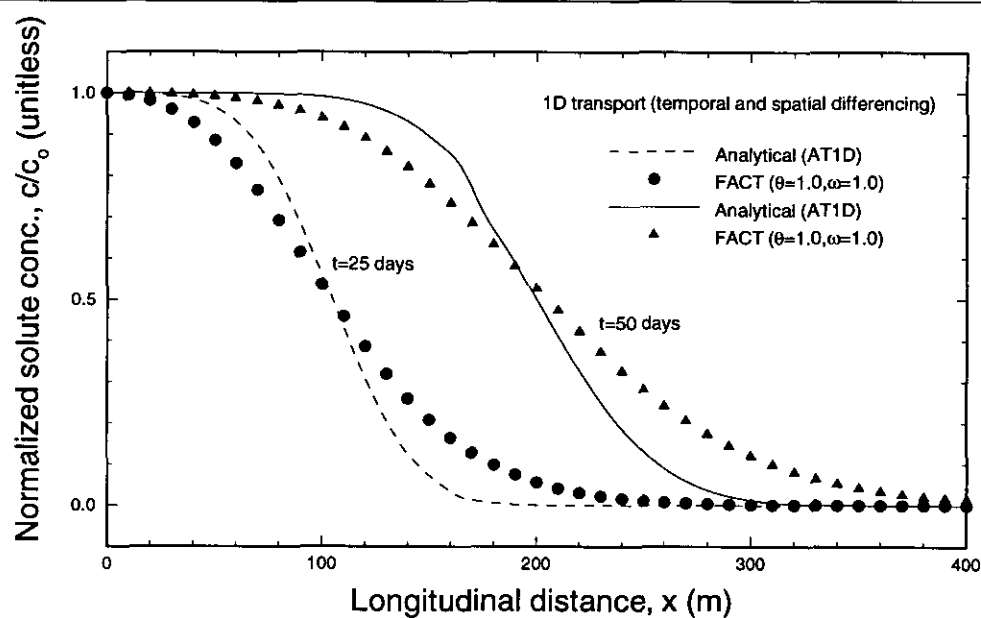


Fig. 4.2.1.11. Concentration profiles for 1D transport showing combined effect of temporal and spatial differencing.

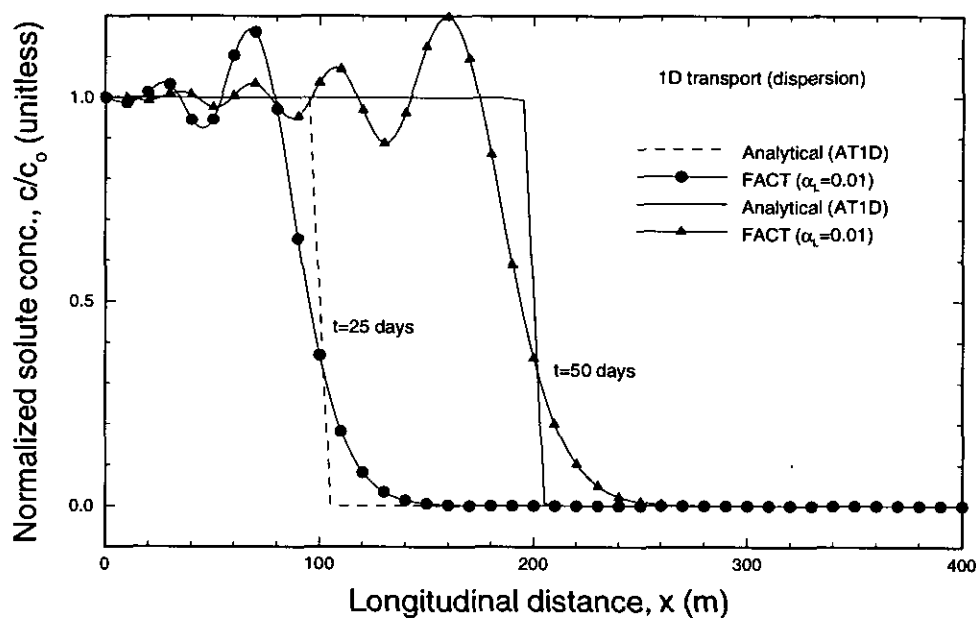


Fig. 4.2.1.12. Concentration profiles for 1D transport at high Peclet number showing effect of dispersion.

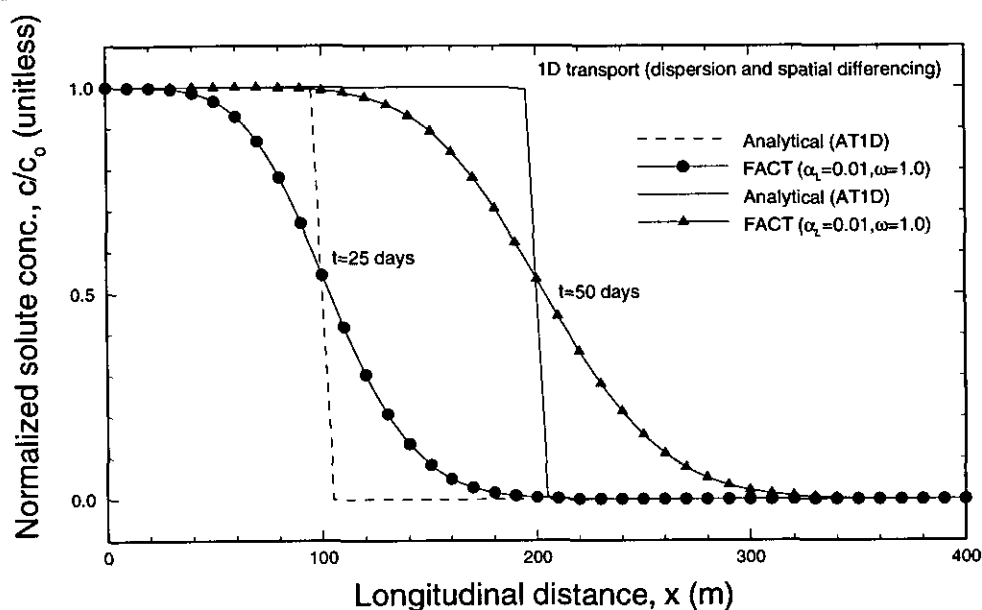


Fig. 4.2.1.13. Concentration profiles for 1D transport at high Peclet number showing effect of complete upstream spatial differencing.

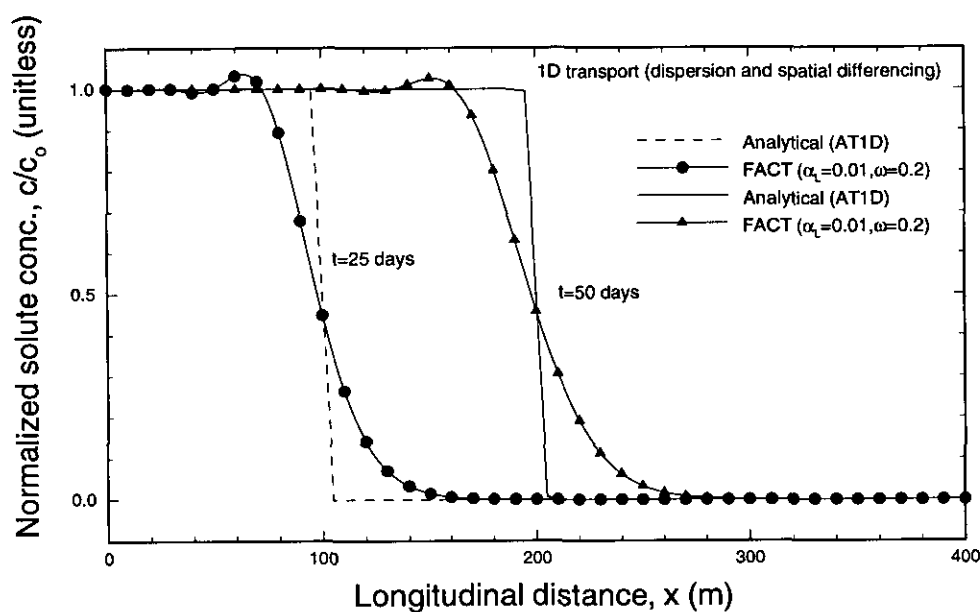


Fig. 4.2.1.14. Concentration profiles for 1D transport at high Peclet number showing effect of optimal upstream spatial differencing.

Table 4.2.1.3

Comparison of analytical and numerical concentration (kg/m³) results for the transient 1D transport problem (base case)

Distance downstream x (m)	Analytical (G&H)	Numerical (FACT)	Analytical (G&H)	Numerical (FACT)
	(t = 25 days)	(t = 25 days)	(t = 50 days)	(t = 50 days)
0.0	1.0000	1.0000	1.0000	1.0000
10.0	0.9996	0.9996	1.0000	1.0000
20.0	0.9983	0.9983	1.0000	1.0000
30.0	0.9945	0.9945	1.0000	1.0000
40.0	0.9853	0.9852	0.9999	1.0000
50.0	0.9662	0.9658	0.9999	0.9999
60.0	0.9312	0.9305	0.9996	0.9996
70.0	0.8744	0.8732	0.9991	0.9991
80.0	0.7922	0.7905	0.9981	0.9980
90.0	0.6856	0.6834	0.9960	0.9959
100.0	0.5616	0.5591	0.9921	0.9920
110.0	0.4318	0.4293	0.9854	0.9852
120.0	0.3096	0.3072	0.9742	0.9740
130.0	0.2057	0.2037	0.9568	0.9565
140.0	0.1262	0.1246	0.9311	0.9306
150.0	0.0712	0.0701	0.8951	0.8943
160.0	0.0368	0.0361	0.8472	0.8462
170.0	0.0174	0.0170	0.7868	0.7855
180.0	0.0075	0.0073	0.7146	0.7131
190.0	0.0030	0.0029	0.6325	0.6308
200.0	0.0011	0.0010	0.5441	0.5423
210.0	0.0003	0.0003	0.4535	0.4517
220.0	0.0001	0.0001	0.3654	0.3636
230.0	0.0000	0.0000	0.2840	0.2824
240.0	0.0000	0.0000	0.2125	0.2111
250.0	0.0000	0.0000	0.1528	0.1516
260.0	0.0000	0.0000	0.1055	0.1046
270.0	0.0000	0.0000	0.0698	0.0691
280.0	0.0000	0.0000	0.0443	0.0438
290.0	0.0000	0.0000	0.0269	0.0265
300.0	0.0000	0.0000	0.0156	0.0153
310.0	0.0000	0.0000	0.0086	0.0085
320.0	0.0000	0.0000	0.0046	0.0045
330.0	0.0000	0.0000	0.0023	0.0023
340.0	0.0000	0.0000	0.0011	0.0011
350.0	0.0000	0.0000	0.0005	0.0005
360.0	0.0000	0.0000	0.0002	0.0002
370.0	0.0000	0.0000	0.0001	0.0001
380.0	0.0000	0.0000	0.0000	0.0000
390.0	0.0000	0.0000	0.0000	0.0000
400.0	0.0000	0.0000	0.0000	0.0000

Table 4.2.1.4

Comparison of analytical and numerical concentration (kg/m³) results for the transient 1D transport problem (retardation R=2.0)

Distance downstream x (m)	Analytical (G&H)	Numerical (FACT)	Analytical (G&H)	Numerical (FACT)
	(t = 25 days)	(t = 25 days)	(t = 50 days)	(t = 50 days)
0.0	1.0000	1.0000	1.0000	1.0000
10.0	0.9901	0.9900	0.9996	0.9996
20.0	0.9578	0.9574	0.9983	0.9983
30.0	0.8844	0.8836	0.9945	0.9945
40.0	0.7576	0.7562	0.9853	0.9853
50.0	0.5853	0.5836	0.9662	0.9660
60.0	0.3980	0.3963	0.9312	0.9308
70.0	0.2338	0.2323	0.8744	0.8738
80.0	0.1170	0.1159	0.7922	0.7913
90.0	0.0494	0.0487	0.6856	0.6845
100.0	0.0175	0.0171	0.5616	0.5604
110.0	0.0051	0.0050	0.4318	0.4306
120.0	0.0013	0.0012	0.3096	0.3084
130.0	0.0003	0.0002	0.2057	0.2048
140.0	0.0000	0.0000	0.1262	0.1254
150.0	0.0000	0.0000	0.0712	0.0706
160.0	0.0000	0.0000	0.0368	0.0364
170.0	0.0000	0.0000	0.0174	0.0172
180.0	0.0000	0.0000	0.0075	0.0074
190.0	0.0000	0.0000	0.0030	0.0029
200.0	0.0000	0.0000	0.0011	0.0010
210.0	0.0000	0.0000	0.0003	0.0003
220.0	0.0000	0.0000	0.0001	0.0001
230.0	0.0000	0.0000	0.0000	0.0000
240.0	0.0000	0.0000	0.0000	0.0000
250.0	0.0000	0.0000	0.0000	0.0000
260.0	0.0000	0.0000	0.0000	0.0000
270.0	0.0000	0.0000	0.0000	0.0000
280.0	0.0000	0.0000	0.0000	0.0000
290.0	0.0000	0.0000	0.0000	0.0000
300.0	0.0000	0.0000	0.0000	0.0000
310.0	0.0000	0.0000	0.0000	0.0000
320.0	0.0000	0.0000	0.0000	0.0000
330.0	0.0000	0.0000	0.0000	0.0000
340.0	0.0000	0.0000	0.0000	0.0000
350.0	0.0000	0.0000	0.0000	0.0000
360.0	0.0000	0.0000	0.0000	0.0000
370.0	0.0000	0.0000	0.0000	0.0000
380.0	0.0000	0.0000	0.0000	0.0000
390.0	0.0000	0.0000	0.0000	0.0000
400.0	0.0000	0.0000	0.0000	0.0000

Table 4.2.1.5

Comparison of analytical and numerical concentration (kg/m³) results for the transient 1D transport problem (radioactive decay $\lambda_r = 0.01$)

Distance downstream x (m)	Analytical (G&H)	Numerical (FACT)	Analytical (G&H)	Numerical (FACT)
	(t = 25 days)	(t = 25 days)	(t = 50 days)	(t = 50 days)
0.0	1.0000	1.0000	1.0000	1.0000
10.0	0.9753	0.9753	0.9756	0.9756
20.0	0.9506	0.9506	0.9518	0.9518
30.0	0.9245	0.9245	0.9286	0.9286
40.0	0.8950	0.8949	0.9059	0.9059
50.0	0.8587	0.8584	0.8838	0.8838
60.0	0.8112	0.8107	0.8621	0.8621
70.0	0.7484	0.7474	0.8407	0.8407
80.0	0.6677	0.6664	0.8196	0.8196
90.0	0.5705	0.5688	0.7984	0.7984
100.0	0.4623	0.4604	0.7766	0.7766
110.0	0.3524	0.3504	0.7537	0.7536
120.0	0.2508	0.2490	0.7288	0.7286
130.0	0.1657	0.1642	0.7007	0.7005
140.0	0.1012	0.1000	0.6684	0.6681
150.0	0.0568	0.0560	0.6308	0.6304
160.0	0.0293	0.0288	0.5871	0.5865
170.0	0.0138	0.0135	0.5371	0.5363
180.0	0.0060	0.0058	0.4812	0.4804
190.0	0.0023	0.0023	0.4210	0.4200
200.0	0.0008	0.0008	0.3584	0.3573
210.0	0.0003	0.0003	0.2960	0.2949
220.0	0.0001	0.0001	0.2366	0.2356
230.0	0.0000	0.0000	0.1826	0.1817
240.0	0.0000	0.0000	0.1358	0.1350
250.0	0.0000	0.0000	0.0972	0.0965
260.0	0.0000	0.0000	0.0668	0.0662
270.0	0.0000	0.0000	0.0440	0.0436
280.0	0.0000	0.0000	0.0278	0.0275
290.0	0.0000	0.0000	0.0168	0.0166
300.0	0.0000	0.0000	0.0097	0.0096
310.0	0.0000	0.0000	0.0054	0.0053
320.0	0.0000	0.0000	0.0028	0.0028
330.0	0.0000	0.0000	0.0014	0.0014
340.0	0.0000	0.0000	0.0007	0.0007
350.0	0.0000	0.0000	0.0003	0.0003
360.0	0.0000	0.0000	0.0001	0.0001
370.0	0.0000	0.0000	0.0001	0.0001
380.0	0.0000	0.0000	0.0000	0.0000
390.0	0.0000	0.0000	0.0000	0.0000
400.0	0.0000	0.0000	0.0000	0.0000

Table 4.2.1.6

Comparison of analytical and numerical concentration (kg/m³) results for the transient 1D transport problem (retardation R=2.0, radioactive decay $\lambda_r = 0.01$)

Distance downstream x (m)	Analytical (G&H)	Numerical (FACT)	Analytical (G&H)	Numerical (FACT)
	(t = 25 days)	(t = 25 days)	(t = 50 days)	(t = 50 days)
0.0	1.0000	1.0000	1.0000	1.0000
10.0	0.9452	0.9451	0.9522	0.9522
20.0	0.8764	0.8762	0.9061	0.9061
30.0	0.7805	0.7799	0.8607	0.8607
40.0	0.6495	0.6484	0.8145	0.8144
50.0	0.4907	0.4894	0.7647	0.7646
60.0	0.3282	0.3269	0.7082	0.7079
70.0	0.1905	0.1893	0.6417	0.6413
80.0	0.0944	0.0936	0.5637	0.5632
90.0	0.0396	0.0390	0.4754	0.4747
100.0	0.0139	0.0136	0.3811	0.3803
110.0	0.0041	0.0039	0.2879	0.2871
120.0	0.0010	0.0009	0.2034	0.2027
130.0	0.0002	0.0002	0.1336	0.1330
140.0	0.0000	0.0000	0.0812	0.0807
150.0	0.0000	0.0000	0.0454	0.0451
160.0	0.0000	0.0000	0.0233	0.0231
170.0	0.0000	0.0000	0.0110	0.0108
180.0	0.0000	0.0000	0.0047	0.0046
190.0	0.0000	0.0000	0.0019	0.0018
200.0	0.0000	0.0000	0.0007	0.0006
210.0	0.0000	0.0000	0.0002	0.0002
220.0	0.0000	0.0000	0.0001	0.0001
230.0	0.0000	0.0000	0.0000	0.0000
240.0	0.0000	0.0000	0.0000	0.0000
250.0	0.0000	0.0000	0.0000	0.0000
260.0	0.0000	0.0000	0.0000	0.0000
270.0	0.0000	0.0000	0.0000	0.0000
280.0	0.0000	0.0000	0.0000	0.0000
290.0	0.0000	0.0000	0.0000	0.0000
300.0	0.0000	0.0000	0.0000	0.0000
310.0	0.0000	0.0000	0.0000	0.0000
320.0	0.0000	0.0000	0.0000	0.0000
330.0	0.0000	0.0000	0.0000	0.0000
340.0	0.0000	0.0000	0.0000	0.0000
350.0	0.0000	0.0000	0.0000	0.0000
360.0	0.0000	0.0000	0.0000	0.0000
370.0	0.0000	0.0000	0.0000	0.0000
380.0	0.0000	0.0000	0.0000	0.0000
390.0	0.0000	0.0000	0.0000	0.0000
400.0	0.0000	0.0000	0.0000	0.0000

Table 4.2.1.7

Effect grid size (Δx) has on the numerical concentration (kg/m³) results for the transient 1D transport problem (time $t=50$ days)

Distance downstream x (m)	Analytical (G&H)	Numerical (FACT) ($\Delta x = 2$ m)	Numerical (FACT) ($\Delta x = 20$ m)	Numerical (FACT) ($\Delta x = 40$ m)	Numerical (FACT) ($\Delta x = 80$ m)
0.0	1.0000	1.0000	1.0000	1.0000	1.0000
10.0	1.0000	1.0000	-	-	-
20.0	1.0000	1.0000	1.0000	-	-
30.0	1.0000	1.0000	-	-	-
40.0	0.9999	1.0000	1.0000	0.9992	-
50.0	0.9999	0.9999	-	-	-
60.0	0.9996	0.9996	0.9998	-	-
70.0	0.9991	0.9991	-	-	-
80.0	0.9981	0.9980	0.9985	1.0017	1.0166
90.0	0.9960	0.9959	-	-	-
100.0	0.9921	0.9920	0.9927	-	-
110.0	0.9854	0.9852	-	-	-
120.0	0.9742	0.9740	0.9741	0.9769	-
130.0	0.9568	0.9565	-	-	-
140.0	0.9311	0.9306	0.9290	-	-
150.0	0.8951	0.8943	-	-	-
160.0	0.8472	0.8462	0.8428	0.8296	0.7702
170.0	0.7868	0.7855	-	-	-
180.0	0.7146	0.7131	0.7100	-	-
190.0	0.6325	0.6308	-	-	-
200.0	0.5441	0.5423	0.5323	0.5366	-
210.0	0.4535	0.4517	-	-	-
220.0	0.3654	0.3636	0.3674	-	-
230.0	0.2840	0.2824	-	-	-
240.0	0.2125	0.2111	0.2160	0.2316	0.2783
250.0	0.1528	0.1516	-	-	-
260.0	0.1055	0.1046	0.1075	-	-
270.0	0.0698	0.0691	-	-	-
280.0	0.0443	0.0438	0.0437	0.0511	-
290.0	0.0269	0.0265	-	-	-
300.0	0.0156	0.0153	0.0136	-	-
310.0	0.0086	0.0085	-	-	-
320.0	0.0046	0.0045	0.0028	-0.0029	0.0087
330.0	0.0023	0.0023	-	-	-
340.0	0.0011	0.0011	0.0001	-	-
350.0	0.0005	0.0005	-	-	-
360.0	0.0002	0.0002	-0.0002	-0.0039	-
370.0	0.0001	0.0001	-	-	-
380.0	0.0000	0.0000	0.0000	-	-
390.0	0.0000	0.0000	-	-	-
400.0	0.0000	0.0000	0.0000	-0.0005	-0.0228

Table 4.2.1.8

Effect time-step size (Δt) has on the numerical concentration (kg/m³) results for the transient 1D transport problem (time t=50 days)

Distance downstream x (m)	Analytical (G&H)	Numerical (FACT) ($\Delta t = 0.1$ d)	Numerical (FACT) ($\Delta t = 5$ d)	Numerical (FACT) ($\Delta t = 10$ d)	Numerical (FACT) ($\Delta t = 25$ d)
0.0	1.0000	1.0000	1.0000	1.0000	1.0000
10.0	1.0000	1.0000	0.9942	0.9889	1.1141
20.0	1.0000	1.0000	1.0028	1.0280	1.1619
30.0	1.0000	1.0000	0.9985	1.0115	1.1625
40.0	0.9999	1.0000	1.0001	0.9788	1.1303
50.0	0.9999	0.9999	1.0007	0.9664	1.0764
60.0	0.9996	0.9996	0.9992	0.9825	1.0088
70.0	0.9991	0.9991	0.9990	1.0155	0.9337
80.0	0.9981	0.9980	0.9991	1.0481	0.8554
90.0	0.9960	0.9959	0.9971	1.0654	0.7772
100.0	0.9921	0.9920	0.9925	1.0588	0.7012
110.0	0.9854	0.9852	0.9853	1.0262	0.6289
120.0	0.9742	0.9740	0.9732	0.9698	0.5611
130.0	0.9568	0.9565	0.9514	0.8950	0.4984
140.0	0.9311	0.9306	0.9147	0.8080	0.4410
150.0	0.8951	0.8943	0.8601	0.7152	0.3888
160.0	0.8472	0.8462	0.7879	0.6217	0.3417
170.0	0.7868	0.7855	0.7017	0.5318	0.2995
180.0	0.7146	0.7131	0.6073	0.4483	0.2619
190.0	0.6325	0.6308	0.5110	0.3729	0.2284
200.0	0.5441	0.5423	0.4185	0.3066	0.1989
210.0	0.4535	0.4517	0.3341	0.2493	0.1728
220.0	0.3654	0.3636	0.2605	0.2008	0.1499
230.0	0.2840	0.2824	0.1986	0.1602	0.1298
240.0	0.2125	0.2111	0.1483	0.1268	0.1122
250.0	0.1528	0.1516	0.1087	0.0996	0.0969
260.0	0.1055	0.1046	0.0782	0.0777	0.0835
270.0	0.0698	0.0691	0.0554	0.0602	0.0720
280.0	0.0443	0.0438	0.0386	0.0464	0.0619
290.0	0.0269	0.0265	0.0266	0.0355	0.0532
300.0	0.0156	0.0153	0.0180	0.0271	0.0457
310.0	0.0086	0.0085	0.0121	0.0205	0.0392
320.0	0.0046	0.0045	0.0080	0.0155	0.0336
330.0	0.0023	0.0023	0.0052	0.0117	0.0288
340.0	0.0011	0.0011	0.0034	0.0087	0.0246
350.0	0.0005	0.0005	0.0022	0.0065	0.0211
360.0	0.0002	0.0002	0.0014	0.0048	0.0180
370.0	0.0001	0.0001	0.0009	0.0036	0.0154
380.0	0.0000	0.0000	0.0006	0.0027	0.0131
390.0	0.0000	0.0000	0.0003	0.0020	0.0113
400.0	0.0000	0.0000	0.0003	0.0016	0.0102

Table 4.2.1.9

Effect upwind differencing has on the numerical concentration (kg/m³) results for the transient 1D transport problem (spatial differencing $\alpha = 1.0$)

Distance downstream x (m)	Analytical (G&H)	Numerical (FACT)	Analytical (G&H)	Numerical (FACT)
	(t = 25 days)	(t = 25 days)	(t = 50 days)	(t = 50 days)
0.0	1.0000	1.0000	1.0000	1.0000
10.0	0.9996	0.9993	1.0000	1.0000
20.0	0.9983	0.9970	1.0000	1.0000
30.0	0.9945	0.9912	1.0000	0.9999
40.0	0.9853	0.9790	0.9999	0.9998
50.0	0.9662	0.9561	0.9999	0.9996
60.0	0.9312	0.9177	0.9996	0.9991
70.0	0.8744	0.8594	0.9991	0.9981
80.0	0.7922	0.7793	0.9981	0.9962
90.0	0.6856	0.6792	0.9960	0.9928
100.0	0.5616	0.5649	0.9921	0.9872
110.0	0.4318	0.4456	0.9854	0.9781
120.0	0.3096	0.3315	0.9742	0.9642
130.0	0.2057	0.2317	0.9568	0.9440
140.0	0.1262	0.1515	0.9311	0.9157
150.0	0.0712	0.0924	0.8951	0.8781
160.0	0.0368	0.0525	0.8472	0.8301
170.0	0.0174	0.0277	0.7868	0.7717
180.0	0.0075	0.0135	0.7146	0.7036
190.0	0.0030	0.0061	0.6325	0.6277
200.0	0.0011	0.0026	0.5441	0.5465
210.0	0.0003	0.0010	0.4535	0.4635
220.0	0.0001	0.0004	0.3654	0.3822
230.0	0.0000	0.0001	0.2840	0.3058
240.0	0.0000	0.0000	0.2125	0.2372
250.0	0.0000	0.0000	0.1528	0.1780
260.0	0.0000	0.0000	0.1055	0.1292
270.0	0.0000	0.0000	0.0698	0.0906
280.0	0.0000	0.0000	0.0443	0.0613
290.0	0.0000	0.0000	0.0269	0.0400
300.0	0.0000	0.0000	0.0156	0.0251
310.0	0.0000	0.0000	0.0086	0.0152
320.0	0.0000	0.0000	0.0046	0.0089
330.0	0.0000	0.0000	0.0023	0.0050
340.0	0.0000	0.0000	0.0011	0.0027
350.0	0.0000	0.0000	0.0005	0.0014
360.0	0.0000	0.0000	0.0002	0.0007
370.0	0.0000	0.0000	0.0001	0.0003
380.0	0.0000	0.0000	0.0000	0.0002
390.0	0.0000	0.0000	0.0000	0.0001
400.0	0.0000	0.0000	0.0000	0.0000

Table 4.2.1.10

Effect backward Euler has on the numerical concentration (kg/m³) results for the transient 1D transport problem (temporal differencing $\omega = 1.0$)

Distance downstream x (m)	Analytical (G&H)	Numerical (FACT)	Analytical (G&H)	Numerical (FACT)
	(t = 25 days)	(t = 25 days)	(t = 50 days)	(t = 50 days)
0.0	1.0000	1.0000	1.0000	1.0000
10.0	0.9996	0.9996	1.0000	1.0000
20.0	0.9983	0.9982	1.0000	1.0000
30.0	0.9945	0.9941	1.0000	1.0000
40.0	0.9853	0.9844	0.9999	0.9999
50.0	0.9662	0.9643	0.9999	0.9998
60.0	0.9312	0.9280	0.9996	0.9996
70.0	0.8744	0.8698	0.9991	0.9990
80.0	0.7922	0.7868	0.9981	0.9979
90.0	0.6856	0.6804	0.9960	0.9956
100.0	0.5616	0.5580	0.9921	0.9914
110.0	0.4318	0.4308	0.9854	0.9842
120.0	0.3096	0.3114	0.9742	0.9725
130.0	0.2057	0.2098	0.9568	0.9543
140.0	0.1262	0.1313	0.9311	0.9278
150.0	0.0712	0.0762	0.8951	0.8909
160.0	0.0368	0.0409	0.8472	0.8423
170.0	0.0174	0.0203	0.7868	0.7817
180.0	0.0075	0.0093	0.7146	0.7097
190.0	0.0030	0.0040	0.6325	0.6285
200.0	0.0011	0.0016	0.5441	0.5415
210.0	0.0003	0.0006	0.4535	0.4527
220.0	0.0001	0.0002	0.3654	0.3665
230.0	0.0000	0.0001	0.2840	0.2867
240.0	0.0000	0.0000	0.2125	0.2165
250.0	0.0000	0.0000	0.1528	0.1576
260.0	0.0000	0.0000	0.1055	0.1105
270.0	0.0000	0.0000	0.0698	0.0745
280.0	0.0000	0.0000	0.0443	0.0483
290.0	0.0000	0.0000	0.0269	0.0301
300.0	0.0000	0.0000	0.0156	0.0180
310.0	0.0000	0.0000	0.0086	0.0103
320.0	0.0000	0.0000	0.0046	0.0057
330.0	0.0000	0.0000	0.0023	0.0030
340.0	0.0000	0.0000	0.0011	0.0015
350.0	0.0000	0.0000	0.0005	0.0007
360.0	0.0000	0.0000	0.0002	0.0004
370.0	0.0000	0.0000	0.0001	0.0002
380.0	0.0000	0.0000	0.0000	0.0001
390.0	0.0000	0.0000	0.0000	0.0000
400.0	0.0000	0.0000	0.0000	0.0000

Table 4.2.1.11

Effect backward Euler plus upwind differencing has on the numerical concentration (kg/m³) results for the transient 1D transport problem (temporal differencing $\omega = 1.0$, spatial differencing $\alpha = 1.0$)

Distance downstream x (m)	Analytical (G&H)	Numerical (FACT)	Analytical (G&H)	Numerical (FACT)
	(t = 25 days)	(t = 25 days)	(t = 50 days)	(t = 50 days)
0.0	1.0000	1.0000	1.0000	1.0000
10.0	0.9996	0.9992	1.0000	1.0000
20.0	0.9983	0.9968	1.0000	1.0000
30.0	0.9945	0.9908	1.0000	0.9999
40.0	0.9853	0.9782	0.9999	0.9998
50.0	0.9662	0.9546	0.9999	0.9996
60.0	0.9312	0.9154	0.9996	0.9990
70.0	0.8744	0.8565	0.9991	0.9979
80.0	0.7922	0.7763	0.9981	0.9959
90.0	0.6856	0.6767	0.9960	0.9924
100.0	0.5616	0.5638	0.9921	0.9865
110.0	0.4318	0.4465	0.9854	0.9771
120.0	0.3096	0.3346	0.9742	0.9627
130.0	0.2057	0.2365	0.9568	0.9419
140.0	0.1262	0.1572	0.9311	0.9132
150.0	0.0712	0.0980	0.8951	0.8751
160.0	0.0368	0.0573	0.8472	0.8269
170.0	0.0174	0.0314	0.7868	0.7686
180.0	0.0075	0.0161	0.7146	0.7009
190.0	0.0030	0.0077	0.6325	0.6258
200.0	0.0011	0.0035	0.5441	0.5458
210.0	0.0003	0.0015	0.4535	0.4641
220.0	0.0001	0.0006	0.3654	0.3842
230.0	0.0000	0.0002	0.2840	0.3092
240.0	0.0000	0.0001	0.2125	0.2415
250.0	0.0000	0.0000	0.1528	0.1830
260.0	0.0000	0.0000	0.1055	0.1344
270.0	0.0000	0.0000	0.0698	0.0955
280.0	0.0000	0.0000	0.0443	0.0657
290.0	0.0000	0.0000	0.0269	0.0437
300.0	0.0000	0.0000	0.0156	0.0281
310.0	0.0000	0.0000	0.0086	0.0175
320.0	0.0000	0.0000	0.0046	0.0105
330.0	0.0000	0.0000	0.0023	0.0061
340.0	0.0000	0.0000	0.0011	0.0034
350.0	0.0000	0.0000	0.0005	0.0019
360.0	0.0000	0.0000	0.0002	0.0010
370.0	0.0000	0.0000	0.0001	0.0005
380.0	0.0000	0.0000	0.0000	0.0002
390.0	0.0000	0.0000	0.0000	0.0001
400.0	0.0000	0.0000	0.0000	0.0001

Table 4.2.1.12

Effect low longitudinal dispersivity has on the numerical concentration (kg/m³) results for the transient 1D transport problem (longitudinal horizontal dispersivity $\alpha_{LH}=0.01$)

Distance downstream x (m)	Analytical (G&H)	Numerical (FACT)	Analytical (G&H)	Numerical (FACT)
	(t = 25 days)	(t = 25 days)	(t = 50 days)	(t = 50 days)
0.0	1.0000	1.0000	1.0000	1.0000
10.0	1.0000	0.9990	1.0000	1.0001
20.0	1.0000	1.0026	1.0000	0.9998
30.0	1.0000	0.9961	1.0000	1.0003
40.0	1.0000	1.0056	1.0000	0.9997
50.0	1.0000	0.9902	1.0000	1.0002
60.0	1.0000	1.0168	1.0000	1.0001
70.0	1.0000	0.9899	1.0000	0.9996
80.0	1.0000	0.9573	1.0000	1.0006
90.0	1.0000	0.9461	1.0000	0.9995
100.0	0.5000	0.3924	1.0000	0.9999
110.0	0.0000	-0.0024	1.0000	1.0019
120.0	0.0000	0.0000	1.0000	0.9954
130.0	0.0000	0.0000	1.0000	1.0051
140.0	0.0000	0.0000	1.0000	1.0023
150.0	0.0000	0.0000	1.0000	0.9885
160.0	0.0000	0.0000	1.0000	0.9919
170.0	0.0000	0.0000	1.0000	1.0089
180.0	0.0000	0.0000	1.0000	1.0272
190.0	0.0000	0.0000	1.0000	1.0258
200.0	0.0000	0.0000	0.5000	0.4017
210.0	0.0000	0.0000	0.0000	-0.0042
220.0	0.0000	0.0000	0.0000	0.0000
230.0	0.0000	0.0000	0.0000	0.0000
240.0	0.0000	0.0000	0.0000	0.0000
250.0	0.0000	0.0000	0.0000	0.0000
260.0	0.0000	0.0000	0.0000	0.0000
270.0	0.0000	0.0000	0.0000	0.0000
280.0	0.0000	0.0000	0.0000	0.0000
290.0	0.0000	0.0000	0.0000	0.0000
300.0	0.0000	0.0000	0.0000	0.0000
310.0	0.0000	0.0000	0.0000	0.0000
320.0	0.0000	0.0000	0.0000	0.0000
330.0	0.0000	0.0000	0.0000	0.0000
340.0	0.0000	0.0000	0.0000	0.0000
350.0	0.0000	0.0000	0.0000	0.0000
360.0	0.0000	0.0000	0.0000	0.0000
370.0	0.0000	0.0000	0.0000	0.0000
380.0	0.0000	0.0000	0.0000	0.0000
390.0	0.0000	0.0000	0.0000	0.0000
400.0	0.0000	0.0000	0.0000	0.0000

Table 4.2.1.13

Effect low longitudinal dispersivity plus upwind differencing has on the numerical concentration (kg/m³) results for the transient 1D transport problem (longitudinal horizontal dispersivity $\alpha_{LH} = 0.01$, spatial differencing $\alpha = 1.0$)

Distance downstream x (m)	Analytical (G&H)	Numerical (FACT)	Analytical (G&H)	Numerical (FACT)
	(t = 25 days)	(t = 25 days)	(t = 50 days)	(t = 50 days)
0.0	1.0000	1.0000	1.0000	1.0000
10.0	1.0000	1.0000	1.0000	1.0000
20.0	1.0000	1.0000	1.0000	1.0000
30.0	1.0000	1.0000	1.0000	1.0000
40.0	1.0000	1.0000	1.0000	1.0000
50.0	1.0000	0.9999	1.0000	1.0000
60.0	1.0000	0.9982	1.0000	1.0000
70.0	1.0000	0.9859	1.0000	1.0000
80.0	1.0000	0.9302	1.0000	1.0000
90.0	1.0000	0.7779	1.0000	1.0000
100.0	0.5000	0.5225	1.0000	1.0000
110.0	0.0000	0.2574	1.0000	1.0000
120.0	0.0000	0.0870	1.0000	1.0000
130.0	0.0000	0.0192	1.0000	0.9998
140.0	0.0000	0.0027	1.0000	0.9989
150.0	0.0000	0.0002	1.0000	0.9945
160.0	0.0000	0.0000	1.0000	0.9794
170.0	0.0000	0.0000	1.0000	0.9382
180.0	0.0000	0.0000	1.0000	0.8506
190.0	0.0000	0.0000	1.0000	0.7051
200.0	0.0000	0.0000	0.5000	0.5159
210.0	0.0000	0.0000	0.0000	0.3231
220.0	0.0000	0.0000	0.0000	0.1690
230.0	0.0000	0.0000	0.0000	0.0725
240.0	0.0000	0.0000	0.0000	0.0252
250.0	0.0000	0.0000	0.0000	0.0070
260.0	0.0000	0.0000	0.0000	0.0015
270.0	0.0000	0.0000	0.0000	0.0003
280.0	0.0000	0.0000	0.0000	0.0000
290.0	0.0000	0.0000	0.0000	0.0000
300.0	0.0000	0.0000	0.0000	0.0000
310.0	0.0000	0.0000	0.0000	0.0000
320.0	0.0000	0.0000	0.0000	0.0000
330.0	0.0000	0.0000	0.0000	0.0000
340.0	0.0000	0.0000	0.0000	0.0000
350.0	0.0000	0.0000	0.0000	0.0000
360.0	0.0000	0.0000	0.0000	0.0000
370.0	0.0000	0.0000	0.0000	0.0000
380.0	0.0000	0.0000	0.0000	0.0000
390.0	0.0000	0.0000	0.0000	0.0000
400.0	0.0000	0.0000	0.0000	0.0000

Table 4.2.1.14

Effect low longitudinal dispersivity plus partial (optimal) upwind differencing has on the numerical concentration (kg/m³) results for the transient 1D transport problem (longitudinal horizontal dispersivity $\alpha_{LH}=0.01$, spatial differencing $\alpha=0.27$)

Distance downstream x (m)	Analytical (G&H)	Numerical (FACT)	Analytical (G&H)	Numerical (FACT)
	(t = 25 days)	(t = 25 days)	(t = 50 days)	(t = 50 days)
0.0	1.0000	1.0000	1.0000	1.0000
10.0	1.0000	1.0000	1.0000	1.0000
20.0	1.0000	1.0000	1.0000	1.0000
30.0	1.0000	1.0000	1.0000	1.0000
40.0	1.0000	1.0000	1.0000	1.0000
50.0	1.0000	1.0000	1.0000	1.0000
60.0	1.0000	1.0000	1.0000	1.0000
70.0	1.0000	1.0000	1.0000	1.0000
80.0	1.0000	0.9969	1.0000	1.0000
90.0	1.0000	0.9114	1.0000	1.0000
100.0	0.5000	0.5028	1.0000	1.0000
110.0	0.0000	0.0933	1.0000	1.0000
120.0	0.0000	0.0036	1.0000	1.0000
130.0	0.0000	0.0000	1.0000	1.0000
140.0	0.0000	0.0000	1.0000	1.0000
150.0	0.0000	0.0000	1.0000	1.0000
160.0	0.0000	0.0000	1.0000	0.9999
170.0	0.0000	0.0000	1.0000	0.9980
180.0	0.0000	0.0000	1.0000	0.9717
190.0	0.0000	0.0000	1.0000	0.8291
200.0	0.0000	0.0000	0.5000	0.5021
210.0	0.0000	0.0000	0.0000	0.1747
220.0	0.0000	0.0000	0.0000	0.0301
230.0	0.0000	0.0000	0.0000	0.0023
240.0	0.0000	0.0000	0.0000	0.0001
250.0	0.0000	0.0000	0.0000	0.0000
260.0	0.0000	0.0000	0.0000	0.0000
270.0	0.0000	0.0000	0.0000	0.0000
280.0	0.0000	0.0000	0.0000	0.0000
290.0	0.0000	0.0000	0.0000	0.0000
300.0	0.0000	0.0000	0.0000	0.0000
310.0	0.0000	0.0000	0.0000	0.0000
320.0	0.0000	0.0000	0.0000	0.0000
330.0	0.0000	0.0000	0.0000	0.0000
340.0	0.0000	0.0000	0.0000	0.0000
350.0	0.0000	0.0000	0.0000	0.0000
360.0	0.0000	0.0000	0.0000	0.0000
370.0	0.0000	0.0000	0.0000	0.0000
380.0	0.0000	0.0000	0.0000	0.0000
390.0	0.0000	0.0000	0.0000	0.0000
400.0	0.0000	0.0000	0.0000	0.0000

4.2.2 Two-Dimensional Saturated Solute Transport in a Uniform Flow Field

This problem deals with two-dimensional (areal) advection-dispersion of a non-conservative solute species from a point source through an infinite porous medium. It is used to demonstrate the impact that grid orientation with transverse dispersion has on the solution from FACT. A physical schematic of this problem is shown in Fig. 4.2.2.1(a). In practice, the idealized conditions are analogous to continual leakage or injection of a contaminant into a shallow confined aquifer from a small leaking landfill or an improperly sealed fully penetrating injection well (gradients in the vertical direction are assumed to be negligible). It is assumed that the total rate of fluid leakage or injection into the aquifer is negligible and does not disturb the ambient groundwater flow regime. Analytically the problem is treated as a point source in the 2-D areal plane.

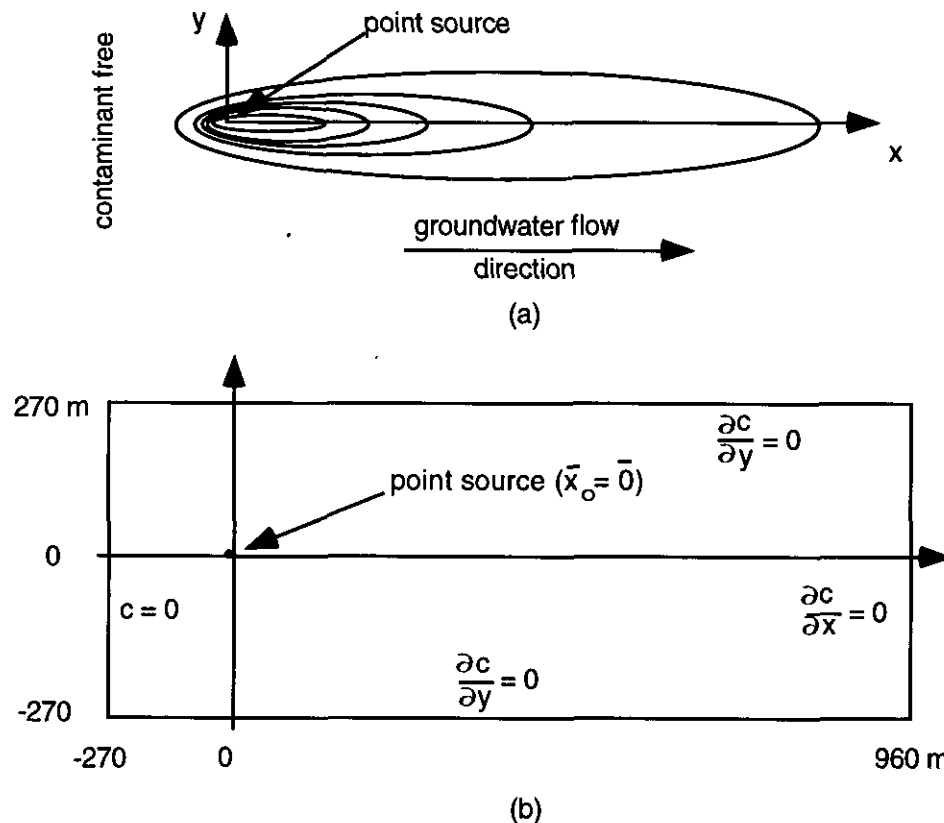


Fig. 4.2.2.1. Schematic diagram for 2D areal solute transport in a confined aquifer.

As illustrated in Fig. 4.2.2.1(b), a non-conservative contaminant is continuously released from a point source downstream of an inflow boundary (containing zero contaminant) into a shallow confined aquifer unit whose groundwater flow is assumed to be uniform. Both hydrodynamic dispersion and molecular diffusion are allowed, as well as, the possibility of radioactive decay and/or adsorption of the transported species. It is assumed that the contaminant mass flow rate at the point source remains constant, the aquifer's flow rate is uniform and constant, and the homogeneous aquifer's properties (such as porosity, soil type, water saturation) are uniform and constant.

FACT CODE MANUAL

Analytic solution: Equation (2.2.13) represents the conservative form of the multi-dimensional advection-dispersion equation for solute transport through a variably saturated porous media. Taking the 2-D form of Eq. (2.2.13) and assuming that one point source exists at the areal location $x = y = 0$, constant water saturation level, and that material coefficients are constants, results in

$$\frac{\partial c}{\partial t} = D'_{xx} \frac{\partial^2 c}{\partial x^2} + D'_{yy} \frac{\partial^2 c}{\partial y^2} - u'_x \frac{\partial c}{\partial x} + \lambda_r c + \frac{qc^*}{\theta_m R} \quad (4.2.2.1)$$

with $D'_{xx} = \alpha_{LH} u'_x$ and $D'_{yy} = \alpha_{TH} u'_y$.

For our infinite (areally) confined aquifer the initial conditions are:

$$c(x, y, 0) = 0 \quad (4.2.2.2a)$$

and the boundary conditions are:

$$c(\pm\infty, y, t) = 0 \quad (4.2.2.2b)$$

$$c(x, \pm\infty, t) = 0 \quad (4.2.2.2c)$$

These boundary conditions are equivalent to assuming that the dispersive flux of solute is zero at plus or minus infinity or

$$\lim_{x \rightarrow \pm\infty} \left(\frac{\partial c}{\partial x} \right) = 0 \quad (4.2.2.2d)$$

$$\lim_{y \rightarrow \pm\infty} \left(\frac{\partial c}{\partial y} \right) = 0 \quad (4.2.2.2e)$$

For finite times there exists finite values of x and y where Eqs. (4.2.2.2d,e) remain valid.

As mentioned above, it is assumed that the total rate of fluid flow, q , into the aquifer due to the source is negligible and does not disturb the ambient groundwater flow regime. In order to have a finite mass flow rate of contaminant requires

$$\lim_{q \rightarrow 0} (qc^*) < \infty \Rightarrow \lim_{q \rightarrow 0} (c^*) = +\infty \quad (4.2.2.2f)$$

Therefore, analytically the concentration of solute entering the aquifer at the point source becomes infinite.

Equation (4.2.2.1), a linear partial differential equation subject to the initial and boundary conditions given by Eqs. (4.2.2.2a,b,c), can be solved by employing an appropriate Green's function for the point source and applying the Laplace and Fourier transform techniques. For details see Yeh (1981). The general solution for a continuous point source takes the form:

$$c(x, y, t) = \frac{qc^*}{\theta_m R} \int_0^t G(x|\xi; y|\eta; t|\tau) d\tau \quad (4.2.2.3a)$$

where $G(x|\xi; y|\eta; t|\tau)$ is the Green's function over the domain space. For our analytical problem we shall limit our flow field to flow parallel to the x-axis only. This results in a dispersion tensor that is diagonal and a separable Green's function. It can be shown that for simple geometry such as separable coordinate system, Green's function, G , can be expressed as:

$$G(x|\xi; y|\eta; t|\tau) = G_1(x|\xi; t|\tau)G_2(y|\eta; t|\tau) \quad (4.2.2.3b)$$

where for a point source in the x-direction (infinite domain, parallel to flow):

$$G_1(x|\xi; t|\tau) = \frac{1}{\sqrt{4\pi D'_{xx}(t-\tau)}} \exp \left[-\frac{\{(x-\xi) - u'_x(t-\tau)\}^2}{4D'_{xx}(t-\tau)} - \lambda_r(t-\tau) \right] \quad (4.2.2.3c)$$

and for a point source in the y-direction (infinite domain, transverse to flow):

$$G_2(y|\eta; t|\tau) = \frac{1}{\sqrt{4\pi D'_{yy}(t-\tau)}} \exp \left[-\frac{(y-\eta)^2}{4D'_{yy}(t-\tau)} \right] \quad (4.2.2.3d)$$

The evaluation of the analytic expressions, Eqs. (4.2.2.3a,b,c,d), for a specific problem is performed numerically and has been performed using the computer code, AT123D by Yeh (1981).

FACT numerical simulation and comparison: In FACT we will model this 2-D areal problem using a finite element mesh containing many elements in the horizontal plane that is only one element deep in the vertical direction. The point source given above now becomes a line source that extends the entire vertical distance of the elements whose strength per unit length is

$$(qc^*)' = \frac{qc^*}{\Delta z_{\text{element}}} \delta(x)\delta(y) \quad (4.2.2.4)$$

and is located at the same areal location (in FACT point and line sources are limited to node locations only). Zero diffusive flux boundary conditions at the vertical faces of the mesh domain will ensure that no concentration gradients appear in the vertical direction.

Even though we are considering an aquifer unit with infinite extent in the areal directions, our numerical model has finite size. At our inflow boundary we shall assume that the incoming fluid remains contaminant free (i.e., the contaminant concentration immediately upstream of the source does not extend back up to the inflow boundary). For the parameters chosen (i.e., longitudinal dispersivity, Darcy velocity, and source location), the above assumption remains valid over the time period of interest.

Also, FACT requires knowledge about both the total volumetric flow rate, q , and its solute concentration entering the aquifer at the line source. An arbitrarily small but finite value for q was chosen to maintain computed solute concentration values near the source to acceptable values. Steep concentration gradients near a source can result in oscillatory behavior unless the local grid is sufficiently refined. For demonstration purposes, we

FACT CODE MANUAL

have chosen uniform coarse grids and are primarily interested in results away from the source location. The simulations are done by specifying a velocity field and running the solute transport option only. In this way, the flow rate entering the aquifer due to the line source does not alter the aquifer flow field.

Values of the physical parameters used in the verification simulations are presented in Table 4.2.2.1. For the conservative solute transport cases the parameters were selected based on data from a field investigation on hexavalent chromium contamination reported by Perlumutter and Lieber (1970) and Wilson and Miller (1978). An analytical solution to this problem is also available from Wilson and Miller (1978). For the non-conservative solute transport cases the values of retardation and decay constants were chosen arbitrarily to test the performance of FACT transport modules.

Table 4.2.2.1

Values of the physical parameters, the finite element grid, time-step data, and some key parameters used in the two-dimensional transport problem (base case and its variations)

Physical parameters	Base case	Range tested
Darcy velocity, U_x	0.161 m/d	-
Porosity, ϕ	0.35	-
Longitudinal dispersivity, α_{LH}	21.3 m	-
Transverse dispersivity, α_{TH}	4.3 m	-
Apparent molecular dispersion coefficient, $\theta_m \tau D^*$	0.0 m ² /d	-
Water saturation, S_w	1.0	-
radioactive decay coef., λ_T	0.0 d ⁻¹	0.0, 0.005
Soil density, ρ_s	1.23077 kg/m ³	-
Solute distribution coefficient, K_d	0.0 m ³ /kg	0.0, 0.4375
Boundary solute concentration, c_0	0.0 kg/m ³	-
Water total volumetric flowrate (line source), q	0.2 m ³ /d	-
Contaminant total mass flowrate (line source), $q c^*$	0.235844 kg/d	-
Grid specifics		
Element lengths, $\Delta x = \Delta y$	30 m	-
Element height, Δz	33.5 m	-
Number nodes in x-dir	42	-
Number nodes in y-dir	19 (parallel grid) 42 (diagonal grid)	-
Number nodes in z-dir	2	-
Time steps		
Time duration	1400 d	-
number time-steps	14	-
time-step size, Δt	100 d	-

Table 4.2.2.1

(Continued)

Key computed parameters		
Retardation factor, R	1.0	1.0,2.0
Bulk soil density, ρ_b	0.8 kg/m ³	-
Phasic velocity, u_x	0.46 m/d	-
Retarded phasic velocity, u'_x	0.46 m/d	0.46,0.23
Retarded longitudinal dispersion coefficient, D'_{xx}	9.798 m ² /d	9.7898,4.899
Retarded transverse dispersion coefficient, D'_{yy}	1.978 m ² /d	1.978,0.989
Retarded cross dispersion coefficient, D'_{xy}	0.0 m ² /d	-
Cell Fourier number, $Fo_x; Fo_y$	1.0887,0.2198	1.0887,0.5443; 0.2198,0.1099
Cell Courant number, $Co_x; Co_y$	1.533;0.0	1.533,0.767;0.0
Cell Peclet number, $Pe_x; Pe_y$	1.4085;0.0	1.4085,0.7042,2.8169;0.0

In 1-D transport only longitudinal dispersion is active; while, in a 2-D transport problem both longitudinal and transverse dispersion can occur. In a general 2-D transport problem the off-diagonal terms of the dispersion coefficient tensor are typically non-zero. In FACT the resulting dispersive flux cross-term products (see Eq. (2.2.20), such as

$$\frac{\partial}{\partial x} \left[D_{xy} \left(\frac{\partial c}{\partial y} \right) \right] \quad (4.2.2.5)$$

are handled consistently and are not "lumped". The lumping approximation is more commonly used in finite difference algorithms (see Faust, et. al., 1993) to accommodate their matrix solution requirements, none of which is required in FACT. Typically, lumping greatly over estimates transverse dispersion. Also for many algorithms, grid orientation effects occur even though the these cross-product terms are handled in a consistent formulation.

To examine these grid orientation effects in FACT, two base case grids were chosen for this problem: (1) a grid aligned parallel to the aquifer flow direction consisting of 738 rectangular brick elements uniformly sized (30 m in length) with 41 elements along the x-axis and 18 along the y-axis and (2) a grid aligned at a 45° diagonal to the aquifer flow direction consisting of 1681 rectangular brick elements uniformly sized (30 m in length) with 41 elements along the x-axis and y-axis. Figures 4.2.2.2 and 4.2.2.3 illustrate the finite element grids chosen and the boundary conditions applied along the six outer domain surfaces, respectively. At the channel inlet boundary(s) (left; left and front), the concentration of solute in the incoming water is set to 0.0 kg/m³. Due to the finite overall length of our mesh, at the outflow boundary(s) (right; right and back) the dispersive flux

FACT CODE MANUAL

is set to zero, while the advective flux is calculated as part of the solution. In addition, for the parallel grid the dispersive flux is set to zero at the transverse faces (front and back). The element sizes for both grid orientations are the same and the results shown should represent grid orientation effects only.

Since this is a 2-D problem, solute concentration gradients do not exist in the vertical direction (z direction). Therefore, the dispersive fluxes along these two faces (top and bottom) are set to zero. By default, in the standard finite element formulation zero dispersive fluxes are automatically applied to all outer domain surfaces unless otherwise specified. The aquifer is assumed to be completely saturated.

For this problem several simulations were performed. As summarized in Table 4.2.2.2, simulations were performed for both base cases (parallel and diagonal grids) and then four additional runs were made varying certain key physical parameters and FACT options to demonstrate their impact on the final results. For each simulation a transient calculation was performed for a 1400 day duration and the results from FACT at this end time are compared to the analytical solution given by Eq. (4.2.2.3). As shown in Table 4.2.2.1, a range of cell Peclet, cell material Courant, and cell Fourier numbers were tested.

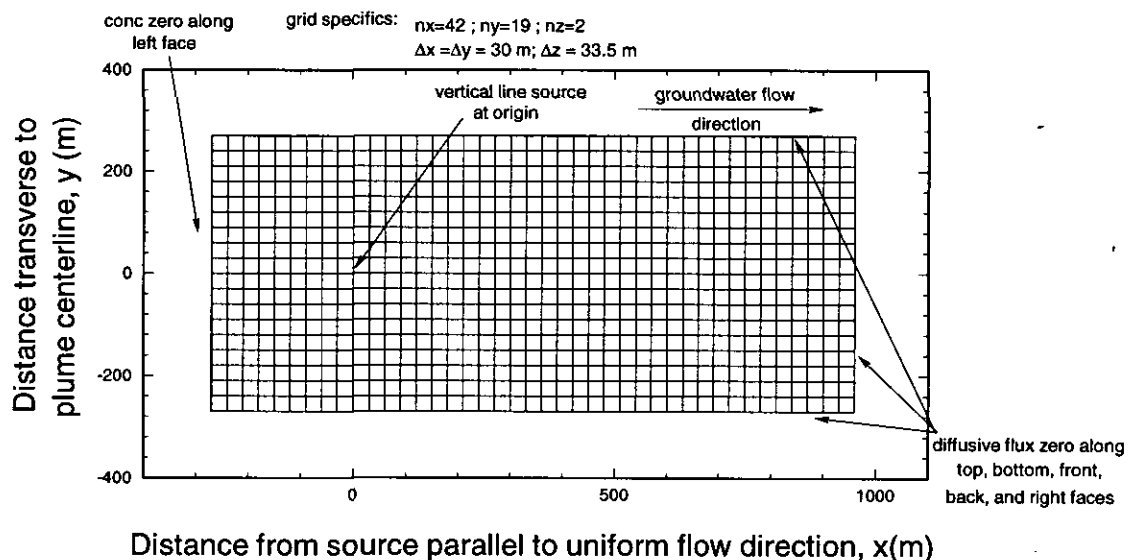


Fig. 4.2.2.2. FACT parallel mesh and boundary conditions for 2D transport.

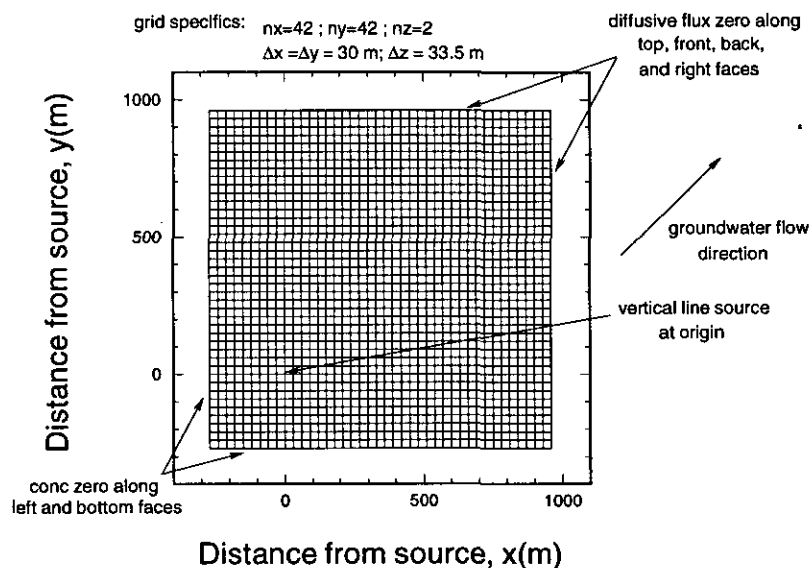


Fig. 4.2.2.3. FACT diagonal mesh and boundary conditions for 2D transport.

The results of all the simulations (both numerical and analytical) are shown in Figs. 4.2.2.4 through 4.2.2.13. These results are also presented in tabular form for comparison in Tables 4.2.2.3 through 4.2.2.7. The analytical results were computed from the computer code AT123D (Yeh, 1981). The FACT numerical results are labeled either "FACT Parallel grid" or "FACT Diagonal grid" for the base cases and have additional nomenclature for the other runs (e.g., "FACT Parallel grid ($\lambda_r = 0.005$)" represents the run where all parameters were at their base case values for the parallel grid model except for the radioactive decay parameter that was set to 0.005).

Table 4.2.2.2

Summary of simulations performed (base cases and their variations) on the two-dimensional transport problem

FACT Options	Base case (parallel)	Base case (diagonal)	A	B	C	D
spatial differencing centered [Bubnov], $\alpha = 0$ upstream [Petrov], $\alpha = 1$	x	x			x	x
Mesh Options						
parallel grid	x		x		x	x
diagonal grid		x		x		
Physical Parameters						
radioactive decay coef., $\lambda_T =$ 0.0 d ⁻¹	x	x	x	x	x	
$\lambda_T = 0.005$ d ⁻¹						x
Solute distribution coef., $k_d =$ 0.0 m ³ /kg	x	x	x	x		x
$k_d = 0.4375$ m ³ /kg					x	

The results presented in Figs. 4.2.2.4 and 4.2.2.5 represent our base case (parallel and diagonal) simulations. The concentration contours at 1400 days exhibit slight oscillatory behavior near the leading and outer edge of the source plume and transverse to the aquifer flow direction. These results are also compared to the analytical solution in Figs. 4.2.2.6 through 4.2.2.8. The computed concentration profiles in the direction of groundwater flow along a line through the source are shown in Fig. 4.2.2.6. Figures 4.2.2.7 and 4.2.2.8 show computed concentration profiles perpendicular to the groundwater flow direction at the source and approximately 420 m downstream of the source location for the two alternative grids, respectively. The results away from the source show good comparison between the analytical solution and the numerical results for both grid orientations. Many algorithms would show noticeable differences between these results based upon grid orientation effects not shown here by FACT. For such codes aligning the grid in the direction of dominant groundwater flow is strongly recommended. For FACT no significant grid orientation effects occur; therefore, one should base their grid alignment on other features of the conceptual model (e.g., principle directions of the hydraulic conductivity tensor).

As mentioned early, the analytic solution yields an infinite solute concentration as one approaches the location of the point source. Note that the FACT simulations presented here employed a small, but finite, flow rate at the point source. Thus the solute concentration of the incoming source was (see Table 4.2.2.1 for parameter values):

$$c^* = \frac{qc^*}{q} \rightarrow \frac{0.235844 \text{ kg/d}}{0.2 \text{ m}^3/\text{d}} = 1.17922 \text{ kg/m}^3 \quad (4.2.2.6)$$

FACT CODE MANUAL

which still represents a fairly large concentration level. In an attempt to predict the very steep concentration gradients near the point source, FACT exhibits on our coarse mesh oscillations as shown in Fig. 4.2.2.8. These oscillations were large enough to produce negative solute concentrations near the point source. We also failed to predict the high concentration at the point source (i.e., compare 1.17922 to 0.0015 kg/m³ given in Table 4.2.2.5).

One might be tempted to correct these oscillations by employing fully upstream spatial weighting as was successfully done in the 1-D transport problem discussed earlier. A comparison between central (base cases) and fully upstream spatial weighting (cases A and B) simulation runs are shown in Fig. 4.2.2.9. Figure 4.2.2.9 shows computed concentration profiles perpendicular to the groundwater flow direction at the source location for the two alternative grids with and without upstream spatial weighting. As shown, upstream weighting can reduce these oscillations such that only positive solute concentrations exist (i.e., minimize our undershoot); however, the basic oscillations still exist and can only be omitted by mesh refinement. Figures 4.2.2.10 and 4.2.2.11 show concentration carpet plots on the diagonal grid, where the lower contour value was set to zero, for the central and upstream weighting options, respectively. Negative concentration regions will show up as black zones. As indicated, the fully upstream weighting option results show no negative concentration levels (case B).

By adjusting the solute distribution coefficient such that the retardation factor becomes 2.0 (case C), the retarded dispersion and velocity are halved. These results can be compared to the un-retarded base case (parallel grid) in Fig. 4.2.2.12 where the spread of the plume has been greatly reduced.

By employing a non-zero radioactive decay coefficient such that the solute now becomes a non-conservative transport species (cases D), the solute concentration profiles are reduced especially at the higher concentration levels. These results can be compared to the base case (parallel grid) in Fig. 4.2.2.13.

Based upon these calculations, some general guidance and observations came be given when performing solute transport with FACT:

- Grid orientation effects are not present in the current formulation of FACT; therefore, one should base their grid alignment on other features of the conceptual model.
- Point/line sources with high solute concentrations will exhibit steep concentration gradients near the source location. A physical concentration values (resulting from significant undershoot) can be reduced by applying upstream spatial weighting; however, to eliminate the oscillatory behavior near the point/line source mesh refinement must be performed.
- Excellent solute concentration profile predictions can be achieved on coarse meshes; even though, oscillations may be present near the point/line sources.

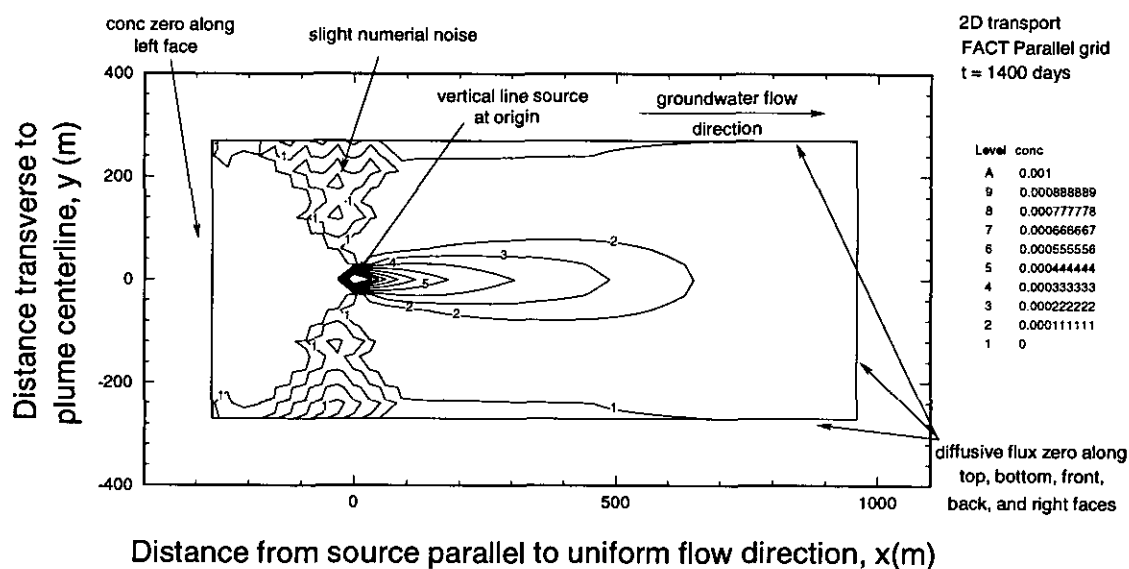


Fig. 4.2.2.4. FACT concentration profile for 2D transport of the base case on the parallel grid.

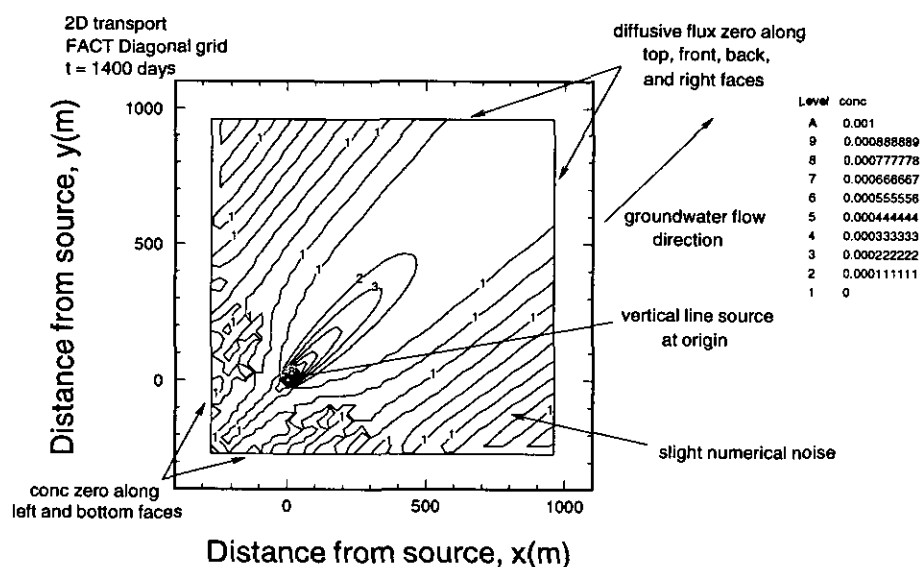


Fig. 4.2.2.5. FACT concentration profile for 2D transport of the base case on the diagonal grid.

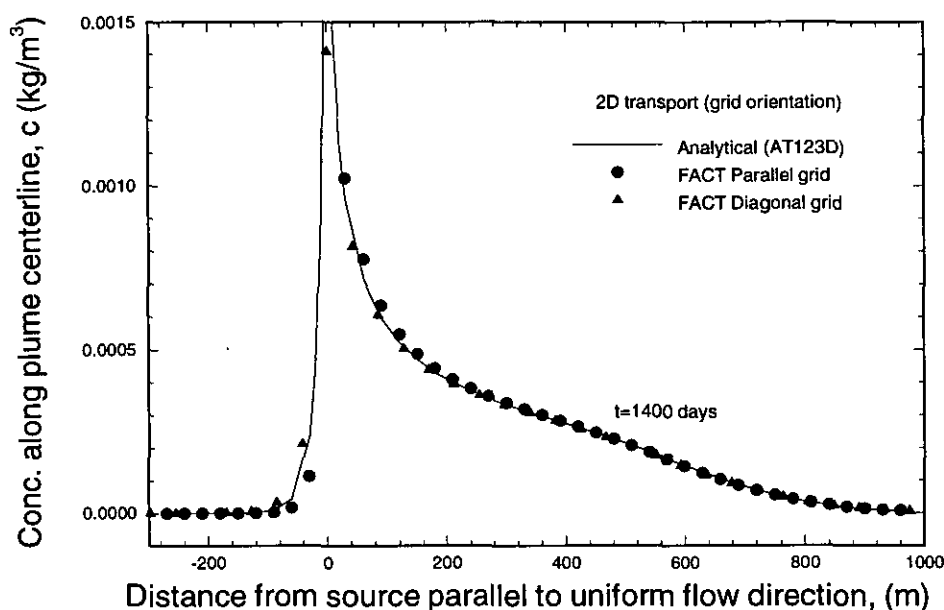


Fig. 4.2.2.6. Concentration profiles for 2D transport of the base case along plume centerline.

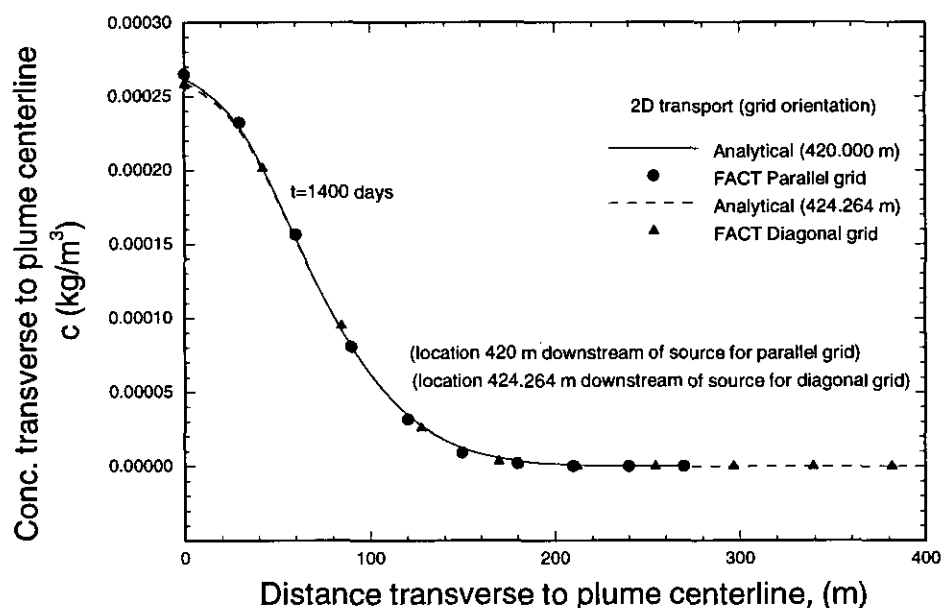


Fig. 4.2.2.7. Concentration profiles for 2D transport of the base case transverse to plume centerline located 420 m downstream of the source.

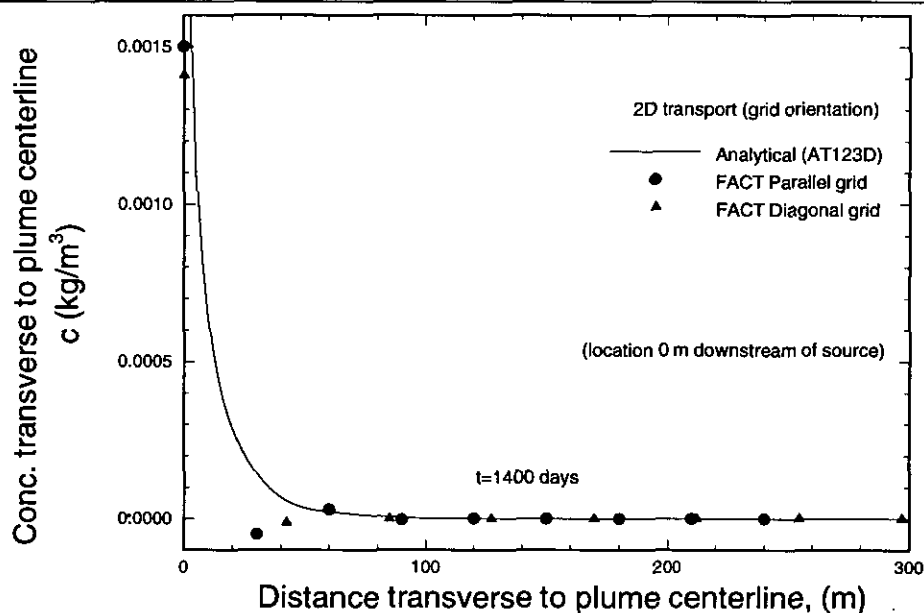


Fig. 4.2.2.8. Concentration profiles for 2D transport of the base case transverse to plume centerline located 0 m downstream of the source.

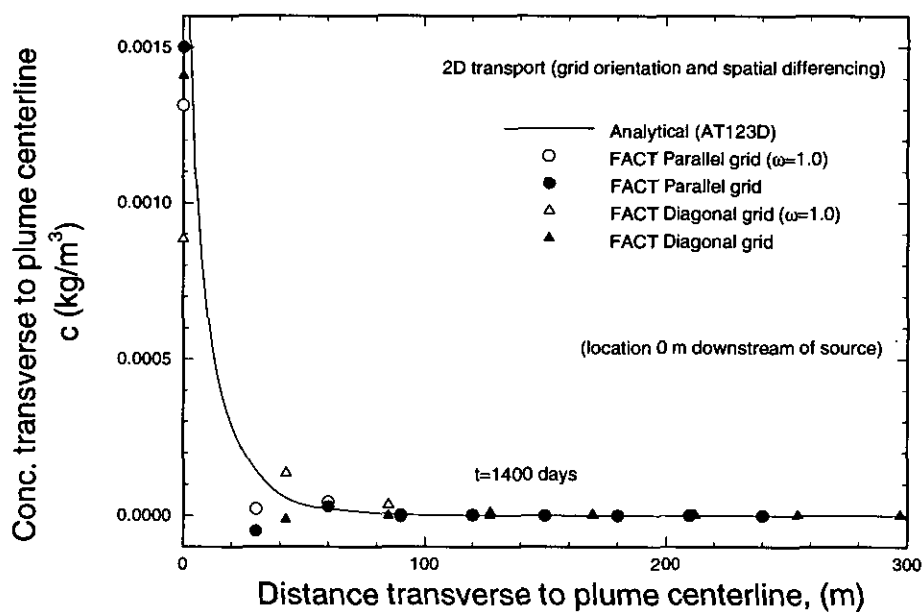


Fig. 4.2.2.9. Effect of complete upstream spatial differencing on concentration profiles for 2D transport transverse to plume centerline located 0 m downstream of the source.

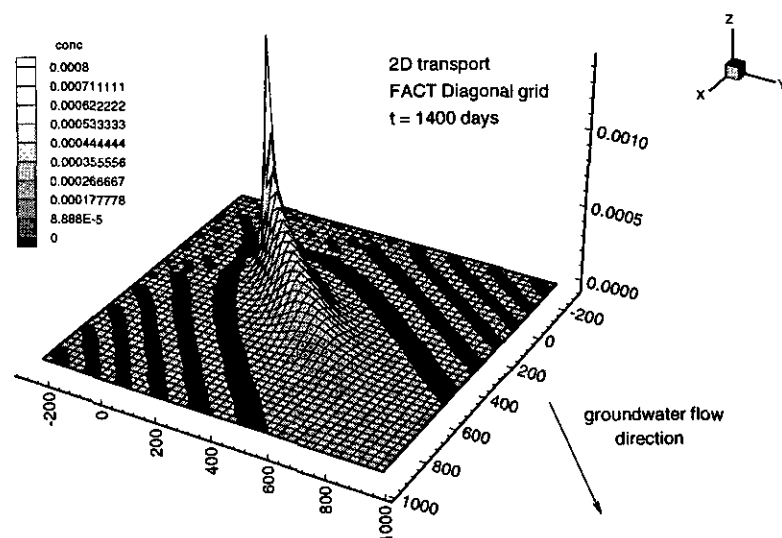


Fig. 4.2.2.10. FACT concentration profile (carpet plot) for 2D transport of the base case showing the effect of centered spatial differencing.

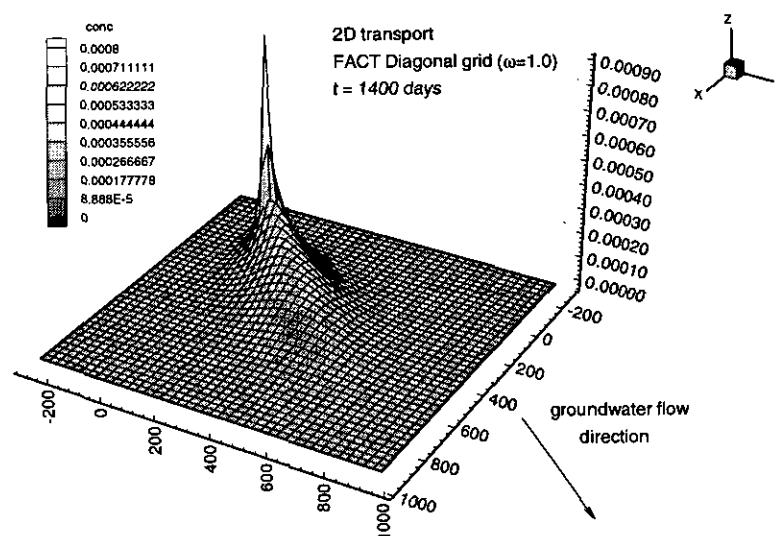


Fig. 4.2.2.11. FACT concentration profile (carpet plot) for 2D transport of the base case showing the effect of complete upstream spatial differencing.

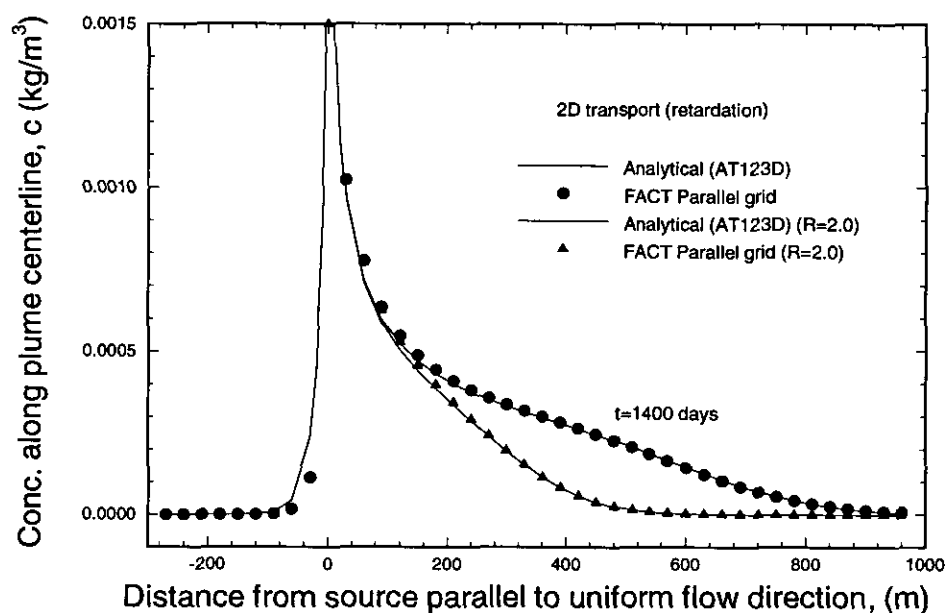


Fig. 4.2.2.12. Concentration profiles for 2D transport showing effect of retardation.

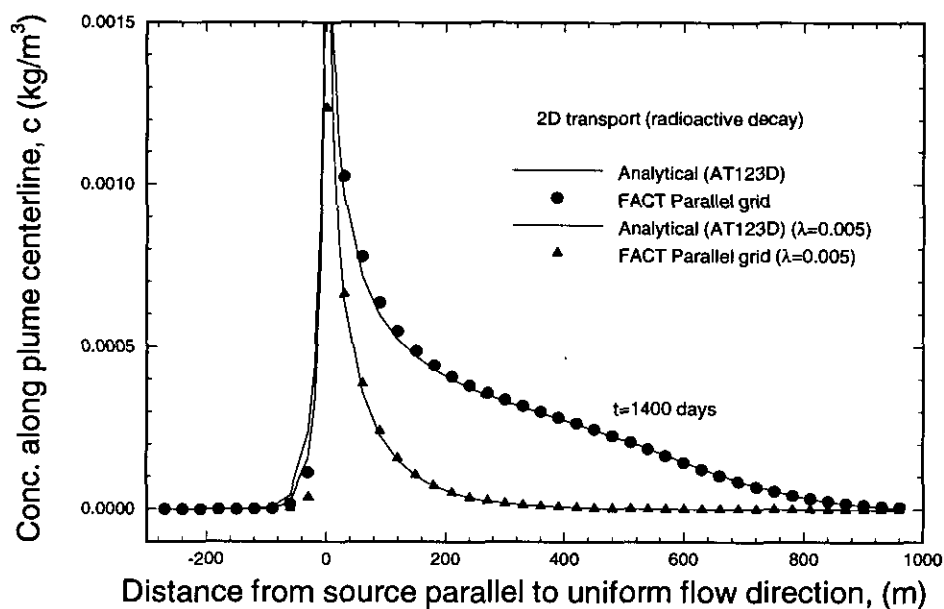


Fig. 4.2.2.13. Concentration profiles for 2D transport showing effect of radioactive decay.

Table 4.2.2.3

Effect grid orientation has on the numerical concentration (kg/m³) results along the plume centerline for the transient 2D transport problem (base case, t=1400 days)

Distance down- stream, x (m)	Analytical (AT123D)	Numerical (FACT) (parallel grid)	Distance down- stream, (m)	Analytical (AT123D)	Numerical (FACT) (diagonal grid)
-270.0	0.1099E-08	0.8976E-08	-381.8	0.4655E-11	0.1491E-09
-240.0	0.4777E-08	0.1029E-07	-339.4	0.3703E-10	0.1707E-09
-210.0	0.2088E-07	0.1956E-07	-297.0	0.2938E-09	0.4155E-09
-180.0	0.9208E-07	0.6621E-07	-254.6	0.2340E-08	0.2487E-08
-150.0	0.4109E-06	0.2916E-06	-212.1	0.1880E-07	0.1973E-07
-120.0	0.1867E-05	0.1391E-05	-169.7	0.1536E-06	0.1656E-06
-90.0	0.8724E-05	0.6905E-05	-127.3	0.1290E-05	0.1443E-05
-60.0	0.4284E-04	0.3614E-04	-84.9	0.1141E-04	0.1339E-04
-30.0	0.2359E-03	0.2134E-03	-42.4	0.1137E-03	0.1406E-03
0.0	∞	0.2012E-02	0.0	∞	0.1853E-02
30.0	0.9648E-03	0.1010E-02	42.4	0.8336E-03	0.8326E-03
60.0	0.7165E-03	0.7317E-03	84.9	0.6130E-03	0.6102E-03
90.0	0.5967E-03	0.6038E-03	127.3	0.5080E-03	0.5059E-03
120.0	0.5223E-03	0.5264E-03	169.7	0.4432E-03	0.4415E-03
150.0	0.4701E-03	0.4729E-03	212.1	0.3976E-03	0.3962E-03
180.0	0.4308E-03	0.4328E-03	254.6	0.3626E-03	0.3614E-03
210.0	0.3996E-03	0.4010E-03	297.0	0.3338E-03	0.3327E-03
240.0	0.3737E-03	0.3749E-03	339.4	0.3083E-03	0.3073E-03
270.0	0.3516E-03	0.3525E-03	381.8	0.2841E-03	0.2832E-03
300.0	0.3319E-03	0.3326E-03	424.3	0.2598E-03	0.2590E-03
330.0	0.3137E-03	0.3143E-03	466.7	0.2343E-03	0.2337E-03
360.0	0.2964E-03	0.2969E-03	509.1	0.2074E-03	0.2068E-03
390.0	0.2794E-03	0.2798E-03	551.5	0.1790E-03	0.1785E-03
420.0	0.2622E-03	0.2626E-03	594.0	0.1500E-03	0.1496E-03
450.0	0.2445E-03	0.2448E-03	636.4	0.1213E-03	0.1210E-03
480.0	0.2261E-03	0.2263E-03	678.8	0.9429E-04	0.9411E-04
510.0	0.2068E-03	0.2070E-03	721.2	0.7021E-04	0.7012E-04
540.0	0.1869E-03	0.1870E-03	763.7	0.4992E-04	0.4989E-04
570.0	0.1664E-03	0.1665E-03	806.1	0.3379E-04	0.3381E-04
600.0	0.1458E-03	0.1459E-03	848.5	0.2173E-04	0.2177E-04
630.0	0.1255E-03	0.1255E-03	891.0	0.1325E-04	0.1329E-04
660.0	0.1060E-03	0.1060E-03	933.4	0.7645E-05	0.7687E-05
690.0	0.8762E-04	0.8760E-04	975.8	0.4170E-05	0.4204E-05
720.0	0.7087E-04	0.7084E-04	1018.2	0.2148E-05	0.2172E-05
750.0	0.5601E-04	0.5597E-04	1060.7	0.1044E-05	0.1059E-05
780.0	0.4322E-04	0.4317E-04	1103.1	0.4780E-06	0.4870E-06
810.0	0.3252E-04	0.3247E-04	1145.5	0.2062E-06	0.2111E-06
840.0	0.2385E-04	0.2380E-04	1187.9	0.8371E-07	0.8624E-07
870.0	0.1703E-04	0.1699E-04	1230.4	0.3198E-07	0.3318E-07
900.0	0.1184E-04	0.1182E-04	1272.8	0.1149E-07	0.1202E-07
930.0	0.8003E-05	0.8154E-05	1315.2	0.3879E-08	0.4139E-08
960.0	0.5262E-05	0.6510E-05	1357.6	0.1231E-08	0.2153E-08

Table 4.2.2.4

Effect grid orientation has on the numerical concentration (kg/m³) results transverse to the plume centerline (located 420 m downstream of the source) for the transient 2D transport problem (base case, t=1400 days)

Distance transverse, y (m)	Analytical (AT123D)	Numerical (FACT) (parallel grid)	Distance transverse, (m)	Analytical (AT123D)	Numerical (FACT) (diagonal grid)
0.0	0.2622E-03	0.2626E-03	0.0	0.2598E-03	0.2590E-03
30.0	0.2290E-03	0.2296E-03	42.4	0.1988E-03	0.1993E-03
60.0	0.1538E-03	0.1543E-03	84.9	0.9190E-04	0.9252E-04
90.0	0.8117E-04	0.8102E-04	127.3	0.2753E-04	0.2705E-04
120.0	0.3464E-04	0.3391E-04	169.7	0.5741E-05	0.5204E-05
150.0	0.1228E-04	0.1157E-04	212.1	0.8746E-06	0.6699E-06
180.0	0.3686E-05	0.3273E-05	254.6	0.9966E-07	0.5596E-07
210.0	0.9510E-06	0.7732E-06	297.0	0.8553E-08	0.2710E-08
240.0	0.2123E-06	0.1553E-06	339.4	0.5521E-09	0.5224E-10
270.0	0.4116E-07	0.4927E-07	381.8	0.2666E-10	-0.5468E-12

Table 4.2.2.5

Effect grid orientation has on the numerical concentration (kg/m³) results transverse to the plume centerline (located 0 m downstream of the source) for the transient 2D transport problem (base case, t=1400 days)

Distance transverse, y (m)	Analytical (AT123D)	Numerical (FACT) (parallel grid)	Distance transverse, (m)	Analytical (AT123D)	Numerical (FACT) (diagonal grid)
0.0	∞	0.2012E-02	0.0	∞	0.1853E-02
30.0	0.1425E-03	0.1405E-03	42.4	0.6361E-04	0.5108E-04
60.0	0.2161E-04	0.1862E-04	84.9	0.4999E-05	0.3182E-05
90.0	0.3712E-05	0.2971E-05	127.3	0.4435E-06	0.2218E-06
120.0	0.6695E-06	0.5062E-06	169.7	0.4040E-07	0.1535E-07
150.0	0.1230E-06	0.8795E-07	212.1	0.3551E-08	0.9302E-09
180.0	0.2252E-07	0.1510E-07	254.6	0.2828E-09	0.4045E-10
210.0	0.4020E-08	0.2484E-08	297.0	0.1923E-10	0.5959E-12
240.0	0.6839E-09	0.3828E-09	339.4	0.1066E-11	-0.6391E-13
270.0	0.1086E-09	0.1014E-09	381.8	0.4645E-13	0.1541E-14

Table 4.2.2.6

Effect grid orientation and complete upstream spatial differencing has on the numerical concentration (kg/m³) results transverse to the plume centerline (located 0 m downstream of the source) for the transient 2D transport problem (spatial differencing $\alpha = 1.0$, $t = 1400$ days)

Distance transverse, y (m)	Analytical (AT123D)	Numerical (FACT) (parallel grid)	Distance transverse, (m)	Analytical (AT123D)	Numerical (FACT) (diagonal grid)
0.0	∞	0.1838E-02	0.0	∞	0.1565E-02
30.0	0.1425E-03	0.1631E-03	42.4	0.6361E-04	0.7687E-04
60.0	0.2161E-04	0.2789E-04	84.9	0.4999E-05	0.7745E-05
90.0	0.3712E-05	0.5678E-05	127.3	0.4435E-06	0.8447E-06
120.0	0.6695E-06	0.1218E-05	169.7	0.4040E-07	0.8602E-07
150.0	0.1230E-06	0.2615E-06	212.1	0.3551E-08	0.7076E-08
180.0	0.2252E-07	0.5419E-07	254.6	0.2828E-09	0.3410E-09
210.0	0.4020E-08	0.1045E-07	297.0	0.1923E-10	-0.1091E-10
240.0	0.6839E-09	0.1837E-08	339.4	0.1066E-11	-0.2200E-11
270.0	0.1086E-09	0.5381E-09	381.8	0.4645E-13	0.2419E-12

Table 4.2.2.7

Effect retardation or radioactive decay has on the numerical concentration (kg/m³) results along the plume centerline for the transient 2D transport problem (retardation $R=2.0$ or radioactive decay $\lambda_r=0.005$, $t=1400$ days)

Distance downstream, x (m)	Analytical (AT123D)	Numerical (FACT) ($R=2.0$) (parallel grid)	Analytical (AT123D)	Numerical (FACT) ($\lambda=0.005$) (parallel grid)
-270.0	0.7491E-09	0.2168E-08	0.8109E-10	0.2086E-09
-240.0	0.3666E-08	0.3235E-08	0.4615E-09	0.3312E-09
-210.0	0.1753E-07	0.1111E-07	0.2646E-08	0.1370E-08
-180.0	0.8242E-07	0.5294E-07	0.1532E-07	0.8191E-08
-150.0	0.3846E-06	0.2643E-06	0.8986E-07	0.5242E-07
-120.0	0.1799E-05	0.1326E-05	0.5370E-06	0.3441E-06
-90.0	0.8556E-05	0.6749E-05	0.3305E-05	0.2328E-05
-60.0	0.4245E-04	0.3578E-04	0.2141E-04	0.1661E-04
-30.0	0.2351E-03	0.2126E-03	0.1564E-03	0.1344E-03
0.0	∞	0.2010E-02	∞	0.1760E-02
30.0	0.9613E-03	0.1006E-02	0.6396E-03	0.6723E-03
60.0	0.7100E-03	0.7253E-03	0.3581E-03	0.3664E-03
90.0	0.5852E-03	0.5924E-03	0.2260E-03	0.2286E-03
120.0	0.5032E-03	0.5074E-03	0.1502E-03	0.1512E-03
150.0	0.4400E-03	0.4428E-03	0.1028E-03	0.1032E-03
180.0	0.3856E-03	0.3876E-03	0.7167E-04	0.7185E-04
210.0	0.3353E-03	0.3368E-03	0.5063E-04	0.5070E-04
240.0	0.2869E-03	0.2879E-03	0.3611E-04	0.3613E-04
270.0	0.2397E-03	0.2404E-03	0.2595E-04	0.2595E-04
300.0	0.1945E-03	0.1950E-03	0.1876E-04	0.1874E-04
330.0	0.1523E-03	0.1527E-03	0.1362E-04	0.1361E-04
360.0	0.1147E-03	0.1149E-03	0.9931E-05	0.9917E-05
390.0	0.8272E-04	0.8280E-04	0.7263E-05	0.7250E-05
420.0	0.5694E-04	0.5693E-04	0.5325E-05	0.5314E-05
450.0	0.3730E-04	0.3724E-04	0.3911E-05	0.3902E-05
480.0	0.2321E-04	0.2312E-04	0.2876E-05	0.2869E-05
510.0	0.1369E-04	0.1359E-04	0.2116E-05	0.2110E-05
540.0	0.7646E-05	0.7550E-05	0.1556E-05	0.1551E-05
570.0	0.4035E-05	0.3957E-05	0.1143E-05	0.1139E-05
600.0	0.2011E-05	0.1953E-05	0.8369E-06	0.8341E-06
630.0	0.9454E-06	0.9065E-06	0.6105E-06	0.6083E-06
660.0	0.4189E-06	0.3950E-06	0.4428E-06	0.4411E-06
690.0	0.1748E-06	0.1614E-06	0.3189E-06	0.3176E-06
720.0	0.6869E-07	0.6175E-07	0.2276E-06	0.2265E-06
750.0	0.2539E-07	0.2208E-07	0.1606E-06	0.1598E-06
780.0	0.8829E-08	0.7372E-08	0.1119E-06	0.1113E-06
810.0	0.2886E-08	0.2293E-08	0.7690E-07	0.7640E-07
840.0	0.8865E-09	0.6639E-09	0.5197E-07	0.5158E-07
870.0	0.2559E-09	0.1785E-09	0.3450E-07	0.3420E-07
900.0	0.6938E-10	0.4449E-10	0.2246E-07	0.2227E-07
930.0	0.1766E-10	0.1029E-10	0.1433E-07	0.1447E-07

960.0	0.4222E-11	0.3373E-11	0.8939E-08	0.1113E-07
-------	------------	------------	------------	------------

4.2.3 Three-Dimensional Saturated Solute Transport in a Uniform Flow Field

This problem deals with three-dimensional advection-dispersion of a conservative solute species from a point source through an infinite porous medium. Based upon the problem definition, this problem results in an analytic solution that is axisymmetric in solute concentrations. However, the problem will be solved analytically and numerically in 3-D Cartesian coordinates. It is used to demonstrate FACT's capability to solve 3-D transport problems and to yield 3-D results that are indeed axisymmetric. This problem also tests FACT's formulation of transverse dispersion in more than one dimension. The physical schematic of this problem is essentially the same as for the 2-D transport problem discussed in Section 4.2.2 and shown in Fig. 4.2.2.1(a). In practice, the idealized conditions are analogous to continual leakage, leaching, or injection of a contaminant into a large confined aquifer from buried waste in a landfill or an improperly sealed partially penetrating injection well. It is assumed that the total rate of fluid leakage, leaching, or injection into the aquifer is negligible and does not disturb the ambient groundwater flow regime. Analytically and numerically the problem is treated as a point source in 3-D Cartesian coordinates.

As illustrated in Fig. 4.2.2.1(b), a conservative contaminant is continuously released from a point source downstream of an inflow boundary (containing zero contaminant) into a large aquifer unit whose groundwater flow is assumed to be uniform. The point source is located at a depth such that end effects at the top and bottom of the aquifer unit are negligible. Both hydrodynamic dispersion and molecular diffusion are allowed for the transported species. It is assumed that the contaminant mass flow rate at the point source remains constant, the aquifer's flow rate is uniform and constant, the aquifer is sufficiently large to neglect end effects, and the homogeneous aquifer's properties (such as porosity, soil type, water saturation) are uniform and constant.

Analytic solution: Equation (2.2.13) represents the conservative form of the multi-dimensional advection-dispersion equation for solute transport through a variably saturated porous media. Taking the 2-D form of Eq. (2.2.13) and assuming that one point source exists at the location $x = y = z = 0$, constant water saturation level, and that material coefficients are constants, results in

$$\frac{\partial c}{\partial t} = D'_{xx} \frac{\partial^2 c}{\partial x^2} + D'_{yy} \frac{\partial^2 c}{\partial y^2} + D'_{zz} \frac{\partial^2 c}{\partial z^2} - u'_x \frac{\partial c}{\partial x} + \lambda_r c + \frac{qc^*}{\theta_m R} \quad (4.2.3.1)$$

where $D'_{xx} = \alpha_{LH} u'_x$, $D'_{yy} = \alpha_{TH} u'_y$ and $D'_{zz} = \alpha_{TV} u'_z$.

For our infinite aquifer the initial conditions are:

$$c(x, y, z, 0) = 0 \quad (4.2.3.2a)$$

and the boundary conditions are:

$$c(\pm\infty, y, z, t) = 0 \quad (4.2.3.2b)$$

$$c(x, \pm\infty, z, t) = 0 \quad (4.2.3.2c)$$

$$c(x, y, \pm\infty, t) = 0 \quad (4.2.3.2d)$$

These boundary conditions are equivalent to assuming that the dispersive flux of solute is zero at plus or minus infinity or

$$\lim_{x \rightarrow \pm\infty} \left(\frac{\partial c}{\partial x} \right) = 0 \quad (4.2.2.2e)$$

$$\lim_{y \rightarrow \pm\infty} \left(\frac{\partial c}{\partial y} \right) = 0 \quad (4.2.2.2f)$$

$$\lim_{z \rightarrow \pm\infty} \left(\frac{\partial c}{\partial z} \right) = 0 \quad (4.2.2.2g)$$

For finite times there exists finite values of x , y , and z where Eqs. (4.2.3.2e,f,g) remain valid.

As mentioned above, it is assumed that the total rate of fluid flow, q , into the aquifer due to the source is negligible and does not disturb the ambient groundwater flow regime. In order to have a finite mass flow rate of contaminant requires

$$\lim_{q \rightarrow 0} (qc^*) < \infty \Rightarrow \lim_{q \rightarrow 0} (c^*) = +\infty \quad (4.2.2.2f)$$

Therefore, analytically the concentration of solute entering the aquifer at the point source becomes infinite.

Equation (4.2.3.1), a linear partial differential equation subject to the initial and boundary conditions given by Eqs. (4.2.3.2a,b,c,d), can be solved by employing an appropriate Green's function for the point source and applying the Laplace and Fourier transform techniques. For details see Yeh (1981). The general solution for a continuous point source takes the form:

$$c(x, y, z, t) = \frac{qc^*}{\theta_m R} \int_0^t G(x|\xi; y|\eta; z|\zeta; t|\tau) d\tau \quad (4.2.3.3a)$$

where $G(x|\xi; y|\eta; z|\zeta; t|\tau)$ is the Green's function over the domain space. For our analytical problem we shall limit our flow field to flow parallel to the x -axis only. This results in a dispersion tensor that is diagonal and a separable Green's function. It can be shown that for simple geometry such as separable coordinate system, Green's function, G , can be expressed as:

$$G(x|\xi; y|\eta; z|\zeta; t|\tau) = G_1(x|\xi; t|\tau) G_2(y|\eta; t|\tau) G_3(z|\zeta; t|\tau) \quad (4.2.3.3b)$$

where for a point source in the x -direction (infinite domain, parallel to flow):

$$G_1(x|\xi; t|\tau) = \frac{1}{\sqrt{4\pi D'_{xx}(t-\tau)}} \exp \left[-\frac{\{(x-\xi) - u'_x(t-\tau)\}^2}{4D'_{xx}(t-\tau)} - \lambda_r(t-\tau) \right] \quad (4.2.3.3c)$$

and for a point source in the y-direction (infinite domain, transverse to flow):

$$G_2(y|\eta; t|\tau) = \frac{1}{\sqrt{4\pi D'_{yy}(t-\tau)}} \exp \left[-\frac{(y-\eta)^2}{4D'_{yy}(t-\tau)} \right] \quad (4.2.3.3d)$$

and for a point source in the z-direction (infinite domain, transverse to flow):

$$G_3(z|\zeta; t|\tau) = \frac{1}{\sqrt{4\pi D'_{zz}(t-\tau)}} \exp \left[-\frac{(z-\zeta)^2}{4D'_{zz}(t-\tau)} \right] \quad (4.2.3.3e)$$

The evaluation of the analytic expressions, Eqs. (4.2.3.3a,b,c,d,e), for a specific problem is performed numerically and has been performed using the computer code AT123D by Yeh (1981).

FACT numerical simulation and comparison: In FACT we will model this axisymmetric problem using a 3-D finite element mesh containing many elements in all three directions. The point source given above will be located at the mid-plane of our mesh (in FACT point and line sources are limited to node locations only).

Even though we are considering an aquifer unit with infinite extent in the areal and vertical directions, our numerical model has finite size. At our inflow boundary we shall assume that the incoming fluid remains contaminant free (i.e., the contaminant concentration immediately upstream of the source does not extend back up to the inflow boundary). We also assume that the vertical extent of the top and bottom faces of our mesh from the point source is sufficient distance that negligible amounts of contaminant reaches these boundary faces. For the parameters chosen (i.e., longitudinal dispersivity, Darcy velocity, and source location), the above assumption remains valid over the time period of interest.

Also, FACT requires knowledge about both the total volumetric flow rate, q , and its solute concentration entering the aquifer at the line source. An arbitrarily small but finite value for q was chosen to maintain computed solute concentration values near the source to acceptable values. Steep concentration gradients near a source can result in oscillatory behavior unless the local grid is sufficiently refined. For demonstration purposes, we have chosen uniform coarse grids and are primarily interested in results away from the source location. The simulations are done by specifying a velocity field and running the solute transport option only. In this way, the flow rate entering the aquifer due to the line source does not alter the aquifer flow field.

Values of the physical parameters used in the verification simulations are presented in Table 4.2.3.1. For the conservative solute transport case the parameters were selected based on data from a field investigation on hexavalent chromium contamination reported by Perlumutter and Lieber (1970) and Wilson and Miller (1978).

FACT CODE MANUAL

In 1-D transport only longitudinal dispersion is active; while, in a 2-D transport problem both longitudinal and transverse dispersion can occur. In 3-D transport transverse dispersion occurs throughout the plane perpendicular to the flow direction. In a general 3-D transport problem the off-diagonal terms of the dispersion coefficient tensor are typically non-zero. If the grid is aligned parallel to the groundwater flow direction, then only the diagonal terms of the hydrodynamic dispersion tensor are non-zero (see Eq. (2.2.20)).

Table 4.2.3.1

Values of the physical parameters, the finite element grid, time-step data, and some key parameters used in the three-dimensional transport problem (base case)

Physical parameters	Base case
Darcy velocity, U_x	0.161 m/d
Porosity, ϕ	0.35
Longitudinal dispersivity, α_{LH}	21.3 m
Transverse dispersivity, α_{TH} , α_{TV}	4.3 m
Apparent molecular dispersion coefficient, $\theta_m \tau D^*$	0.0 m ² /d
Water saturation, S_w	1.0
radioactive decay coef., λ_T	0.0 d ⁻¹
Soil density, ρ_s	1.23077 kg/m ³
Solute distribution coefficient, k_d	0.0 m ³ /kg
Boundary solute concentration, c_0	0.0 kg/m ³
Water total volumetric flowrate (point source), q	0.1 m ³ /d
Contaminant total mass flowrate (point source), qc^*	0.117922 kg/d
Grid specifics	
Element lengths, $\Delta x = \Delta y = \Delta z$	30 m
Number nodes in x-dir	83
Number nodes in y-dir	37 (parallel grid)
Number nodes in z-dir	37
Time steps	
Time duration	1400 d
number time-steps	140
time-step size, Δt	10 d
Key computed parameters	
Retardation factor, R	1.0
Bulk soil density, ρ_b	0.8 kg/m ³
Phasic velocity, u_x	0.46 m/d
Retarded phasic velocity, u'_x	0.46 m/d
Retarded longitudinal dispersion coefficient, D'_{xx}	9.798 m ² /d
Retarded transverse dispersion coefficients, $D'_{yy} = D'_{zz}$	1.978 m ² /d
Retarded cross dispersion coefficients, $D'_{xy} = D'_{xz} = D'_{yz}$	0.0 m ² /d
Cell Fourier number, $Fo_x; Fo_y = Fo_z$	0.435; 0.088
Cell Courant number, $Co_x; Co_y = Co_z$	0.307; 0.0
Cell Peclet number, $Pe_x; Pe_y = Pe_z$	0.704; 0.0

FACT CODE MANUAL

To examine in FACT transverse dispersion into a plane perpendicular to groundwater flow without the added complication of cross-term products resulting from the dispersion tensor, a base case grid was chosen for this problem that is aligned parallel to the aquifer flow direction. This grid consists of 106,272 rectangular brick elements uniformly sized (15 m in length) with 82 elements along the x-axis and 36 along the y- and z-axes, respectively.

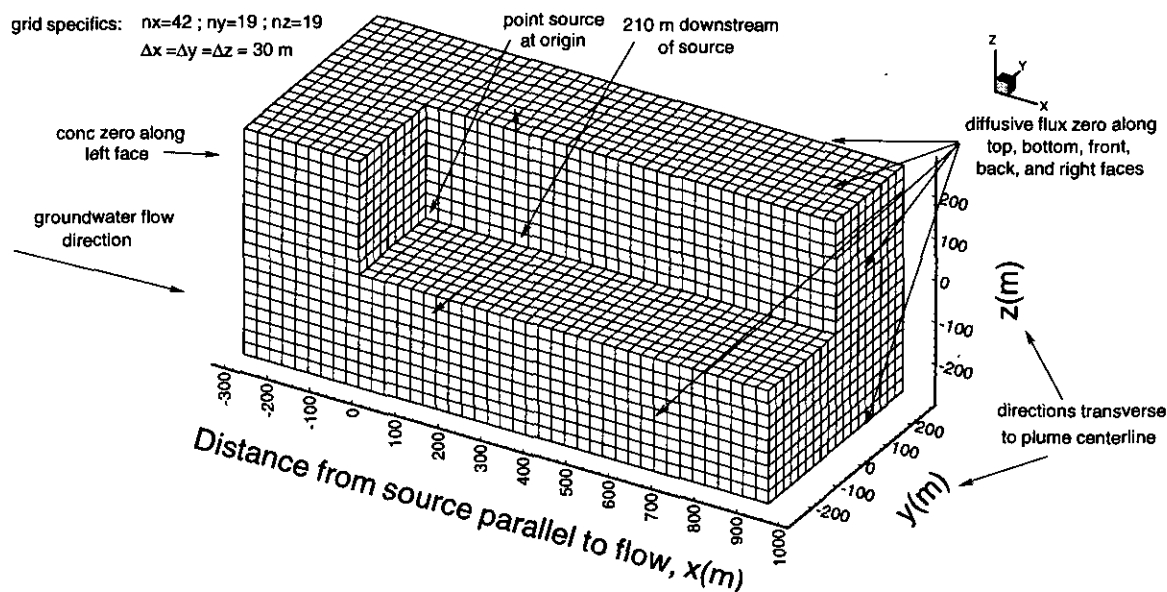


Fig. 4.2.3.1. FACT parallel mesh and boundary conditions for 3D transport. A 3D perspective was chosen where a section of the domain has been cut out to highlight the plume centerline.

Figure 4.2.3.1 illustrates the finite element grid chosen and the boundary conditions applied along the six outer domain surfaces. At the channel inlet boundary (left), the concentration of solute in the incoming water is set to 0.0 kg/m^3 . Due to the finite overall length of our mesh, at the outflow boundary (right) the dispersive flux is set to zero, while the advective flux is calculated as part of the solution. In addition, the dispersive flux is set to zero at the transverse faces (front, back, top, and bottom). By default, in the standard finite element formulation zero dispersive fluxes are automatically applied to all outer domain surfaces unless otherwise specified. The aquifer is assumed to be completely saturated. A cut-away of the 3-D mesh was performed in Fig. 4.2.3.1 to help illustrate the actual location of the point source. The point source was placed at the mid-point of a x plane where the x plane chosen was located 300 m upstream of the inflow boundary. Also shown in Fig. 4.2.3.1 are two arrows 120 m downstream of the source indicating the location (along each line) where results were tabulated in Table 4.2.3.2.

For this problem only the base case simulation was performed. For this simulation a transient calculation was performed for a 1400 day duration and the results from FACT at this end time are compared to the analytical solution given by Eq. (4.2.3.3).

The results from the simulations (both numerical and analytical) are shown in Figs. 4.2.3.2 through 4.2.3.4. These results are also presented in tabular form for comparison

FACT CODE MANUAL

in Table 4.2.3.2. The analytical results were computed from the computer code AT123D (Yeh, 1981). The FACT numerical results are labeled "FACT Parallel grid" and have additional nomenclature to represent which transverse direction is being considered (e.g., "(y axis)").

The results of the simulation at 1400 days duration are presented in Fig. 4.2.3.2 in the form of a contour plot. A section of the domain has been cut out to highlight the plume centerline and its basic axisymmetric behavior.

These results are also compared to the analytical solution in Figs. 4.2.3.3 and 4.2.3.4. The computed concentration profiles in the direction of groundwater flow along a line through the source and plume centerline are shown in Fig. 4.2.3.3. Figure 4.2.3.4 shows computed concentration profiles perpendicular to the groundwater flow direction and plume centerline (i.e., y-axis and z-axis) 120 m downstream of the source. The results away from the source show good comparison between the analytical solution and the numerical results for both transverse directions. These results indicate that the concentration plume predicted by FACT is axisymmetric as well.

Based upon these calculations, the following observation came be given when performing solute transport with FACT:

- FACT accurately handles axisymmetric problems employing its 3-D Cartesian coordinate system. Run times are longer, but not excessive.

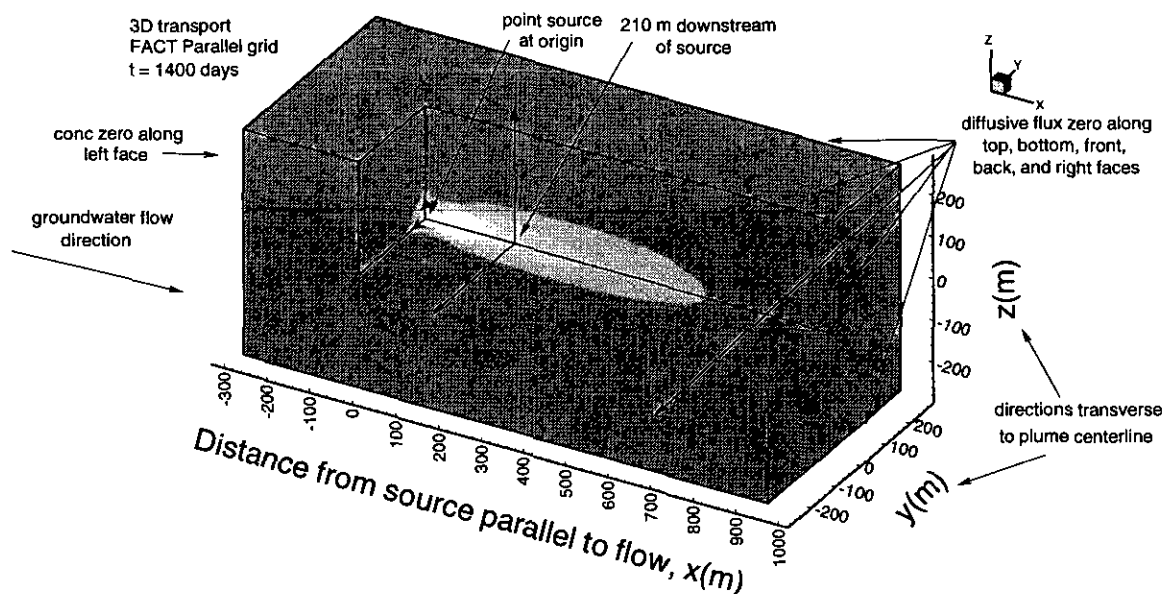


Fig. 4.2.3.2. FACT concentration profile for 3D transport of the base case on a parallel grid where a section of the domain has been cut out to highlight the plume centerline and its axisymmetric behavior.

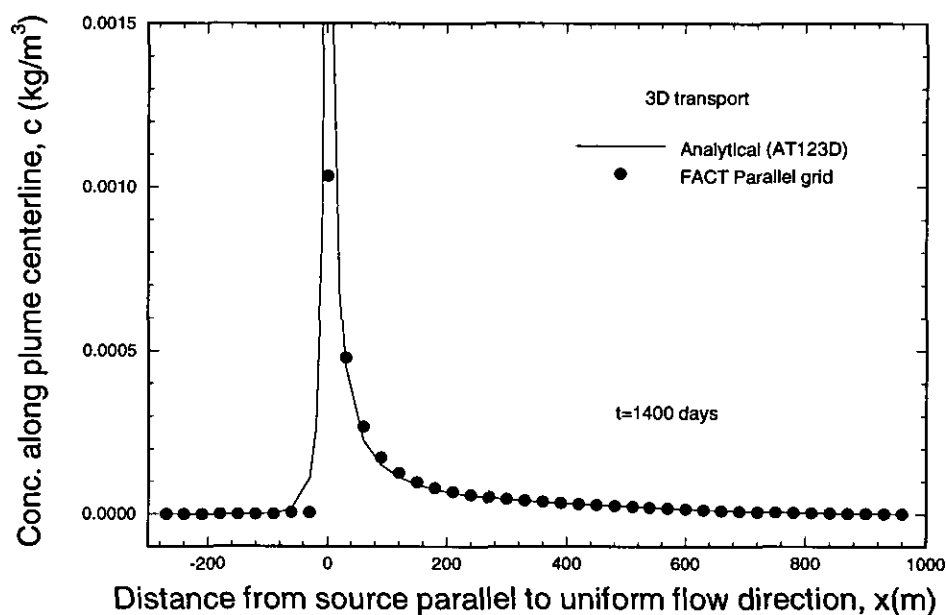


Fig. 4.2.3.3. Concentration profile for 3D transport of the base case along plume centerline.

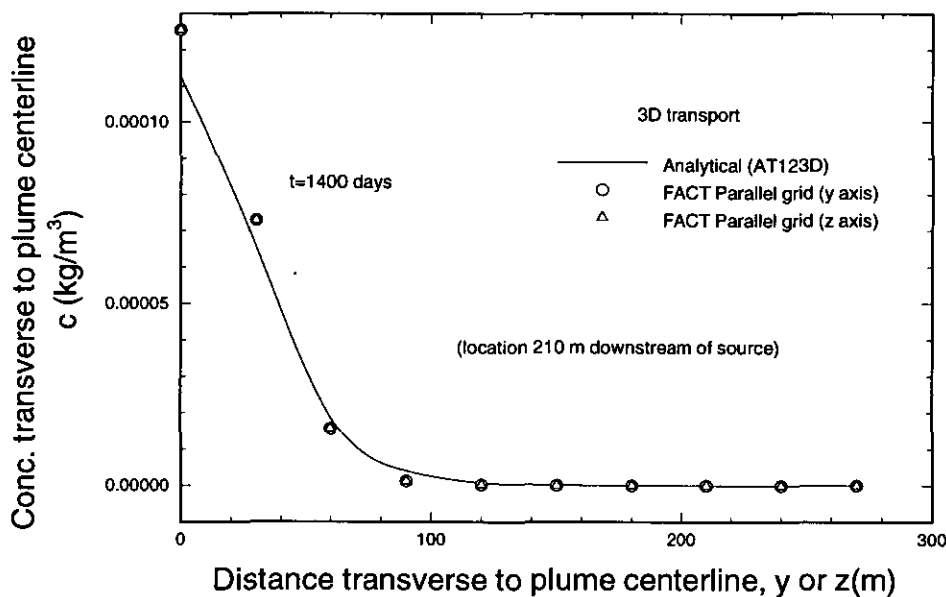


Fig. 4.2.3.4. Concentration profiles for 3D transport of the base case transverse to plume centerline (in both y and z directions) located 210 m downstream of the source.

Table 4.2.3.2

Comparison of analytical and numerical concentration (kg/m³) results for the transient 3D transport problem (base case, t=1400 days)

Distance downstream x (m) and transverse y or z(m)	Analytical (AT123D) (along plume centerline)	Numerical (FACT) (parallel grid) (along plume centerline)	Analytical (AT123D) (120 m downstream, transverse)	Numerical (FACT) (120 m downstream, transverse y)	Numerical (FACT) (120 m downstream, transverse z)
-270.0	0.1559E-09	0.1033E-08	-	-	-
-240.0	0.7192E-09	0.1232E-08	-	-	-
-210.0	0.3367E-08	0.2694E-08	-	-	-
-180.0	0.1608E-07	0.1060E-07	-	-	-
-150.0	0.7895E-07	0.5253E-07	-	-	-
-120.0	0.4037E-06	0.2827E-06	-	-	-
-90.0	0.2202E-05	0.1633E-06	-	-	-
-60.0	0.1351E-04	0.1057E-04	-	-	-
-30.0	0.1105E-03	0.9005E-04	-	-	-
0.0	infinity	0.2345E-02	0.1129E-03	0.1151E-03	0.1151E-03
30.0	0.4518E-03	0.5021E-03	0.6570E-04	0.6739E-04	0.6739E-04
60.0	0.2259E-03	0.2379E-03	0.1865E-04	0.1773E-04	0.1773E-04
90.0	0.1506E-03	0.1549E-03	0.4030E-05	0.3477E-05	0.3477E-05
120.0	0.1129E-03	0.1151E-03	0.7937E-06	0.6339E-06	0.6339E-06
150.0	0.9032E-04	0.9161E-04	0.1504E-06	0.1120E-07	0.1120E-07
180.0	0.7523E-04	0.7608E-04	0.2771E-07	0.1918E-07	0.1918E-07
210.0	0.6442E-04	0.6501E-04	0.4926E-08	0.3120E-08	0.3120E-08
240.0	0.5627E-04	0.5671E-04	0.8318E-09	0.4741E-09	0.4741E-09
270.0	0.4988E-04	0.5021E-04	0.1310E-09	0.1240E-09	0.1240E-09
300.0	0.4468E-04	0.4494E-04			
330.0	0.4033E-04	0.4054E-04			
360.0	0.3658E-04	0.3675E-04			
390.0	0.3325E-04	0.3339E-04			
420.0	0.3021E-04	0.3033E-04			
450.0	0.2738E-04	0.2747E-04			
480.0	0.2469E-04	0.2476E-04			
510.0	0.2209E-04	0.2215E-04			
540.0	0.1958E-04	0.1963E-04			
570.0	0.1714E-04	0.1718E-04			
600.0	0.1480E-04	0.1483E-04			
630.0	0.1258E-04	0.1260E-04			
660.0	0.1050E-04	0.1050E-04			
690.0	0.8596E-05	0.8607E-05			
720.0	0.6893E-05	0.6900E-05			
750.0	0.5407E-05	0.5411E-05			
780.0	0.4144E-05	0.4146E-05			
810.0	0.3101E-05	0.3100E-05			
840.0	0.2262E-05	0.2260E-05			
870.0	0.1608E-05	0.1606E-05			
900.0	0.1113E-05	0.1113E-05			
930.0	0.7501E-06	0.7647E-06			
960.0	0.4915E-06	0.6092E-06			

4.3 Dual-Domain (Mobile/Immobile) Transport Problems

In the following two sections we present two one-dimensional solute transport problems that test the implementation of the dual-domain mass transfer model in FACT. The first set of problems is a direct comparison to the five analytical cases computed by van Genuchten and Wierenga (1976). The second problem set is a code-to-code comparison of FACT and the chromatography program, VERSE-LC (Whitley et al., 1998).

4.3.1 One-Dimensional Saturated Solute Transport in a Uniform Flow Field with First-Order Mobile/Immobile Mass Transfer (van Genuchten and Wierenga analytical cases)

This problem deals with one-dimensional advection-dispersion of a non-conservative solute species from a pulse input of solute through a semi-infinite column with first-order mobile/immobile mass transfer and linear adsorption. The implementation of the first-order mobile/immobile mass transfer model into the FACT finite element framework is tested by comparison to analytical solutions derived by van Genuchten and Wierenga (1976).

Analytic solution: For linear adsorption, the governing transport equations for the mobile and immobile water phases, Eqs. (15) and (16) of van Genuchten and Wierenga, are

$$(\theta_m + f\rho K)\frac{\partial C_m}{\partial t} + [\theta_{im} + (1-f)\rho K]\frac{\partial C_{im}}{\partial t} = \theta_m D \frac{\partial^2 C_m}{\partial z^2} - v_m \theta_m \frac{\partial C_m}{\partial z} \quad (4.3.1.1)$$

$$[\theta_{im} + (1-f)\rho K]\frac{\partial C_{im}}{\partial t} = \alpha(C_m - C_{im}) \quad (4.3.1.2)$$

where

C_m solute concentration in the mobile phase, ML^{-3}

C_{im} solute concentration in the immobile phase, ML^{-3}

D dispersion coefficient, L^2T^{-1}

f fraction of the solid surfaces in contact with the mobile phase, dimensionless

K adsorption constant, L^3M^{-1}

t time, T

z distance, L

α mass transfer coefficient, T^{-1}

v_m soil moisture flux in the mobile phase, LT^{-1}

θ water content, $\theta = \theta_m + \theta_{im}$, L^3L^{-3}

θ_m mobile water content, L^3L^{-3}

θ_{im} immobile water content, L^3L^{-3}

FACT CODE MANUAL

ρ bulk density, ML^{-3}

For a semi-infinite column and a pulse input of solute, the boundary and initial conditions are

$$\lim_{z \rightarrow 0^+} \left(v_m C_m - D \frac{\partial C_m}{\partial z} \right) = \begin{cases} v_m C_0 & 0 \leq t < t_1 \\ 0 & t \geq t_1 \end{cases} \quad (4.3.1.3)$$

$$\lim_{z \rightarrow \infty} [C_m(z, t)] = 0 \quad (4.3.1.4)$$

$$C_m(z, 0) = C_{im}(z, 0) = 0. \quad (4.3.1.5)$$

Eqs. (4.3.1.1) and (4.3.1.2) are cast in non-dimensional form by introducing the following dimensionless variables

$$T = v_0 t / L = v_m t \phi / L \quad (4.3.1.6)$$

$$x = z / L \quad (4.3.1.7)$$

$$\phi = \theta_m / \theta = \theta_m / (\theta_m + \theta_{im}) \quad (4.3.1.8)$$

$$c_m = C_m / C_0, \quad c_{im} = C_{im} / C_0 \quad (4.3.1.9)$$

$$P = v_m L / D \quad (4.3.1.10)$$

$$\bar{\alpha} = \alpha L / q \quad (4.3.1.11)$$

as

$$\phi R_m \frac{\partial c_m}{\partial T} + (1 - \phi) R_{im} \frac{\partial c_{im}}{\partial T} = \frac{1}{P} \frac{\partial^2 c_m}{\partial x^2} - \frac{\partial c_m}{\partial x} \quad (4.3.1.12)$$

$$(1 - \phi) R_{im} \frac{\partial c_{im}}{\partial T} = \bar{\alpha} (c_m - c_{im}) \quad (4.3.1.13)$$

where the mobile and immobile phase retardation factors are

$$R_m = 1 + \frac{f \rho K}{\theta_m} \quad (4.3.1.14)$$

$$R_{im} = 1 + \frac{(1 - f) \rho K}{\theta_{im}} \quad (4.3.1.15)$$

The average retardation factor R for linear adsorption is defined as

$$R = 1 + \frac{\rho K}{\theta} \quad (4.3.1.16)$$

Define further the dimensionless parameter, β , as

$$\beta = \frac{\theta_m + \rho f K}{\theta + \rho K} = \phi \frac{R_m}{R} \quad (4.3.1.17)$$

Substituting Eqs. (4.3.1.16) and (4.3.1.17) into Eqs. (4.3.1.12) and (4.3.1.13) yields

$$\beta R \frac{\partial c_m}{\partial T} + (1-\beta)R \frac{\partial c_{im}}{\partial T} = \frac{1}{P} \frac{\partial^2 c_m}{\partial x^2} - \frac{\partial c_m}{\partial x} \quad (4.3.1.18)$$

$$(1-\beta)R \frac{\partial c_{im}}{\partial T} = \bar{\alpha}(c_m - c_{im}) \quad (4.3.1.19)$$

The boundary and initial conditions in dimensionless form are

$$\lim_{x \rightarrow 0^+} \left(c_m - \frac{1}{P} \frac{\partial c_m}{\partial x} \right) = \begin{cases} 1 & 0 \leq T < T_1 \\ 0 & T \geq T_1 \end{cases} \quad (4.3.1.20)$$

$$\lim_{x \rightarrow \infty} [c_m(x, T)] = 0 \quad (4.3.1.21)$$

$$c_m(x, 0) = c_{im}(x, 0) = 0 \quad (4.3.1.22)$$

van Genuchten has shown that the solutions of Eqs. (4.3.1.18) and (4.3.1.19) become

$$c_m(x, T) = \begin{cases} c_1(x, T) & 0 \leq T < T_1 \\ c_1(x, T) - c_1(x, T - T_1) & T \geq T_1 \end{cases} \quad (4.3.1.23)$$

$$c_{im}(x, T) = \begin{cases} c_2(x, T) & 0 \leq T < T_1 \\ c_2(x, T) - c_2(x, T - T_1) & T \geq T_1 \end{cases} \quad (4.3.1.24)$$

where

$$c_1(x, T) = G(x, T) \exp(-\bar{\alpha}T/\beta R) + \frac{\bar{\alpha}}{R} \int_0^T G(x, \tau) H_1(T, \tau) d\tau \quad (4.3.1.25)$$

$$c_2(x, T) = \bar{\alpha} \int_0^T G(x, \tau) H_2(T, \tau) d\tau \quad (4.3.1.26)$$

$$\begin{aligned} G(x, T) = & \frac{1}{2} \left[\operatorname{erfc} \left\{ (P/4\beta R T)^{1/2} (\beta R x - T) \right\} \right. \\ & - \frac{1}{2} (1 + P x + P T / \beta R) \exp(P x) \operatorname{erfc} \left\{ (P/4\beta R T)^{1/2} (\beta R x + T) \right\} \\ & \left. + (P T / \pi \beta R)^{1/2} \exp \left\{ -P (\beta R x - T)^2 / 4\beta R T \right\} \right] \end{aligned} \quad (4.3.1.27)$$

$$H_1(T, \tau) = \exp(-u - v) \left\{ I_0(\xi) / \beta + I_1(\xi) (u/v)^{1/2} / (1 - \beta) \right\} \quad (4.3.1.28)$$

$$H_2(T, \tau) = \exp(-u - v) \left\{ I_0(\xi) / (1 - \beta) + I_1(\xi) (v/u)^{1/2} / \beta \right\} \quad (4.3.1.29)$$

$$u = \bar{\alpha}\tau/\beta R \quad v = \bar{\alpha}(T - \tau)/(1 - \beta)R \quad \xi = 2(uv)^{1/2} \quad (4.3.1.30)$$

Equation (4.3.1.23) was solved numerically using the IMSL™ libraries to evaluate the various functions (e.g. erfc) and to perform numerical quadrature of the time-dependent integrals. The van Genuchten paper has several errors including the expression for Eq. (4.3.1.27). The solution to Eqs. (4.3.1.18) and (4.3.1.19) have not been independently confirmed.

The parameter settings for the five van Genuchten analytical cases, Figs. 2 to 6 of van Genuchten and Wierenga (1976), are given in Tables 4.3.1.1 to 4.3.1.5.

Table 4.3.1.1

Parameters for van Genuchten ϕ Analytical Case

Physical parameters	Value
Volumetric flow velocity, q	10 cm/day
Water content, θ	0.4
Bulk density, ρ	1.30 g/cm ³
Dispersion coefficient, D	30 cm ² /day
Fraction of mobile water, ϕ	0.35, 0.50, 0.65, 0.85, 0.999
Fraction of adsorption sites in contact with mobile water, f	0.40
Adsorption constant, K	0.5 cm ³ /g
Mass transfer coefficient, α	0.15 day ⁻¹
Dimensionless pulse period, T_1	3
Soil column length, L	30 cm
Key dimensionless parameters	
Mobile water content, θ_m	0.14, 0.2, 0.26, 0.34, 0.3996
Average retardation factor, R	2.625
Dimensionless parameter, β	0.381, 0.438, 0.495, 0.571, 0.628
Dimensionless parameter, $\bar{\alpha}$	0.45
Dimensionless parameter, P	71.4, 50.0, 38.5, 29.4, 25.0

Table 4.3.1.2

Parameters for van Genuchten f Analytical Case

Physical parameters	Value
Volumetric flow velocity, q	10 cm/day
Water content, θ	0.4
Bulk density, ρ	1.30 g/cm ³
Dispersion coefficient, D	30 cm ² /day
Fraction of mobile water, ϕ	0.65
Fraction of adsorption sites in contact with mobile water, f	0.25, 0.40, 0.55, 0.70
Adsorption constant, K	0.5 cm ³ /g
Mass transfer coefficient, α	0.15 day ⁻¹
Dimensionless pulse period, T_1	3
Soil column length, L	30 cm
Key dimensionless parameters	
Mobile water content, θ_m	0.26
Average retardation factor, R	2.625
Dimensionless parameter, β	0.402, 0.495, 0.588, 0.681
Dimensionless parameter, $\bar{\alpha}$	0.45
Dimensionless parameter, P	38.5

Table 4.3.1.3Parameters for van Genuchten α Analytical Case

Physical parameters	Value
Volumetric flow velocity, q	10 cm/day
Water content, θ	0.4
Bulk density, ρ	1.30 g/cm ³
Dispersion coefficient, D	30 cm ² /day
Fraction of mobile water, ϕ	0.65
Fraction of adsorption sites in contact with mobile water, f	0.40
Adsorption constant, K	0.5 cm ³ /g
Mass transfer coefficient, α	0.0, 0.05, 0.15, 0.50, 2.0, ∞ day ⁻¹
Dimensionless pulse period, T_1	3
Soil column length, L	30 cm
Key dimensionless parameters	
Mobile water content, θ_m	0.26
Average retardation factor, R	2.625
Dimensionless parameter, β	0.495
Dimensionless parameter, $\bar{\alpha}$	0.0, 0.15, 0.45, 1.5, 6.0, ∞
Dimensionless parameter, P	38.5

Table 4.3.1.4

Parameters for van Genuchten D Analytical Case

Physical parameters	Value
Volumetric flow velocity, q	10 cm/day
Water content, θ	0.4
Bulk density, ρ	1.30 g/cm ³
Dispersion coefficient, D	0, 5, 30, 50, 100 cm ² /day
Fraction of mobile water, ϕ	0.65
Fraction of adsorption sites in contact with mobile water, f	0.40
Adsorption constant, K	0.5 cm ³ /g
Mass transfer coefficient, α	0.15 day ⁻¹
Dimensionless pulse period, T_1	3
Soil column length, L	30 cm
Key dimensionless parameters	
Mobile water content, θ_m	0.26
Average retardation factor, R	2.625
Dimensionless parameter, β	0.495
Dimensionless parameter, $\bar{\alpha}$	0.45
Dimensionless parameter, P	∞ , 230.8, 38.5, 23.1, 11.5

Table 4.3.1.5

Parameters for van Genuchten K Analytical Case

Physical parameters	Value
Volumetric flow velocity, q	10 cm/day
Water content, θ	0.4
Bulk density, ρ	1.30 g/cm ³
Dispersion coefficient, D	30 cm ² /day
Fraction of mobile water, ϕ	0.65
Fraction of adsorption sites in contact with mobile water, f	0.40
Adsorption constant, K	0.0, 0.25, 0.50, 0.75, 1.0, 2.0 cm ³ /g
Mass transfer coefficient, α	0.15 day ⁻¹
Dimensionless pulse period, T_1	3
Soil column length, L	30 cm
Key dimensionless parameters	
Mobile water content, θ_m	0.26
Average retardation factor, R	1.0, 1.813, 2.625, 3.438, 4.25, 7.5
Dimensionless parameter, β	0.65, 0.538, 0.495, 0.473, 0.459, 0.433
Dimensionless parameter, $\bar{\alpha}$	0.45
Dimensionless parameter, P	38.5

FACT numerical simulation and comparison: Values of the basic physical parameters used in the verification simulations are presented in Table 4.3.1.6. The grid chosen consists of 101 rectangular brick elements uniformly sized (0.3 cm in length) and stacked along the x-axis. At the column inlet boundary (left face) a third-type boundary condition is applied which represents a surface integral of qc^* ($q = 10$ cm/day, $c^* = 1$ μ g/day) equally distributed among the four nodes at $x = 0$. The column is leached with 3 pore volumes (3.6 secs) of solute at a constant flux (q) of 10 cm/day. Due to the finite overall length of our mesh, at the outflow boundary (right face) the dispersive flux is set to zero, while the advective flux is calculated as part of the solution. Since this is a 1-D problem, solute concentrations do not exist in the transverse directions (y and z directions). Therefore, the dispersive fluxes along these four faces (top, bottom, front and back) are set to zero. The column is modeled as being fully saturated at a water content of 0.40 (total porosity of 0.40). For each simulation a transient calculation was performed for an 8 pore volume duration (9.6 secs) utilizing 9600 time steps of 0.01 days. The mesh spacing and time step size were chosen to keep the cell Peclet and Courant numbers less than 1 (if possible). Five different parameters (θ_m/θ , f , α , D and k_d) were varied to compute column effluent (breakthrough) curves for each FACT simulation and then compared to the analytical cases in (van Genuchten and Wierenga, 1976).

Figure 4.3.1.1 shows the influence of the fraction of mobile water (θ_m/θ) on the shape of the breakthrough concentration curve. Values of the different parameters used in the simulations are given in Table 4.3.1.7. The FACT results are in good agreement with analytical results. When the amount of immobile liquid increases (i.e. θ_m/θ decreases), advective transfer is increasingly confined to a smaller flow area of the column, resulting in a higher solute velocity in the mobile liquid and hence leading to an earlier breakthrough of the solute in the effluent. Also, the slope of the breakthrough curve at higher concentrations is influenced by a change in θ_m/θ . However, as long as some immobile liquid is present ($\theta_m/\theta = 0.999$) extensive tailing will occur, since approximately 60% ($f = 0.40$) of the solute has to diffuse to those sorption sites which are in equilibrium with the immobile liquid.

Approximately the same set of curves as shown in Fig. 4.3.1.1 is obtained when the parameter f is allowed to vary (Fig. 4.3.1.2). This parameter describes the amount of adsorption taking place inside the region of the soil in contact with the mobile liquid, as a fraction of total adsorption. Values of the different parameters used in the simulations are given in Table 4.3.1.8. The FACT results are in good agreement with analytical results. When f increases, i.e. when relatively more adsorption occurs in the region of soil in contact with mobile liquid, the solute will appear later in the effluent. When $f = 1$, adsorption takes place only in the region of soil in contact with the mobile liquid. The solute can only be stored in the immobile liquid. Both f and θ_m/θ have the same effect on the shape of the breakthrough curves. They both determine the fraction of the retardation occurring the region of soil in contact with the mobile liquid.

Figure 4.3.1.3 shows the influence of the mass transfer coefficient α . Values of the different parameters used in the simulations are given in Table 4.3.1.9. The FACT results are in good agreement with analytical results. When $\alpha = 0$, there is no diffusion of solute into the immobile liquid. The breakthrough curve acquires a more or less symmetrical shape. When α is small, a slow exchange of solute between mobile and immobile liquid takes place, causing a significant decrease in peak concentration and considerable tailing. With increasing values of the mass transfer coefficient, the rate of exchange between the mobile and immobile liquid increases, eventually leading to an equilibrium state where the concentrations in both mobile and immobile liquid are identical.

The influence of the dispersion coefficient D on the breakthrough curves is shown in Fig. 4.3.1.4. Values of the difference parameters used in the simulations are given in Table 4.3.1.10. The FACT results are in good agreement with the analytical results except at low values of dispersion coefficient (i.e. high Peclet numbers). The influence of D on the shape of the calculated breakthrough curves is not very large. There are discontinuities in the breakthrough curve at both 1.3 and 4.3 pore volumes for the limiting case when D becomes zero (i.e. infinite Peclet number). We can conclude from Fig. 4.3.1.4 that an estimated dispersion coefficient may be adequate for predicting breakthrough curves.

Figure 4.3.1.5 finally shows the influence of the distribution coefficient K on the shape and position of the breakthrough curves. Values of the different parameters used in the

FACT CODE MANUAL

simulations are given in Table 4.3.1.11. The FACT results are in good agreement with analytical results. The curve $K = 0$ represents the solution for a nonsorbing medium with no retardation. When K increases, the solute appears later in the effluent, while the peak concentration decreases somewhat. Also the tailing becomes more pronounced with increasing values of K . This is to be expected since more and more solute is allowed to diffuse into and be adsorbed by the region of soil in contact with the immobile liquid. After passage of the solute pulse the solute slowly diffuses back into the mobile liquid, resulting in extensive tailing.

Table 4.3.1.6

Base Parameters in FACT simulation of van Genuchten Analytical Cases

Physical parameters	Value
Darcy velocity, q	10 cm/day
Water saturation, S_w	1.0
Particle mass density, ρ_s	2.166666 g/cm ³
Total porosity, ϕ	0.40
Longitudinal vertical, transverse horizontal and transverse vertical dispersivities, $\alpha_{LV}, \alpha_{TH}, \alpha_{TV}$	0.0 cm
Apparent molecular dispersion coefficient, $\phi S_w \tau D^*$	0.0 cm ² /d
Radioactive decay coefficient, λ_r	0.0 day ⁻¹
1st-order reaction rate (mobile), λ_m	0.0 day ⁻¹
1st-order reaction rate (immobile), λ_{im}	0.0 day ⁻¹
Boundary solute concentration, C_0	1.0 μ g/cm ³
Water volumetric flowrate (per point source), q	0.225 cm ³ /day
Contaminant mass flowrate (per point source), qc^*	0.225 μ g/day
Pulse period, t_1	3.6 days
Grid specifics	
Element lengths, $\delta x = \delta y = \delta z$	0.3 cm
Number nodes in x-direction	101
Number nodes in y-direction	2
Number nodes in z-direction	2
Time steps	
Time duration	9.6 days
number time-steps	960
time-step size, δt	0.01 day
Key computed parameters	
Water content, θ	0.40
Bulk soil density, ρ_b	1.30 g/cm ³

Table 4.3.1.7Parameter Settings in FACT simulation of van Genuchten ϕ Analytical Case

Physical parameters	Value
Distribution coefficient, k_d	0.5 cm ³ /μg
Dispersion coefficient, D	30 cm ² /day
Longitudinal horizontal dispersivity, α_{LH}	0.42, 0.6, 0.78 1.02, 1.1988 cm
Fraction of mobile water, θ_m/θ	0.35, 0.50, 0.65, 0.85, 0.999
Fraction of adsorption sites in contact with mobile water, f	0.40
Mass transfer coefficient, α	0.15 day ⁻¹
Key computed parameters	
Mobile water content, θ_m	0.14, 0.2, 0.26, 0.34, 0.3996
Immobile water content, θ_{im}	0.26, 0.2, 0.14, 0.06, 0.0004
Mobile retardation factor, R_m	2.86, 2.30, 2.00, 1.76, 1.65
Immobile retardation factor, R_{im}	2.50, 2.95, 3.79, 7.50, 976
Phasic velocity, u_x	71.4, 50.0, 38.5, 29.4, 25.0 cm/day
Retarded phasic velocity, u'_x	25.0, 21.7, 19.2, 16.7, 15.2 cm/day
Retarded dispersion coefficient, D'_{xx}	10.5, 13.0, 15.0, 17.0, 18.2 cm ² /day
Cell Peclet number, Pe_x	0.71, 0.50, 0.38, 0.29, 0.25
Cell Courant number, Co_x	0.83, 0.72, 0.64, 0.56, 0.51

Table 4.3.1.8

Parameter Settings in FACT simulation of van Genuchten f Analytical Case

Physical parameters	Value
Distribution coefficient, k_d	0.5 cm ³ /μg
Dispersion coefficient, D	30 cm ² /day
Longitudinal horizontal dispersivity, α_{LH}	0.78 cm
Fraction of mobile water, θ_m/θ	0.65
Fraction of adsorption sites in contact with mobile water, f	0.25, 0.40, 0.55, 0.70
Mass transfer coefficient, α	0.15 day ⁻¹
Key computed parameters	
Mobile water content, θ_m	0.26
Immobile water content, θ_{im}	0.14
Mobile retardation factor, R_m	1.63, 2.00, 2.38, 2.75
Immobile retardation factor, R_{im}	4.48, 3.79, 3.09, 2.39
Phasic velocity, u_x	38.5 cm/day
Retarded phasic velocity, u'_x	23.7, 19.2, 16.2, 14.0 cm/day
Retarded dispersion coefficient, D'_{xx}	18.5, 15.0, 12.6, 10.9 cm ² /day
Cell Peclet number, Pe_x	0.38
Cell Courant number, Co_x	0.79, 0.64, 0.54, 0.47

Table 4.3.1.9Parameter Settings in FACT simulation of van Genuchten α Analytical Case

Physical parameters	Value
Distribution coefficient, k_d	0.5 cm ³ /μg
Dispersion coefficient, D	30 cm ² /day
Longitudinal horizontal dispersivity, α_{LH}	0.78 cm
Fraction of mobile water, θ_m/θ	0.65
Fraction of adsorption sites in contact with mobile water, f	0.40
Mass transfer coefficient, α	0.0, 0.05, 0.15 0.50, 2.0, ∞ day ⁻¹
Key computed parameters	
Mobile water content, θ_m	0.26
Immobile water content, θ_{im}	0.14
Mobile retardation factor, R_m	2.0
Immobile retardation factor, R_{im}	3.79
Phasic velocity, u_x	38.5 cm/day
Retarded phasic velocity, u'_x	19.2 cm/day
Retarded dispersion coefficient, D'_{xx}	15.0 cm ² /day
Cell Peclet number, Pe_x	0.38
Cell Courant number, Co_x	0.64

Table 4.3.1.10

Parameter Settings in FACT simulation of van Genuchten D Analytical Case

Physical parameters	Value
Distribution coefficient, k_d	0.5 cm ³ /μg
Dispersion coefficient, D	0, 5, 30, 50, 100 cm ² /day
Longitudinal horizontal dispersivity, α_{LH}	0.0, 0.13, 0.78, 1.3, 2.6 cm
Fraction of mobile water, θ_m/θ	0.65
Fraction of adsorption sites in contact with mobile water, f	0.40
Mass transfer coefficient, α	0.15 day ⁻¹
Key computed parameters	
Mobile water content, θ_m	0.26
Immobile water content, θ_{im}	0.14
Mobile retardation factor, R_m	2.0
Immobile retardation factor, R_{im}	3.79
Phasic velocity, u_x	38.5 cm/day
Retarded phasic velocity, u'_x	19.2 cm/day
Retarded dispersion coefficient, D'_{xx}	0.0, 2.5, 15.0, 25, 50 cm ² /day
Cell Peclet number, Pe_x	∞, 2.31, 0.38, 0.23, 0.12
Cell Courant number, Co_x	0.64

Table 4.3.1.11

Parameter Settings in FACT simulation of van Genuchten K Analytical Case

Physical parameters	Value
Distribution coefficient, k_d	0.0, 0.25, 0.5, 0.75, 1.0, 2.0 cm ³ /μg
Dispersion coefficient, D	30 cm ² /day
Longitudinal horizontal dispersivity, α_{LH}	0.78 cm
Fraction of mobile water, θ_m/θ	0.65
Fraction of adsorption sites in contact with mobile water, f	0.40
Mass transfer coefficient, α	0.15 day ⁻¹
Key computed parameters	
Mobile water content, θ_m	0.26
Immobile water content, θ_{im}	0.14
Mobile retardation factor, R_m	1.0, 1.5, 2.0, 2.5, 3.0, 5.0
Immobile retardation factor, R_{im}	1.0, 2.39, 3.79, 5.18, 6.57, 12.14
Phasic velocity, u_x	38.5 cm/day
Retarded phasic velocity, u'_x	38.5, 25.6, 19.2, 15.4, 12.8, 7.7 cm/day
Retarded dispersion coefficient, D'_{xx}	30, 20, 15, 12, 10, 6 cm ² /day
Cell Peclet number, Pe_x	0.38
Cell Courant number, Co_x	1.28, 0.85, 0.64, 0.51, 0.43, 0.26

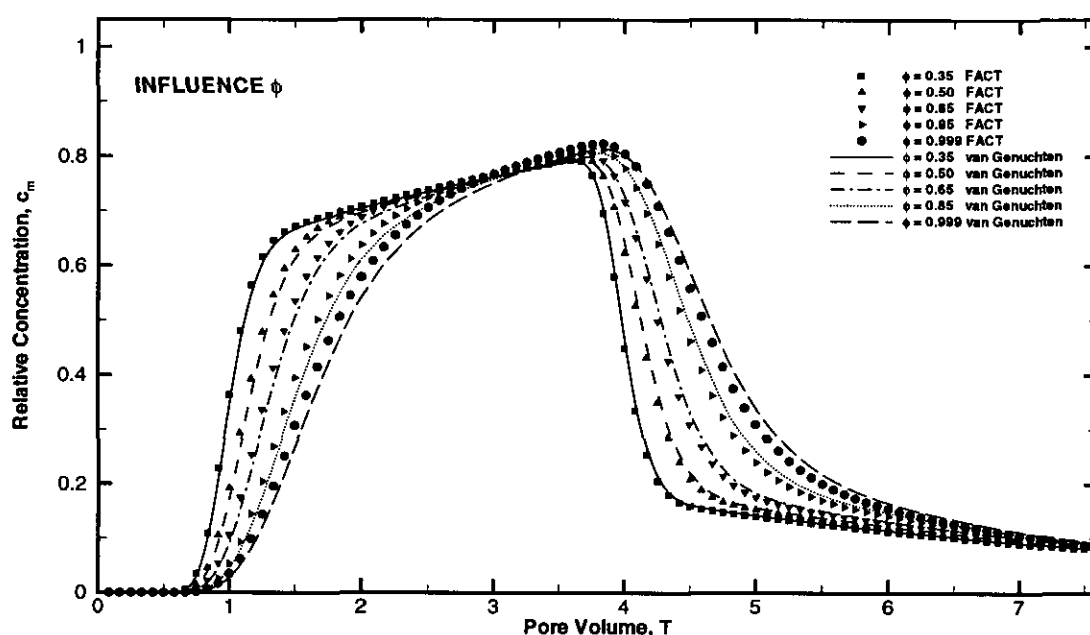


Fig. 4.3.1.1 Calculated breakthrough curves for a sorbing medium as influenced by the fraction of mobile liquid, ϕ

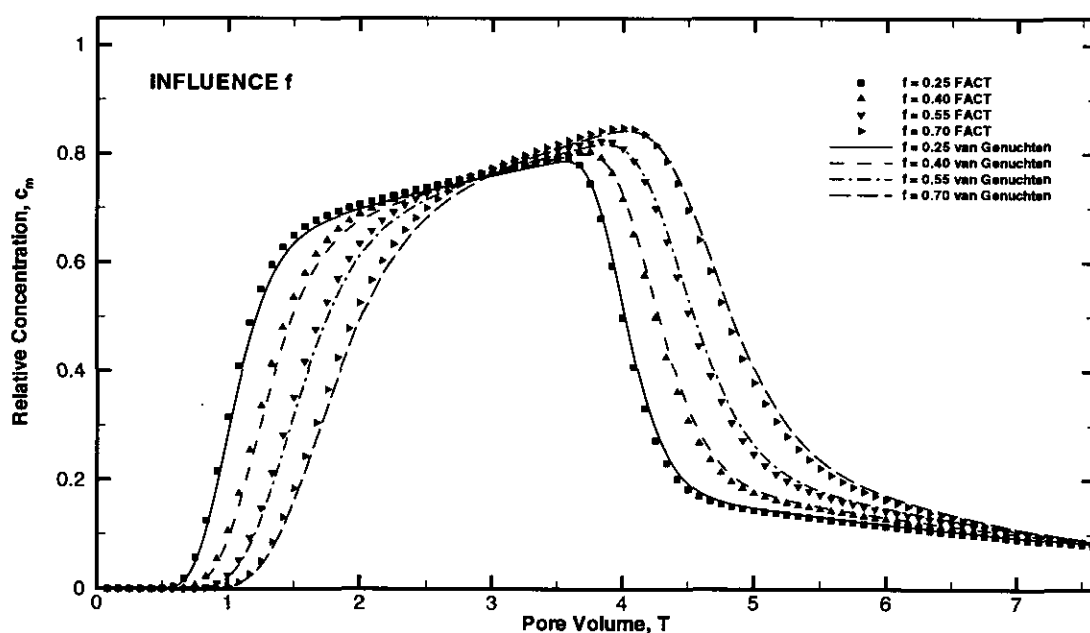


Fig. 4.3.1.2 Calculated breakthrough curves for a sorbing medium as influenced by the fraction of adsorption sites in the dynamic region, f

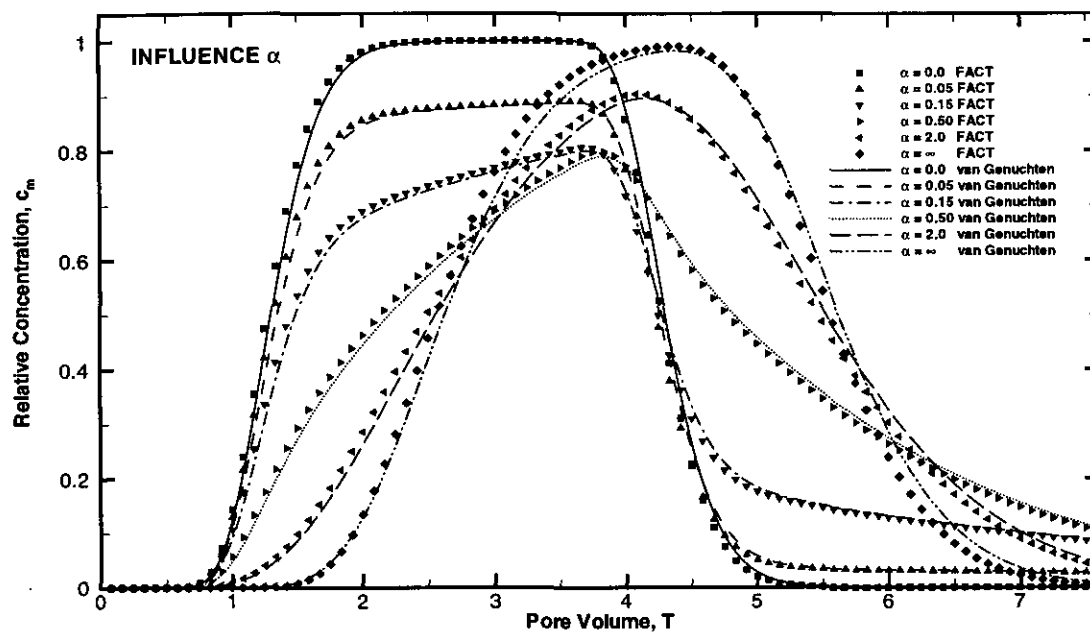


Fig. 4.3.1.3 Calculated breakthrough curves for a sorbing medium as influenced by the mass transfer coefficient, α

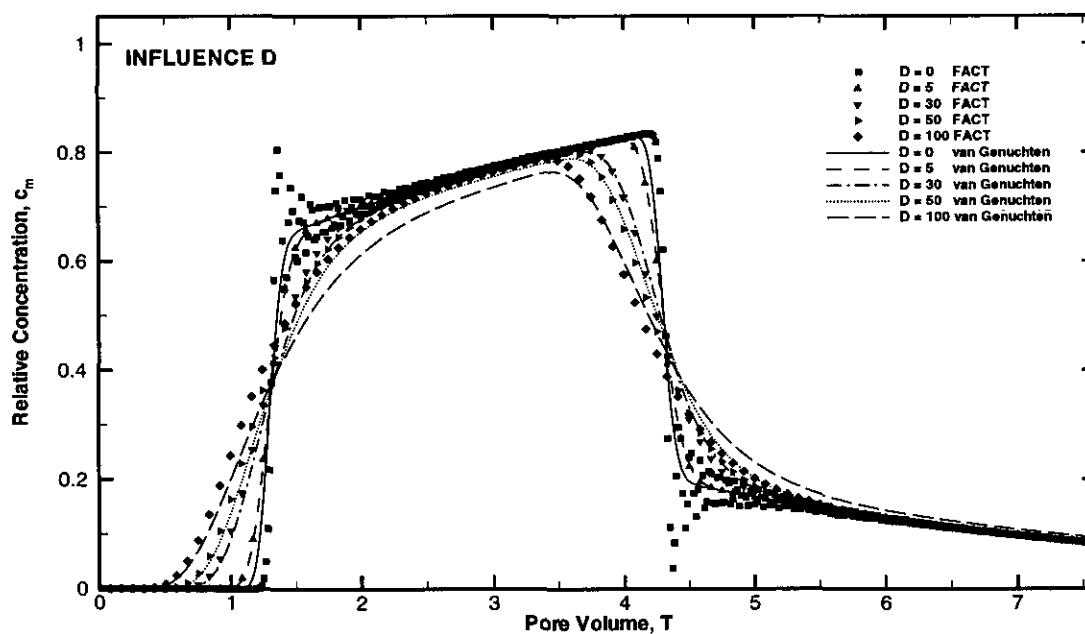


Fig. 4.3.1.4 Calculated breakthrough curves for a sorbing medium as influenced by the dispersion coefficient, D

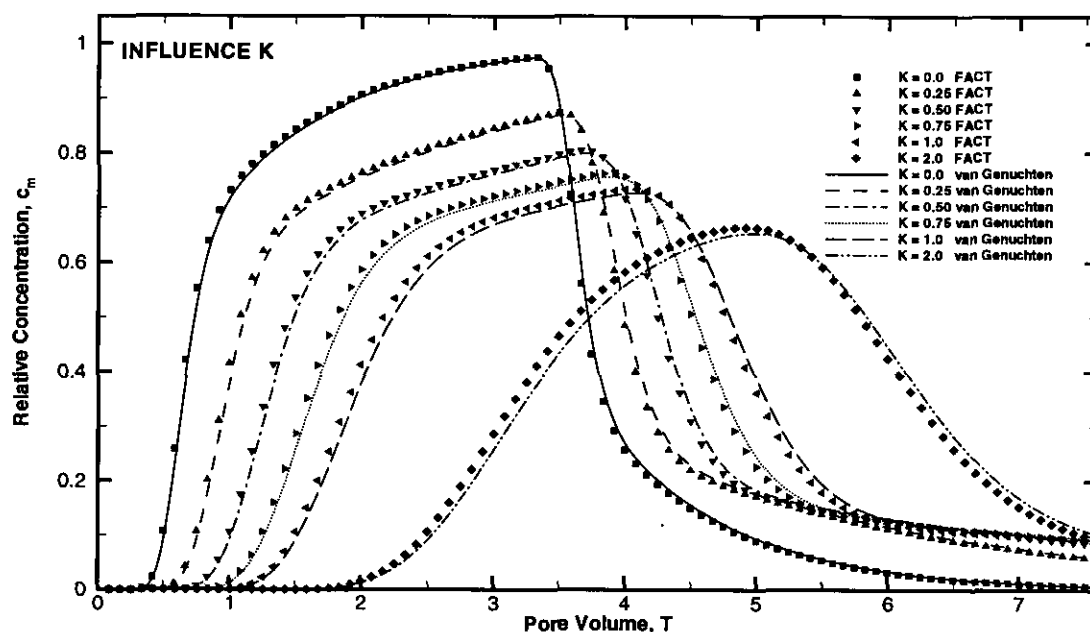


Fig. 4.3.1.5 Calculated breakthrough curves for a sorbing medium as influenced by the adsorption coefficient, K

4.3.2 One-Dimensional Saturated Solute Transport in a Uniform Flow Field with First-Order Mobile/Immobile Mass Transfer (VERSE-LC Comparison)

This problem deals with one-dimensional advection-dispersion of a non-conservative solute species with a unit step change in concentration at the inlet through a semi-infinite column with first-order mobile/immobile mass transfer and linear adsorption. The implementation of the first-order mobile/immobile mass transfer model into the FACT finite element framework is tested by making a code-to-code comparison to VERSE-LC.

VERSE-LC solution: The rate model equations in VERSE-LC (Whitley et al., 1998) consider mass transfer effects such as axial dispersion, convection, film mass transfer, intraparticle diffusion, and surface diffusion. Various equilibrium and non-equilibrium isotherms are available in the model. Non-equilibrium isotherms are used when adsorption/desorption rates are slower than mass transfer rates. Modes of operation include frontal, isocratic and gradient elution, and displacement chromatography. Processes with step functions (ideal or dispersed), flow rate changes, and forward and reverse flow can be simulated. In addition to fixed beds, fluidized beds and moving beds can also be simulated. VERSE-LC is not sorbent specific; any ion exchange, hydrophobic interaction, reverse phase, or affinity sorbent system can be treated.

The non-dimensional mobile phase equation with mass transfer between the flowing bed fluid and the non-porous particles is

$$\frac{\partial c_b}{\partial T} = \frac{1}{Pe_b} \frac{\partial^2 c_b}{\partial x^2} - \frac{\partial c_b}{\partial x} - N_f (c_b - c_p) \quad (4.3.2.1)$$

FACT CODE MANUAL

where the dimensionless axial dispersion is defined as

$$\frac{1}{Pe_b} = \frac{E_b}{u_0 L} \quad (4.3.2.2)$$

The dimensionless film mass transfer is

$$N_f = 3 \left[\frac{L}{R} \right] \frac{(1 - \epsilon_b) k_f}{\epsilon_b u_0} \quad (4.3.2.3)$$

The boundary and initial conditions are

$$\begin{aligned} x = 0, \quad \frac{\partial c_b}{\partial x} &= Pe_b (c_b - c_f(\theta)) \\ x = 1, \quad \frac{\partial c_b}{\partial x} &= 0 \\ \theta = 0, \quad c_b &= c_b(x, 0) \end{aligned} \quad (4.3.2.4)$$

The non-dimensional particle surface equation is

$$\left[\frac{3Lk_f}{Ru_0} \right] (c_b - c_p) = \left[\frac{\bar{C}_T}{C_e} \right] Y_\ell \quad (4.3.2.5)$$

where Y_ℓ represents the equilibrium adsorption term

$$Y_\ell = \frac{\partial \bar{c}_p}{\partial c_p} \frac{\partial c_p}{\partial \theta} \quad (4.3.2.6)$$

The initial condition is

$$\theta = 0, \quad \bar{c}_p = \bar{c}_p(0) \quad (4.3.2.7)$$

The multicomponent Langmuir isotherm is given as

$$\bar{C}_p = \frac{aC_p}{1 + bC_p} \quad (4.3.2.8)$$

Using the definitions for the scaled mobile and solid phase concentrations

$$\bar{c}_p = \frac{\bar{C}_p}{\bar{C}_T} \quad \text{and} \quad c_p = \frac{C_p}{C_e} \quad (4.3.2.9)$$

respectively, into Eq. (4.3.2.8) with $b = 0$ to yield a linear isotherm gives

$$\bar{c}_p = \left[\frac{C_e}{\bar{C}_T} \right] a c_p \quad (4.3.2.10)$$

Substituting the derivative of Eq. (4.3.2.10) into Eq. (4.3.2.6) and rearranging Eq. (4.3.2.5) gives

$$a \frac{\partial c_p}{\partial T} = \left[\frac{3Lk_f}{Ru_0} \right] (c_b - c_p) \quad (4.3.2.11)$$

Multiplying both sides of Eq. (4.3.2.11) by $(1 - \epsilon_b)/\epsilon_b$ yields

$$\frac{(1 - \epsilon_b)a}{\epsilon_b} \frac{\partial c_p}{\partial T} = N_f (c_b - c_p) \quad (4.3.2.12)$$

The Langmuir coefficient "a" in Eq. (4.3.2.8) for a linear isotherm is given as

$$a = a_{(\text{actual})} = \rho_s k_d \quad (4.3.2.13)$$

However, inside VERSE-LC the Langmuir coefficient "a" is divided by volume fractions depending on whether the porous or nonporous modeling option is chosen. VERSE-LC assumes as input that Eq. (4.3.2.13) is

$$a_{(\text{VERSE})} = \rho_b k_d = \begin{cases} \rho_s (1 - \epsilon_b) (1 - \epsilon_p) k_d & \text{porous model} \\ \rho_s (1 - \epsilon_b) k_d & \text{nonporous model} \end{cases} \quad (4.3.2.14)$$

For these set of simulations, we are using the nonporous model in VERSE-LC. Therefore, the Langmuir coefficient "a" based on Eqs. (4.3.2.13) and (4.3.2.14) is

$$a = a_{(\text{actual})} = \frac{a_{(\text{VERSE})}}{1 - \epsilon_b} \quad (4.3.2.15)$$

Substituting Eq. (4.3.2.15) into (4.3.2.12) yields the particle surface (immobile) equation

$$\frac{a_{(\text{VERSE})}}{\epsilon_b} \frac{\partial c_p}{\partial T} = N_f (c_b - c_p) \quad (4.3.2.16)$$

Equations (4.3.2.1) and (4.3.2.16) represent the mobile phase and particle surface (immobile) equations solved by VERSE-LC for these simulations.

The parameter settings used in the VERSE-LC simulations are given in Table 4.3.2.1.

Table 4.3.2.1

Parameter Settings for the VERSE-LC Simulations

Physical parameters	Value
Axial dispersion coefficient, E_b	20.0 cm ² /min
Particle radius, R	100.0 μ m
Volumetric flow, Q	157.08 ml/min
Interparticle void fraction, ϵ_b	0.3
Intraparticle void fraction, ϵ_p	0.0
Particle mass density, ρ_s	1.0 g/ml
Film mass transfer parameter, k_f	0.0, 0.00001, 0.0001, 0.001, 3.0 cm/min
Langmuir coefficient, $a_{\text{(actual)}}$	0.42857
Langmuir coefficient, $a_{\text{(VERSE)}}$	0.3
Langmuir coefficient, $b_{\text{(VERSE)}}$	0.0
Initial concentration, $c_b(x, 0)$	0.0
Inlet solute concentration, $c_b(0, T)$	1.0
Grid specifics	
Column length, L	500.0 cm
Column diameter, D	10.0 cm
Time specifics	
Time duration, t_{max}	250.0 min
Key computed parameters	
Cross-sectional area, A	78.5398 cm ²
Interstitial velocity, u_0	6.66668 cm/min
L/R	50000
Peclet number, Pe_b	166.67
Film mass transfer, N_f	0.0, 0.525, 5.25, 52.5, 157500.0

In order to perform a term by term comparison to the FACT transport equations, we must convert Eqs. (4.3.2.1) and (4.3.2.16) to their dimensional form as

$$\epsilon_b \frac{\partial c_b}{\partial t} = \epsilon_b E_b \frac{\partial^2 c_b}{\partial z^2} - \epsilon_b u_0 \frac{\partial c_b}{\partial z} - \left(\frac{3}{R} \right) (1 - \epsilon_b) k_f (c_b - c_p) \quad (4.3.2.17)$$

$$a_{\text{(VERSE)}} \frac{\partial c_p}{\partial t} = \left(\frac{3}{R} \right) (1 - \epsilon_b) k_f (c_b - c_p) \quad (4.3.2.18)$$

The governing transport equations for the mobile and immobile water phase in FACT are, respectively

$$\{ \theta_m + f(1 - \phi) \rho_s k_d \} \frac{\partial c_m}{\partial t} = D \frac{\partial^2 c_m}{\partial z^2} - U \frac{\partial c_m}{\partial z} - \alpha (c_m - c_{im}) \quad (4.3.2.19)$$

$$\{\theta_{im} + (1-f)(1-\phi)p_s k_d\} \frac{\partial c_{im}}{\partial t} = \alpha(c_m - c_{im}) \quad (4.3.2.20)$$

The following is a term by term comparison of the FACT and VERSE-LC transport equations.

$$c_m = c_b, \quad c_{im} = c_p \quad \text{concentrations} \quad (4.3.2.21)$$

$$\theta_m + f(1-\phi)p_s k_d = \epsilon_b \quad \text{mobile phase time term} \quad (4.3.2.22)$$

$$\theta_{im} + (1-f)(1-\phi)p_s k_d = a_{(VERSE)} \quad \text{immobile phase time term} \quad (4.3.2.23)$$

$$D = \alpha_{LH} U = \epsilon_b E_b \quad \text{dispersion term} \quad (4.3.2.24)$$

$$q = \epsilon_b u_0 \quad \text{advection term} \quad (4.3.2.25)$$

$$\alpha = \left(\frac{3}{R} \right) (1 - \epsilon_b) K_f (c_b - c_p) \quad \text{mass transfer term} \quad (4.3.2.26)$$

FACT numerical simulation and comparison: Values of the basic physical parameters used in the verification simulations are presented in Table 4.3.2.2. The grid chosen consists of 501 rectangular brick elements uniformly sized (1.0 cm in length) and stacked along the x-axis. At the column inlet boundary (left face) a first-type Dirichlet boundary condition, $c_m(0,t)=1.0$, is applied to the mobile solute concentration at the four nodes. Due to the finite overall length of our mesh, at the outflow boundary (right face) the dispersive flux is set to zero, while the advective flux is calculated as part of the solution. Since this is a 1-D problem, solute concentrations do not exist in the transverse directions (y and z directions). Therefore, the dispersive fluxes along these four faces (top, bottom, front and back) are set to zero. The column is modeled as being fully saturated at a water content of 0.30 (total porosity of 0.30). For each simulation a transient calculation was performed for 250 min utilizing 2500 time steps of 0.1 min. The mesh spacing and time step size were chosen to keep the cell Peclet and Courant numbers less than 1 (if possible). The first-order mass transfer coefficient, α , was varied from 0 to 630 min⁻¹. The two limits chosen adequately establish the no adsorption and adsorption equilibrium conditions. The column concentration profiles at 50 min (Fig. 4.3.2.1) and the effluent (breakthrough) curves (Fig. 4.3.2.2) are computed for each FACT simulation and then compared to the VERSE-LC results. The agreement between FACT and VERSE-LC is excellent.

Table 4.3.2.2

Parameter Settings in FACT simulation of VERSE-LC Test Case

Physical parameters	Value
Darcy velocity, q	2 cm/min
Water saturation, S_w	1.0
Distribution coefficient, k_d	0.42857 ml/g
Particle mass density, ρ_s	1.0 g/ml
Total porosity, ϕ	0.30
Longitudinal horizontal dispersivity, α_{LH}	3.0 cm
Longitudinal vertical, transverse horizontal and transverse vertical dispersivities, $\alpha_{LV}, \alpha_{TH}, \alpha_{TV}$	0.0 cm
Apparent molecular dispersion coefficient, $\phi S_w \tau D^*$	0.0 cm ² /min
Radioactive decay coefficient, λ_r	0.0 min ⁻¹
1st-order reaction rate (mobile), λ_m	0.0 min ⁻¹
1st-order reaction rate (immobile), λ_{im}	0.0 min ⁻¹
Boundary solute concentration, $c_m(0, t)$	1.0
Fraction of mobile water, θ_m/θ	0.3
Fraction of adsorption sites in contact with mobile water, f	0.0
Mass transfer coefficient, α	0.0, 0.0021, 0.021, 0.21, 630 min ⁻¹
Grid specifics	
Element lengths, $\delta x = \delta y = \delta z$	1.0 cm
Number nodes in x-direction	501
Number nodes in y-direction	2
Number nodes in z-direction	2
Time steps	
Time duration	250 min
number time-steps	2500
time-step size, δt	0.1 min
Key computed parameters	
Water content, θ	0.3
Mobile water content, θ_m	0.3
Immobile water content, θ_{im}	0.0
Bulk soil density, ρ_b	0.7 g/ml
Mobile retardation factor, R_m	1.0
Immobile retardation factor, R_{im}	∞
Phasic velocity, u_x	6.66668 cm/min

Physical parameters	Value
Retarded phasic velocity, u'_x	6.66668 cm/min
Retarded dispersion coefficient, D'_{xx}	20.0 cm ² /min
Cell Peclet number, Pe_x	0.333
Cell Courant number, Co_x	0.666

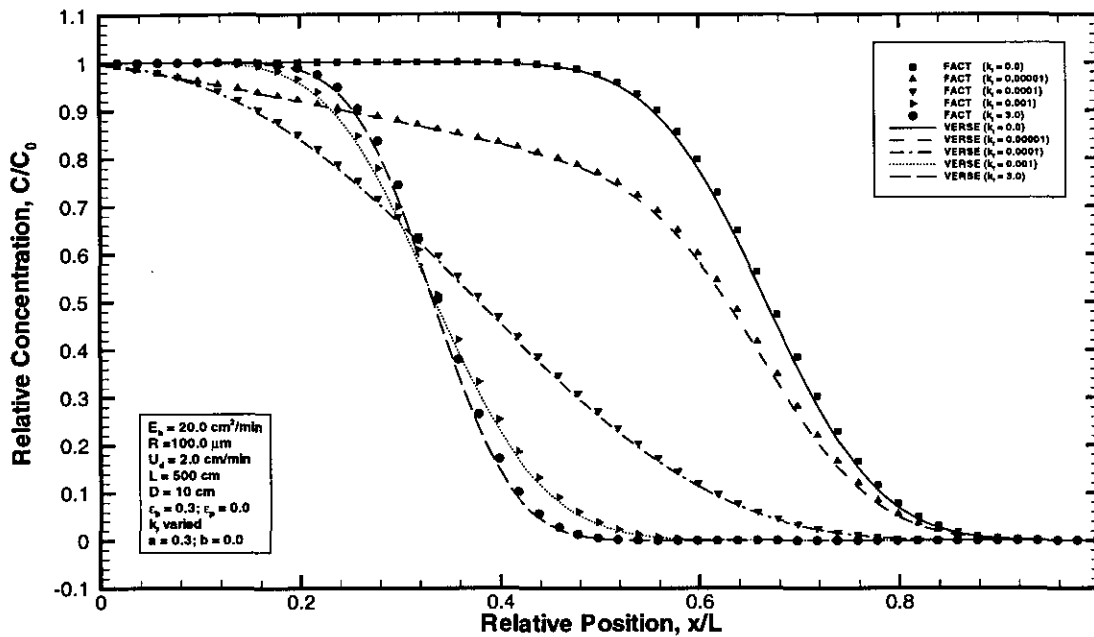


Fig. 4.3.2.1 Relative solute concentration profile comparison for VERSE-LC at 50 minutes

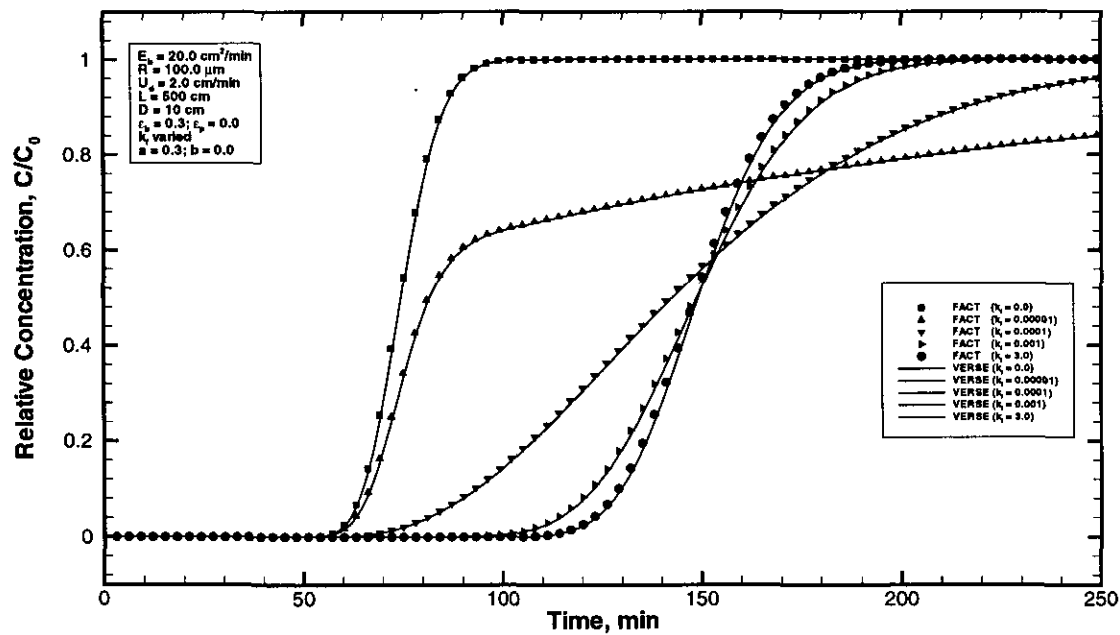


Fig. 4.3.2.2 Break-through curve comparison for VERSE-LC at 500 cm

5 Problem Definition and Simulation Procedure

A general procedure for using FACT to simulate groundwater flow and/or solute transport in subsurface systems is outlined below. The procedure (which is broken up into five major steps) is concurrently applied as needed to an example problem to further illustrate the process.

5.1 Conceptual Model

Develop a conceptual model of the physical application. Prepare a schematic description of the problem, its geometry, and the important features such as shown in Fig. 5.1. The diagram should identify zones of different material properties and potential boundary conditions, as well as locations of wells, contamination sources, surface water, etc. Determine whether flow, transport or both flow and transport simulation is desired, and whether the simulations will be steady-state, transient or both (e.g. steady-state flow and transient solute transport). Determine whether the system is confined or unconfined. For unconfined systems, decide whether detailed knowledge of unsaturated zone behavior is important. If so, then 'real' soil characteristic curves should be supplied to FACT. Otherwise, pseudo-soil characteristic curves should be supplied. In many circumstances pseudo-soil properties are quite adequate. Physical phenomena important to the problem should be identified so that these effects can be included in the simulation.

Next assemble the information and data needed to quantitatively define the conceptual model and/or calibrate the model. Example data requirements for groundwater flow problems include well head data, elevations and thickness of hydrostratigraphic units, hydraulic properties such as conductivities, source bed areas, and leakance coefficients, groundwater recharge and withdrawal. Example data inputs for solute transport problems include longitudinal and transverse dispersivities, solute properties (e.g., retardation and decay coefficients), contaminant source characteristics (location, geometry, concentration, fluxes, and decay constants), and groundwater velocities.

5.2 Model Grid

Define model coordinate system and create finite element mesh. The grid coordinate axes form a right hand Cartesian system with the z axis pointing in the upward vertical direction. In general, proper areal orientation of the mesh coordinate system is dependent on the principal axes of the hydraulic conductivity tensor and, to a lesser extent, orientation of any known no-flow surfaces (or other boundary conditions such as river BC's). If the application involves an anisotropic conductivity field, then the finite element grid should be aligned with the principal axes of the hydraulic conductivity tensor to be consistent with the FACT governing equation for groundwater flow. The current version of FACT assumes that the principle axes of the anisotropic behavior is spatially invariant. Therefore, an average orientation must be determined. Mesh boundaries should generally be aligned with no-flow surfaces whenever possible to simplify boundary condition specification and minimize data requirements.

FACT CODE MANUAL

The overall mesh dimensions should envelope the physical region of interest at a minimum. It is frequently desirable to expand the mesh beyond this region of interest in order to take advantage of convenient physical features for boundary condition specification, such as groundwater divides (no-flow B.C.) and rivers (river B.C.) and wells (prescribed head and/or concentration B.C.). Some of these concepts are illustrated in Fig. 5.2 which shows a finite element mesh superimposed upon the schematic diagram of Fig. 5.1. The left boundary in the plan view was positioned to be coincident with a pair of wells for which the head is known. The lower plan view boundary is aligned with a flow line. The bottom of the mesh in the cross-sectional view is aligned with an impermeable layer.

Once the orientation and overall mesh dimensions have been decided, the computational domain is discretized in each of the coordinate directions. Although FACT is based on a three-dimensional Cartesian formulation, one- and two-dimensional Cartesian models can be created by specifying only one element along the 'absent' coordinate axes or axis, respectively. The proper number of elements/nodes for 'present' coordinate axes depends on the physical phenomena being simulated, hydrostratigraphy and other geometric features, desired accuracy, and the computer resources available to the user. Significant user judgment and/or trial-and-error experimentation may be required to determine the proper grid resolution. Regarding accuracy, the verification problems presented in Section 4 can be used to develop a feel for accuracy as a function of spatial discretization. Verification Problem 4.2.1 is especially instructive for solute transport applications and contains some general guidelines for grid spacing. In particular, the cell Peclet number should be less than 2 ideally and no more than about 10 in practice. The cell Peclet number (dimensionless grouping) is defined as $u_i \Delta x_i / D_i$ where Δx_i is the element dimension for the i 'th coordinate direction, u_i is the local pore velocity in that direction, U_i / ϕ , and D_i is the local dispersion coefficient.

FACT utilizes eight-noded trilinear hexahedron finite elements which may be fully orthogonal, or areally orthogonal but vertically deformed as shown in Fig. 5.4. The vertical deformation is restricted to a permissible variation in the element depth and the areal coordinates of the deformed 8-node element must be the same at the top and bottom of each corner. Deformed elements enable the user to accurately model stratigraphic surfaces which are generally non-planar, and/or to conform the grid to layers of varying thickness. These concepts are illustrated in Fig. 5.2. For the lower portion of the mesh, each hydrostratigraphic layer has been assigned one computational mesh layer. However in the upper portion of the mesh, the mesh conforms to the entire thickness between the ground surface and a deep confining unit. The mesh does not align with intermediate low permeability layers. Deformed elements do introduce an added degree of numerical approximation in the influence matrix formulation of the flow and transport equations since the numerical scheme computationally assumes the elements to be entirely orthogonal. To properly handle deformed elements, two-point Gauss-Legendre quadrature is available. See verification Problem 4.1.4 for an example involving deformed elements.

FACT CODE MANUAL

Any element may be made inactive by the user. No calculations are performed for inactive elements and no flow occurs normal to their six faces. Inactive elements are effectively deleted from the physical simulation and can be used to model irregular geometries with little impact on overall computation work load. See Fig. 5.2 for a specific example.

Mesh nodes are globally numbered sequentially as

$$ig = ix + (iy - 1)nnx + (iz - 1)nnxy$$

where

ix	-	node position along x-axis (ix = 1, ..., nnx)
iy	-	node position along y-axis (iy = 1, ..., nny)
iz	-	node position along z-axis (iz = 1, ..., nnz)
nnx	-	number of nodes in x direction
nnxy	-	number of nodes in xy plane

Mesh elements are globally numbered similarly as

$$ie = ix + (iy - 1)nex + (iz - 1)nexy$$

where

ix	-	element position along x-axis (ix = 1, ..., nex)
iy	-	element position along y-axis (iy = 1, ..., ney)
iz	-	element position along z-axis (iz = 1, ..., nez)
nex	-	number of elements in x direction
nexy	-	number of elements in xy plane

This numbering scheme is illustrated in Fig. 5.3 for the example problem.

For transient simulations the time domain must also be discretized. The proper temporal discretization depends on the physical phenomena being simulated, desired accuracy and the computer resources available to the user. The (linear) transport governing equations have been discretized in the time domain with enough implicitness to make the resulting numerical equation set unconditionally stable. The flow equations are unconditionally stability when linear (i.e. properties do not depend on head and boundary conditions are linear). There is no time step constraint for these cases. For a nonlinear flow equation resulting from head-dependent properties (and/or non-linear boundary conditions) encountered in an unsaturated flow, unconditional stability cannot generally be rigorously shown. If stability problems are encountered due to strong nonlinearities, the time step should be reduced. Time steps which yield a cell Courant number less than 1 throughout the mesh for each coordinate direction will usually result in a stable simulation. The dimensionless Courant number is defined as $Co = u_i \Delta t / \Delta x_i$ where Δx_i is the element dimension for the i 'th coordinate direction, u_i is the local retarded pore velocity in that direction, $U_i / \theta R$, and Δt the time step. Stability aside, time steps satisfying $Co < 1$ may be needed to achieve sufficient accuracy regardless of the linearity of the equation set. See verification Problem 4.2.1 for an illustrative example.

5.3 Material Properties and Boundary Conditions

Define hydraulic properties, boundary conditions, and initial conditions. Hydraulic properties, such as conductivity and specific storage, are assigned to elements. For small grids and simple conceptual models, property assignments can be done by hand. For sufficiently large grids or complex conceptual models, a user-developed automated or semi-automated process for specifying element properties will be required.

Boundary conditions, sources and sinks, and initial conditions are defined on a nodal basis. The flow boundary condition and source/sink options at a node are

- specified head
- specified mixture flow
- pumping/injection well
- recirculation well
- head-dependent source bed (aquitard, river, drain or general head)
- vertical head-dependent line source
- combined recharge/drain (head-dependent)
- recharge

The recharge boundary condition is a special case of the more general prescribed flow B.C. which allows the user to easily specify recharge in the uppermost plane of nodes. The head-dependent boundary conditions are defined in Section 3.1.7. The transport boundary condition and source/sink options at a node are

- specified concentration
- specified solute mass flow
- pumping/injection well
- recirculation well
- combined recharge/drain
- recharge

Figure 5.2 illustrates how these boundary condition options might be applied to the application shown schematically in Fig. 5.1. Boundary conditions may be steady-state or transient. For transient boundary conditions, the transient function may be represented as a step function, a first-degree spline or a cubic spline.

The initial value of head and/or concentration must be specified at each node. In general, the user supplies a default value for all nodes or specifies the values on a node by node basis. The output from a simulation can be conveniently used as the initial conditions for a subsequent run through FACT I/O options.

For simulations involving only transport, the steady-state velocity in each coordinate direction must be specified at each element. As with the initial conditions, the user generally supplies a default value and then overrides the default specification on an element by element basis. The velocity output from a simulation can be conveniently used as input to a subsequent run through FACT I/O options.

FACT CODE MANUAL

5.4 FACT Input Files

Create the necessary FACT input file(s). Detailed instructions for creating a FACT input file(s) are presented in Section 7. Using Section 7, translate the conceptual model into a FACT input file(s).

5.5 FACT Execution

Execute the FACT code and analyze output file(s). FACT output files are described in detail in Section 7.

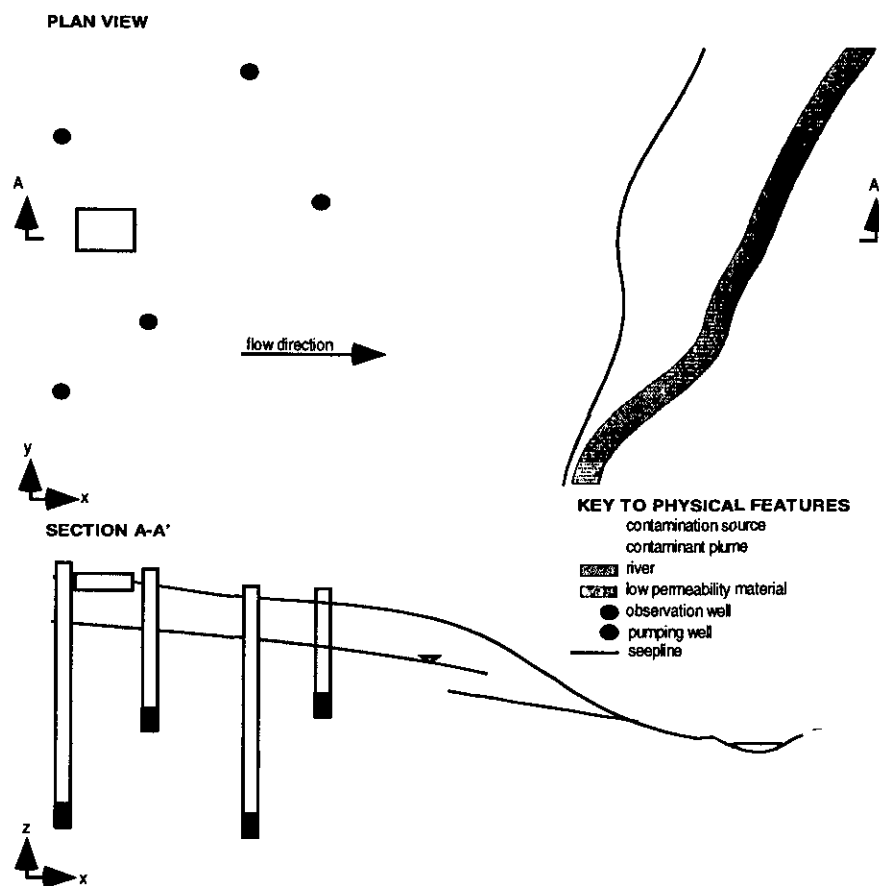


Fig. 5.1. Schematic drawing of an example groundwater flow and solute transport problem.

FACT CODE MANUAL

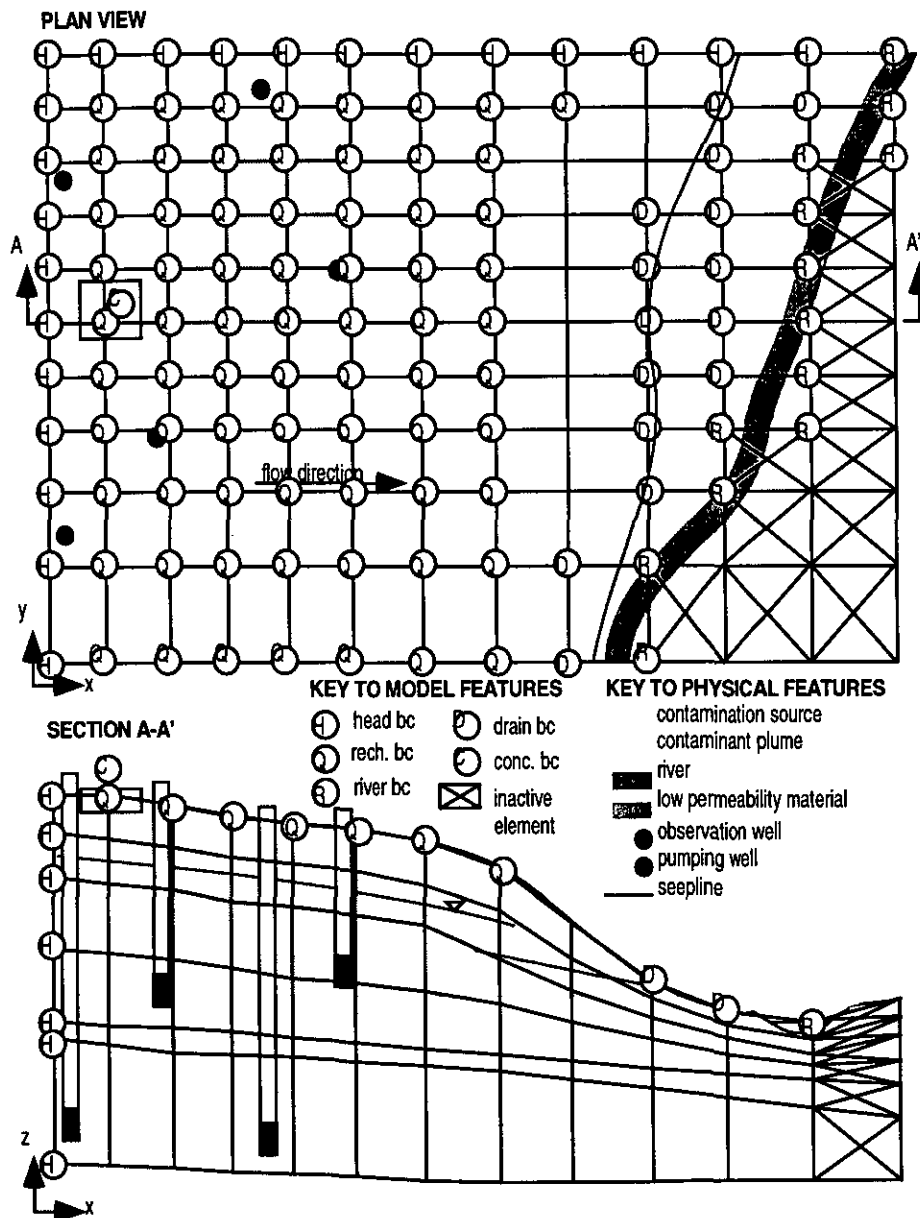


Fig. 5.2. An example FACT mesh with boundary conditions overlain on Fig. 5.1 schematic.

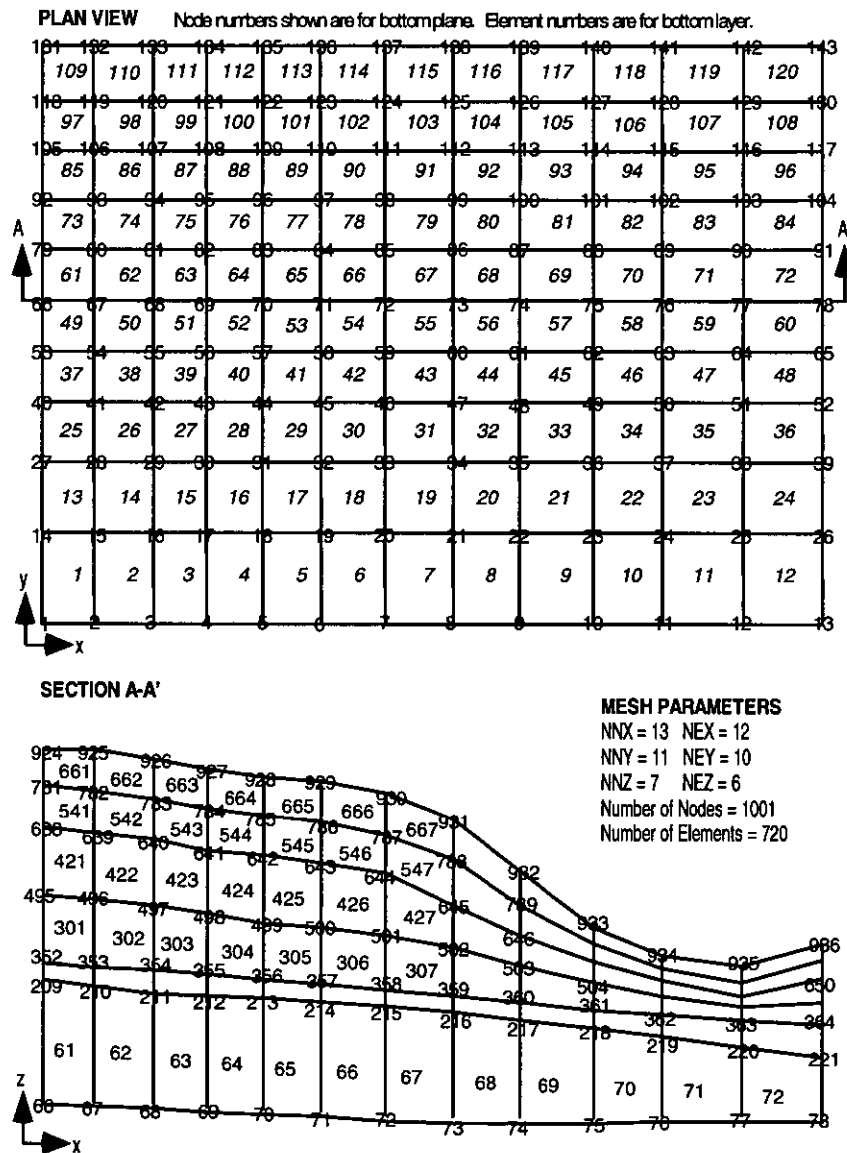


Fig. 5.3. FACT node and element numbers for mesh shown in Fig. 5.2.

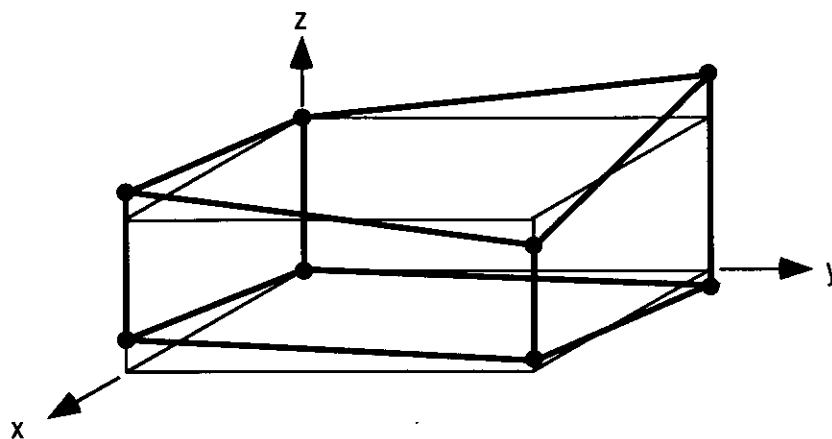


Fig. 5.4. Deformed eight-noded hexahedron element.